Probing Covalency in Actinide Molecules: A Computational Toolbox for Magnetic Resonance

A thesis submitted to the University of Manchester for the degree of
Doctor of Philosophy
in the Faculty of Science and Engineering

2022

Letitia I. Birnoschi
Department of Chemistry

Contents

Word Count: 31,300

Terms and abbreviations

AMFI	Atomic Mean-Field Integrals
AO	Atomic Orbital
BLB	Brillouin-Lévy-Berthier
BO	Born-Oppenheimer
CASSCF	Complete Active Space Self-Consistent Field
CI	Configuration Interaction
CSF	Configuration State Function
DFT	Density Functional Theory
DKH	Douglas-Kroll-Hess
DMRG	Density Matrix Renormalisation Group
EPR	Electron Paramagnetic Resonance
FC	Fermi Coupling
FCI	Full Configuration Interaction
GUGA	Graphical Unitary Group Approach
HFC	Hyperfine Coupling
HFCC	Hyperfine Coupling Constant
MCSCF	Multiconfigurational Self-Consistent Field
mDE	modified Dirac Equation
MO	Molecular Orbital
NMR	Nuclear Magnetic Resonance
OZ	Orbital-Zeeman
PCE	Picture Change Effect
PSO	Paramagnetic Spin-Orbit
RASCI	Restricted Active Space Configuration Interaction
RASSCF	Restricted Active Space Self-Consistent Field
RASSI	Restricted Active Space State Interaction
RHF	Restricted Hartree-Fock
RKB	Restricted Kinetic Balance
ROHF	Restricted Open-shell Hartree-Fock
SCF	Self-Consistent Field
SCI	Super-CI
SD	Spin-Dipole
SF	Spin-Free

SO	Spin-Orbit
SOC	Spin-Orbit Coupling
SOMF	Spin-Orbit Mean Field
SP	Spin Polarisation
SZ	Spin-Zeeman
UHF	Unrestricted Hartree-Fock
X2C	eXact-2-Component

Abstract

Magnetic resonance techniques are able to accurately probe the interactions between electron spins, nuclear spins and external magnetic fields; this information is encoded in a set of effective spin Hamiltonian parameters. Of particular interest are hyperfine coupling constants (HFCCs), which display a strong dependence on unpaired electron (spin) density, thus providing important insight into chemical bonding.

In particular, spin delocalisation can be used as a measure of covalency in paramagnetic actinide (An) molecules. The complexity of An bonding results from the possibility of valence electrons occupying some or all of the 5f, 6d, 7s and 7p orbitals, requiring sophisticated electronic structure techniques to be described *ab initio*. The non-trivial An valence space is partly a manifestation of the strong scalar relativistic and spin-orbit coupling (SOC) effects, which also need to be included in theoretical models of An chemistry.

The interpretation of isotropic HFCCs as measures of spin density at the nucleus is based on a non-relativistic Schrödinger-Pauli framework. This formalism breaks down for heavy elements, as the significant relativistic effects require a 4-component Dirac treatment. However, 4-component electronic structure approaches are unfeasible for all but the simplest systems. The computational cost can be reduced by decoupling the electronic and the positronic degrees of freedom in the Dirac Hamiltonian via a unitary transformation. Care must be taken to also apply this transformation to the hyperfine coupling operator, otherwise a picture-change error (PCE) is introduced.

Our aim is to devise a computational methodology for determining relativistic, PCE-corrected HFCCs for chemical systems of arbitrary size and complexity. With this in mind, we developed Hyperion, a Python-based program that computes SF-X2C-decoupled g-values and HFCCs from active space wavefunctions, with or without SOC included *a posteriori*. Herein, we use Hyperion to determine HFCCs for selected atoms, as well as for two An complexes previously characterised via pulsed EPR techniques. For the latter, we further employ Hyperion results to simulate hyperfine sublevel correlation (HYSCORE) spectra, thus facilitating a direct comparison with experimental data.

Declaration of originality

I hereby confirm that no portion of the work referred to in the thesis has been submitted in support of an application for another degree or qualification of this or any other university or other institute of learning.

Copyright statement

i The author of this thesis (including any appendices and/or schedules to this thesis) owns certain copyright or related rights in it (the "Copyright") and s/he has given The University of Manchester certain rights to use such Copyright, including for administrative purposes.

ii Copies of this thesis, either in full or in extracts and whether in hard or electronic copy, may be made *only* in accordance with the Copyright, Designs and Patents Act 1988 (as amended) and regulations issued under it or, where appropriate, in accordance with licensing agreements which the University has from time to time. This page must form part of any such copies made.

iii The ownership of certain Copyright, patents, designs, trademarks and other intellectual property (the "Intellectual Property") and any reproductions of copyright works in the thesis, for example graphs and tables ("Reproductions"), which may be described in this thesis, may not be owned by the author and may be owned by third parties. Such Intellectual Property and Reproductions cannot and must not be made available for use without the prior written permission of the owner(s) of the relevant Intellectual Property and/or Reproductions.

iv Further information on the conditions under which disclosure, publication and commercialisation of this thesis, the Copyright and any Intellectual Property and/or Reproductions described in it may take place is available in the University IP Policy (see `http://documents.manchester.ac.uk/DocuInfo.aspx?DocID=24420`), in any relevant Thesis restriction declarations deposited in the University Library, The University Library's regulations (see `http://www.library.manchester.ac.uk/about/regulations/`) and in The University's policy on Presentation of Theses.

Acknowledgements

It feels surreal to finally look at a completed thesis – I would be lying if I said there weren't times when I thought I could not possibly finish this work. I am immensely grateful for all the support I have received from my partner, Alex, and from my family. Thank you! I don't think I could have done it without you.

I thank Professor Nicholas Chilton for his guidance and patience throughout the past 3 and a half years, and also for entrusting me with the most interesting research project I have ever worked on (although I might be biased). Thank you also to the Chilton group members for making office life – and, post-March 2019, Zoom meetings – less mundane. To Jon Kragskow and Julia Evans, thank you for all the corridor chats, the memes and for listening to me talk (too much) about CASSCF.

Lastly, I would like to acknowledge the support from the IT Services team at the University of Manchester for providing the Computational Shared Facility, which hosted about a third of the calculations presented in this thesis. Special thanks go to Dr Daniel Corbett, who helped set up the machine that ran the other two thirds of the calculations.

Chapter 1

Introduction

1.1 Rationale for alternative format and organisation of thesis

This thesis is the result of a multi-stage approach to develop a computational tool for characterising actinide complexes via magnetic resonance parameters determined *ab initio*. In order to achieve this goal, it was first necessary to devise a suitable strategy for tackling the electronic structure in actinide complexes. Although active space wavefunction methods were identified as the most appropriate solution at the onset of this research project, questions regarding algorithm type, active space selection criteria or the inclusion of spin-orbit coupling did not have a clear answer yet. Only after refining our electronic structure approach, it was possible to conceptualise and implement a software solution – the Hyperion program – to determine EPR g-tensors and hyperfine coupling constants within the chosen wavefunction-based framework. After some initial testing, the full performance of Hyperion was assessed against a previous experimental pulsed EPR study of selected actinide complexes.[1] Following an overview of the fundamental theoretical aspects, the structure of this thesis follows the chronological progress of the research project, with each manuscript representing a discrete stage, as detailed below.

Paper one: "Anomalous Magnetism of Uranium(IV)-Oxo and -Imido Complexes Reveals Unusual Doubly-Degenerate Electronic Ground States"
J.A. Seed, L. Birnoschi, E. Lu, F. Tuna, A.J. Wooles, N.F. Chilton and S.T. Liddle, *Chem*, **7**, 1666–1680

In this work, CASSCF-SO and crystal field parametrisation techniques are used to elucidate the unusually high low-temperature magnetic moments measured in two newly-synthesised uranium(IV) complexes. We discover that the axial oxo and imido ligands generate pseudo-symmetric electronic structures that result in pseudo-doublet spin-orbit ground states, giving rise to atypical magnetic profiles. Both complexes are best modelled using a minimal active space, however state-averaging results in an overestimated first energy gap. A crystal field model is employed to further improve the predicted electronic spectrum via optimisation with respect to experimental measurements of temperature-dependent magnetism.

J.A.S. prepared and characterised the compounds. L.B. carried out and interpreted the

CASSCF-SO calculations and the subsequent crystal field parameter analysis. J.A.S., E.L., and F.T. carried out and interpreted the SQUID magnetometry. A.J.W. collected, solved, and refined all the crystallographic data. N.F.C. and S.T.L. assisted with data analysis, directed the research, and wrote the manuscript with input from all the authors.

Paper two: "Hyperion: A New Computational Tool for Relativistic Ab Initio Hyperfine Coupling"
L. Birnoschi and N.F. Chilton, *J. Chem. Theory Comput.* 2022, **18**, 8, 4719–4732

This manuscript provides a comprehensive description of Hyperion, a Python-based program for computing relativistic g-tensors and hyperfine coupling parameters from active space wavefunctions, with or without spin-orbit coupling (SOC) included *a posteriori*. Hyperion also includes a new orbital decomposition method for assisting active space selection for calculations of hyperfine coupling. For benchmarking purposes, we determine hyperfine coupling constants of selected alkali metal, transition metal and lanthanide atoms, based on CASSCF-SO, RASSCF-SO and RASCI-SO calculations in OpenMolcas. Our results are in excellent agreement with experimental data from atomic spectroscopy, as well as theoretical predictions from 4-component relativistic calculations.

The entire paper is the work of L.B. N.F.C. provided guidance and assisted with writing the manuscript.

Paper three: "A Relativistic Quantum Chemical Investigation of Actinide Covalency Measured by EPR Spectroscopy"
L. Birnoschi and N.F. Chilton, *unpublished*

This work investigates actinide covalency in two $AnCp^{tt}_3$ (An = Th, U) complexes using the Hyperion package to obtain relativistic g-tensors and hyperfine coupling constants, which are further employed in simulations of hyperfine sublevel correlation (HYSCORE) spectra. We compare our results to experimental data reported by Formanuik *et al*, in order to assess the performance of fully *ab initio* models of ligand hyperfine coupling. The extent of covalency in $AnCp^{tt}_3$ is quantified via Mulliken spin population analysis, which uncovers different patterns in the spin density transfer between An and the ligand atoms.

The entire paper is the work of L.B. N.F.C. provided guidance and assisted with writing the manuscript.

1.2 Actinide covalency and connection to hyperfine coupling

The study of actinide bonding is primarily motivated by the need to improve separations of lanthanide (Ln) and actinide (An) ions in spent nuclear fuel processing.[2] Although such separations are complicated by the similar ionic radii of Ln and An, differences in bonding modes can be exploited via strategic complexation. Whereas Ln compounds are largely ionic due to the contracted nature of the valence 4f shell, An 5f orbitals are sufficiently expanded to overlap with ligand orbitals, thus giving rise to covalent bonds. Actinide covalency is thought to occur either as a result of enhanced orbital overlap (overlap-driven covalency)[3] or due to incidental orbital degeneracy (energy-degeneracy-driven covalency)[4]. This interpretation follows the rationale of MO theory and is possibly oversimplified, however, even from a state-of-the-art electronic structure perspective, An bonding is non-trivial due to the potential involvement of 5f, 6d, 7s and 7p orbitals.[5]

A method for quantifying An covalency is therefore highly desirable, so as to facilitate the systematic screening of families of complexes and the identification of periodic trends. Analytical schemes based on Mulliken (electron) populations, natural localised molecular orbitals and the Quantum Theory of Atoms in Molecules (QTAIM) have previously been employed in investigations of An covalency.[3,6–8] Powerful insight was obtained by supporting computational findings with experimental data from X-ray absorption spectroscopy (XAS)[9] or Nuclear Magnetic Resonance (NMR) spectroscopy.[8,10,11] In essence, all analytical schemes mentioned divide the electron density distribution – usually determined computationally via Density Functional Theory (DFT) – into segments assigned to specific atoms and/or bonds; partitioning is done at the basis function level (e.g. Mulliken,[12] Löwdin)[13] or at the wavefunction level (e.g. natural population analysis,[14] QTAIM).[15] The applicability of each formalism depends on the underlying assumptions, which range from a (somewhat arbitrary) equal distribution of shared electron density among atoms (Mulliken)[12] to a rigorous model of molecular structure as an open quantum system (QTAIM).[15] The results of population analysis can be roughly qualified as physical or unphysical, based on chemical intuition and/or experimental insight, however electron populations themselves are not physical observables and cannot be experimentally validated. Hence, it is important to consider multiple quantifiers so as to avoid drawing biased conclusions.

Spin population analysis is a less frequently used technique that can be applied to paramagnetic species. In the context of paramagnetic An complexes, the presence of ligand atoms with non-zero spin populations suggests that the unpaired electrons (the spins) are delocalised, which can be interpreted as a departure from the ionic bonding regime – *ergo*, covalency. Although the approaches used to divide electron density should also be applicable to spin density and therefore yield a similarly varied array of spin population techniques, currently only Mulliken spin population analysis is widely supported by electronic structure software. However, spin delocalisation can also be quantified through hyperfine coupling constants (HFCCs) measured via Electron Paramagnetic Resonance (EPR) spectroscopy. This possibility of directly relating a theoretical measure of covalency to a phys-

ical observable was exploited by Formanuik *et al* in the first pulsed EPR study of An covalency,[1] wherein empirical relationships between HFCCs and spin populations were used to extract ligand spin populations from hyperfine sublevel correlation (HYSCORE) data.

Hyperfine coupling (HFC) strength is proportional to spin density and scales as r_{N}^{-3}, where r_{N} is the electron spin-magnetic nucleus distance; as such, HFCCs are particularly sensitive to small variations in the spin density distribution. However, this also makes HFCCs challenging to determine computationally due to the strong dependence on electron correlation, which requires a multiconfigurational electronic structure approach and thus relatively expensive calculations. There is currently no established general strategy for electronic structure studies targeting HFCCs,[†] although previous work in this area has shown that basis set size, polarisation functions and configuration excitation level all have a non-negligible impact on accuracy.[16–25] We note that Kohn-Sham DFT, which is a single-configurational approach, has been extensively used to calculate HFC parameters for organic radicals and transition metal complexes, with good results,[26–28] however a growing body of evidence indicates that this is due to fortuitous error cancellation.[24,29] From among wavefunction-based algorithms, active space methods, such as Complete Active Space Self-Consistent Field (CASSCF), provide the most flexibility in terms of balance between accuracy – determined by the proportion of correlation effects captured – and cost. Flexibility is further enhanced by the variety of implementations available, particularly within the OpenMolcas software.[30] It is not surprising, therefore, that a number of recent HFC studies make use of active space methods, ranging from Restricted Active Space Self-Consistent Field (RASSCF)[31,32] to Density Matrix Renormalisation Group CASSCF (DMRGSCF).[33] Nevertheless, there is still scope for further investigation, particularly regarding active space selection strategies targeting HFCC accuracy.

The magnetic properties of actinide complexes are heavily influenced by relativistic effects, which are conventionally split into two categories: spin-independent, or scalar relativistic (SR), and spin-dependent; from the latter category, spin-orbit coupling (SOC) is most important. SR effects are most prominent near atomic nuclei and therefore affect HFCCs; they are usually accounted for by using a scalar-relativistic Hamiltonian in the electronic structure optimisation, in place of the usual (non-relativistic) Schrödinger Hamiltonian. Meanwhile, there are various approaches to calculating spin-orbit (SO) effects; in the weak SOC limit, these can be treated as perturbations, however strong SOC should be included in the zeroth order Hamiltonian to obtain a qualitatively accurate electronic wavefunction. Strong relativistic effects are an additional complicating factor for *ab initio* models of HFC, as the Fermi Contact (FC) contribution related to spin density at the nucleus does not arise naturally in relativistic theories.[34] Hence, the direct relationship between isotropic HFCCs – which are equal to the FC contribution in the non-relativistic, no-SOC limit – and spin population cannot be reliably used in relativistic systems.

We therefore set out to develop a relativistic, fully *ab initio* framework for determining

[†]A common denominator in previous theoretical HFC work is the use of uncontracted basis sets, however this becomes unfeasible for large, experimentally-relevant molecules.

HFCCs, with a view to study An covalency in experimentally-relevant molecules. We employ active space wavefunction-based methods and contracted basis sets to maintain feasible computational costs, and explore the impact of active space selection on predicted HFCCs. In order to assess the accuracy of this methodology, hyperfine structure measurements from atomic spectroscopy are used as benchmarks. For larger systems, where low symmetry precludes the straightforward determination of HFCCs from EPR measurements, HYSCORE spectra are simulated based on the computed HFCCs and compared with experimental spectra. Finally, spin delocalisation and hence An covalency are quantified via Mulliken spin population analysis.

References

(1) A. Formanuik, A.-M. M. Ariciu, F. Ortu, R. Beekmeyer, A. Kerridge, F. Tuna, E. J. L. McInnes and D. P. Mills, *Nature Chemistry*, 2017, **9**, 578–583.

(2) K. A. Pace, V. V. Klepov, A. A. Berseneva and H. C. zur Loye, *Chemistry - A European Journal*, 2021, **27**, 5835–5841.

(3) E. Lu, S. Sajjad, V. E. Berryman, A. J. Wooles, N. Kaltsoyannis and S. T. Liddle, *Nature Communications*, 2019, **10**, 1–10.

(4) J. Su, E. R. Batista, K. S. Boland, S. E. Bone, J. A. Bradley, S. K. Cary, D. L. Clark, S. D. Conradson, A. S. Ditter, N. Kaltsoyannis, J. M. Keith, A. Kerridge, S. A. Kozimor, M. W. Löble, R. L. Martin, S. G. Minasian, V. Mocko, H. S. La Pierre, G. T. Seidler, D. K. Shuh, M. P. Wilkerson, L. E. Wolfsberg and P. Yang, *Journal of the American Chemical Society*, 2018, **140**, 17977–17984.

(5) S. K. Singh, C. J. Cramer and L. Gagliardi, *Inorganic Chemistry*, 2020, **59**, 6815–6825.

(6) M. J. Tassel and N. Kaltsoyannis, *Dalton Transactions*, 2010, **39**, 6719–6725.

(7) D. D. Schnaars, A. J. Gaunt, T. W. Hayton, M. B. Jones, I. Kirker, N. Kaltsoyannis, I. May, S. D. Reilly, B. L. Scott and G. Wu, *Inorganic Chemistry*, 2012, **51**, 8557–8566.

(8) J. Du, J. A. Seed, V. E. Berryman, N. Kaltsoyannis, R. W. Adams, D. Lee and S. T. Liddle, *Nature Communications*, 2021, **12**, 1–11.

(9) D. C. Sergentu, T. J. Duignan and J. Autschbach, *Journal of Physical Chemistry Letters*, 2018, **9**, 5583–5591.

(10) S. L. Staun, D. C. Sergentu, G. Wu, J. Autschbach and T. W. Hayton, *Chemical Science*, 2019, **10**, 6431–6436.

(11) M. Autillo, L. Guerin, T. Dumas, M. S. Grigoriev, A. M. Fedoseev, S. Cammelli, P. L. Solari, D. Guillaumont, P. Guilbaud, P. Moisy, H. Bolvin and C. Berthon, *Chemistry - A European Journal*, 2019, 4435–4451.

(12) R. S. Mulliken, *Journal of Chemical Physics*, 1955, **23**, 1833.

(13) P. O. Löwdin, *Advances in Quantum Chemistry*, 1970, **5**, 185–199.

(14) A. E. Reed and F. Weinhold, *Journal of Chemical Physics*, 1985, **83**, 1736–1740.

(15) R. F. Bader, *Chemical Reviews*, 1991, **91**, 893–928.

(16) B. Engels, S. D. Peyerimhoff and E. R. Davidson, *Molecular Physics*, 1987, **62**, 109–127.

(17) D. Feller and E. R. Davidson, *Journal of Chemical Physics*, 1988, **88**, 7580–7587.

(18) C. W. Bauschlicher, S. R. Langhoff, H. Partridge and D. P. Chong, *Journal of Chemical Physics*, 1988, **89**, 2985–2992.

(19) I. Carmichael, *Journal of Chemical Physics*, 1989, **91**, 1072–1078.

(20) B. Engels and S. D. Peyerimhoff, *Molecular Physics*, 1989, **67**, 583–600.

(21) C. W. Bauschlicher, *Journal of Chemical Physics*, 1990, **92**, 518–521.

(22) B. Engels, *Chemical Physics Letters*, 1991, **179**, 398–404.

(23) D. M. Chipman, *Theoretica Chimica Acta*, 1992, **82**, 93–115.

(24) B. Engels, Ab Initio Post-Hartree-Fock Calculations of Hyperfine Coupling Tensors and Their Comparison with DFT Approaches, in *Calculation of NMR and EPR Parameters: Theory and Applications*, WILEY-VCH, 2004, ch. 30, pp. 483–492.

(25) P. Jakobsen and F. Jensen, *Journal of Chemical Physics*, 2019, **151**.

(26) L. Hermosilla, P. Calle, J. M. García De La Vega and C. Sieiro, *Journal of Chemical Physics*, 2005, **109**, 1114–1124.

(27) S. Kossmann, B. Kirchner and F. Neese, *Molecular Physics*, 2007, **105**, 2049–2071.

(28) Z. W. Windom, A. Perera and R. J. Bartlett, *Journal of Chemical Physics*, 2021, **156**, 094107.

(29) M. Witwicki, P. K. Walencik and J. Jezierska, *Journal of Molecular Modeling*, 2020, **26**.

(30) F. Aquilante, N. Ferré, J. Autschbach, I. Conti, A. Baiardi, L. D. Vico, S. Battaglia, A. Veniamin, D. Ernst, J. Norell, R. Lindh, M. Delcey, I. F. Galván, L. Freitag, M. Garavelli, X. Gong, S. Knecht, A. Nenov, M. Lundberg, I. Schapiro, M. Odelius, Q. M. Phung, L. Ungur, F. Segatta, M. Olivucci, L. Seijo, T. B. Pedersen, L. Pedraza-gonzález, J. Segarra-martí, K. Pierloot, M. Vacher, M. Reiher, A. Valentini, V. Veryazov, I. Conti, I. F. Galván and L. Freitag, *Journal of Chemical Physics*, 2020, **152**, 1–33.

(31) K. Sharkas, B. Pritchard and J. Autschbach, *Journal of Chemical Theory and Computation*, 2015, **11**, 538–549.

(32) R. Feng, T. J. Duignan and J. Autschbach, *Journal of Chemical Theory and Computation*, 2020, 1–8.

(33) T. N. Lan, Y. Kurashige and T. Yanai, *Journal of Chemical Theory and Computation*, 2014, **11**, 73–81.

(34) W. Kutzelnigg, *Theoretica Chimica Acta*, 1988, **73**, 173–200.

Chapter 2

Theoretical Background

2.1 Wavefunction theory of electronic structure

2.1.1 Born-Oppenheimer approximation

The theoretical treatment of electronic structure starts with the Born-Oppenheimer (BO) approximation, also known as the clamped nucleus approximation, which assumes that electrons adjust instantaneously to nuclear motion. For a fixed set of nuclear coordinates described by the vector $\mathbf{R}$, the electronic structure can be elucidated by solving the eigenvalue problem

$$\widehat{H}_{\mathrm{e}}\Psi_{\mathrm{e}}(\mathbf{r};\mathbf{R}) = E_{\mathrm{e}}(\mathbf{R})\Psi_{\mathrm{e}}(\mathbf{r};\mathbf{R}), \tag{2.1}$$

where $\widehat{H}_{\mathrm{e}}$ is the electronic Hamiltonian to be diagonalised, $E_{\mathrm{e}}(\mathbf{R})$ is the electronic energy at the fixed geometry and $\Psi_{\mathrm{e}}(\mathbf{r};\mathbf{R})$ is the electronic wavefunction. The *e* subscript will henceforth be dropped, as this work is concerned exclusively with electronic operators, energies and wavefunctions determined within the BO framework. In the non-relativistic (nr) limit, the electronic problem is described by the Schrödinger Hamiltonian

$$\widehat{H}^{(0)}_{\mathrm{nr}} = \frac{1}{2m_e}\sum_i \widehat{\mathbf{p}}_i \cdot \widehat{\mathbf{p}}_i - \frac{e^2}{4\pi\epsilon_0}\sum_{i,N}\frac{Z_N}{R_{Ni}} + \frac{e^2}{4\pi\epsilon_0}\sum_{i>j}\frac{1}{r_{ij}}, \tag{2.2}$$

where the three sums correspond to kinetic, electron-nucleus and electron-electron interaction terms, respectively. Note that summations in Equation 2.2 run over electrons i, j and/or nuclei N.

2.1.2 Single-configurational methods

The simplest electronic structure model of an N_{e}-electron system assumes that each electron is subjected to a mean field resulting from the combined influence of all nuclei and the remaining $N_{\mathrm{e}} - 1$ electrons. This results in a single-configurational description where electrons are distributed among a set of spin-orbitals $\{\chi_j(\mathbf{r}_i, m_{S,i})\}$, which are functions of one-electron spatial coordinates ($\mathbf{r}_i$) and spin projection ($m_{s,i}$). We henceforth use the notation $\mathbf{x}_i$ to denote the vector containing both spatial and spin coordinates of the i^{th} electron. Since the Schrödinger Hamiltonian does not contain any spin-dependent terms, it is

common practice to separate spatial and spin degrees of freedom by writing spin orbitals as

$$\chi_{p\sigma}(\mathbf{x}_i) = \phi_p(\mathbf{r}_i)\ \sigma(m_{S,i}) \tag{2.3}$$

where $\phi_p(\mathbf{r}_i)$ is a spatial orbital – or, simply, an orbital – and $\sigma(m_{S,i})$ is a one-electron spin function denoted as $|\alpha\rangle$ for a spin-up electron ($m_S = 1/2$) or as $|\beta\rangle$ for a spin-down electron ($m_S = -1/2$). The occupation number of a spatial orbital can be 2 (doubly-occupied orbital with spin-paired electrons), 1 (singly occupied orbital with one unpaired electron) or 0 (unoccupied orbital).

The multi-electron wavefunction is conceptually the product of single-electron spin orbitals, however the wavefunction must be anti-symmetrised in order to satisfy the Pauli exclusion principle, which ensures that the electronic wavefunction changes sign upon swapping two electron labels and that no two electrons occupy the same quantum state. Mathematically, the appropriately anti-symmetrised N_e-electron configuration is represented as a Slater determinant:

$$|\chi_1\chi_2\cdots\chi_{N_\mathrm{e}}\rangle = \frac{1}{\sqrt{N_\mathrm{e}!}}\begin{vmatrix} \chi_1(\mathbf{x}_1) & \chi_2(\mathbf{x}_1) & \cdots & \chi_n(\mathbf{x}_1) \\ \chi_1(\mathbf{x}_2) & \chi_2(\mathbf{x}_2) & \cdots & \chi_n(\mathbf{x}_2) \\ \vdots & \vdots & \ddots & \vdots \\ \chi_1(\mathbf{x}_{N_\mathrm{e}}) & \chi_2(\mathbf{x}_{N_\mathrm{e}}) & \cdots & \chi_n(\mathbf{x}_{N_\mathrm{e}}) \end{vmatrix}. \tag{2.4}$$

A Slater determinant can therefore be succinctly represented as a set of spin-orbital occupation numbers. Although Slater determinants are eigenfunctions of the spin projection operator $\widehat{S}_z$, they do not have a defined total spin, since multiple spin multiplicities can give rise to the same spin projection. It is then useful to linearly combine determinants to form Configuration State Functions (CSFs),[1] which are eigenfunctions of the total spin operator $\widehat{S}^2$, and can be represented as sets of (spatial) orbital occupation numbers. By using CSFs in electronic structure calculations instead of Slater determinants, the spin multiplicity of the system is preserved. Additionally, the number of CSFs formed for a spin S by distributing N_e electrons among N_o orbitals, Equation 2.5 (see Appendix A for derivation), is smaller than the corresponding number of Slater determinants, Equation 2.6, which has important consequences for the computational cost of multiconfigurational algorithms (Sections 2.1.3 and 2.1.4).

$$N_\mathrm{CSF}(N_\mathrm{e}, N_\mathrm{o}, S) = \frac{2S+1}{N_\mathrm{o}+1}\binom{N_\mathrm{o}+1}{N_\mathrm{e}/2 - S}\binom{N_\mathrm{o}+1}{N_\mathrm{e}/2 + S + 1} \tag{2.5}$$

$$N_\mathrm{det}(N_\mathrm{e}, N_\mathrm{o}) = \binom{2N_\mathrm{o}}{N_\mathrm{e}} \tag{2.6}$$

In single-configurational electronic structure methods, the occupied molecular orbitals (MOs) are modelled as linear combinations of basis functions (most commonly a non-orthogonal set of atomic orbitals, AOs). MO expansion coefficients are optimised via a self-consistent

field (SCF) procedure by solving the secular equation

$$\boldsymbol{FC} = \boldsymbol{SC}\epsilon, \tag{2.7}$$

where $\boldsymbol{F}$ is the matrix representation of the Fock operator in the AO basis, $\boldsymbol{C}$ contains all MO coefficients, $\boldsymbol{S}$ is the AO overlap matrix and ϵ is the MO energy. The Fock operator is a one-electron approximation of the electronic Hamiltonian in Equation 2.2, obtained by replacing the two-electron interaction term with a mean-field potential generated by $N_\mathrm{e} - 1$ electrons.

Single-configurational SCF algorithms applied to closed-shell systems are known as Restricted Hartree-Fock (RHF) and result in identical spatial distributions for spin-paired electrons. In the case of open-shell systems, orbitals associated with paired electrons can either be identical (Restricted Open-Shell Hartree-Fock, ROHF)[2] or different (Unrestricted Hartree-Fock, UHF). ROHF methods represent the wavefunction as a CSF,[3] while UHF uses a single Slater determinant model where the α and β spin-orbital manifolds are associated with different secular equations. Although computationally cheaper than ROHF, UHF wavefunctions suffer from spin contamination and are not usually true spin eigenfunctions – that is, their spin projection $\langle \widehat{S}_z \rangle$ is not integer or half-integer – which affects the accuracy of predicted energies and properties.

2.1.3 Multiconfigurational methods

The single-configurational description of electronic structure is unreliable for a large number of chemical systems, ranging from "simple" dimers[4,5] to buckminsterfullerene,[6] and including, in particular, orbitally-degenerate molecules such as lanthanide and actinide complexes.[7] The difference between the total energy and the SCF prediction is known as correlation energy and is mostly a result of the instantaneous electron-electron interaction (dynamical correlation). However, there is also a second contribution, the static or non-dynamical correlation, which does not have a physical origin, but rather results from the inability of a single configuration to provide a qualitatively correct picture of the electronic structure.

In order to represent electron correlation in the context of wavefunction theory (WFT), we introduce the Configuration Interaction (CI) ansatz, Equation 2.8, which represents the N-electron wavefunction as a linear combination of configurations Φ_I (Slater determinants or CSFs) defined with respect to a fixed set of MOs. When the summation in (2.8) includes all possible configurations obtained by distributing N electrons among all the MOs, the resulting wavefunction ansatz is known as Full Configuration Interaction (Full CI, FCI); in the limit of an infinite basis set, the FCI wavefunction is exact. We note that herein we use spin-adapted techniques and therefore all CI-type wavefunctions are defined in terms of CSFs.

$$\Psi_\mathrm{CI} = \sum_I C_I \Phi_I. \tag{2.8}$$

The vast majority of multiconfigurational techniques implement a CI ansatz where the expansion coefficients C_I are optimised variationally. Unfortunately, the computational cost of such algorithms scales exponentially with the number of orbitals, rendering FCI optimisation unfeasible for all but the simplest systems. Truncated expansions that include a subset of all possible CSFs are usually a reasonable compromise; as the CI expansion of dynamically correlated systems is dominated by one particular configuration (the *reference* configuration), robust configuration selection criteria can be defined using the energy and/or the excitation level[†] with respect to the reference.

Common electronic structure approaches involve an initial SCF step, followed by a multiconfigurational method such as CI to account for correlation.[‡] This is an excellent strategy for modelling dynamical correlation, as the SCF calculation provides an optimal orbital-based description of the reference, which, in most cases, already provides a qualitatively correct picture of the electronic structure. The orbital basis is less important for excited configurations, as they are associated with much smaller CI coefficients. Instead, the accuracy of the variational CI energy is primarily determined by the size of the accessible configuration space.

A different strategy is necessary, however, to model strongly correlated systems. Within the CI framework, strong correlation manifests as a multireference wavefunction, containing multiple large contributions to the CI expansion. As a result, single-configurational methods cannot provide a suitable starting point for the correlation-including step. Instead, MOs should be optimised with respect to all reference configurations via a Multiconfigurational SCF (MCSCF) procedure.

MCSCF methods represent the wavefunction as a CI expansion in terms of selected configurations, with the goal of optimising both the CI coefficients and the underlying MOs self-consistently.[8,9] Although general MCSCF frameworks allow for arbitrary configuration selections, the most widely used approaches are based on the concept of an *active space*,[10,11] wherein a user-defined number of electrons and set of orbitals completely determine which configurations are included in the MCSCF wavefunction.

2.1.4 CASSCF and RASSCF

Complete Active Space (CAS) theories[10–12] divide the molecular orbital space into three categories: inactive orbitals, which are doubly occupied in all considered configurations, active orbitals, having variable occupation, and virtual orbitals, which remain unoccupied. The multiconfigurational wavefunction is then represented as a superposition of all CSFs obtained by distributing a predetermined number of active electrons among the active orbitals. Although CI methods traditionally use a determinant-based expansion for the wavefunc-

[†]The excitation level of a Slater determinant or CSF with respect to the reference corresponds to the number of (spin-)orbitals that have different occupations in the two configurations. A configuration that differs from the reference by one (spin-)orbital is a single excitation (or a "single"), one that differs by two spin orbitals is a "double" and so on. Note that the same configuration – understood in the general, electrons-in-orbitals sense – can be associated with different excitation levels, depending on whether a CSF- or a determinant-based description is used.

[‡]For this reason, multiconfigurational methods are also known as post-Hartree-Fock, or post-HF, methods.

tion, as this results in an easily vectorisable implementation, the Split Graphical Unitary Group Approach (Split GUGA)[13–16] enables modern CASSCF codes to employ a CSF-based description instead,[§] thus preserving spin symmetry and maintaining relatively low memory and storage requirements (c.f. equations 2.5 and 2.6). In particular, the CASSCF implementation in OpenMolcas uses a spin-free formalism, that is, from the $2S+1$ spin-adapted eigenstates $|SM\rangle$ that form a spin multiplet, only the state with the maximum projection – the "spin-free" state $|SS\rangle$ – is explicitly determined.

The CASSCF method optimises both the CI coefficients and the MOs; CI-only variants that keep the MOs constant are referred to as CASCI. While the CI problem is a straightforward diagonalisation of the Hamiltonian matrix in configuration space, CASSCF orbital optimisation seeks to solve the Brillouin-Lévy-Berthier (BLB) problem:[10]

$$\left\langle 0 \left| \widehat{H} \left(\widehat{E}_{pq} - \widehat{E}_{qp} \right) \right| 0 \right\rangle = 0, \qquad \widehat{E}_{pq} = \widehat{a}^{\dagger}_{p\alpha} \widehat{a}_{q\alpha} + \widehat{a}^{\dagger}_{p\beta} \widehat{a}_{q\beta}. \tag{2.9}$$

In Equation 2.9, $|0\rangle$ is the CASSCF wavefunction and $\widehat{E}_{pq}$ denotes a (singlet) excitation operator from orbital q to orbital p. $\widehat{E}_{pq}$ is formally defined using second-quantisation creation ($\widehat{a}^{\dagger}$) and annihilation ($\widehat{a}$) operators. The CASSCF wavefunction is invariant with respect to orbital rotations within the inactive, active and virtual subspaces and, as a result, only BLB elements with p and q belonging to different subspaces have to be considered. Modern CASSCF codes, including the OpenMolcas implementation employed herein, solve the BLB problem via the Super-CI (SCI) formalism. The SCI wavefunction,

$$|\text{SCI}\rangle = |0\rangle + \sum_{p>q} c_{pq} \, |p \rightarrow q\rangle \, , \tag{2.10}$$

is constructed by adding to $|0\rangle$ all singly-excited configurations $|p \rightarrow q\rangle$ (SX states) of the form

$$|p \rightarrow q\rangle = \left(\widehat{E}_{pq} - \widehat{E}_{qp} \right) |0\rangle \, . \tag{2.11}$$

The BLB equation 2.9 therefore reduces to a CI-type problem wherein the coefficients c_{pq} are optimised; this is solved approximately due to computational constraints.[10,11] The natural orbitals obtained by diagonalising the Super-CI one-particle density matrix are then used as the new orbital set. When determining more than one electronic state/root (state-averaged CASSCF, SA-CASSCF), a weighted average of state-specific Super-CI density matrices is diagonalised instead – this yields *pseudonatural* orbitals. We note that all state-averaged calculations reported in this thesis use equal weightings for the optimised roots.

Restricted Active Space (RAS) approaches[17] are an extension of the CAS model, allowing the active orbitals to be partitioned into three subspaces, RAS1, RAS2 and RAS3. The RAS1 orbitals are mostly doubly-occupied and a user-defined maximum number of electrons is allowed out of the entire subspace. Similarly, RAS3 orbitals are mostly unoccupied, with a user-defined maximum number of electrons allowed into the subspace. RAS2 is the active

[§]Note that the OpenMolcas implementation of CASSCF still uses Slater determinants in the innermost subroutines of the CI optimisation steps.

space in CAS-type calculations in which all excitation levels are allowed. Due to these restrictions, RASSCF and RASCI algorithms can accommodate a larger number of active orbitals compared to CASSCF/CASCI, at the expense of slower convergence due to orbital rotations between RAS subspaces being strongly coupled to CI rotations.[17] RAS methods are suited for electronic structure problems requiring large active spaces [†] or for incorporating (some) dynamical correlation effects into the orbital optimisation procedure. Hence, this method is well-suited to modelling hyperfine coupling, which is particularly sensitive to dynamical correlation and to variations in the MO basis.

The flexibility of active space methods makes them an attractive option for a wide variety of chemical systems, as the size of the calculation can be tuned to give an optimal balance between accuracy and cost. It comes as no surprise, then, that this area of computational chemistry has seen a number of exciting developments in recent years. The exponentially scaling Davidson diagonalisation employed for CI optimisation drastically limits the applicability of CASSCF. As a result, new implementations have been proposed, where the standard CI eigensolver is replaced by an approximate, lower-scaling method such as stochastic Quantum Monte Carlo CI (commonly referred to as FCIQMC),[18] Density Matrix Renormalisation Group (DMRG)[19,20] or Heat-bath CI (HCI).[21] The first two approaches are implemented in OpenMolcas, while the latter is available as part of the PySCF package.[22,23] Aside from the CI solver, the AO basis size also poses difficulties, as integrals have to be transformed after each orbital optimisation iteration; Sun and coworkers provide a solution to this problem in the form of an AO-driven CASSCF algorithm,[24] also implemented in PySCF. Most recently, a Localised Active Space SCF (LASSCF) method has been proposed as an electronic structure strategy for strongly correlated systems with weakly entangled subunits.[25]

The additional parameters introduced by new implementations naturally require extensive benchmarking to establish optimal/recommended values, as well as ranges of applicability. Nevertheless, a varied toolkit of active space techniques is ideal for tackling electronic structure problems at the forefront of chemical research – including, but not limited to, actinide complexes – where the large number of degrees of freedom and the complex electron interactions render conventional approaches unfeasible.

2.1.5 Chemical properties in second quantisation

The expectation value of a one-particle operator $\widehat{F}$ with respect to an N-electron wavefunction Ψ is expressed in first quantisation as

$$\left\langle \Psi \left| \widehat{F} \right| \Psi \right\rangle = \int \widehat{F}(\mathbf{x}_1)\, \gamma_1(\mathbf{x}_1, \mathbf{x}_1)\; \mathrm{d}\mathbf{x}_1, \tag{2.12}$$

[†] The largest feasible active space within CASSCF is around CAS(16,16), although the exact limit also depends on the spin multiplicity and on the AO basis size.

where $\gamma_1(\mathbf{x}_1, \mathbf{x}_1')$ denotes the first-order/one-particle reduced density matrix

$$\gamma_1(\mathbf{x}_1, \mathbf{x}_1') = N \int \Psi^*(\mathbf{x}_1, \mathbf{x}_2, \dots \mathbf{x}_N)\ \Psi(\mathbf{x}_1, \mathbf{x}_2, \dots \mathbf{x}_N)\ \mathrm{d}\mathbf{x}_2 \dots \mathrm{d}\mathbf{x}_N. \tag{2.13}$$

Note that all integrals in equations 2.12 and 2.13 are evaluated over the entire physical space and over all spin states. Although equation 2.12 is exact, the continuous integrals over an infinite range of spatial coordinates are impractical to implement in orbital-based electronic structure algorithms. Instead, expectation values are represented in *second quantisation*, using matrix elements ($F_{p\sigma,q\tau}$) over spin-orbitals, together with creation ($\widehat{a}^\dagger_{p\sigma}$) and annihilation ($\widehat{a}_{q\tau}$) operators which enable the "movement" of electrons in configuration space. The expectation value of $\widehat{F}$ hence becomes

$$\left\langle \Psi \left| \widehat{F} \right| \Psi \right\rangle = \sum_{p\sigma q\tau} F_{p\sigma,q\tau}\ \left\langle \Psi \left| \widehat{a}^\dagger_{p\sigma} \widehat{a}_{q\tau} \right| \Psi \right\rangle, \tag{2.14}$$

where

$$F_{p\sigma,q\tau} = \int \phi_p^*(\mathbf{r})\ \sigma^*(m_S)\ \widehat{F}(\mathbf{r})\ \phi_q(\mathbf{r})\ \tau(m_S)\, \mathrm{d}\mathbf{r}\, \mathrm{d}m_S. \tag{2.15}$$

Products of creation and annihilation operators are represented in matrix form by (reduced) density matrices (RDMs). The one-particle RDM (1-RDM) of state $|\Psi\rangle$ – i.e. the second quantisation equivalent of equation 2.13 – is formally defined in spin-orbital space as

$$\Gamma_{p\sigma,q\tau} = \int \Psi^*(\mathbf{x}_1, \mathbf{x}_2, \dots \mathbf{x}_N)\ \widehat{a}^\dagger_{p\sigma} \widehat{a}_{q\tau}\ \Psi(\mathbf{x}_1, \mathbf{x}_2, \dots \mathbf{x}_N)\ \mathrm{d}\mathbf{x}_1\, \mathrm{d}\mathbf{x}_2 \dots \mathrm{d}\mathbf{x}_N. \tag{2.16}$$

If $\widehat{F}$ only acts on functions of spatial coordinates, then the spin degree of freedom in equation 2.15 can be integrated out.[‡] The resulting expectation value can then be evaluated in (spatial) orbital space, using the *spin-summed* 1-RDM,

$$P^{\alpha+\beta}_{pq} = \Gamma_{p\alpha,q\alpha} + \Gamma_{p\beta,q\beta}\ , \tag{2.17}$$

as

$$\left\langle \Psi \left| \widehat{F} \right| \Psi \right\rangle = \sum_{pq} F_{pq}\ P^{\alpha+\beta}_{pq}, \qquad F_{pq} = \int \phi_p^*(\mathbf{r})\ \widehat{F}(\mathbf{r})\ \phi_q(\mathbf{r})\, \mathrm{d}\mathbf{r}. \tag{2.18}$$

Note that the elements of $\boldsymbol{P}^{\alpha+\beta}$ are integrals of the excitation operators $\widehat{E}_{pq}$ introduced in equation 2.9.

If, on the other hand, $\widehat{F}$ acts on both spatial and spin functions, its second quantisation representation in orbital space is less straightforward to derive. To begin with, consider a one-particle operator of the form

$$\widehat{F}(\mathbf{r}, m_S) = \widehat{V}(\mathbf{r})\ \widehat{S}_z(m_S), \tag{2.19}$$

[‡]The term "integration" is used loosely here, as the domain of m_S consists of two values, $+1/2$, corresponding to $|\alpha\rangle$, and $-1/2$, corresponding to $|\beta\rangle$, hence the "integral" is really just a discrete sum of two terms.

where we have used $\widehat{S}_z$ to denote the one-electron spin projection operator and $\widehat{V}(\mathbf{r})$ to represent the purely spatial part of $\widehat{F}$. The effect of $\widehat{S}_z$ on one-electron spin functions is, by convention,

$$\widehat{S}_z \left|\alpha\right\rangle = +\frac{1}{2} \left|\alpha\right\rangle, \qquad \widehat{S}_z \left|\beta\right\rangle = -\frac{1}{2} \left|\beta\right\rangle, \tag{2.20}$$

hence

$$\left\langle \alpha \left| \widehat{S}_z \right| \alpha \right\rangle = +\frac{1}{2}, \tag{2.21}$$

$$\left\langle \beta \left| \widehat{S}_z \right| \beta \right\rangle = -\frac{1}{2}, \tag{2.22}$$

$$\left\langle \alpha \left| \widehat{S}_z \right| \beta \right\rangle = \left\langle \beta \left| \widehat{S}_z \right| \alpha \right\rangle = 0, \tag{2.23}$$

since $\left|\alpha\right\rangle$ and $\left|\beta\right\rangle$ are orthogonal. For a pair of orbitals p and q, we have

$$F_{p\alpha,q\alpha} = +\frac{1}{2} \int \phi_p^*(\mathbf{r})\, \widehat{V}(\mathbf{r})\, \phi_q(\mathbf{r})\, \mathrm{d}\mathbf{r} = +\frac{1}{2}\, V_{pq}, \tag{2.24}$$

$$F_{p\beta,q\beta} = -\frac{1}{2} \int \phi_p^*(\mathbf{r})\, \widehat{V}(\mathbf{r})\, \phi_q(\mathbf{r})\, \mathrm{d}\mathbf{r} = -\frac{1}{2}\, V_{pq}, \tag{2.25}$$

and

$$\left\langle \Psi \left| \widehat{F} \right| \Psi \right\rangle = \frac{1}{2} \sum_{pq} V_{pq} \left\langle \Psi \left| \widehat{a}^\dagger_{p\alpha} \widehat{a}_{q\alpha} - \widehat{a}^\dagger_{p\beta} \widehat{a}_{q\beta} \right| \Psi \right\rangle \tag{2.26}$$

$$= \frac{1}{2} \sum_{pq} V_{pq}\, P^{\alpha-\beta}_{pq}. \tag{2.27}$$

In equation 2.27, we have introduced the one-particle reduced spin density matrix $\boldsymbol{P}^{\alpha-\beta}$ – usually referred to as spin density matrix or spin 1-RDM – with elements

$$P^{\alpha-\beta}_{pq} = \Gamma_{p\alpha,q\alpha} - \Gamma_{p\beta,q\beta}\ . \tag{2.28}$$

Although the present discussion has so far focused on expectation values, we note that the calculation of matrix elements between different N-electron wavefunctions follows the same principles, with state-specific 1-RDMs replaced by one-particle *transition density matrices* (1-TDMs). While state-specific 1-RDMs are real and symmetric for real wavefunctions, 1-TDMs are not generally symmetric, but they are always real for real wavefunctions.

We are now in a position to consider a general one-particle operator acting on both spatial and spin functions,

$$\widehat{F} = \widehat{\mathbf{V}}(\mathbf{r}) \cdot \widehat{\mathbf{S}} \tag{2.29}$$

$$= \widehat{V}^x\, \widehat{S}_x + \widehat{V}^y\, \widehat{S}_y + \widehat{V}^z\, \widehat{S}_z \tag{2.30}$$

$$= \widehat{V}^+\, \widehat{S}_- - \widehat{V}^-\, \widehat{S}_+ + \widehat{V}^z\, \widehat{S}_z. \tag{2.31}$$

Equations 2.30 and 2.31 are expansions of $\widehat{F}$ in terms of Cartesian and spherical tensor

operators, respectively. The relationship between the two sets is given by

$$\widehat{V}^{\pm} = \widehat{V}^{x} \pm i\widehat{V}^{y}\,, \qquad \widehat{S}_{\pm} = \widehat{S}_{x} \pm i\widehat{S}_{y}, \tag{2.32}$$

where i denotes the imaginary unit. Although the Cartesian expansion is simpler, spherical operators are better suited to determinations of matrix elements with respect to spin eigenfunctions – we therefore employ the latter in the remainder of this section. The second quantisation representation of $\widehat{F}$ is

$$\widehat{F} = \sum_{pq} \left(V^{+}_{pq}\, \widehat{T}^{1,-1}_{pq} - V^{-}_{pq}\, \widehat{T}^{1,1}_{pq} + V^{z}_{pq}\, \widehat{T}^{1,0}_{pq} \right), \tag{2.33}$$

where $\widehat{T}^{1,1}_{pq}$, $\widehat{T}^{1,-1}_{pq}$, and $\widehat{T}^{1,0}_{pq}$ are spherical *triplet excitation operators* defined as

$$\widehat{T}^{1,1}_{pq} = -\widehat{a}^{\dagger}_{p\alpha}\widehat{a}_{q\beta} \tag{2.34}$$

$$\widehat{T}^{1,-1}_{pq} = \widehat{a}^{\dagger}_{p\beta}\widehat{a}_{q\alpha} \tag{2.35}$$

$$\widehat{T}^{1,0}_{pq} = \frac{1}{2}\left(\widehat{a}^{\dagger}_{p\alpha}\widehat{a}_{q\alpha} - \widehat{a}^{\dagger}_{p\beta}\widehat{a}_{q\beta} \right). \tag{2.36}$$

Note that the matrix representation of $\widehat{T}^{1,0}_{pq}$ is the spin 1-RDM $\boldsymbol{P}^{\alpha-\beta}$ multiplied by a factor of $1/2$.

Together with the singlet operator $\widehat{E}_{pq}$, the triplet excitation operators form a set of tensors that transform as spin eigenfunctions. As a result, their matrix elements with respect to spin eigenstates $|SM\rangle$ – where S is the spin quantum number and M denotes the spin projection – can be calculated using the Wigner-Eckart (WE) theorem, equation 2.37.

$$\left\langle ASM \left| \widehat{T}^{[k]}(q) \right| BS'M' \right\rangle = \langle S'M'kq\,|SM\rangle \left\langle AS \left|\left| \widehat{\mathbf{T}}^{[k]} \right|\right| BS' \right\rangle \tag{2.37}$$

Above, we added the labels A and B to the bra-ket notation to denote an arbitrary set of spin-independent quantum numbers, highlighting the applicability of WE theorem to electronic wavefunctions having different spatial parts. The first element on the right-hand-side of equation 2.37 denotes a Clebsch-Gordan (CG) coefficient, while the second is independent of the spin projection and is known as a WE-reduced matrix element. Equation 2.37 uses conventional tensor operator notation for clarity, however note that the tensor index q should not be confused with the orbital label employed in second quantisation expressions. To avoid any further confusion, we henceforth drop the general notation and instead refer to the corresponding second quantisation excitation operators:

$$\widehat{T}^{[0]}(0) \to \widehat{E}_{pq}\,; \qquad \widehat{T}^{[1]}(1) \to \widehat{T}^{1,1}_{pq}\,; \qquad \widehat{T}^{[1]}(-1) \to \widehat{T}^{1,-1}_{pq}\,; \qquad \widehat{T}^{[1]}(0) \to \widehat{T}^{1,0}_{pq}\,. \tag{2.38}$$

The coupling between spin-adapted states $|ASM\rangle$ and $|BS'M'\rangle$ under a mixed spin-spatial

operator $\widehat{F}$ can therefore be expressed as

$$\begin{aligned}\left\langle ASM \left| \widehat{F} \right| BS'M' \right\rangle = \sum_{pq} \Big(& V_{pq}^{+} \ \langle S'M'1 \ -1 \, | SM \rangle \ \left\langle AS \left\| \widehat{\mathbf{T}}_{pq}^{[1]} \right\| BS' \right\rangle \\ & - V_{pq}^{-} \ \langle S'M'1 \ 1 \, | SM \rangle \ \left\langle AS \left\| \widehat{\mathbf{T}}_{pq}^{[1]} \right\| BS' \right\rangle \\ & + V_{pq}^{z} \ \langle S'M'1 \ 0 \, | SM \rangle \ \left\langle AS \left\| \widehat{\mathbf{T}}_{pq}^{[1]} \right\| BS' \right\rangle \Big) . \end{aligned} \tag{2.39}$$

The WE theorem is essential for calculating spin-dependent properties from spin-free electronic structure data. Matrix elements of the type $\left\langle ASS \left| \widehat{T}_{pq}^{1,0} \right| BS'S' \right\rangle$ are straightforwardly determined via equation 2.27 and only require the spin 1-RDM (1-TDM) of the spin-free state(s) and the integrals V_{pq} in the orbital basis. The results can then be divided by the appropriate CG coefficient to obtain the WE-reduced elements, which are subsequently used in 2.39 to determine matrix elements between states of arbitrary spin projection M.[§] An example of this methodology is described in Section 2.1.6.

We end this overview by highlighting some particularities of matrix rotations between orbital bases. Most electronic structure frameworks employ a set of non-orthogonal AOs, while optimised MOs are made orthonormal; transformations between the two bases are therefore a common occurrence in both electronic structure optimisations and property calculations. It is worthwhile to note that, while density matrices (spin or spin-summed, 1-RDMs or 1-TDMs) and matrices of spatial integrals V_{pq} share a common orbital basis, they transform differently. As such, for a spatial integral matrix $\boldsymbol{V}$ and a density matrix $\boldsymbol{P}$, AO↔MO rotations are expressed as:

$$\boldsymbol{V}^{\text{MO}} = \boldsymbol{C}^{\top} \ \boldsymbol{V}^{\text{AO}} \ \boldsymbol{C} \tag{2.40}$$

$$\boldsymbol{V}^{\text{AO}} = \boldsymbol{S} \ \boldsymbol{C} \ \boldsymbol{V}^{\text{MO}} \ \boldsymbol{C}^{\top} \ \boldsymbol{S} \tag{2.41}$$

$$\boldsymbol{P}^{\text{MO}} = \boldsymbol{C}^{\top} \ \boldsymbol{S} \ \boldsymbol{P}^{\text{AO}} \ \boldsymbol{S} \ \boldsymbol{C} \tag{2.42}$$

$$\boldsymbol{P}^{\text{AO}} = \boldsymbol{C} \ \boldsymbol{P}^{\text{MO}} \ \boldsymbol{C}^{\top} \, , \tag{2.43}$$

where $\boldsymbol{S}$ is the AO overlap matrix and $\boldsymbol{C}$ is the matrix of MO coefficient (column) vectors. The validity of these expressions can be verified by checking that the integral

$$\left\langle \Psi \left| \widehat{V} \right| \Psi \right\rangle = \text{Tr} \left[\boldsymbol{V}^{\top} \boldsymbol{P} \right] = \text{Tr} \left[\boldsymbol{P}^{\top} \boldsymbol{V} \right] \tag{2.44}$$

is invariant under orbital basis transformations.

2.1.6 State interaction methods for spin-orbit coupling

The Restricted Active Space State Interaction (RASSI) method is used to determine the spin-orbit coupling between spin-adapted CASSCF/RASSCF states via a quasi-degenerate per-

[§]Within the Hyperion implementation, this is referred to as the spin-free ($|ASS\rangle$ states) to spin-free+spin ($|ASM\rangle$ states) basis transformation.

turbation theory (QDPT) formalism.[26] Unlike traditional perturbative approaches, RASSI is suitable for systems exhibiting strong SOC, while also being more computationally affordable compared to variational SOC-including algorithms.

RASSI models spin-orbit coupling based on the Breit-Pauli (BP) spin-orbit Hamiltonian,

$$H_{\mathrm{SO}}^{\mathrm{BP}} = \sum_i H_{\mathrm{SO}}^{\mathrm{BP}}(i) + \sum_{i \neq j} H_{\mathrm{SO}}^{\mathrm{BP}}(i,j), \tag{2.45}$$

with the one-electron ($H_{\mathrm{SO}}^{\mathrm{BP}}(i)$) and two-electron ($H_{\mathrm{SO}}^{\mathrm{BP}}(i,j)$) contributions defined as

$$H_{\mathrm{SO}}^{\mathrm{BP}}(i) \quad = \frac{e^2\hbar}{2\,m_e^2\,c^2} \sum_N \frac{\mathrm{Z}_N}{r_N^3}\,\mathbf{s}_i \cdot \mathbf{l}_{iN}\ , \tag{2.46}$$

$$H_{\mathrm{SO}}^{\mathrm{BP}}(i,j) = -\frac{e^2\hbar}{2\,m_e^2\,c^2}\,\frac{\mathbf{l}_{ij}}{r_{ij}^3} \cdot (\mathbf{s}_i + 2\mathbf{s}_j)\ . \tag{2.47}$$

In Equations 2.46 and 2.47, $\mathbf{l}_{iN}$ and $\mathbf{l}_{ij}$ denote the orbital angular momentum of electron i with respect to nucleus N and with respect to electron j, respectively, while Z_N represents the bare nuclear charge of N. To circumvent handling computationally expensive two-electron integrals, an effective one-electron representation – the spin-orbit mean-field (SOMF) approximation[27] – is employed:

$$\begin{aligned} H_{pq}^{\mathrm{SOMF}} = \ & \left\langle p \left| \widehat{H}_{\mathrm{SO}}(1) \right| q \right\rangle + \frac{1}{2} \sum_t n_t \left[\left\langle pt \left| \widehat{H}_{\mathrm{SO}}(1,2) \right| qt \right\rangle \right. \\ & \left. - \left\langle pt \left| \widehat{H}_{\mathrm{SO}}(1,2) \right| tq \right\rangle - \left\langle tp \left| \widehat{H}_{\mathrm{SO}}(1,2) \right| qt \right\rangle \right], \end{aligned} \tag{2.48}$$

where indices p, q and t correspond to spin-orbitals, n_t are effective orbital occupation numbers, and $\widehat{H}_{\mathrm{SO}}(1)$ and $\widehat{H}_{\mathrm{SO}}(1,2)$ denote one-electron and two-electron SOC operators, respectively. Within RASSI, computational cost is further reduced by only considering one-center integrals when constructing the H_{pq}^{SOMF} matrix elements[†] and using atomic average valence occupations[§] for n_t – this is known as the method of Atomic Mean-Field Integrals (AMFI).[28]

As the AMFI spin-orbit Hamiltonian is an effective spin-dependent one-electron operator, its general form can be written as

$$\widehat{H}_{\mathrm{SO}}^{\mathrm{AMFI}} = \widehat{\mathbf{V}}^{\mathrm{AMFI}}(\mathbf{r}) \cdot \widehat{\mathbf{S}}, \tag{2.49}$$

which is identical to operator in Equation 2.29. $\widehat{\mathbf{V}}^{\mathrm{AMFI}}(\mathbf{r})$ is constructed entirely from atomic parameters and, as a result, its integrals can be evaluated in the AO basis prior to the electronic structure calculation.

[†] In other words, integrals between basis functions on different atoms are not included.

[§] The average valence occupation of a given atom is p/m, where p is the number of valence electrons and m, the number of valence orbitals.

Following the strategy outlined in section 2.1.5, the SO Hamiltonian matrix $\boldsymbol{H}_{\text{SO}}$ (we drop the AMFI superscript for brevity) is constructed in the $|ASM\rangle$ basis derived optimised spin-free states from CASSCF/RASSCF. Wigner-Eckart-reduced AMFI matrix elements are evaluated as

$$V^k_{AB} = \sum_{pq} {}^{A\to B}P^{\text{WE}}_{pq}\, V^k_{pq}, \qquad k = x, y, z\,, \tag{2.50}$$

where we have introduced the WE-reduced 1-TDM between states $|ASS\rangle$ and $|BS'S'\rangle$,

$${}^{A\to B}P^{\text{WE}}_{pq} = \frac{1}{2\,\langle S'S'1\;0\,|SS\rangle}\; {}^{A\to B}P^{\alpha-\beta}_{pq}. \tag{2.51}$$

Using WE-reduced 1-RDMs and 1-TDMs is more efficient than computing WE-reduced matrix elements for each term in the second quantisation expansion, c.f. equation 2.39. As $\widehat{H}_{\text{SO}}$ is a one-electron spin-dependent operator, only matrix elements with $\Delta S = 0, \pm 1$ and $\Delta M = 0, \pm 1$ are non-zero; for reference, we include general expressions for these below.

$$\left\langle A\,S\,M\left|\widehat{H}_{\text{SO}}\right|B\,S+1\,M\pm1\right\rangle = -\frac{1}{2}\sqrt{\frac{(S\pm M+1)(S\pm M+2)}{(S+1)(2S+1)(2S+3)}}\;(\pm V^x_{AB} + V^y_{AB}) \tag{2.52}$$

$$\left\langle A\,S\,M\left|\widehat{H}_{\text{SO}}\right|B\,S+1\,M\right\rangle = \sqrt{\frac{(S+1)^2-M^2}{(S+1)(2S+1)(2S+3)}}\;V^z_{AB} \tag{2.53}$$

$$\left\langle A\,S\,M\left|\widehat{H}_{\text{SO}}\right|B\,S\,M\pm1\right\rangle = \pm\frac{1}{2}\sqrt{\frac{(S\mp M)(S\pm M+1)}{S(S+1)(2S+1)}}\;(\pm V^x_{AB} + V^y_{AB}) \tag{2.54}$$

$$\left\langle A\,S\,M\left|\widehat{H}_{\text{SO}}\right|B\,S\,M\right\rangle = \frac{M}{\sqrt{S(S+1)(2S+1)}}\;V^z_{AB} \tag{2.55}$$

$$\left\langle A\,S\,M\left|\widehat{H}_{\text{SO}}\right|B\,S-1\,M\pm1\right\rangle = \frac{1}{2}\sqrt{\frac{(S\mp M)(S\mp M-1)}{S(2S-1)(2S+1)}}\;(\pm V^x_{AB} + V^y_{AB}) \tag{2.56}$$

$$\left\langle A\,S\,M\left|\widehat{H}_{\text{SO}}\right|B\,S-1\,M\right\rangle = \sqrt{\frac{S^2-M^2}{S(2S-1)(2S+1)}}\;V^z_{AB} \tag{2.57}$$

Once constructed, the $\boldsymbol{H}_{\text{SO}}$ matrix is then diagonalised to yield SO eigenstates as linear combinations of the original $|ASM\rangle$ states.

2.2 Relativistic quantum chemistry

2.2.1 Decoupling of the Dirac equation

The electron density of heavy elements is strongly influenced by relativity, particularly in the vicinity of nuclei, where electrons travel at appreciable fractions of the speed of light. For this reason, any approach designed to model HFC in actinide complexes must include

relativistic effects to be meaningful. Any relativistic electronic structure problem formally starts from the one-electron Dirac equation or from the many-electron Breit equation.[29] The 4-component (4c) solutions (known as *spinors*) diagonalise the relativistic Hamiltonian and give rise to an energy spectrum containing both positive and negative values, which are identified as electronic and positronic eigenstates, respectively.

Consider the generalised form of a 4-component many-electron Hamiltonian,[30]

$$\widehat{\mathbf{H}}_{4c} = \sum_{i,N} \begin{pmatrix} V_{iN} & c(\boldsymbol{\sigma}_i \cdot \widehat{\mathbf{p}}_i) \\ c(\boldsymbol{\sigma}_i \cdot \widehat{\mathbf{p}}_i) & V_{iN} - 2m_e c^2 \end{pmatrix} + \frac{1}{2} \sum_{i \neq j} \widehat{\mathbf{g}}(i,j) + \boldsymbol{V}_{NN}. \tag{2.58}$$

Here, $\boldsymbol{\sigma}_i$ and $\widehat{\mathbf{p}}_i$ are operators acting on the coordinates of electron i, $\widehat{\mathbf{g}}(i,j)$ acts on the coordinates of electrons i and j, while V_{iN} and $\boldsymbol{V}_{NN}$ denote the electron-nucleus and nucleus-nucleus interaction potentials, respectively. $\boldsymbol{\sigma}_i$ is the 3-vector of Pauli matrices, $\widehat{\mathbf{p}}_i$ is the linear momentum operator, c is the speed of light and m_e, the rest mass of the electron. The first term on the right-hand side represents the Dirac Hamiltonian, written in 2×2 block form, where each block is a 2-component operator.

Relativistic electronic structure calculations reported herein make use of the Dirac-Coulomb Hamiltonian, where the 2-electron contribution only includes the Coulomb interaction,

$$g^{C}(i,j) = \frac{e^2}{4\pi\epsilon_0} \sum_{i>j} \frac{1}{r_{ij}}, \tag{2.59}$$

which essentially amounts to taking the non-relativistic limit of electrodynamics.[30] The relativistic many-electron Hamiltonian can be improved by additionally including the Breit term,[31]

$$g^{B}(i,j) = -\frac{e^2}{8\pi\epsilon_0} \left[\frac{\boldsymbol{\alpha}_i \cdot \boldsymbol{\alpha}_j}{r_{ij}} + \frac{(\boldsymbol{\alpha}_i \cdot \mathbf{r}_{ij})(\boldsymbol{\alpha}_j \cdot \mathbf{r}_{ij})}{r_{ij}^3} \right], \tag{2.60}$$

yielding the Dirac-Coulomb-Breit (DCB) Hamiltonian. In Equation 2.60, $\boldsymbol{\alpha}_i$ and $\boldsymbol{\alpha}_j$ are 3-vectors of Dirac matrices. We note that the DCB Hamiltonian is not implemented in OpenMolcas and is therefore not used in this work.

It is possible to solve the Dirac-Coulomb(-Breit) equation self-consistently; the algorithm is known as Dirac-Hartree-Fock (DHF) and has been employed in HFCC calculations, albeit only for atoms[32,33] and open-shell diatomics.[34,35] Relativistic self-consistent algorithms have seen slow progress due to early issues caused by the finite-basis representation of the Dirac Hamiltonian; this problem was labelled "finite basis set disease"[36] and manifested as spurious low-energy intruder states.[37] A solution was proposed in the early 80s, in the form of restricted kinetic balance (RKB).[38]

The most significant drawback of DHF, particularly with regards to HFCCs, is the inability to account for electron correlation.[35] From among the correlation-including 4-component methods available, multiconfigurational Dirac-Fock (MCDF) and relativistic coupled-

cluster (CC) are notable examples that have been involved in HFC studies.[33,39] While the 4-component level of theory is the most elegant formalism describing relativistic electronic structure, its various implementations require significant computational resources, especially when correlation is required. Computational cost could be reduced by employing a 4-component DFT method,[40] which has been successfully applied to a series of $4d^1$ and $5d^1$ complexes.[41] However, just as any DFT approach, this is only appropriate for single-reference problems.

A common strategy to increase the efficiency of a relativistic approach is decoupling the positronic degrees of freedom (the lower/small component) from the electronic degrees of freedom (the upper/large component), thereby reducing the electronic structure problem to a 2-component framework. In what follows, we discuss strategies for decoupling the one-electron Dirac Hamiltonian; however, many-electron electronic structure methods seek to decouple the 4-component one-electron Fock operator, which additionally includes an effective potential resulting from the interaction of an electron with other electrons. If two-electron magnetic and retardation effects are ignored – which can be achieved by ignoring the Breit term – then the effective electron-electron contribution can be represented as a scalar potential, [42] i.e. in a form similar to the electron-nucleus potential V_{iN}. Hence, the Dirac operator and the Fock operator only differ in the form of the electrostatic potential V and have otherwise similar matrix representations; as such, the decoupling strategies discussed below are applicable to both.

Decoupling can either be achieved by elimination of the small (lower) component (ESC) or by a unitary transformation that reduces the 4-component Hamiltonian to a block-diagonal form. The former method is based on the 2-component ESC equation[43]

$$(V - E)\,\psi^{\mathrm{U}} + \frac{1}{2m_{\mathrm{e}}e^2}\,\left[(c\,\boldsymbol{\sigma}\cdot\widehat{\mathbf{p}})\omega(c\,\boldsymbol{\sigma}\cdot\widehat{\mathbf{p}})\right]\,\psi^{\mathrm{U}} = 0, \tag{2.61}$$

where ψ^{U} is the upper component of the 4-spinor and ω is given by

$$\omega = \left[1 - \frac{V-E}{2m_{\mathrm{e}}c^2}\right]^{-1} = \sum_{k=0}^{\infty}\left(\frac{V-E}{2m_{\mathrm{e}}c^2}\right)^k. \tag{2.62}$$

The order of the unnormalised ESC (UESC) calculation is given by the last term of the truncated sum.

The scalar parameter ω can also be written as

$$\omega = \frac{2m_{\mathrm{e}}c^2}{2m_{\mathrm{e}}c^2 - V}\left[1 + \frac{E}{2m_{\mathrm{e}}c^2 - V}\right]^{-1}, \tag{2.63}$$

which forms the basis of the regular approximation (RA) family of elimination methods. The lowest order truncation of this expression defines the zero order regular approximation (ZORA). This is perhaps the most popular relativistic formalism in theoretical HFCC studies and has been widely used in combination with DFT.[44–46] Autschbach[47] studied the

performance of this approach for HFC integrals and concluded that, while ZORA accurately predicts the properties related to valence electrons, it fails to describe core shells correctly.

Filatov and Cremer used the improved infinite order regular approximation (IORA) in combination with *ab initio* methods[48] and with DFT[49] to predict isotropic HFCCs for atoms and some mercury molecules. They found that IORA with a modified metric (IORAmm) yields reasonable results as long as a balanced description of spin polarisation is available from the electronic structure theory. In a later study,[50] the normalised elimination of the small component (NESC) formalism was employed within wavefunction theory to predict hyperfine parameters of selected mercury compounds.

One major disadvantage of ESC methods is their reliance on energy-dependent parameters that are not variational. This can be circumvented by decoupling the 4-component problem via a unitary transformation $\widehat{\mathbf{U}}$ that block-diagonalises the Dirac Hamiltonian ($\widehat{\mathbf{H}}_{\mathrm{D}}$):

$$\widehat{\mathbf{H}}_{\mathrm{bd}} = \widehat{\mathbf{U}}^{\dagger}\,\widehat{\mathbf{H}}_{\mathrm{D}}\,\widehat{\mathbf{U}} = \begin{pmatrix} \widehat{H}_{\mathrm{bd}}^{(+)} & 0 \\ 0 & \widehat{H}_{\mathrm{bd}}^{(-)} \end{pmatrix}. \tag{2.64}$$

The Douglas-Kroll-Hess (DKH) transformation relies on the expansion of the Hamiltonian in powers of the external potential V. A series of unitary matrices $\widehat{\mathbf{U}}_k$ sequentially remove off-diagonal terms up to order k, yielding a DKHn Hamiltonian decoupled to n^{th} order in V:

$$\widehat{\mathbf{H}}_{\mathrm{DKH}n} = \widehat{\mathbf{U}}_n \cdots \widehat{\mathbf{U}}_1\,\widehat{\mathbf{H}}_{\mathrm{D}}\,\widehat{\mathbf{U}}_1^{\dagger} \cdots \widehat{\mathbf{U}}_n^{\dagger}. \tag{2.65}$$

In the context of HFCC calculations, scalar relativistic DKH has been successfully used in conjunction with DFT,[51,52] orbital-optimised second-order Møller-Plesset theory (OO-MP2),[53] and DMRGSCF.[54] Malkin *et al* were the first to investigate the advantages of using a finite nucleus within a DFT/DKH2 approach[52] over the usual point nucleus;[51] a general increase in accuracy was observed for predicted HFCCs of atoms and small molecules. Sandhofer *et al*[53] compared DKH calculations starting from the default free-particle Foldy-Wouthuysen (fpFW) transformation and from its gauge-invariant correspondent (denoted by fπFW), concluding that the latter produces divergent HFCCs. Finally, Lan *et al*[54] implemented the higher order DKH3 transformation (and corresponding property operators) combined with DMRGSCF to compute scalar relativistic hyperfine data for small transition metal molecules.

When adopting a transformation-based decoupling approach, care must be taken to apply the same unitary transformation to the property operators. If this is not done, the calculated molecular integrals are inaccurate – this is known as the picture change effect (PCE). PCE is significant in regions close to the nuclei of heavy elements, therefore affecting HFC parameters. For example, Sharkas *et al*[55] employed a scalar relativistic DKH scheme combined with CASSCF/RASSI to describe SR and SOC effects, respectively. However, the hyperfine operators used were not picture change corrected, thus limiting the applicability of this method to electrons in light atoms/ligands or in high angular momentum orbitals (where the HFC is dominated by the PSO mechanism).

It is also possible to determine the overall unitary transformation $\widehat{\mathbf{U}}$ iteratively in a two-step (the Barysz-Sadlej-Snijders technique, BSS)[56] or a one-step (eXact-2-component, X2C)[57] procedure. The PCE problem is straightforward to solve in this case, since $\widehat{\mathbf{U}}$ is readily available. Autschbach used the X2C approximation with Hartree-Fock and Kohn-Sham orbitals to determine HFCCs of selected atoms and the HgH radical,[58] then later combined the X2C methodology with CASSCF-SO and RASSCF-SO wavefunctions.[59] The disadvantage of such iterative schemes is that the 4-component Dirac operator must be diagonalised to determine the transfer operator $\widehat{X}$ relating the upper component ψ^{U} to the lower component ψ^{L} of the Dirac 4-spinor:[42]

$$\psi^{\mathrm{L}} = \widehat{X}\psi^{\mathrm{U}}. \tag{2.66}$$

The unitary transformation directly depends on $\widehat{X}$.

For a complete picture of the available relativistic methods for determining magnetic properties, the direct perturbation theory (DPT) approach should also be mentioned. In the DPT framework, relativistic and hyperfine effects are treated as perturbations and HFCCs, as second-order properties. Hyperfine integrals were successfully derived by Hennum *et al*[60] using this formalism. DPT approaches the correct limit as $c \to \infty$ since it formally starts from the non-relativistic limit of the Dirac equation, the Lévy-Leblond equation.[61] However, this perturbative treatment is only valid in the weakly relativistic regime, which is generally not applicable to actinide complexes.

2.2.2 X2C-1e decoupling

Herein, we use the X2C decoupling approach[62,63] to model relativistic effects in the electronic structure and in magnetic properties such as hyperfine coupling. In order to derive the decoupling transformation, we start from Dyall's modified Dirac equation (mDE),[29]

$$\widehat{\mathbf{H}}_{\mathrm{mDE}} \begin{pmatrix} \psi^{\mathrm{U}} \\ \chi^{\mathrm{U}} \end{pmatrix} = E \begin{pmatrix} 1 & 0 \\ 0 & \frac{1}{2m_{\mathrm{e}}c^2}\widehat{T} \end{pmatrix} \begin{pmatrix} \psi^{\mathrm{U}} \\ \chi^{\mathrm{U}} \end{pmatrix}, \tag{2.67}$$

obtained by substituting the restricted kinetic balance (RKB) relation into the one-electron Dirac equation. The 4-component mDE solutions have an upper component, ψ^{U}, and a pseudo-upper component, χ^{U}, both of which can be represented using the same basis set of one-center, one-electron functions (AOs). The mDE Hamiltonian is

$$\widehat{\mathbf{H}}_{\mathrm{mDE}} = \begin{pmatrix} V & \widehat{T} \\ \widehat{T} & \frac{1}{4m_{\mathrm{e}}^2c^2}\widehat{W} - \widehat{T} \end{pmatrix}, \tag{2.68}$$

with

$$\widehat{T} = \frac{\widehat{\mathbf{p}}\cdot\widehat{\mathbf{p}}}{2m_{\mathrm{e}}}, \tag{2.69}$$

$$\widehat{W} = (\boldsymbol{\sigma}\cdot\widehat{\mathbf{p}})V(\boldsymbol{\sigma}\cdot\widehat{\mathbf{p}}). \tag{2.70}$$

Projecting the modified Dirac equation onto an AO basis yields[42]

$$\begin{pmatrix} \boldsymbol{V} & \boldsymbol{T} \\ \boldsymbol{T} & \frac{1}{4m_{\mathrm{e}}^2c^2}\boldsymbol{W} - \boldsymbol{T} \end{pmatrix} \begin{pmatrix} \boldsymbol{C}_{\mathrm{U}}^{(+)} \\ \boldsymbol{C}_{\mathrm{L}}^{(+)} \end{pmatrix} = \begin{pmatrix} \boldsymbol{S} & \boldsymbol{0} \\ \boldsymbol{0} & \frac{1}{2m_{\mathrm{e}}c^2}\boldsymbol{T} \end{pmatrix} \begin{pmatrix} \boldsymbol{C}_{\mathrm{U}}^{(+)} \\ \boldsymbol{C}_{\mathrm{L}}^{(+)} \end{pmatrix} \epsilon^{(+)}, \tag{2.71}$$

where we use $\boldsymbol{V}$, $\boldsymbol{T}$, $\boldsymbol{W}$ and $\boldsymbol{S}$ to denote matrix representations of $\widehat{V}$, $\widehat{T}$, $\widehat{W}$, and the AO overlap, respectively. $\boldsymbol{C}_{\mathrm{U}}^{(+)}$ and $\boldsymbol{C}_{\mathrm{L}}^{(+)}$ are coefficient vectors associated with the upper and the lower components[§] of an electronic eigenstate with energy $\epsilon^{(+)}$. These coefficients can be determined via diagonalisation the 4-component operator in equation 2.71; subsequently, the transfer matrix $\boldsymbol{X}$ is calculated as

$$\boldsymbol{X} = \boldsymbol{C}_{\mathrm{L}}^{(+)} \left(\boldsymbol{C}_{\mathrm{U}}^{(+)}\right)^{-1}. \tag{2.72}$$

Note that the above relation is simply the matrix form of equation 2.66. It is then possible to obtain the upper-upper (UU) and lower-upper (LU) blocks of the 4-component X2C decoupling matrix $\boldsymbol{U}$ using[64]

$$\boldsymbol{U}_{\mathrm{UU}} = \boldsymbol{S}^{-1/2} \left(\boldsymbol{S}^{-1/2}\, \tilde{\boldsymbol{S}}\, \boldsymbol{S}^{-1/2}\right)^{-1/2} \boldsymbol{S}^{1/2}\,, \tag{2.73}$$

$$\boldsymbol{U}_{\mathrm{LU}} = \boldsymbol{X}\, \boldsymbol{U}_{\mathrm{UU}}\,, \tag{2.74}$$

where

$$\tilde{\boldsymbol{S}} = \boldsymbol{S} + \frac{1}{2m_{\mathrm{e}}c^2}\boldsymbol{X}^{\dagger}\boldsymbol{T}\boldsymbol{X}. \tag{2.75}$$

For electronic structure calculations, we are interested in the upper-upper block of the decoupled (block-diagonalised) 4-component Hamiltonian,

$$\boldsymbol{H}_{\mathrm{bd}}^{(+)} = \boldsymbol{U}_{\mathrm{UU}}^{\dagger}\boldsymbol{V}\boldsymbol{U}_{\mathrm{UU}} + \boldsymbol{U}_{\mathrm{UU}}^{\dagger}\boldsymbol{T}\boldsymbol{U}_{\mathrm{LU}} + \boldsymbol{U}_{\mathrm{LU}}^{\dagger}\boldsymbol{T}\boldsymbol{U}_{\mathrm{UU}} + \boldsymbol{U}_{\mathrm{LU}}^{\dagger}\left(\frac{1}{4m_{\mathrm{e}}^2c^2}\boldsymbol{W} - \boldsymbol{T}\right)\boldsymbol{U}_{\mathrm{LU}}\,. \tag{2.76}$$

Equation 2.76 represents the one-electron part of the X2C 2-component Hamiltonian. For modelling two-electron interactions, most practical implementations use the bare (untransformed) Coulomb operator. This approach is known as X2C-1e, however it is usually referred to simply as X2C. Scalar-relativistic decoupling (SR-X2C)[65] can be achieved by only considering the spin-independent part of the $\widehat{W}$ operator, i.e. the first term on the right-hand-side of equation 2.77.

$$(\boldsymbol{\sigma}\cdot\widehat{\mathbf{p}})\,\widehat{V}\,(\boldsymbol{\sigma}\cdot\widehat{\mathbf{p}}) = \widehat{\mathbf{p}}\,\widehat{V}\cdot\widehat{\mathbf{p}} + i\boldsymbol{\sigma}\cdot\left(\widehat{\mathbf{p}}\,\widehat{V}\times\widehat{\mathbf{p}}\right) \tag{2.77}$$

SF-X2C matrices can be represented using scalar (1-component) basis functions and are therefore compatible with the 1-component framework underlying non-relativistic electronic structure programs. Herein, we employ the SF-X2C(-1e) implementation within the

[§]The coefficient vector $\boldsymbol{C}_{\mathrm{L}}^{(+)}$ is the same regardless of whether the RKB condition is applied to the Dirac equation (the mDE approach, where the 4-spinor has an upper and a pseudo-upper component) or to the lower component basis set (in which case the Dirac equation is unchanged). Hence, for clarity, we use the L subscript to denote quantities related to the positronic (lower/pseudo-upper) degrees of freedom.

OpenMolcas software.[66]

It is worth noting that, despite adopting the SF-X2C approach, we later include spin-orbit coupling via state interaction, hence effectively augmenting the zeroth order (unperturbed) Hamiltonian with a SOC term. The SOC operator constructed by the OpenMolcas RASSI module is derived from the Breit-Pauli/first-order DKH theory[27] and is hence formally inconsistent with the X2C model. Nevertheless, such a combination models the electronic structure of SOC-including systems well.[59] Recently, Liu and Cheng developed an atomic mean-field spin-orbit formalism for X2C-1e.[67] In the future, this could be used to improve the relativistic model used herein, provided that the X2C AMFI formalism can be adapted to the 1-component framework of OpenMolcas.

2.3 Magnetic properties in quantum chemistry

2.3.1 The electron-Zeeman effect and hyperfine coupling

According to the principle of minimal coupling,[68] the interaction between an electron and one or more magnetic fields can be modelled *ab initio* by substituting

$$\widehat{\mathbf{p}}_i \rightarrow \widehat{\mathbf{p}}_i + e\mathbf{A}_i \tag{2.78}$$

into the Hamiltonian eigenvalue equation. In 2.78, $\mathbf{A}$ represents the vector potential associated with the magnetic field; vector potentials for an external magnetic field $\mathbf{B}$ and for a nuclear spin $\mathbf{I}_\mathrm{N}$ with a point-like magnetic moment are given in equations 2.79 and 2.80, respectively.

$$\mathbf{A}_{\mathrm{Zee},i} = \frac{1}{2}\,\mathbf{B} \times (\mathbf{r}_i - \mathbf{R}_\mathrm{G}) = \frac{1}{2}\,\mathbf{B} \times \mathbf{r}_{\mathrm{G},i} \tag{2.79}$$

$$\mathbf{A}_{\mathrm{N},i} = g_\mathrm{N}\mu_\mathrm{N}\,\frac{\mu_0}{4\pi}\left(\mathbf{I}_\mathrm{N} \times \frac{\mathbf{r}_{\mathrm{N},i}}{r^3_{\mathrm{N},i}}\right) \tag{2.80}$$

Herein, $\mathbf{R}_\mathrm{G}$ represents the gauge origin,[‡] μ_0 is the vacuum permeability, g_N is the nuclear g-factor, μ_N is the nuclear magneton and $\mathbf{r}_{\mathrm{N},i} = \mathbf{r}_i - \mathbf{R}_\mathrm{N}$ is the position vector of electron i with respect to nucleus N.

In the non-relativistic regime, the operator identity

$$\widehat{\mathbf{p}}_i \cdot \widehat{\mathbf{p}}_i = (\boldsymbol{\sigma}_i \cdot \widehat{\mathbf{p}}_i)\,(\boldsymbol{\sigma}_i \cdot \widehat{\mathbf{p}}_i)\,, \tag{2.81}$$

where $\boldsymbol{\sigma}_i$ is the 3-vector of Pauli matrices representing the spin of electron i, is applied together with 2.78 to add magnetic coupling to the Schrödinger equation (equation 2.2),

[‡]In molecules containing a single heavy atom, the gauge origin is usually chosen to be the position of the heavy nucleus.

yielding

$$\begin{aligned}\widehat{H}_{\mathrm{nr}}(\mathbf{A}) =& \frac{1}{2m_e}\sum_i \{\widehat{\mathbf{p}}_i\cdot\widehat{\mathbf{p}}_i + e\,(\boldsymbol{\sigma}_i\cdot\widehat{\mathbf{p}}_i)\,(\boldsymbol{\sigma}_i\cdot\mathbf{A}_i) + e\,(\boldsymbol{\sigma}_i\cdot\mathbf{A}_i)\,(\boldsymbol{\sigma}_i\cdot\widehat{\mathbf{p}}_i) \\ &+ e^2\,(\boldsymbol{\sigma}_i\cdot\mathbf{A}_i)\,(\boldsymbol{\sigma}_i\cdot\mathbf{A}_i)\} - \frac{e^2}{4\pi\epsilon_0}\sum_{i,N}\frac{Z_N}{R_{Ni}} + \frac{e^2}{4\pi\epsilon_0}\sum_{i>j}\frac{1}{r_{ij}}. \end{aligned} \tag{2.82}$$

As this work focuses on one-particle operators, we henceforth drop the explicit summation over i for simplicity. Collecting $\mathbf{A}$-dependent terms from 2.82 into a one-electron magnetic perturbation operator $\widehat{H}^{\mathrm{pert}}_{\mathrm{nr}}$, we obtain

$$\widehat{H}^{\mathrm{pert}}_{\mathrm{nr}} = \widehat{H}^{(1)}_{\mathrm{nr}} + \widehat{H}^{(2)}_{\mathrm{nr}}, \tag{2.83}$$

$$\widehat{H}^{(1)}_{\mathrm{nr}} = \frac{e}{2m_e}\left\{\widehat{\mathbf{p}}\cdot\mathbf{A} + \mathbf{A}\cdot\widehat{\mathbf{p}} + i\boldsymbol{\sigma}\cdot(\widehat{\mathbf{p}}\times\mathbf{A}) + i\boldsymbol{\sigma}\cdot(\mathbf{A}\times\widehat{\mathbf{p}})\right\}, \tag{2.84}$$

$$\widehat{H}^{(2)}_{\mathrm{nr}} = \frac{e^2}{2m_e}\,\mathbf{A}\cdot\mathbf{A}, \tag{2.85}$$

where i is the imaginary unit and we have used the Dirac relation,

$$(\boldsymbol{\sigma}\cdot\mathbf{a})(\boldsymbol{\sigma}\cdot\mathbf{b}) = \mathbf{a}\cdot\mathbf{b} + i\boldsymbol{\sigma}\cdot(\mathbf{a}\times\mathbf{b}). \tag{2.86}$$

Note that the non-relativistic magnetic perturbation operator has a first-order contribution, $\widehat{H}^{(1)}_{\mathrm{nr}}$, and a second-order contribution, $\widehat{H}^{(2)}_{\mathrm{nr}}$. The latter is known as the non-relativistic diamagnetic interaction.

The expression for $\widehat{H}^{(1)}_{\mathrm{nr}}$ can be transformed by employing the product rule for the differential operator $\widehat{\mathbf{p}} = -i\hbar\boldsymbol{\nabla}$,

$$\begin{aligned}\widehat{H}^{(1)}_{\mathrm{nr}}\,|\psi\rangle = \frac{e}{2m_e}\;\{&-i\hbar\,[\boldsymbol{\nabla}\cdot\mathbf{A}] + 2\,\mathbf{A}\cdot\widehat{\mathbf{p}} + \hbar\boldsymbol{\sigma}\cdot[\boldsymbol{\nabla}\times\mathbf{A}] - i\boldsymbol{\sigma}\cdot(\mathbf{A}\times\widehat{\mathbf{p}}) \\ &+ i\boldsymbol{\sigma}\cdot(\mathbf{A}\times\widehat{\mathbf{p}})\;\}\;|\psi\rangle\,, \end{aligned} \tag{2.87}$$

where the square brackets indicate that the enclosed $\boldsymbol{\nabla}$ only acts within the brackets. In Coulomb gauge, $\boldsymbol{\nabla}\cdot\mathbf{A} = 0$ and therefore the first term is zero. Using the relationship between the magnetic field and the vector potential, $\mathbf{B} = \boldsymbol{\nabla}\times\mathbf{A}$, Equation 2.87 becomes

$$\widehat{H}^{(1)}_{\mathrm{nr}}\,|\psi\rangle = \frac{e}{2m_e}\,\{\,2\,\mathbf{A}\cdot\widehat{\mathbf{p}} + \hbar\boldsymbol{\sigma}\cdot\mathbf{B}\,\}\,|\psi\rangle\,. \tag{2.88}$$

Non-relativistic electron-Zeeman and HFC perturbation operators are derived by substituting 2.79 and 2.80 into 2.88 and using the turnover rule (i.e. integration by parts) for $\widehat{\mathbf{p}}$, yielding

$$\widehat{H}^{(1)}_{\mathrm{nr,\,Zee}} = \mu_{\mathrm{B}}\,\mathbf{B}\cdot\left(\mathbf{r}_{\mathrm{G}}\times\boldsymbol{\nabla} + 2\,\widehat{\mathbf{S}}\right), \tag{2.89}$$

$$\widehat{H}^{(1)}_{\mathrm{nr,\,N}} = \frac{\mu_0}{4\pi}g_{\mathrm{N}}\mu_{\mathrm{N}}\mu_{\mathrm{B}}\,\mathbf{I}_{\mathrm{N}}\cdot\left\{\left(\frac{8\pi}{3}\delta(\mathbf{r}_{\mathrm{N}}) + \frac{3\mathbf{r}_{\mathrm{N}}\mathbf{r}_{\mathrm{N}}^{\top} - r_{\mathrm{N}}^2\mathbf{1}}{r_{\mathrm{N}}^5}\right)\cdot\widehat{\mathbf{S}} - i\,\frac{\mathbf{r}_{\mathrm{N}}\times\boldsymbol{\nabla}}{r_{\mathrm{N}}^3}\right\}. \tag{2.90}$$

Note that $\boldsymbol{\nabla}$ is the gradient operator with respect to electronic coordinates and that we have employed the relation $\boldsymbol{\sigma} = 2\,\widehat{\mathbf{S}}$ to obtain expressions in terms of the one-electron spin operator $\widehat{\mathbf{S}}$. The two terms in equation 2.89 correspond to the orbital-Zeeman (OZ) and the spin-Zeeman (SZ) contributions, respectively, while the terms in 2.90 represent the Fermi Coupling (FC), spin-dipole (SD) and paramagnetic spin-orbit (PSO) interactions, respectively. The FC term arises because the HFC potential $\mathbf{A}_\mathrm{N}$ (equation 2.80) has a singularity at $r_\mathrm{N} = 0$; as a result, when applying the turnover rule for $\widehat{\mathbf{p}}$, derivatives have to be taken in the distribution sense.[69]

Applying the same methodology to the modified Dirac equation (equation 2.68), we obtain the 4-component magnetic perturbation

$$\widehat{H}^{\mathrm{pert}}_{\mathrm{mDE}} = \widehat{H}^{(1)}_{\mathrm{mDE}} = \frac{e}{2m_e} \begin{pmatrix} \mathbf{0} & (\boldsymbol{\sigma}\cdot\mathbf{A})(\boldsymbol{\sigma}\cdot\widehat{\mathbf{p}}) \\ (\boldsymbol{\sigma}\cdot\widehat{\mathbf{p}})(\boldsymbol{\sigma}\cdot\mathbf{A}) & \mathbf{0} \end{pmatrix}. \tag{2.91}$$

Note that this operator only has a first-order contribution, unlike its non-relativistic counterpart. It has previously been shown[70] that, in the relativistic regime, diamagnetic interactions do not appear explicitly in the magnetic-field-dependent Dirac Hamiltonian; instead, they are encoded in the coupling between positive-energy (electronic) states and negative-energy (positronic) states.[†] Fortunately, this does not affect the determination of first-order properties such as g-values and HFCCs, which constitute the subject of this work.

After X2C decoupling, the picture-change-corrected 2-component operator

$$\widehat{H}^{(1)}_{\mathrm{X2C}} = \frac{e}{2m_e} \left\{ \widehat{U}^\dagger_{\mathrm{UU}}\,(\boldsymbol{\sigma}\cdot\mathbf{A})(\boldsymbol{\sigma}\cdot\widehat{\mathbf{p}})\,\widehat{U}_{\mathrm{LU}} + \widehat{U}^\dagger_{\mathrm{LU}}\,(\boldsymbol{\sigma}\cdot\widehat{\mathbf{p}})(\boldsymbol{\sigma}\cdot\mathbf{A})\,\widehat{U}_{\mathrm{UU}} \right\} \tag{2.92}$$

can be used to evaluate magnetic properties for electrons-only wavefunctions. Below, we give expressions for the X2C-transformed electron-Zeeman operator (equations 2.93, 2.94 and 2.95) and for the X2C-transformed HFC operator (equations 2.96, 2.97 and 2.98).

$$\widehat{H}^{(1)}_{\mathrm{X2C,\,Zee}} = \widehat{H}^{\mathrm{SZ}}_{\mathrm{X2C,\,Zee}} + \widehat{H}^{\mathrm{OZ}}_{\mathrm{X2C,\,Zee}}\,, \tag{2.93}$$

$$\widehat{H}^{\mathrm{SZ}}_{\mathrm{X2C,\,Zee}} = \mu_\mathrm{B}\,\mathbf{B}\cdot\left\{ \widehat{U}^\dagger_{\mathrm{UU}}\left(-\mathbf{r}_\mathrm{G}\cdot\boldsymbol{\nabla} + \mathbf{r}_\mathrm{G}\boldsymbol{\nabla}^\top\right)\widehat{U}_{\mathrm{LU}} + \widehat{U}^\dagger_{\mathrm{LU}}\left(-\mathbf{r}_\mathrm{G}\cdot\boldsymbol{\nabla} + \mathbf{r}_\mathrm{G}\boldsymbol{\nabla}^\top\right)^\dagger\widehat{U}_{\mathrm{UU}} \right\}\cdot\widehat{\mathbf{S}}\,, \tag{2.94}$$

$$\widehat{H}^{\mathrm{OZ}}_{\mathrm{X2C,\,Zee}} = \frac{i}{2}\,\mu_\mathrm{B}\,\mathbf{B}\cdot\left\{ -\widehat{U}^\dagger_{\mathrm{UU}}\,(\mathbf{r}_\mathrm{G}\times\boldsymbol{\nabla})\,\widehat{U}_{\mathrm{LU}} + \widehat{U}^\dagger_{\mathrm{LU}}\,(\mathbf{r}_\mathrm{G}\times\boldsymbol{\nabla})^\dagger\,\widehat{U}_{\mathrm{UU}} \right\}\,, \tag{2.95}$$

$$\widehat{H}^{(1)}_{\mathrm{X2C,\,N}} = \widehat{H}^{\mathrm{FC+SD}}_{\mathrm{X2C,\,N}} + \widehat{H}^{\mathrm{PSO}}_{\mathrm{X2C,\,N}}\,, \tag{2.96}$$

$$\begin{aligned} \widehat{H}^{\mathrm{FC+SD}}_{\mathrm{X2C,\,N}} = 2\,\mu_\mathrm{B} g_\mathrm{N}\mu_\mathrm{N}\,\frac{\mu_0}{4\pi}\,\mathbf{I}_\mathrm{N}\cdot\Bigg\{ & \widehat{U}^\dagger_{\mathrm{UU}}\left(-\frac{\mathbf{r}_\mathrm{N}}{r_\mathrm{N}^3}\cdot\boldsymbol{\nabla} + \frac{\mathbf{r}_\mathrm{N}}{r_\mathrm{N}^3}\,\boldsymbol{\nabla}^\top\right)\widehat{U}_{\mathrm{LU}} \\ & + \widehat{U}^\dagger_{\mathrm{LU}}\left(-\frac{\mathbf{r}_\mathrm{N}}{r_\mathrm{N}^3}\cdot\boldsymbol{\nabla} + \frac{\mathbf{r}_\mathrm{N}}{r_\mathrm{N}^3}\,\boldsymbol{\nabla}^\top\right)^\dagger\widehat{U}_{\mathrm{UU}} \Bigg\}\cdot\widehat{\mathbf{S}}\,, \end{aligned} \tag{2.97}$$

[†] This coupling between eigenstates of the Dirac equation should not be confused with the coupling between electronic and positronic degrees of freedom of an electronic state, i.e. between the upper and lower components of the 4-spinor. Only the latter is removed via techniques such as X2C decoupling.

$$\widehat{H}^{\mathrm{PSO}}_{\mathrm{X2C,\,N}} = i\,\mu_{\mathrm{B}} g_{\mathrm{N}} \mu_{\mathrm{N}}\,\frac{\mu_0}{4\pi}\,\mathbf{I}_{\mathrm{N}} \cdot \left\{ -\widehat{U}^{\dagger}_{\mathrm{UU}} \left(\frac{\mathbf{r}_{\mathrm{N}}}{r^3_{\mathrm{N}}} \times \boldsymbol{\nabla} \right) \widehat{U}_{\mathrm{LU}} + \widehat{U}^{\dagger}_{\mathrm{LU}} \left(\frac{\mathbf{r}_{\mathrm{N}}}{r^3_{\mathrm{N}}} \times \boldsymbol{\nabla} \right)^{\dagger} \widehat{U}_{\mathrm{UU}} \right\} . \quad (2.98)$$

Since our chosen electronic structure approach yields spin-adapted wavefunctions or linear combinations thereof, it is possible to evaluate matrix elements for operators 2.93-2.98 entirely within a 1-component framework.

2.3.2 Temperature-dependent magnetic properties

Magnetic susceptibility and magnetisation can be determined *ab initio* from integrals of the magnetic moment operator,

$$\widehat{\mu}_{\alpha} = -\left.\frac{\partial \widehat{H}_{\mathrm{Zee}}}{\partial B_{\alpha}}\right|_{B_{\alpha}=0}, \qquad \alpha = x, y, z, \quad (2.99)$$

where $\widehat{H}_{\mathrm{Zee}}$ is the Zeeman operator and B_{α} is a component of the external magnetic field vector. Note that, in this section, α and β indices denote Cartesian directions.

The SINGLE_ANISO module[71] of OpenMolcas computes elements of the molar magnetic susceptibility tensor $\boldsymbol{\chi}$ as a Boltzmann average over the manifold of electronic states λ, using the Van Vleck equation:[72]

$$\chi_{\alpha\beta} = \frac{N_{\mathrm{A}}}{Q_0} \sum_{\lambda} e^{-E_{\lambda}/k_{\mathrm{B}}T} \left[\sum_{a,a'} \frac{\langle \lambda a \,|\widehat{\mu}_{\alpha}|\, \lambda a' \rangle \langle \lambda a' \,|\widehat{\mu}_{\beta}|\, \lambda a \rangle}{k_{\mathrm{B}}\,T} - \sum_{\lambda' \neq \lambda} \sum_{a,a'} \frac{\langle \lambda a \,|\widehat{\mu}_{\alpha}|\, \lambda' a' \rangle \langle \lambda' a' \,|\widehat{\mu}_{\beta}|\, \lambda a \rangle + \langle \lambda a \,|\widehat{\mu}_{\beta}|\, \lambda' a' \rangle \langle \lambda' a' \,|\widehat{\mu}_{\alpha}|\, \lambda a \rangle}{E_{\lambda'} - E_{\lambda}} \right], \quad (2.100)$$

where $Q_0 = \sum_{\lambda} e^{-E_{\lambda}/k_{\mathrm{B}}T}$ is the partition function, N_{A} is Avogadro's number, and a and a' index degenerate states with energies E_{λ} and $E_{\lambda'}$, respectively. The magnetic susceptibility for a specific direction $\mathbf{n}$ of the applied field is calculated as[73]

$$\chi(\mathbf{n}) = \sum_{\alpha,\beta} \cos\theta_{\alpha}\, \chi_{\alpha\beta}\, \cos\theta_{\beta}\,, \quad (2.101)$$

where $\cos\theta_{\alpha}$ and $\cos\theta_{\beta}$ are directional cosines; the powder magnetic susceptibility is then obtained by integrating $\chi(\mathbf{n})$ over multiple directions. In Chapter 3 of this work, we use the calculated molar susceptibility χ_{M} for powder to determine the effective magnetic moment[74]

$$\mu_{\mathrm{eff}} = \frac{1}{\mu_{\mathrm{B}}} \sqrt{\frac{3 k_{\mathrm{B}} T \chi_{\mathrm{M}}}{\mu_0 N_{\mathrm{A}}}} \quad (2.102)$$

as a function of temperature.

The molar magnetisation vector **M** is straightforwardly determined by contracting the molar susceptibility tensor with the applied field **B**,

$$M_\alpha = \chi_{\alpha\beta}\, B_\beta\,. \tag{2.103}$$

For specific temperature and field values, integrating the projection of **M** onto multiple directions yields the powder magnetisation $M(B,T)$. In Chapter 3, we use this methodology, as implemented in SINGLE_ANISO, to obtain the low-temperature powder magnetisation as a function of the applied field.

2.4 HYSCORE Spectroscopy

The electron spin echo envelope modulation (ESEEM) family of pulsed EPR techniques is designed to detect weak (< 5 MHz) nuclear frequencies in paramagnetic species.[75] ESEEM experiments rely on a sequence of single-frequency microwave pulses applied at pre-defined time intervals, which manipulate the sample magnetisation such that the amplitude of the generated echo is modulated by frequencies corresponding to transitions between spin Hamiltonian eigenstates. In particular, hyperfine sublevel correlation (HYSCORE) spectroscopy is a two-dimensional four-pulse ESEEM technique that facilitates the identification of hyperfine couplings, especially in systems with several nuclear spins.

In what follows, we describe the HYSCORE pulse sequence using an example system with one $S = 1/2$ electron spin and one $I = 1/2$ nuclear spin. The 4 possible spin states for this system are $|m_S\, m_I\rangle$, with $m_S = +1/2$ ($|m_S\rangle = |\alpha\rangle$) or $m_S = -1/2$ ($|m_S\rangle = |\beta\rangle$), and similarly for m_I. In practice, the measured sample is an ensemble of non-interacting $S = 1/2$, $I = 1/2$ subsystems (e.g. a sample of hydrogen atoms), wherein the distribution of state occupations is described by the ensemble density matrix $\boldsymbol{D}$.

Transfer of density into a matrix element of $\boldsymbol{D}$ (as a result of an applied pulse, for example) corresponds to one of the following phenomena: polarisation (P), nuclear coherence (NC), EPR-allowed electron coherence ($\mathrm{EC_a}$) or EPR-forbidden electron coherence ($\mathrm{EC_f}$). Equation 2.104 shows the ensemble density matrix represented in the $|m_S\, m_I\rangle$ basis, as well as the phenomenon that each element relates to.

$$\boldsymbol{D} = \begin{pmatrix} \langle\alpha\alpha\,|\alpha\alpha\rangle & \langle\alpha\alpha\,|\alpha\beta\rangle & \langle\alpha\alpha\,|\beta\alpha\rangle & \langle\alpha\alpha\,|\beta\beta\rangle \\ \langle\alpha\beta\,|\alpha\beta\rangle & \langle\alpha\alpha\,|\alpha\beta\rangle & \langle\alpha\beta\,|\beta\alpha\rangle & \langle\alpha\beta\,|\beta\beta\rangle \\ \langle\beta\alpha\,|\alpha\alpha\rangle & \langle\beta\alpha\,|\alpha\beta\rangle & \langle\beta\alpha\,|\beta\alpha\rangle & \langle\beta\alpha\,|\beta\beta\rangle \\ \langle\beta\beta\,|\alpha\alpha\rangle & \langle\beta\beta\,|\alpha\beta\rangle & \langle\beta\beta\,|\beta\alpha\rangle & \langle\beta\beta\,|\beta\beta\rangle \end{pmatrix} \rightarrow \begin{pmatrix} \mathrm{P} & \mathrm{NC} & \mathrm{EC_a} & \mathrm{EC_f} \\ \mathrm{NC} & \mathrm{P} & \mathrm{EC_f} & \mathrm{EC_a} \\ \mathrm{EC_a} & \mathrm{EC_f} & \mathrm{P} & \mathrm{NC} \\ \mathrm{EC_f} & \mathrm{EC_a} & \mathrm{NC} & \mathrm{P} \end{pmatrix}. \tag{2.104}$$

At the beginning of the HYSCORE experiment, the electron magnetisation is aligned with the external magnetic field (conventionally along the z axis) and the density matrix is diagonal. The first $\pi/2$ pulse converts the polarisation states into electron coherences – in other words, density is transferred from the diagonal elements to the off-diagonal 2×2 blocks

of $\boldsymbol{D}$ (see Scheme 2.1).[75] After an elapsed time τ, the second $\pi/2$ pulse converts some of the electron coherences into nuclear coherences. In the case of non-selective pulses and anisotropic hyperfine coupling, the $\pi/2 \rightarrow \tau \rightarrow \pi/2$ sequence also generates EC and nuclear polarisation, [75] however this pathway is not shown in Scheme 2.1. During the third step of the sequence, a π pulse transfers the NCs from one m_S manifold onto the other. The final $\pi/2$ pulse converts NCs and NPs into ECs that generate a detectable echo. The four pulses in the HYSCORE sequence are separated by evolution times labelled as τ, t_1 and t_2, during which the system evolves according to the spin Hamiltonian

$$\widehat{H}_S = \mathbf{B} \cdot \boldsymbol{g} \cdot \mathbf{S} + \mathbf{I}_\mathrm{N} \cdot \boldsymbol{a}_\mathrm{N} \cdot \mathbf{S}. \tag{2.105}$$

τ is fixed throughout the HYSCORE experiment, while t_1 and t_2 are varied independently.

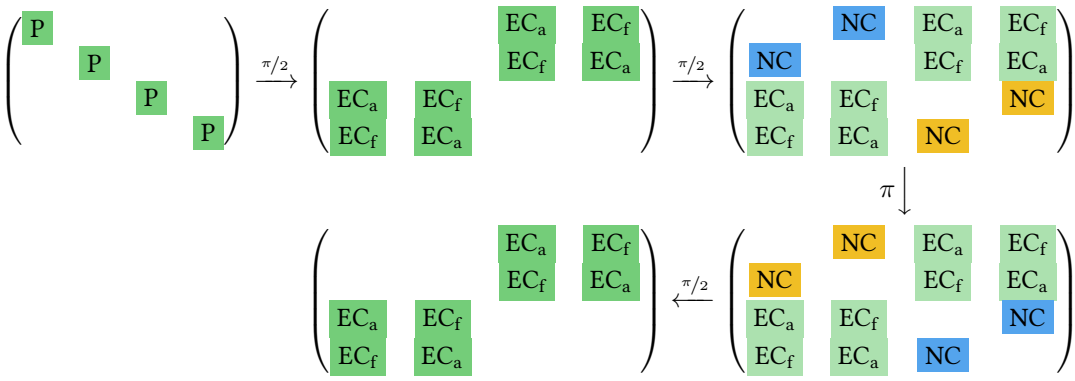

Scheme 2.1. Schematic representation of changes to the density matrix of a $S = 1/2$, $I = 1/2$ system, after each pulse applied during a HYSCORE experiment. Note that colours only highlight groups of matrix elements; identical colours do not indicate equality.

The time-dependent echo is Fourier-transformed in the t_1 and t_2 dimensions to yield a 2D map of signal intensity against (ν_1, ν_2). Cross peaks corresponding to weak hyperfine couplings appear in the $(+,+)$ quadrant of the HYSCORE spectrum, while strong hyperfine couplings appear in the $(-,+)$ quadrant. The spectrum is mirrored with respect to the ν_2 axis and hence, only the positive ν_1 half is usually shown. In the case of disordered samples, such as solid solutions, hyperfine couplings appear as broad ridges instead of sharp cross peaks. The horizontal spread of a ridge with respect to the anti-diagonal at $(\nu_\mathrm{N}, \nu_\mathrm{N})$ (where ν_N is the Larmor frequency for nucleus N) is correlated with HFC anisotropy.[75]

For systems where the electron spin is interacting with multiple magnetic nuclei, the total echo modulation for HYSCORE can be determined via the product rule,[76]

$$V_\mathrm{tot}(\tau, t_1, t_2) = \frac{1}{2}\left[\prod_{i=1}^{N} V_i^{\alpha\beta}(\tau, t_1, t_2) + \prod_{i=1}^{N} V_i^{\beta\alpha}(\tau, t_1, t_2)\right], \tag{2.106}$$

where $V_i^{\alpha\beta}$ are contributions from nuclear coherences transferred from the $|m_S\rangle = |\alpha\rangle$ manifold to the $|m_S\rangle = |\beta\rangle$ manifold after the π pulse and vice-versa for $V_i^{\beta\alpha}$. The spectrum complexity increases quickly with the number of nuclei and with the spin multiplicity; as

such, HYSCORE data is often analysed via a bottom-up approach, wherein simulated spectra are generated based on trial HFC parameters and compared to the measured signal. This is the approach adopted in Chapter 5, where we use Hyperion-calculated EPR parameters together with EasySpin[76,77] to simulate ^{1}H and ^{13}C HYSCORE spectra for two paramagnetic actinide complexes.

References

(1) T. Helgaker, P. Jørgensen and J. Olsen, *Molecular Electronic-Structure Theory*, John Wiley & Sons Ltd., 2000.

(2) C. C. Roothaan, *Reviews of Modern Physics*, 1960, **32**, 179–185.

(3) K. R. Glaesemann and M. W. Schmidt, *Journal of Physical Chemistry A*, 2010, **114**, 8772–8777.

(4) K. A. Peterson and T. H. Dunning, *Journal of Physical Chemistry*, 1995, **99**, 3898–3901.

(5) M. B. Hall, *Polyhedron*, 1987, **6**, 679–684.

(6) D. Stück, T. A. Baker, P. Zimmerman, W. Kurlancheek and M. Head-Gordon, *Journal of Chemical Physics*, 2011, **135**, 194306.

(7) M. Dolg and P. Fulde, *Chemistry - A European Journal*, 1998, **4**, 200–204.

(8) K. Ruedenberg, L. M. Cheung and S. T. Elbert, *International Journal of Quantum Chemistry*, 1979, **16**, 1069–1101.

(9) R. Shepard, The Multiconfigurational Self-Consistent Field Method, in *Ab Initio Methods in Quantum Chemistry - II*, John Wiley & Sons, 1987, pp. 63–200.

(10) B. O. Roos, *International Journal of Quantum Chemistry*, 1980, **14**, 175–189.

(11) B. O. Roos, P. R. Taylor and P. E. M. Siegbahn, *Chemical Physics*, 1980, **48**, 157–173.

(12) B. O. Roos, The Complete Active Space Self-consistent Field Method and its Applications in Electronic Structure Calculations, in *Ab Initio Methods in Quantum Chemistry - II*, John Wiley & Sons, 1987, pp. 399–444.

(13) P. E. Siegbahn, *Journal of Chemical Physics*, 1979, **70**, 5391–5397.

(14) H. Lischka, R. Shepard, F. B. Brown and I. Shavitt, *International Journal of Quantum Chemistry*, 1981, **20**, 91–100.

(15) M. D. Gould and J. Paldus, *Journal of Chemical Physics*, 1990, **92**, 7394–7401.

(16) M. D. Gould and J. S. Battle, *Journal of Chemical Physics*, 1993, **99**, 5961–5975.

(17) P. Å. Malmqvist, A. Rendell and B. O. Roos, *Journal of Physical Chemistry*, 1990, **94**, 5477–5482.

(18) G. L. Manni, S. D. Smart and A. Alavi, *Journal of Chemical Theory and Computation*, 2016, **12**, 1245–1258.

(19) S. Knecht, E. D. Hedegård, S. Keller, A. Kovyrshin, Y. Ma, A. Muolo, C. J. Stein and M. Reiher, *CHIMIA*, 2016, **70**, 244–251.

(20) S. Battaglia, S. Keller and S. Knecht, *Journal of Chemical Theory and Computation*, 2018, **14**, 2353–2369.

(21) J. E. Smith, B. Mussard, A. A. Holmes and S. Sharma, *Journal of Chemical Theory and Computation*, 2017, **13**, 5468–5478.

(22) Q. Sun, T. C. Berkelbach, N. S. Blunt, G. H. Booth, S. Guo, Z. Li, J. Liu, J. D. McClain, E. R. Sayfutyarova, S. Sharma, S. Wouters and G. K. L. Chan, *Wiley Interdisciplinary Reviews: Computational Molecular Science*, 2018, **8**.

(23) Q. Sun, X. Zhang, S. Banerjee, P. Bao, M. Barbry, N. S. Blunt, N. A. Bogdanov, G. H. Booth, J. Chen, Z. H. Cui, J. J. Eriksen, Y. Gao, S. Guo, J. Hermann, M. R. Hermes, K. Koh, P. Koval, S. Lehtola, Z. Li, J. Liu, N. Mardirossian, J. D. McClain, M. Motta, B. Mussard, H. Q. Pham, A. Pulkin, W. Purwanto, P. J. Robinson, E. Ronca, E. R. Sayfutyarova, M. Scheurer, H. F. Schurkus, J. E. Smith, C. Sun, S. N. Sun, S. Upadhyay, L. K. Wagner, X. Wang, A. White, J. D. Whitfield, M. J. Williamson, S. Wouters, J. Yang, J. M. Yu, T. Zhu, T. C. Berkelbach, S. Sharma, A. Y. Sokolov and G. K. L. Chan, *Journal of Chemical Physics*, 2020, **153**.

(24) Q. Sun, J. Yang and G. K. L. Chan, *Chemical Physics Letters*, 2017, **683**, 291–299.

(25) M. R. Hermes, R. Pandharkar and L. Gagliardi, *Journal of Chemical Theory and Computation*, 2020, **16**, 4923–4937.

(26) P. Å. Malmqvist, B. O. Roos and B. Schimmelpfennig, *Chemical Physics Letters*, 2002, **357**, 230–240.

(27) B. A. Heß, C. M. Marian, U. Wahlgren and O. Gropen, *Chemical Physics Letters*, 1996, **251**, 365–371.

(28) O. Christiansen, J. Gauss and B. Schimmelpfennig, *Physical Chemistry Chemical Physics*, 2000, **2**, 965–971.

(29) K. G. Dyall and K. J. Fægri, *Introduction to Relativistic Quantum Chemistry*, Oxford University Press, 2007.

(30) T. Saue, *ChemPhysChem*, 2011, **12**, 3077–3094.

(31) K. J. Fægri and K. G. Dyall, Basis sets for relativistic calculations, in *Relativistic Electronic Structure Theory, Part 1: Fundamentals*, ed. P. Schwerdtfeger, Elsevier, 2002, vol. 11, ch. 5, pp. 259–290.

(32) L. Tterlikkis, S. Mahanti and T. Das, *Physical Review*, 1968, **176**, 10–19.

(33) K. Talukdar, S. Sasmal, M. K. Nayak, N. Vaval and S. Pal, *Physical Review A*, 2018, **98**, 1–8.

(34) R. Arratia-Perez and D. A. Case, *Journal of Chemical Physics*, 1983, **79**, 4939–4949.

(35) H. M. Quiney and P. Belanzoni, *Chemical Physics Letters*, 2002, **353**, 253–258.

(36) A. I. Kuleff, Y. I. Delchev, P. T. Yotov, T. Mineva and J. Maruani, *International Journal of Quantum Chemistry*, 2002, **89**, 227–236.

(37) I. P. Grant and H. M. Quiney, Relativistic Self-Consistent Fields, in *Relativistic Electronic Structure Theory, Part 1: Fundamentals*, ed. P. Schwerdtfeger, Elsevier, 2002, vol. 11, ch. 3, pp. 107–202.

(38) Y. Ishikawa, R. C. Binning and K. M. Sando, *Chemical Physics Letters*, 1983, **101**, 111–114.

(39) S. Song, G. Wang, A. Ye and G. Jiang, *Journal of Physics B*, 2007, **40**, 475–484.

(40) E. Malkin, M. Repisk, S. Komorovsk, P. MacH, O. L. Malkina and V. G. Malkin, *Journal of Chemical Physics*, 2011, **134**.

(41) S. Gohr, P. Hrobárik, M. Repiský, S. Komorovský, K. Ruud and M. Kaupp, *Journal of Physical Chemistry A*, 2015, **119**, 12892–12905.

(42) D. Peng and M. Reiher, *Theoretical Chemistry Accounts*, 2012, **131**, 1081.

(43) A. Wolf, M. Reiher and B. A. Hess, Two-component methods and the generalised Douglas-Kroll transformation, in *Relativistic Electronic Structure Theory, Part 1: Fundamentals*, ed. P. Schwerdtfeger, Elsevier, 2002, vol. 11, ch. 11, pp. 622–663.

(44) E. Van Lenthe, A. Van Der Avoird and P. E. Wormer, *Journal of Chemical Physics*, 1998, **108**, 4783–4796.

(45) P. Belanzoni, E. Van Lenthe and E. J. Baerends, *Journal of Chemical Physics*, 2001, **114**, 4421–4433.

(46) P. Verma and J. Autschbach, *Journal of Chemical Theory and Computation*, 2013, **9**, 1932–1948.

(47) J. Autschbach, *Theoretical Chemistry Accounts*, 2004, **112**, 52–57.

(48) M. Filatov and D. Cremer, *Journal of Chemical Physics*, 2004, **121**, 5618–5622.

(49) M. Filatov and D. Cremer, *Journal of Chemical Physics*, 2005, **123**.

(50) M. Filatov, W. Zou and D. Cremer, *Journal of Physical Chemistry A*, 2012, **116**, 3481–3486.

(51) I. Malkin, O. L. Malkina, V. G. Malkin and M. Kaupp, *Chemical Physics Letters*, 2004, **396**, 268–276.

(52) E. Malkin, I. Malkin, O. L. Malkina, V. G. Malkin and M. Kaupp, *Physical Chemistry Chemical Physics*, 2006, **8**, 4079–4085.

(53) B. Sandhoefer, S. Kossmann and F. Neese, *Journal of Chemical Physics*, 2013, **138**.

(54) T. N. Lan, Y. Kurashige and T. Yanai, *Journal of Chemical Theory and Computation*, 2014, **11**, 73–81.

(55) K. Sharkas, B. Pritchard and J. Autschbach, *Journal of Chemical Theory and Computation*, 2015, **11**, 538–549.

(56) M. Barysz, A. J. Sadlej and J. G. Snijders, *International Journal of Quantum Chemistry*, 1997, **65**, 225–239.

(57) W. Kutzelnigg and W. Liu, *Journal of Chemical Physics*, 2005, **123**.

(58) J. Autschbach, *Journal of Chemical Theory and Computation*, 2017, **13**, 710–718.

(59) R. Feng, T. J. Duignan and J. Autschbach, *Journal of Chemical Theory and Computation*, 2020, 1–8.

(60) A. C. Hennum, W. Klopper and T. Helgaker, *Journal of Chemical Physics*, 2001, **115**, 7356–7363.

(61) W. Kutzelnigg, Perturbation Theory of Relativistic Effects, in *Relativistic Electronic Structure Theory, Part 1: Fundamentals*, ed. P. Schwerdtfeger, Elsevier, 2002, vol. 11, ch. 12, pp. 664–757.

(62) W. Liu and D. Peng, *Journal of Chemical Physics*, 2006, **125**.

(63) W. Liu and W. Kutzelnigg, *Journal of Chemical Physics*, 2007, **126**.

(64) J. Autschbach, D. Peng and M. Reiher, *Journal of Chemical Theory and Computation*, 2012, **8**, 4239–4248.

(65) L. Cheng and J. Gauss, *Journal of Chemical Physics*, 2014, **141**.

(66) F. Aquilante, N. Ferré, J. Autschbach, I. Conti, A. Baiardi, L. D. Vico, S. Battaglia, A. Veniamin, D. Ernst, J. Norell, R. Lindh, M. Delcey, I. F. Galván, L. Freitag, M. Garavelli, X. Gong, S. Knecht, A. Nenov, M. Lundberg, I. Schapiro, M. Odelius, Q. M. Phung, L. Ungur, F. Segatta, M. Olivucci, L. Seijo, T. B. Pedersen, L. Pedraza-gonzález, J. Segarra-martí, K. Pierloot, M. Vacher, M. Reiher, A. Valentini, V. Veryazov, I. Conti, I. F. Galván and L. Freitag, *Journal of Chemical Physics*, 2020, **152**, 1–33.

(67) J. Liu and L. Cheng, *Journal of Chemical Physics*, 2018, **148**.

(68) W. Liu, *Handbook of Relativistic Quantum Chemistry*, Springer Nature, 2016.

(69) W. Kutzelnigg, *Theoretica Chimica Acta*, 1988, **73**, 173–200.

(70) W. Kutzelnigg, *Physical Review A - Atomic, Molecular, and Optical Physics*, 2003, **67**, 12.

(71) L. F. Chibotaru and L. Ungur, *Journal of Chemical Physics*, 2012, **137**.

(72) M. Gerloch and R. F. McMeeking, *Journal of the Chemical Society, Dalton Transactions*, 1975, 2443–2451.

(73) F. Aquilante, J. Autschbach, R. K. Carlson, L. F. Chibotaru, M. G. Delcey, L. De Vico, I. Fdez. Galván, N. Ferré, L. M. Frutos, L. Gagliardi, M. Garavelli, A. Giussani, C. E. Hoyer, G. Li Manni, H. Lischka, D. Ma, P. Å. Malmqvist, T. Müller, A. Nenov, M. Olivucci, T. B. Pedersen, D. Peng, F. Plasser, B. Pritchard, M. Reiher, I. Rivalta, I. Schapiro, J. Segarra-Martí, M. Stenrup, D. G. Truhlar, L. Ungur, A. Valentini, S. Vancoillie, V. Veryazov, V. P. Vysotskiy, O. Weingart, F. Zapata and R. Lindh, *Journal of Computational Chemistry*, 2016, **37**, 506–541.

(74) J. I. Hoppeé, *Journal of Chemical Education*, 1972, **49**, 505.

(75) S. Van Doorslaer, Hyperfine spectroscopy: ESEEM, in *EPR Spectroscopy : Fundamentals and Methods*, ed. D. Goldfarb and S. Stoll, John Wiley & Sons, Ltd., 2018, ch. 18, pp. 379–400.

(76) S. Stoll and R. D. Britt, *Physical Chemistry Chemical Physics*, 2009, **11**, 6614–6625.

(77) S. Stoll and A. Schweiger, *Journal of Magnetic Resonance*, 2006, **178**, 42–55.

Chapter 3

Paper one: ”Anomalous Magnetism of Uranium(IV)-Oxo and -Imido Complexes Reveals Unusual Doubly-Degenerate Electronic Ground States”

Anomalous Magnetism of Uranium(IV)-Oxo and -Imido Complexes Reveals Unusual Doubly-Degenerate Electronic Ground States

J. A. Seed[1], L. Birnoschi[1], E. Lu[1], F. Tuna[1,2], A. J. Wooles[1], N. F. Chilton[1], and S. T. Liddle[1]

[1]Department of Chemistry, The University of Manchester, Oxford Road, Manchester, M13 9PL, United Kingdom

[2]Photon Science Institute, The University of Manchester, Oxford Road, Manchester, M13 9PL, United Kingdom

Abstract

A fundamental part of characterising any metal complex is understanding its electronic ground state, for which magnetometry provides key insight. Most uranium(IV) complexes exhibit low-temperature magnetic moments tending to zero, consistent with a non-degenerate spin-orbit ground state. However, there is a growing number of uranium(IV) complexes with low-temperature magnetic moments $\geq 1\,\mu_B$, suggesting a degenerate ground state, but the electronic structure implications and origins have been unclear. We report uranium(IV)-oxo and -imido complexes with low-temperature magnetic moments ca. 1.5-1.6 μ_B and show that they exhibit near-doubly degenerate spin-orbit ground states. We determine that this results from the strong point-charge-like donor properties of oxo and imido anions generating pseudo-symmetric electronic structures, and that traditional crystal field arguments are useful for understanding electronic structure and magnetic properties of uranium(IV). This suggests that a significant number of uranium(IV) complexes might benefit from a close re-evaluation of the nature of their spin-orbit ground states.

1 Introduction

The nature of coordinated ligands and the formal oxidation state of uranium modulate the key effects of inter-electronic repulsion (IER), spin-orbit coupling (SOC), and the crystal field (CF), which together determine the electronic structure of any uranium complex.[1] Some or all of these effects can be of comparable magnitudes where early actinides are concerned. Therefore, more than anywhere else in the periodic table, the electronic structure of early actinides can be intrinsically very complex and challenging to study, yet it is fundamentally important to understand because it dictates the nature of the electronic ground state, which in turn is intimately connected to the bonding, reactivity, and physicochemical properties of a molecule. As uranium is a central element in civil nuclear energy production,[2–4] resolving the long-standing challenge of nuclear waste could in the future utilise selective extraction methods that exploit a better understanding of covalency differences in uranium-ligand bonding, which are intrinsically connected to the underlying electronic structure.

One of the most valuable and informative methods for characterising paramagnetic open-shell uranium complexes is by variable-temperature magnetometry, since this can give direct insight into the nature of the ground state and formal oxidation state. The free uranium(IV) ion, which has a ground $^3H_4$ ground state in Russell-Saunders formalism, is predicted to exhibit a magnetic moment of 3.58 μ_B, however due to significant CF effects in molecular complexes, this is often around 2.0–2.5 μ_B at 298 K and usually decreases smoothly towards ≈0.3-0.5 μ_B at 2 K;[5–8] the decrease is due to depopulation of excited CF states into a magnetic singlet ground state (A) with appreciable temperature independent paramagnetism (TIP);[7,9] note that this is not an $S = 0$ spin-singlet ground state, but rather a singly-degenerate spin-orbit state – though rare examples of complexes with $S = 0$ ground states do exist, e.g. $[(C_5Me_4H)_3UNO]$.[9,10] Such behaviour is known for O_h-symmetric $[UX_6]^{2-}$,[5,11,12] and occurs because the $J = 4$ spin-orbit multiplet splits into A_1, E, T_1, and T_2 irreducible representations in O_h symmetry,[13] for which the A_1 singlet state is lowest in energy.[11,14]

The A_1 state is diamagnetic because it is composed of approximately 58% $m_J = 0$, 21% $m_J = -4$ and 21% $m_J = +4$,[11] where the $m_J = 0$ state is itself diamagnetic and the equal contributions of the $m_J = \pm 4$ states cancel each other out; this can also be mapped to spin and orbital contributions to the m_J states, which can be calculated via Clebsch-Gordan

coefficients[15] and measured experimentally.[12] On the other hand, compounds of different symmetry may not show a decrease to near-zero magnetic moment at low temperature, signifying the presence of a degenerate paramagnetic ground state (E). For example, uranocene, [U(η^8-C_8H_8)$_2$],[16] has a magnetic moment of ≈2.6 μ_B at 300 K[17] that decreases to 1.35 μ_B at 4 K:[18] in this case, the D_{8h} symmetry of the solid-state structure splits the $J = 4$ spin-orbit multiplet into A_1, E_1, E_2, E_3, and B_1+B_2 irreducible representations, for which E_3 ($m_J = \pm 3$) is the ground state.[19–21]

Outside of "simple" high-symmetry complexes, sufficiently low-symmetry coordination geometries will usually exhibit a singlet (A) spin-orbit ground state;[5,7,22] this is because uranium(IV) has two unpaired electrons and is thus a non-Kramers ion, and hence there is no requirement for any electronic degeneracies in the $J = 4$ spin-orbit multiplet after the action of the CF, because the CF effect for 5f-orbitals is significant. However, there are now a growing number of formally low-symmetry uranium(IV) complexes with innocent ligands where the low-temperature (<2 K) magnetic moments are quite high (≥1 μ_B),[23–39] suggesting that something is differentiating these complexes. Empirically, singlet ground states tend to be observed with monoanionic ligands, regardless of the (pseudo-)symmetry, and higher magnetic moments have increasingly been observed at low-temperature when stronger di- or tri-anionic ligands are present, implying a (pseudo-)doublet (E) spin-orbit ground state.[22] Hence, there is increasing evidence that there is a threshold CF strength for which high-symmetry arguments, and thus a switching of spin-orbit ground state, might be invoked.

Previously, we reported that the N-heterocyclic olefin H2C=C(NMeCH)$_2$ reacts with [U^{III}(N″)$_3$] (N″ = N(SiMe$_3$)$_2$) to produce the mesoionic carbene complex [U(N″)$_3${CN(Me)C(Me)N(Me)CH}] that exhibits a $U^{III} \rightarrow C$ 1-electron back-bond interaction.[40] Seeking to widen the family of uranium mesoionic carbene complexes we targeted uranium(V) derivatives. However, we find instead that the basic reactivity properties of the N-heterocyclic olefin become a complicating factor, promoting cyclometallation and disproportionation reactions, generating rare examples of uranium(IV)-oxo and -imido complexes. We find that these complexes exhibit unusually high low-temperature magnetic moments, for complexes formally of C_1 symmetry, and so we investigated the electronic structure of these complexes to address the nature of the electronic ground state. This has permitted us to unambiguously verify that pseudo-C_3-symmetric uranium complexes with a strong axial ligand can have paramagnetic pseudo-doublet (E) spin-orbit ground states,

showing that traditional CF symmetry arguments can dictate the electronic structure and magnetic properties when strong enough point-charge-like ligands are coordinated to uranium.

2 Results and discussion

2.1 Synthetic considerations and spectroscopic characterisation

Treatment of pre-prepared $[U^{V}(O)(N'')_3]$ ($N'' = N(SiMe_3)_2$, **1**)[26] or *in situ* prepared $[U^{V}(NSiMe_3)(N'')_3]$ (**2**, by oxidation of $[U^{III}(N'')_3]$ with N_3SiMe_3) with half an equivalent of the N-heterocyclic olefin $H_2C{=}C(NMeCH)_2$ (**3**) in either diethyl ether or hexane, produces, after work-up and recrystallisation, brown needles of the uranium(IV)-oxo and -imido complexes $[U^{IV}(O)(N'')_3][(Me)C(NMeCH)_2]$ (**4**) or $[U^{IV}(NSiMe_3)(N'')_3][(Me)C(NMeCH)_2]$ (**5**), respectively, Scheme 1. The crystalline yields of **4** and **5** are both 13%, which is low because **4** and **5** decompose in solution affording $HN(SiMe_3)_2$ and unidentified and intractable by-products and because their formation results from disproportionation reactions where the uranium(VI)-cyclometallate complexes $[U^{VI}(O)(N'')_2\{N(SiMe_3)(SiMe_2CH_2)\}]$ (**6**)[41] for **4** and $[U^{VI}(NSiMe_3)(N'')_2\{N(SiMe_3)(SiMe_2CH_2)\}]$ (**7**) for **5**, respectively, form concomitantly, thus limiting the maximum yield in each case to 50%.

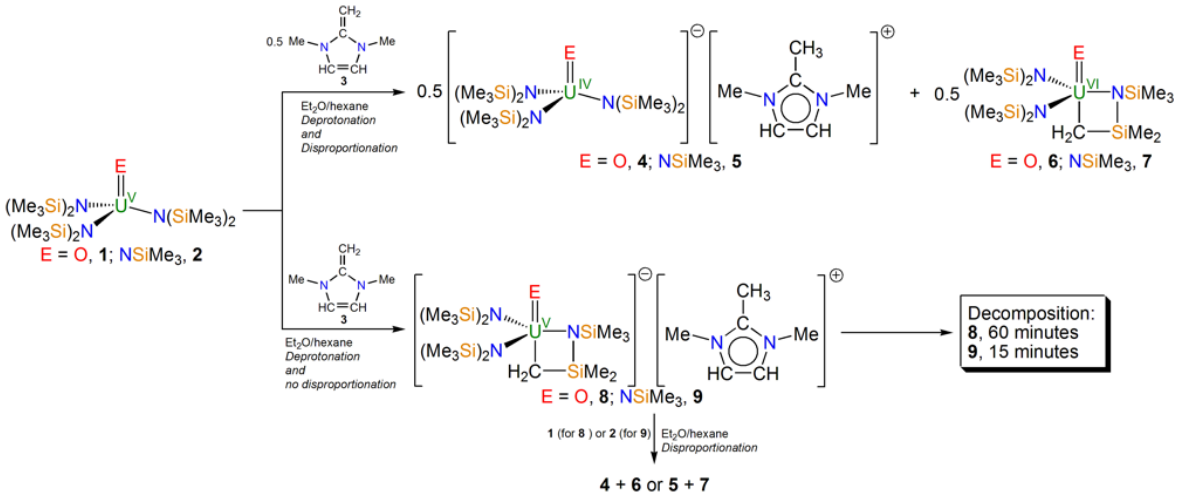

Scheme 1: Synthesis of **4** and **6** or **5** and **7** from **1** or **2**, respectively, when treated with half an equivalent of **3**. Conversely, treatment of **1** or **2** with one equivalent of **3** results in formation of **8** or **9**, respectively. Mixtures of **8** and **9** decompose rapidly, with the times quoted being for total decomposition, but if one further equivalent of **1** or **2**, for **8** or **9** respectively, is already present or added rapidly then 1:1 mixtures of **4** and **6** or **5** and **7** are obtained.

When **1** or **2** are treated with one equivalent of **3**, the uranium(V)-cyclometallate complexes $[U^{V}(O)(N'')_2\{N(SiMe_3)(SiMe_2CH_2)\}][(Me)C(NMeCH)_2]$ (**8**) and

$[U^{V}(NSiMe_3)(N'')_2\{N(SiMe_3)(SiMe_2CH_2)\}][(Me)C(NMeCH)_2]$ (**9**), respectively, are formed quantitatively (see Supplemental Information). Complexes **8** and **9** decompose when they are left in solution for prolonged periods, with complete decomposition found after 60 and 15 minutes, respectively. However, if **8** or **9** are treated quickly with one equivalent of **1** or **2**, respectively, then 1:1 mixtures of disproportionated **4**:**6** or **5**:**7** are formed analogously to the half equivalent reactions with **3** above.

The reactions between **1** or **2** with half an equivalent of **3** clearly produce 1:1 mixtures of **4**:**6** or **5**:**7**, respectively, as a result of disproportionation and cyclometallation. The reactions of **1** and **2** with one equivalent of **3** provide insight into the likely mechanism of this reaction, since cyclometallated **8** or **9** are formed in this situation, but only after addition of further **1** or **2**, which then essentially renders the **1**/**2**:**3** ratio 1:0.5, does disproportionation occur. The cyclometallation can be accounted for by basic **3** promoting C-H activation and H-abstraction, and that the extra cyclometallate donor destabilises the uranium(V) ions in **8** and **9**, as evidenced by their otherwise rapid decomposition, such that oxidation to uranium(VI) is more favourable for the cyclometallate formulation at the expense of an anionic formulation by reduction for the uranium-oxo and -imido components of **4** and **5**. Certainly, the absence of D-incorporation for reactions conducted in D_6-benzene are consistent with this, and $[U^{V}(O)(N'')_2\{N(SiMe_3)(SiMe_2CH_2)\}][MePPh_3]$,[41] that is essentially **8** but with a different counter-cation, is known to be easily oxidised ($E_{1/2}$ =−0.85 V vs. $[Cp_2Fe]^{0/+}$).

Once isolated, **4** and **5** are poorly soluble in aromatic solvents, and they decompose in ethers, but NMR spectroscopic data are consistent with their uranium(IV) formulations and show no evidence of D-incorporation from deuterated solvent (benzene). The six trimethylsilyl groups resonate as one singlet per complex in the ^{1}H NMR spectrum, indicating a symmetric species on the NMR timescale. However, these are shifted upfield relative to **1** and **2** in agreement with the increased electron density at the uranium(IV) centres. For **5**, the trimethylsilyl group of the axial imido ligand is observed in the ^{1}H NMR spectrum at −12.55 ppm, but no ^{1}H NMR resonance for the $[M{=}NSiMe_3]$ group for **2** has been reported so no comparison can be made; however, the ^{29}Si NMR spectra of **4** and **5** exhibit weak resonances at −37.74 and −90.74/−131.19 ppm, respectively, which is within the range of reported ^{29}Si chemical shifts for uranium(IV) complexes.[42] Complexes **6** and **8** were identified by comparison of NMR spectra of reaction mixtures compared to published data and $[U^{V}(O)(N'')_2\{N(SiMe_3)(SiMe_2CH_2)\}][MePPh_3]$,[41] respectively. Complex **9** was identified by NMR spectroscopy with reference to **8**, but **7** could not be unambiguously spectroscopically

identified, most likely because the imido does not stabilise the uranium(VI) oxidation state as well as an oxo, but its fleeting existence seems all but assured given the parallels between these oxo and imido systems with five of the six reaction partners identified.

For both **4** and **5**, the UV/Vis/NIR spectra are dominated by strong charge transfer bands from the UV region to around 20,000 cm^{-1}. Across the range 20,000-5,000 cm^{-1} the spectra are dominated by multiple but weak ($\epsilon < 80$ $M^{-1}cm^{-1}$) absorptions that are characteristic of Laporte forbidden f-f transitions of uranium(IV) ions, in accordance with the pale brown colour of both complexes.[1,6,43]

2.2 Solid state structural characterisation

In order to confirm the formulations of **4** and **5**, their solid-state structures were determined, Figure 1. In gross terms each are very similar, with a separated ion pair formulation and four-coordinate uranium ions. The geometry about uranium in **4** is essentially trigonal monopyramidal, with an average O-U-N_{amide} angle of 96.8(3)° and an average N_{amide}-U-N_{amide} angle of 118.6(3)°, such that the uranium ion lies only 0.279(4) Å above the plane defined by the three N_{amide} centres. In contrast, **5** exhibits a pseudotetrahedral geometry about uranium, with an average N_{imido}-U-N_{amide} angle of 102.39(2)° and an average N_{amide}-U-N_{amide} angle of 115.53(2)°. Thus, the geometries of tetravalent **4** and **5** largely mirror those of pentavalent **1** and **2**, respectively. The U-N_{amide} distances in tetravalent **4** and **5** span the ranges 2.346(7)-2.351(7) Å and 2.359(4)-2.368(4) Å, respectively. For comparison, the U-N_{amide} distances in pentavalent **1** [2.235(1)-2.244(2) Å][26] and **2** [av. 2.295(10) Å][44] are significantly shorter. For **4**, the U-O distance is significantly longer than that of **5** [1.882(6) vs. 1.817(1) Å, respectively] and the U-N_{imido} distance in **5** is significantly longer than that of **2** [1.985(4) vs. 1.910(16) Å, respectively]. More widely, the U-O distance in **4** is comparable to that of [U{OK(18-crown-6)}$(N'')_3$] [1.890(5) Å][45] and the U-N_{imido} bond length in **5** is comparable to those of [U(NDipp)Cl_2($^tBu_2$bpy)$(THF)_2$][46] and [K][U(=NCPh$_3$){N$(SiMe_3)_2\}_3$][47] [1.981(2) Å and 1.9926(14) Å, respectively]. These structural features all support the uranium(IV) formulations of **4** and **5**.

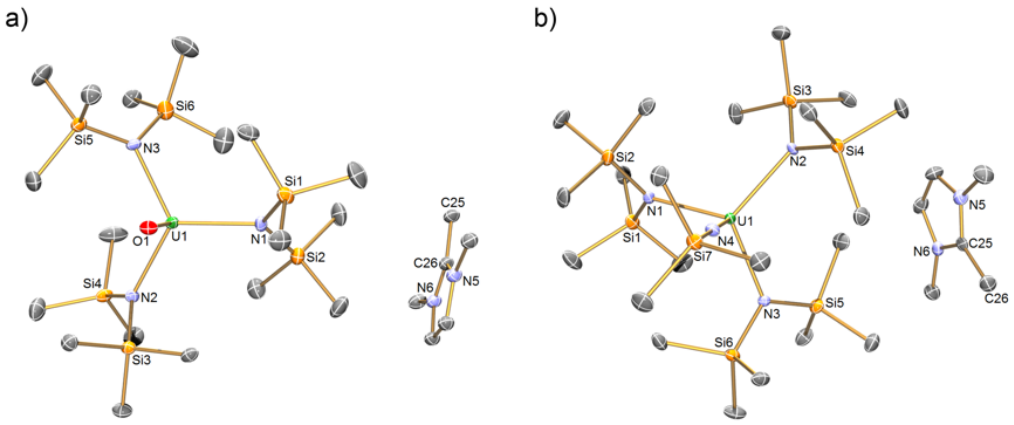

Figure 1: Solid state structures of a) **4** and b) **5** at 150 K with selective labelling. Displacement ellipsoids set at 30% with hydrogen atoms and minor disordered components omitted for clarity.

2.3 Magnetometric characterisation

Powdered samples of **4** and **5** immobilised in eicosane were studied by variable-temperature SQUID magnetometry, Figure 2. Complexes **4** and **5** exhibit magnetic moments of 2.88 and 3.01 μ_B at 300 K, respectively. These values are both lower than the theoretical magnetic moment of 3.58 μ_B for one uranium(IV) ion, which is not uncommon, but they are clearly higher than the maximal magnetic moment of 2.54 μ_B for one uranium(V) ion, and are substantially higher than the reported magnetic moments of **1** and **2** (1.59 μ_B and 2.04 μ_B, respectively, at 300 K). The magnetic moments of **4** and **5** decrease slowly, reaching 2.36 and 2.30 μ_B, respectively, at 20 K, and then decrease more rapidly reaching 1.54 and 1.46 μ_B, respectively, at 2 K, Figure 2. The data for **4** and **5** do not fit the 'classical' behaviour of uranium(IV),[1,6,48] that is the smooth continuous decrease in magnetic moment as the temperature is decreased and tending to zero at low temperature, which prompted us to probe their electronic structures in detail in order to explain this observation.

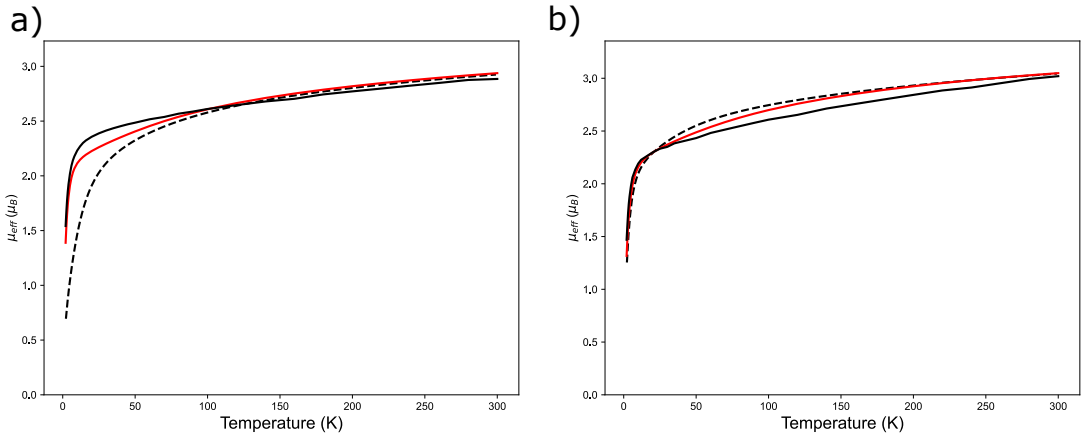

Figure 2: Magnetic moment as a function of temperature for a) **4** and b) **5**, recorded in a field of 0.5 T (black solid lines). Dotted black lines are calculated by CASSCF(2,7)-SO (11 triplets + 9 singlets, see Methods for details) and solid red lines are the best fits with a CF Hamiltonian (using CASSCF(2,7)-SO-calculated parameters) with optimisation of a single parameter (a: B_6^6, b: B_6^3).

2.4 Electronic structure calculations

The uranium(IV) ion has a ground $5f^2$ configuration, with $S = 0$ (singlet) and $S = 1$ (triplet) electron spin quantum numbers. In the absence of SOC, the Russell-Saunders terms arising from IER for this configuration are (in order of increasing energy) ^{3}H, ^{3}F and ^{3}P for $S = 1$ and ^{1}G, ^{1}D, ^{1}I and ^{1}S for $S = 0$. SOC mixes these terms, rendering L and S no longer good quantum numbers, and in the weak SOC limit the Russell-Saunders coupling scheme describes the total angular momentum with quantum number J; for the f^2 configuration, Hund's rules predict a 9-fold degenerate $^3H_4$ ground state. CASSCF-SO calculations of the gas-phase U^{IV} ion reveal the first excited state $^3F_2$ at ca. 5,000 cm^{-1};[7] hence, the SOC is large enough that the first excited multiplet is not $^3H_5$ as it is for $4f^2$ Pr^{III}. Nonetheless, the ground $^3H_4$ multiplet is well separated from excited states such that consideration of this multiplet alone is likely to be sufficient to explain ground state properties such as magnetism. This free-ion picture is not an accurate depiction of the electronic structure in a coordination complex, as bonding to ligands hybridises the valence orbitals and removes much of the electronic degeneracy (i.e. CF splitting). In general for complexes of uranium, the energy scales of IER, SOC and CF can be similar, especially in the case of multiple bonding, and multi-reference *ab initio* electronic structure calculations have emerged as a reliable way to determine the electronic structure of such molecules.[9,49–51] With the present complexes in mind, we first outline the electronic structure of a hypothetical linear $[U^{IV}O]^{2+}$ cation, followed by a hypothetical C_{3v}-symmetric trigonal pyramidal $[U^{IV}OF_3]^-$ anion (F^- is chosen to mimic the monoanionic point charge of the N″ equatorial donors in **4** and **5**), and finally

onto the full complexes **4** and **5**.

Here we take the opportunity to address a point of considerable confusion in the modern literature of the magnetism and electronic structure of 5f-element complexes. Great care must be taken when describing energy splitting for these materials where IER, SOC and CF can all compete, especially when it comes to the distinction between molecular orbital energies and the energies of many-electron SOC-including eigenstates. For instance, if the CF is weak compared to IER and SOC (much like the case for lanthanides) it is somewhat irrelevant to discuss orbital splitting and the only relevant currency is the spin-orbit states. On the other hand, if the CF is strong, then there is a possibility that electronic ground state will no-longer be the free-ion Hund's Rule high-spin state and instead be in a low-spin configuration (much like the situation common for d-block metals), and thus discussing the orbital splitting and electronic populations are crucial. Confusingly, the electronic states arising from both the spin-orbit picture and the "electrons-in-orbitals" picture are both associated with irreducible representations of the molecular point group, and thus a doubly-degenerate spin-orbit state could be described as "E" and so could a doubly-degenerate molecular orbital. Hence, one must always be clear what states are being discussed. In order to avoid confusion, molecular orbitals are conventionally denoted using lowercase letters (e.g. a doubly-degenerate molecular orbital is labelled as "e"), while electronic states have uppercase labels.

It is also important to note here that orbital energies are inherently a single-electron construct, and are not defined in a correlated multi-electron wavefunction. However, we can extract the effective orbital energies from the observed CF splitting of the ground $^3\mathrm{H}_4$ spin-orbit multiplet, by recalling the origin of the Stevens operator equivalent method, which relates the multi-electron CF Hamiltonian to the single-electron CF Hamiltonian.[52] The CF Hamiltonian:

$$\hat{\mathrm{H}}_{\mathrm{CF}} = \sum_{k=2,4,6} \sum_{q=-k}^{k} \mathrm{B}_k^q \, \theta_k \, \hat{\mathrm{O}}_k^q \tag{1}$$

acts on the ground $J = 4$ multiplet, where B_k^q are the CF parameters (CFPs), θ_k are the operator equivalent factors and $\hat{\mathrm{O}}_k^q$ are the Stevens operators (functions of the total angular momentum operators, $\hat{\mathrm{J}}$); for the $^3\mathrm{H}_4$ multiplet of the f^2 configuration, $\theta_2 = -52/2475$, $\theta_4 = -4/5445$ and $\theta_6 = 272/4459455$.[53] CFPs for $[\mathrm{U^{IV}O}]^{2+}$, $[\mathrm{U^{IV}OF_3}]^{-}$, **4** and **5** can be directly extracted from our CASSCF-SO calculations[54] and, using this Hamiltonian, the same CFPs can be applied to the single-electron $l = 3$ basis to extract the effective 5f-orbital split-

ting due to the CF; in this case $\theta_2 = -2/45$, $\theta_4 = 2/495$ and $\theta_6 = -4/3861$,[53] where the $\hat{O}_k^q$ are now written in terms of the single-electron orbital angular momentum operators, $\hat{l}$.

For a linear $[U^{IV}O]^{2+}$ cation where the U=O bond length is taken from the crystal structure of **4** (1.884 Å), the axial CF induced by the oxo anion splits the 5f-orbitals into the $C_{\infty v}$ irreducible representations: E_3 (ϕ) < E_2 (δ) < E_1 (π) < A_1 (σ), Figure 3, where ϕ, δ and π are linear combinations of the m_l functions ±3, ±2 and ±1, respectively, and σ is $m_l = 0$. Here, the ϕ and δ orbitals are formally non-bonding, while the π and σ orbitals are formally antibonding with respect to the U-O bond, which is the origin of the orbital ordering.[51] However, when the CF is smaller than IER and SOC, such as for **4** and **5** (see below), the effect of the CF on top of the IER+SOC states is to remove the degeneracy of the J multiplets. In $C_{\infty v}$ symmetry, the ground $^3H_4$ multiplet is split into four pseudo-doublets and one singlet, and for $[U^{IV}O]^{2+}$: E_4 ($m_J = \pm 4$) < E_3 ($m_J = \pm 3$) < A_1 ($m_J = 0$) < E_1 ($m_J = \pm 1$) < E_2 ($m_J = \pm 2$), Figure 4. Note that because the configuration has an even number of unpaired electrons, it is a non-Kramers system and hence a low symmetry CF could fully remove the degeneracy of the m_J states; thus, we refer to these doublets as pseudo-doublets to distinguish them from Kramers doublets.

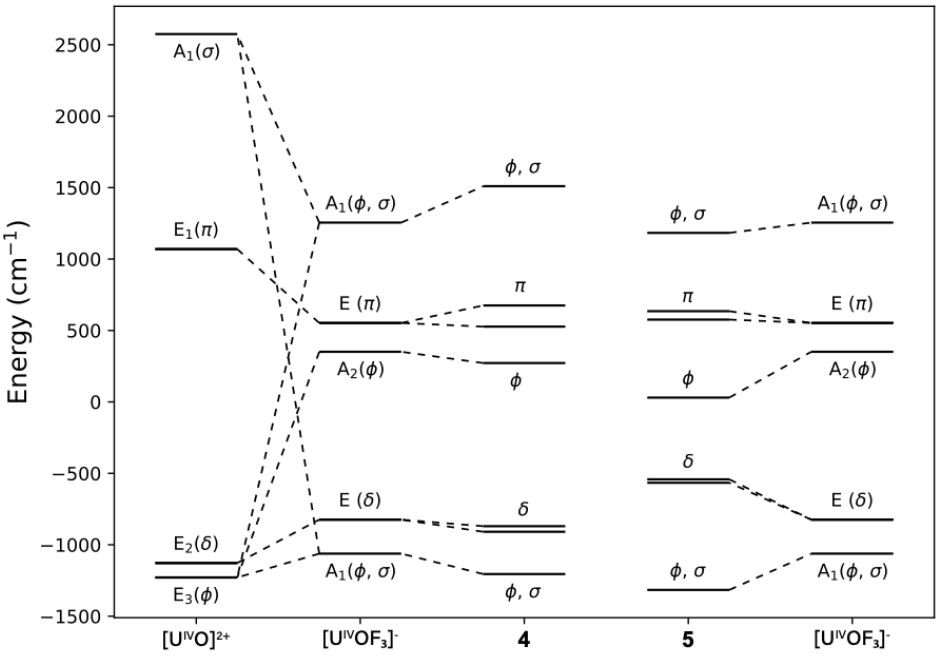

Figure 3: Energies of the 5f orbitals derived using the Stevens operator equivalent method based on the effective crystal field splitting of the $^3H_4$ ground term calculated with CASSCF(2,7)-SO (11 triplets + 9 singlets, see Methods for details). Only dominant contributions to the orbitals of $[U^{IV}OF_3]^-$, **4** and **5** are given. The energy zero corresponds to the 5f orbital energy of a bare U^{IV} ion in vacuum.

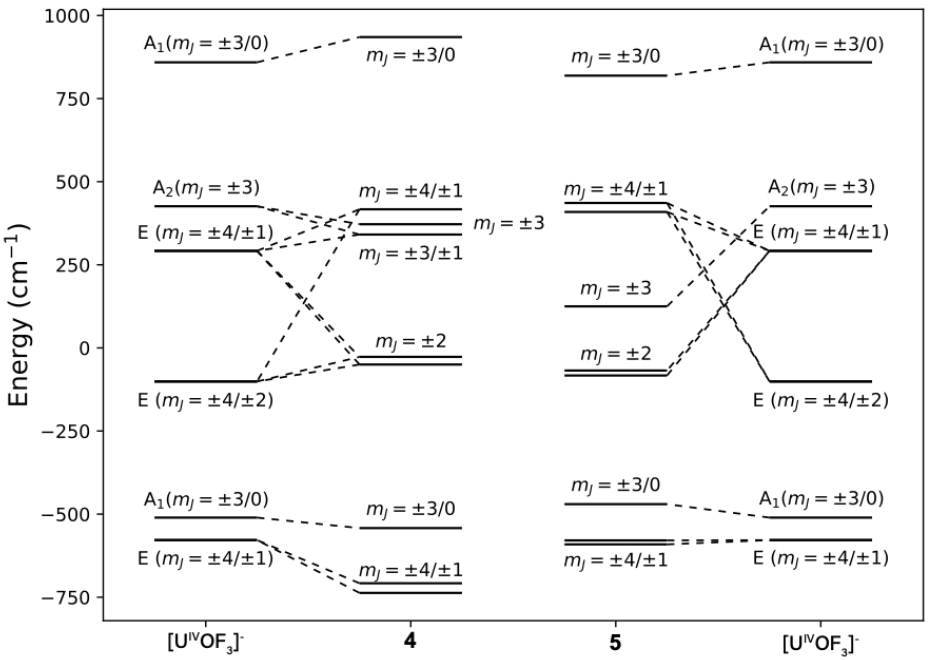

Figure 4: Energies of CF states arising from the $^3H_4$ ground term calculated with CASSCF(2,7)-SO (11 triplets + 9 singlets, see Methods for details). Only dominant contributions to the states are shown. The energy zero corresponds to the $^3H_4$ level of a bare U^{IV} ion in vacuum.

For the C_{3v}-symmetric trigonal pyramidal complex $[U^{IV}OF_3]^-$, where the U=O and U-F bond lengths are taken from the crystal structure of **4** (U=O: 1.884 Å, average U-N: 2.348 Å), we have performed CASSCF-SO calculations with a 2 in 7 active space (see Methods). In C_{3v} symmetry the $^3H_4$ multiplet splits as 2×A_1 ($m_J = \pm 3, 0$), A_2 ($mJ = \pm 3$) and 3×E ($m_J = \pm 4, \pm 2, \pm 1$),[13] Figure 3. Parameterising this splitting of $J = 4$ with the CF Hamiltonian, only B_k^q with $q = 0, 3$ or 6 are non-zero as the CF Hamiltonian must reflect the point symmetry of the molecule,[13] Table S1. In C_{3v} symmetry the f-orbitals split as 2×A_1 (σ, ϕ), A_2 (ϕ) and 2×E (π, π, δ, δ), where the ϕ pair is now split and mixed with σ, and in this case can be physically understood as arising from the bonding/antibonding interactions with the equatorial ligands. When the CF Hamiltonian is recast into the $l = 3$ orbital basis, we find that the orbitals order as $A_1 < E < A_2 < E < A_1$, Figure 3.

Moving to complexes **4** and **5**, CASSCF-SO calculations with a 2 in 7 active space (see Methods) find characteristically similar results to the C_{3v} $[U^{IV}OF_3]^-$ complex, Figures 3 and 4. We find that the ground $^3H_4$ multiplet is well-isolated and that there is a pattern of three pseudo-doublets and three singlets, where the ground pseudo-doublet is dominated by $m_J = \pm 4$ and ± 1, and the first excited singlet is dominated by $m_J = 0$ and ± 3, Tables S2

and S3, and Figure S16. Here, the deviation from exactly degenerate pseudo-doublets is due to the low-symmetry component of the CF (i.e. deviations from C_{3v} symmetry), where the magnitude of the low-symmetry perturbation directly influences the energy gaps within each pseudo-doublet. Magnetic data computed for **4** and **5** on the basis of our CASSCF-SO results show good overall agreement with experiment, but our calculations do not approach the correct low-temperature limit, Figure 2; this is particularly acute for the M vs. H data of **4**, Figure 5. From our CASSCF-SO calculations, the pseudo-doublet ground states are split on the order of 31 and 9 cm^{-1} for **4** and **5**, respectively. In the limit of a truly-degenerate doublet (i.e. in perfect C_{3v} symmetry), we would expect a rapid increase of the magnetisation at low fields as the states split, followed by a slower increase at higher fields (i.e. saturation-like), and in the opposite low-symmetry limit of a well-isolated singlet state, the magnetisation would be near-zero. For both complexes, the CASSCF-SO-calculated magnetisation data are lower than the experimental data, indicating that the splitting in the pseudo-doublet ground state is overestimated by our calculations. We believe the worse agreement between experimental and CASSCF-calculated M vs. H data for **4** compared to **5** is due compound **4** having ca. 20% larger CF splitting than **5** (Table S2 cf. Table S3), meaning the state-average CASSCF wavefunction is less accurate for the lower-lying states than for **5**. There is no significant change in magnetic properties resulting from increasing the size of the active space (8 in 13 active space that includes frontier bonding and anti-bonding orbitals of the U=E unit, Figures S17-S20), which is consistent with previous computational studies of uranium(IV) compounds.[9]

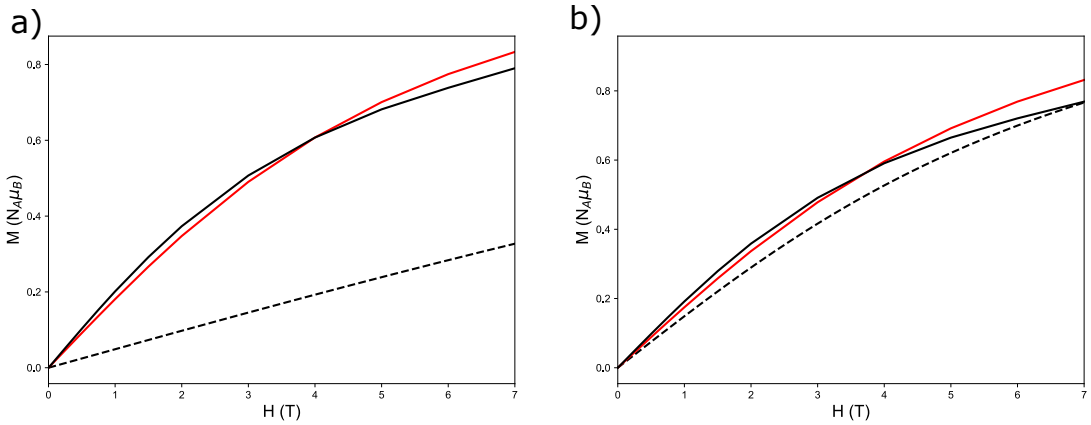

Figure 5: Magnetisation at 4 K as a function of field for a) **4** and b) **5** (black solid lines). Dotted black lines are calculated by CASSCF(2,7)-SO (11 triplets + 9 singlets, see Methods for details) and solid red lines are the best fits with a CF Hamiltonian (using CASSCF(2,7)-SO-calculated parameters) with optimisation of a single parameter (a: B_6^6, b: B_6^3).

Because the low-temperature magnetisation experiment probes only the lowest states, these data provide an experimental measure of the splitting of the ground pseudo-doublet. The

CF Hamiltonian described above provides a flexible model that allows us to modify the CF to reproduce the experimental data and thus indirectly measure the ground state pseudo-doublet splitting. To calculate the magnetic properties, we use the following Hamiltonian in the PHI program:[55]

$$\hat{\mathrm{H}} = \sum_{k=2,4,6} \sum_{q=-k}^{k} \mathrm{B}_k^q \, \theta_k \, \hat{\mathrm{O}}_k^q + \mu_\mathrm{B} \, \hat{\mathbf{J}} \cdot \boldsymbol{g} \cdot \hat{\mathbf{B}} \tag{2}$$

where the second term is the Zeeman Hamiltonian, representing the interaction of the complex with the magnetic field, μ_B is the Bohr magneton, $\hat{\mathbf{B}}$ is the magnetic field and $\boldsymbol{g}$ is the effective g-matrix of the $J = 4$ ground multiplet. We note that this model implies a pure 5f angular momentum basis, and thus anisotropy and hybridisation effects can be approximated with $\boldsymbol{g}$, whose principal values (g_x, g_y, g_z) are also obtained from CASSCF-SO:[56] these values are (0.71, 0.72, 0.76) and (0.73, 0.73, 0.77) for **4** and **5**, respectively, which is slightly reduced from the free-ion Landé factor for the $^3\mathrm{H}_4$ ground multiplet $\mathrm{g}_J = 4/5$.

Starting from the CASSCF-SO-calculated CFPs, Tables S4 and S5, we fit susceptibility and magnetisation data simultaneously by varying only a single CFP. From the resulting sets of parameters, we analyse those that reduce the initial residual error (as defined in PHI)[55] by at least 90%. Additionally, we assume that the initial CASSCF-SO-calculated electronic structure is a good initial guess, and so we discard optimised CFP sets that lead to drastic changes of the overall structure of the $J = 4$ multiplet. This is achieved by examining the root mean squared deviations (RMSD) of the CF energy levels and of the pseudo-doublet energy gaps, Table S6. The energies of the first two excited states of both complexes are shown in Table S7, and μ_eff vs. T and M vs. H curves derived for each possible set of modified CFPs are illustrated in Figures S20 and S21. All acceptable CFP sets give consistent results for the M vs. H data of **5** (Figure S21b and Table S7), indicating a ground pseudo-doublet gap of approximately 8.5(1) cm^{-1} with the first excited singlet state at ca. 120(30) cm^{-1}. Despite having a large energy RMSD, the optimised B_6^3 results show the best agreement with the experimental μ_eff vs. T curve, Figure S21a, suggesting the second excited state lies slightly higher at ca. 198 cm^{-1}, while the ground pseudo-doublet states are separated by 7.9 cm^{-1}. For **4**, only 2 sets of optimised CFPs match our selection criteria, and both predict a ground pseudo-doublet gap of just under 7 cm^{-1} with the singlet state at ca. 190 cm^{-1}. We note that none of these models are "correct" parameterisations of the CF, but rather a means-to-an-end of approximating the experimental pseudo-doublet splitting.

Following our identification that **4** and **5** have near-degenerate E spin-orbit ground states, there are two pertinent questions: *i)* why do these complexes display high-symmetry-like electronic structures despite their formal low symmetry; and *ii)* why do these complexes have E ground states as opposed to A_1 or A_2 ground states (all permissible in C_{3v})?

The answer to *i)* appears to be predominantly related to the presence of di- or tri-anionic ligands;[23–39] indeed, we have previously found that pseudo-C_{3v} uranium(V) complexes with terminal nitrido- and oxo- ligands tend to behave as belonging to a high-symmetry point group, unlike what their C_1 structures would dictate.[51,57] We found that some of the nitrido-complexes have EPR-silent $m_J = \pm 3/2$ ground states (silent in true C_{3v} symmetry), with excited $m_J = \pm 5/2$ states observable by EPR (active even in true C_{3v} symmetry) lying within a few tens of cm^{-1};[51] given the very sensitive nature of EPR, and that we could only observe EPR transitions in the excited state, the ground $m_J = \pm 3/2$ states must be very pure. This corroborates the observation that the corresponding terminal oxo- complex has a $m_J = \pm 3/2$ ground state and is completely EPR silent.[57] Presumably this occurs because there is a hierarchy of influences on the overall CF potential: single strong donor atom $>>$ trigonal equatorial donors $>$ low symmetry perturbations; while for complexes lacking a single strong donor atom, the competition between the "high" and "low" symmetry parts of the CF is enough to remove the appearance of high symmetry.

The answer to *ii)* depends on the nature of the coordination complex, but can be explained using a simple electrostatic model that has arisen to design high-performance single-molecule magnets.[58–60] Each of the spin-orbit m_J states of the free-ion $^3H_4$ term has an aspherical 5f electron distribution that can be calculated analytically.[61] For $m_J = 0$ and ± 1 the shapes are distinctly prolate spheroidal, while for $m_J = \pm 4$ the shape is distinctly oblate spheroidal; $m_J = \pm 2$ and ± 3 are neither oblate nor prolate. In the presence of a highly-charged and multiply-bonded anion like the oxo- or imido- groups in **4** and **5**, simple electrostatic arguments dictate that the $m_J = \pm 4$ state should be lower in energy than the other m_J states, while $m_J = 0$ and ± 1 would be higher in energy. Of course, however, the spin-orbit states must conform to the (pseudo-)symmetry of the complex and are thus linear combinations of the m_J states. As a reminder, in C_{3v} symmetry the states mix as $2\times$ A_1 ($m_J = \pm 3, 0$), A_2 ($m_J = \pm 3$) and $3\times$E ($m_J = \pm 4, \pm 2, \pm 1$),[13] Figure 4. Thus, if the presence of a strong point-charge-like donor atom would favour a $m_J = \pm 4$ ground state, then this would be one of the E states. Conversely, if the complex had only equatorial coordination, then a $m_J = 0$ ground state would be favoured, leading to an A_1 ground state. To demonstrate

this, we have performed CASSCF-SO calculations on the model $[U^{IV}OF_3]^-$ complex where we start from a situation where the F^- ligands are 47 Å away (i.e. the CF splitting is that of $[U^{IV}O]^{2+}$ with $C_{\infty v}$ symmetry, Figure 6 left) and move them in until they arrive at their positions in $[U^{IV}OF_3]^-$ studied above (U-F: 2.348 Å, C_{3v} symmetry, Figure 6 centre), and then move the O^{2-} ligand out from its initial position (U=O: 1.884 Å) to 38 Å away (i.e. the CF splitting is that of $[U^{IV}F_3]^+$ with D_{3h} symmetry, Figure 6 right); as expected we observe a flip from an E ground state to an A_1 ground state between $[U^{IV}OF_3]^-$ and $[U^{IV}F_3]^+$.

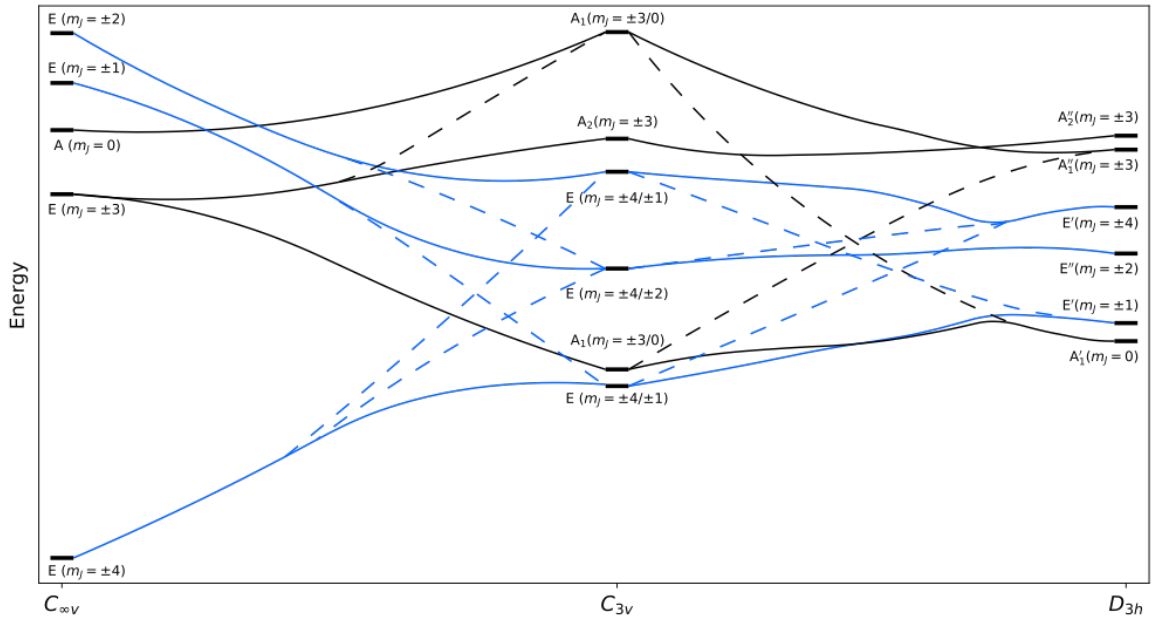

Figure 6: Energies of CF states for a model complex of $[U^{IV}OF_3]^-$ where the U-F bond lengths are reduced from 47 Å ($C_{\infty v}$, left) to 2.348 Å (C_{3v}, centre), and the U-O bond length is increased from 1.884 Å (C_{3v}, centre) to 38 Å (D_{3h}, right). Doubly-degenerate E states are coloured blue and singly-degenerate A states are coloured black. Only dominant contributions to the states are shown.

To test both *i)* and *ii)*, we have performed a CASSCF-SO calculation on **4** where we have removed the oxo- anion, i.e. $[U^{IV}(N'')_3]^+$, while maintaining the formal C_1 symmetry of the crystalline geometry. We find that the ground state is well-described as $m_J = 0$ (i.e. A_1' of D_{3h}, Figure 6, right), and that the excited states are linear combinations of $m_J = \pm1, \pm2, \pm3$ and ±4, respectively, split by ca. 110, 20, 120 and 20 cm^{-1}, respectively (Table S8). The large splitting of 120 cm^{-1} between the $m_J = \pm3$ pair is expected in D_{3h} symmetry (Figure 6, right) due to the allowed B_6^6 crystal field parameter,[13] while the large splitting between the $m_J = \pm1$ states arises from low-symmetry perturbations (i.e. from non-zero $B_k^{(\pm1,\pm2)}$ terms due to structural elements with no, or at most two-fold, rotational symmetry). The presence of this large splitting should be compared to the splittings found between the E states in **4** which are (from CASSCF-SO) 30, 20 and 30 cm^{-1}, respectively, clearly showing that low-symmetry perturbations are less influential in the presence of a strong point-like

donor atom.

In summary, we have demonstrated that treatment of oxo- and imido-triamide complexes of uranium(V) with an N-heterocyclic olefin results not in mesoionic carbene complexes but cyclometallation/disproportionation reactions that generate uranium(IV)-oxo and -imido anion complexes along with uranium(VI)-cyclometallates. The uranium(IV)-oxo and -imido complexes exhibit unusually high low-temperature magnetic moments for such low symmetry systems, that should exhibit magnetic singlet ground states, which prompted an in-depth analysis of their electronic structures using CASSCF-SO and CF methods benchmarked to low-temperature magnetisation and magnetic susceptibility experiments. The experimental magnetisation data indicate a pseudo-doublet (E) ground state for both compounds, split by ca. 7 and 8.5 cm^{-1} for **4** and **5**, respectively, determined by CF modelling of low temperature magnetometry data. These small splittings thus yield uncharacteristically large ground-state magnetic moments for formally C_1-symmetric species, owing to the presence of strong, formally $2-$ point-charge-like oxo- and imido-ligands, along with relatively high pseudo-symmetry approaching C_{3v}. These data permit us to rationalise and confirm the basic principle that a singlet (A) spin-orbit ground state is usually the default for low-symmetry uranium(IV), but this can be flipped to a pseudo-doublet (E) spin-orbit ground state when there are sufficiently strong ligands to dominate the CF. Lastly, this work suggests that there are likely many uranium(IV) complexes with E rather than A spin-orbit ground states on the basis that they exhibit low-temperature magnetic moments of $\geq 1\,\mu_B$ in the presence of strong axial-type donor ligands.

3 Experimental procedures

All manipulations were carried out under an inert atmosphere of dry nitrogen using Schlenk or glove box techniques. Compounds were characterised by single crystal X-ray diffraction, NMR, IR, and UV/Vis/NIR spectroscopies, variable temperature SQUID magnetometry, elemental analysis, and CASSCF-SO methods.

3.1 Preparation of $[U^{IV}(O)(N'')_3][(Me)C(NMeCH)_2]$ (4)

A solution of $H_2C{=}C(NMeCH)_2$ (0.05 g, 0.55 mmol) in Et_2O (5 ml) was added dropwise to a pre-cooled (−78°C) red solution of $[U^{V}(O)(N'')_3]$ (0.74 g, 1.00 mmol) in Et_2O (5 ml). The mixture was allowed to warm to room temperature slowly over 10 minutes, resulting in a colour change to brown. The reaction mixture was stirred for 1 min at room tempera-

ture. After which, the volume of the solution was reduced *in vacuo* by half, filtered using a double-wrapped cannula, and subsequently layered with hexane (5 ml). Storage of the solution at −30°C for 24 hours afforded **4** as brown needle crystals. Yield: 0.11 g, 13%. Anal. Calcd for $C_{24}H_{65}N_5OSi_6U$: C, 34.06; H, 7.74; N, 8.27%. Found: C, 33.58; H, 7.51; N 8.21%. ^{1}H NMR (C_6D_6, 298 K): δ −2.01 (br, s, 54H, Si(CH_3)$_3$), −2.97 (br, s, 2H, (H)C=C(H)), −4.89 (s, 6H, N(CH_3)), 25.26 (s, 3H, C(CH_3)) ppm. ^{29}Si{^{1}H} NMR (C_6D_6, 298 K): δ −37.74 ppm. ATR-IR ν/cm^{-1}: 2941 (s), 2892 (w), 1592 (w), 1553 (m), 1508 (w), 1416 (w), 1235 (s), 1128 (w), 984 (s), 862 (w), 823 (s), 764 (w), 747 (s), 682 (w), 660 (s), 597 (s), 478 (w), 441 (w). Note, complex **4** slowly decomposes in solution at room temperature affording [HN($SiMe_3$)$_2$] and several unidentified products after 24 hours, as indicated by ^{1}H NMR spectroscopy.

3.2 Preparation of [U^{IV}(NSiMe$_3$)(N″)$_3$][(Me)C(NMeCH)$_2$] (5)

To a cold (−78°C) stirring dark purple solution of [U^{III}(N″)$_3$] (0.81 g, 1.00 mmol) in hexane (10 ml) was added Me_3SiN_3 (0.115 g, 1.00 mmol). The mixture was allowed to warm to room temperature slowly over 10 minutes, resulting in a colour change to dark red. The reaction mixture was stirred for 20 minutes at room temperature. After which, the volume was reduced *in vacuo* by half, and a solution of H_2C=C(NMeCH)$_2$ (0.06 g, 0.55 mmol) in toluene (5 ml) was added dropwise. The reaction mixture was stirred for 2 hours at room temperature. After which, the reaction mixture was concentrated to approximately 5 ml and stored at −30°C for 24 hours, to afford **5** as brown needle crystals. Yield: 0.12 g, 13%. Anal. Calcd for $C_{27}H_{74}N_6Si_7U$: C, 35.34; H, 8.13; N, 9.16%. Found: C, 33.80; H, 7.58; N, 8.66%. ^{1}H NMR (C_6D_6, 298 K): δ 43.30 (s, 3H, C(CH_3)), −2.46 (br, s, 54H, Si(CH_3)$_3$), −6.90 (s, 6H, N(CH_3)), −10.87 (s, 2H, (H)C=C(H)), −12.55 (s, 9H, (=N(Si(CH_3)$_3$) ppm. ^{29}Si{^{1}H} NMR (C_6D_6, 298 K): δ −90.74 (=N(Si(CH_3)$_3$)), −131.19 (-N(Si(CH_3)$_3$)) ppm. ATR-IR ν/cm^{-1}: 2958 (m), 2918 (w), 2896 (w), 2849 (w), 1534 (m), 1409 (m), 1246 (s), 1092 (m), 1019 (s), 942 (s), 928 (w), 901 (w), 796 (s, br), 757 (s, br), 725 (w), 661 (s), 605 (s), 595 (w), 437 (w). Note, complex **5** decomposes in solution at room temperature affording [HN($SiMe_3$)$_2$] and several unidentified products after 30 minutes, as indicated by ^{1}H NMR spectroscopy.

3.3 Electronic structure calculations

State-averaged complete active space self-consistent field spin-orbit (CASSCF-SO) calculations are performed with OpenMolcas.[62] Scalar relativistic effects are included via a second-order Douglas-Kroll-Hess (DKH2) Hamiltonian, which is evaluated in a basis of relativistic semi-core correlated atomic natural orbital (ANO-RCC) functions.[63,64] We use basis sets of

VQZP quality on U and the first coordination sphere, and VDZP quality for all other atoms. Two electron integrals are decomposed with the Cholesky method using a threshold of 10^{-8}. CASSCF calculations are performed using a minimal active space of 2 electrons in 7 5f orbitals, averaging over 11 roots for $S = 1$ and 9 roots for $S = 0$, corresponding to the ^{3}H and ^{1}G terms, respectively. The number of optimised roots is a decisive factor, as calculations using more states fail to approach the correct high T limit of χT for both **4** and **5**; this is a result of using state-averaged molecular orbitals, where the representation of the lowest-energy states becomes less optimal as the number of averaged states increases.

4 Supplemental information

Supplemental Information can be found online at
https://doi.org/10.1016/j.chempr.2021.05.001

5 Acknowledgements

We gratefully acknowledge the UK EPSRC (EP/P001386/1, EP/M027015/1, EP/K024000/1), EPSRC EPR National Research Facility (NS/A000055/1) for access to SQUID magnetometry, ERC (CoG612724 and StG851504), Royal Society (UF11005 and URF191320), UK Defence Science and Technology Laboratory (studentship to L.B.), National Nuclear Laboratory, and the University of Manchester for access to the Computational Shared Facility.

6 Author contributions

J.A.S. prepared and characterised the compounds. L.B. carried out and interpreted the CASSCF-SO calculations. J.A.S., E.L., and F.T. carried out and interpreted the SQUID magnetometry. A.J.W. collected, solved, and refined all the crystallographic data. N.F.C. and S.T.L. assisted with data analysis, directed the research, and wrote the manuscript with input from all the authors.

7 Declaration of interests

The authors declare no competing interests or conflicts.

Supplementary Information

S1 General Experimental Considerations

All manipulations were carried out under an inert atmosphere of dry nitrogen using Schlenk techniques, or in an MBraun UniLab glovebox operating under an atmosphere of dry nitrogen with H_2O and $O_2 < 0.1$ ppm. All glassware was silylated and dried either by overnight storage in an oven at 150°C or by flame-drying with subsequent cooling under 10^{-3} mm Hg vacuum followed by repeated alternate evacuation and purging with nitrogen. Solvents were dried by passage through activated alumina towers and degassed prior to use. All solvents were stored over potassium mirrors, except for ethers that were stored over activated 4 Å molecular sieves. Deuterated solvent was distilled from a potassium mirror and degassed by three freeze pump-thaw cycles and stored under N_2. The compounds $[U(N'')_3]$, 1,3-dimethyl-2-methylene imidazoline $[H_2C{=}C(NMeCH)_2]$, and $[UO\{N(SiMe_3)_2\}_3]$[65–67] were synthesised according to published procedures. ^1H, $^{13}C\{^1H\}$, and $^{29}Si\{^1H\}$ NMR spectra were recorded on a Bruker 400 spectrometer operating at 400.1, 100.6, and 79.5 MHz, respectively; chemical shifts are quoted in ppm and are relative to TMS (^1H, ^{13}C, ^{29}Si). Samples were prepared in the glovebox and placed in J. Young PTFE 5 mm screw-topped borosilicate NMR tubes. FTIR spectra were recorded on a Bruker Alpha spectrometer with a Platinum-ATR module in the glovebox. UV/Vis/NIR spectra were recorded on a Perkin Elmer Lambda 750 spectrometer where data were collected in 1 mm path length cuvettes and were run versus the appropriate reference solvent. Static variable-temperature magnetic moment data were recorded in an applied DC field of 0.5 T on a Quantum Design MPMS XL7 superconducting quantum interference device (SQUID) magnetometer using doubly recrystallised powdered samples. Samples were carefully checked for purity and data reproducibility between several independently prepared batches for each compound examined. Care was taken to ensure complete thermalization of the sample before each data point was measured, and samples were immobilised in an eicosane matrix to prevent sample reorientation during measurements. Diamagnetic corrections were applied using tabulated Pascal constants and measurements were corrected for the effect of the blank sample holders (flame sealed Wilmad NMR tube and straw) and eicosane matrix. CHN microanalyses were carried out by Martin Jennings and Anne Davies (University of Manchester). Considerable issues were repeatedly and consistently encountered obtaining CHN data for **4** and **5**. Specifically, despite loading pristine crystalline material into the elemental analysis combustion boats, in common with other organosilicon-rich compounds,[68] silicon-carbide formation precluded

complete combustion and the instrument temperature could not be raised high enough to overcome this problem. Combustion aids did not ameliorate this situation. This issue was compounded by the fact that crystalline samples of **4** and **5** decomposed over a short time frame. Nevertheless, the characterisation data when taken together support the proposed formulation of **4** and **5**.

S2 NMR Spectra

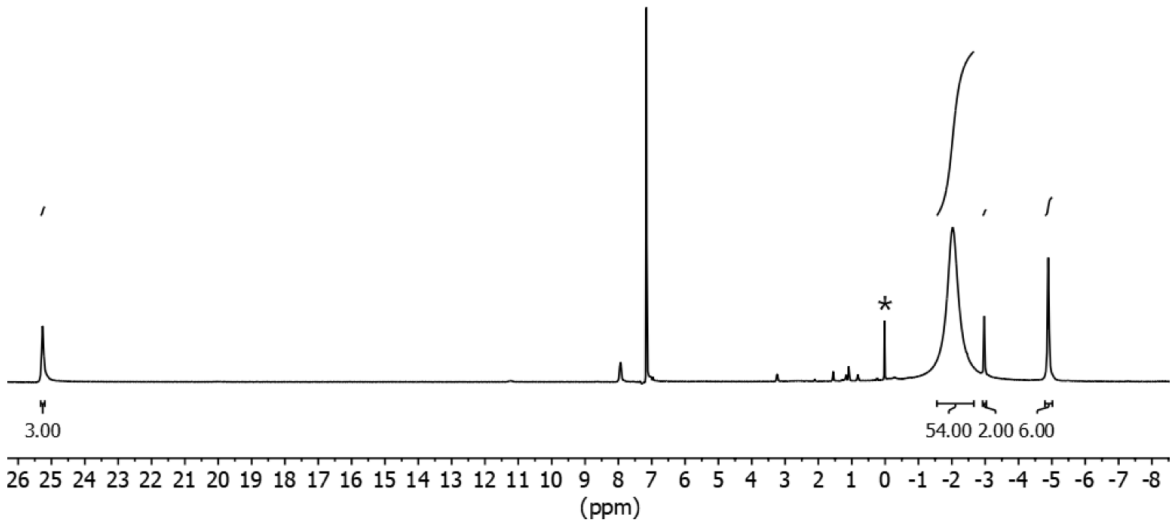

Figure S1: ^{1}H NMR spectrum of **4** – asterisk (*) denotes decomposition products.

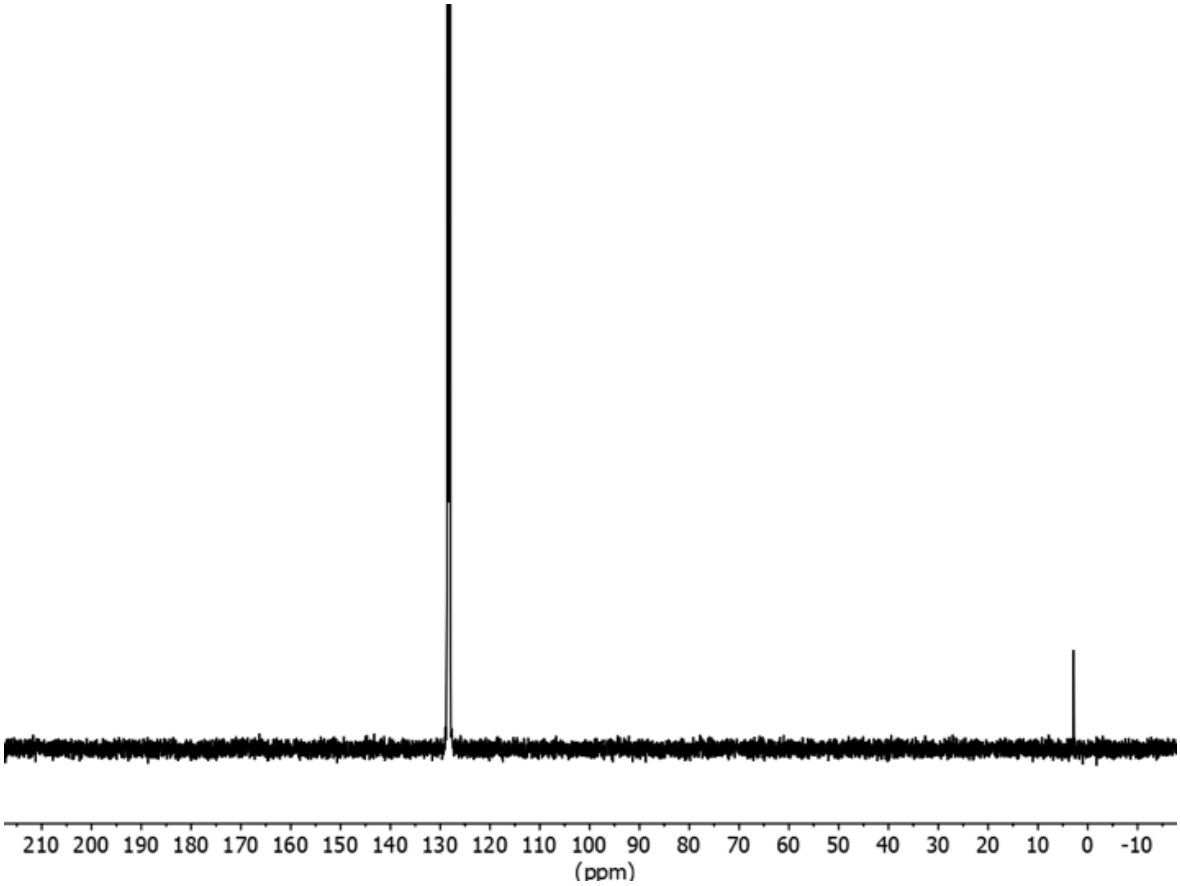

Figure S2: $^{13}C\{^{1}H\}$ NMR spectrum of **4**.

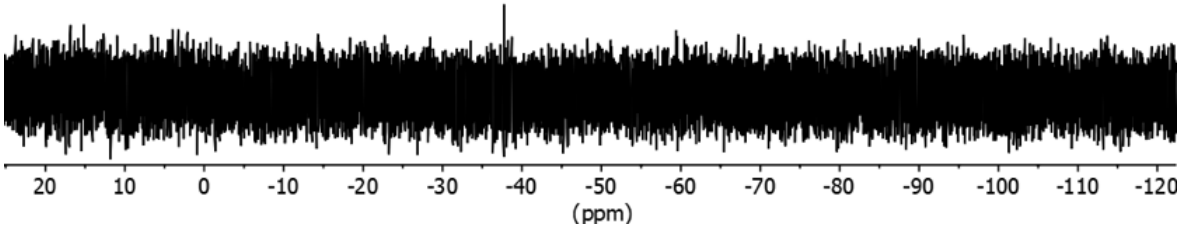

Figure S3: $^{29}Si\{^{1}H\}$ NMR spectrum of **4**.

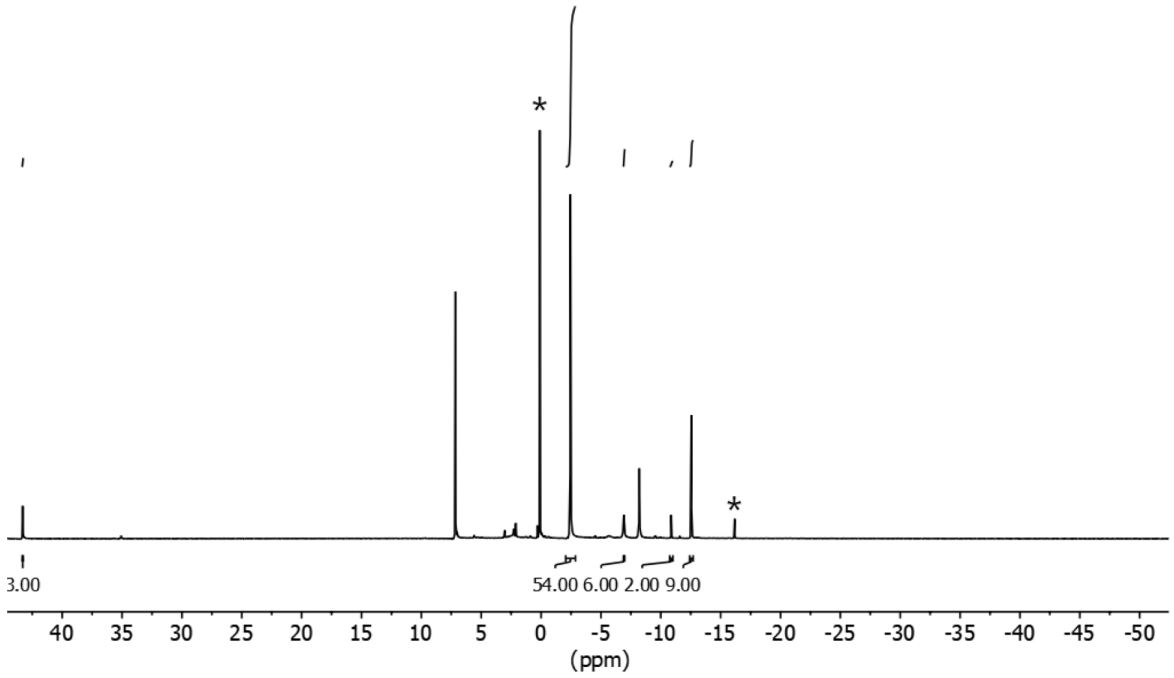

Figure S4: ^{1}H NMR spectrum of **5** – asterisk (*) denotes decomposition products.

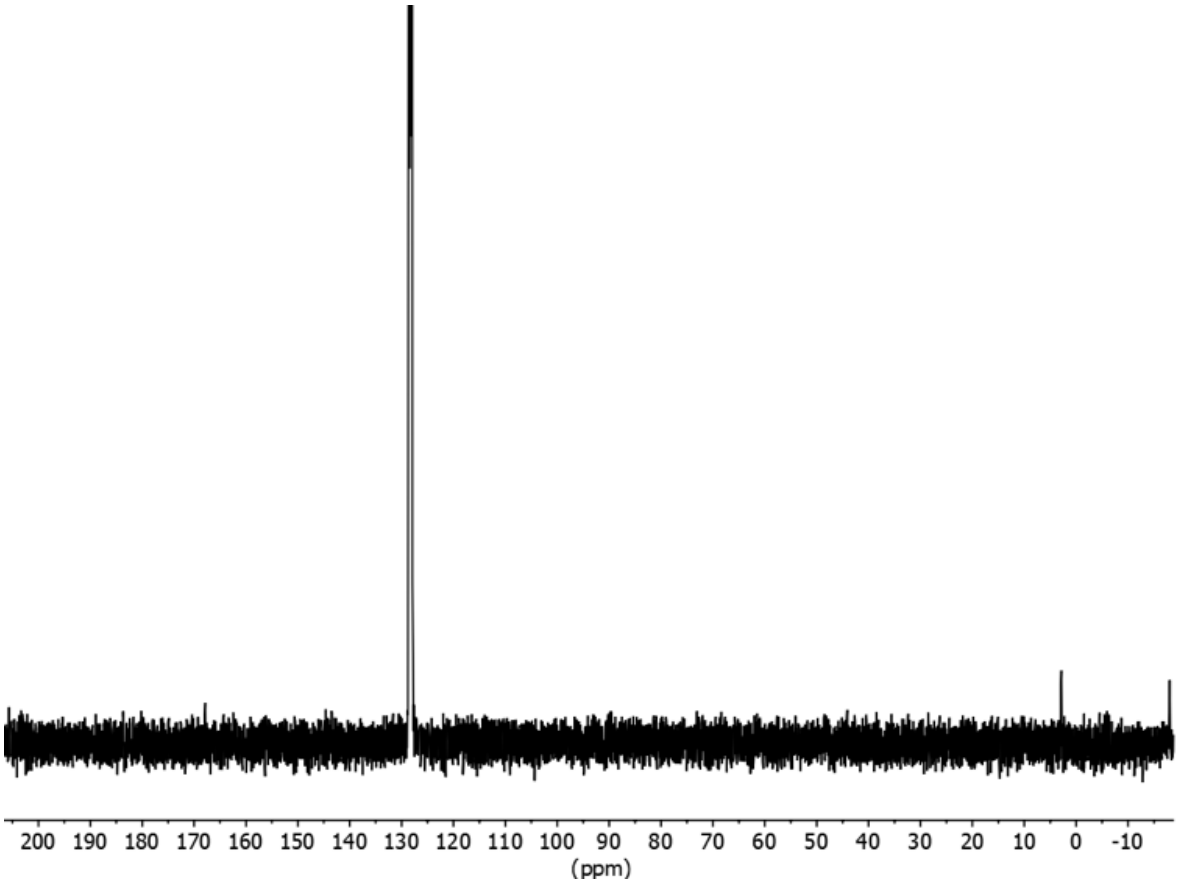

Figure S5: $^{13}C\{^{1}H\}$ NMR spectrum of **5**.

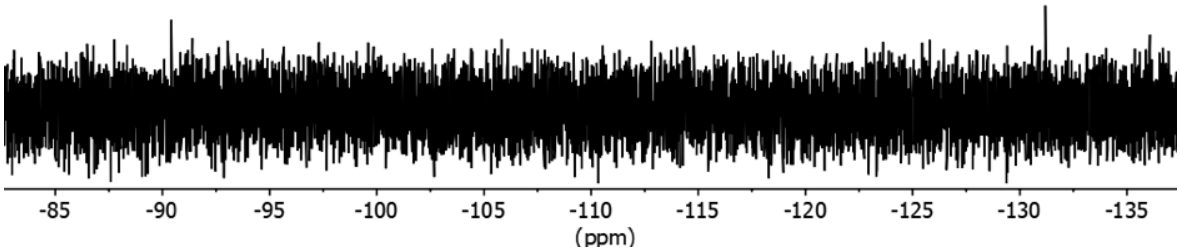

Figure S6: $^{29}Si\{^{1}H\}$ NMR spectrum of **5**.

S3 IR Spectra

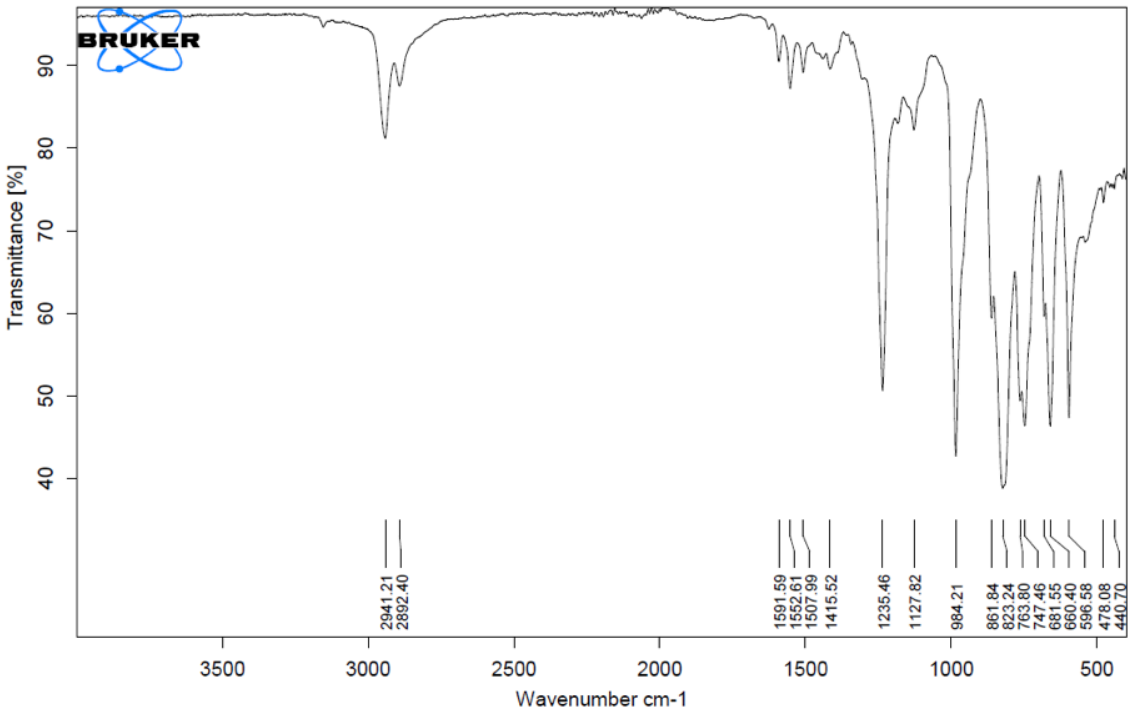

Figure S7: FTIR spectrum of **4**.

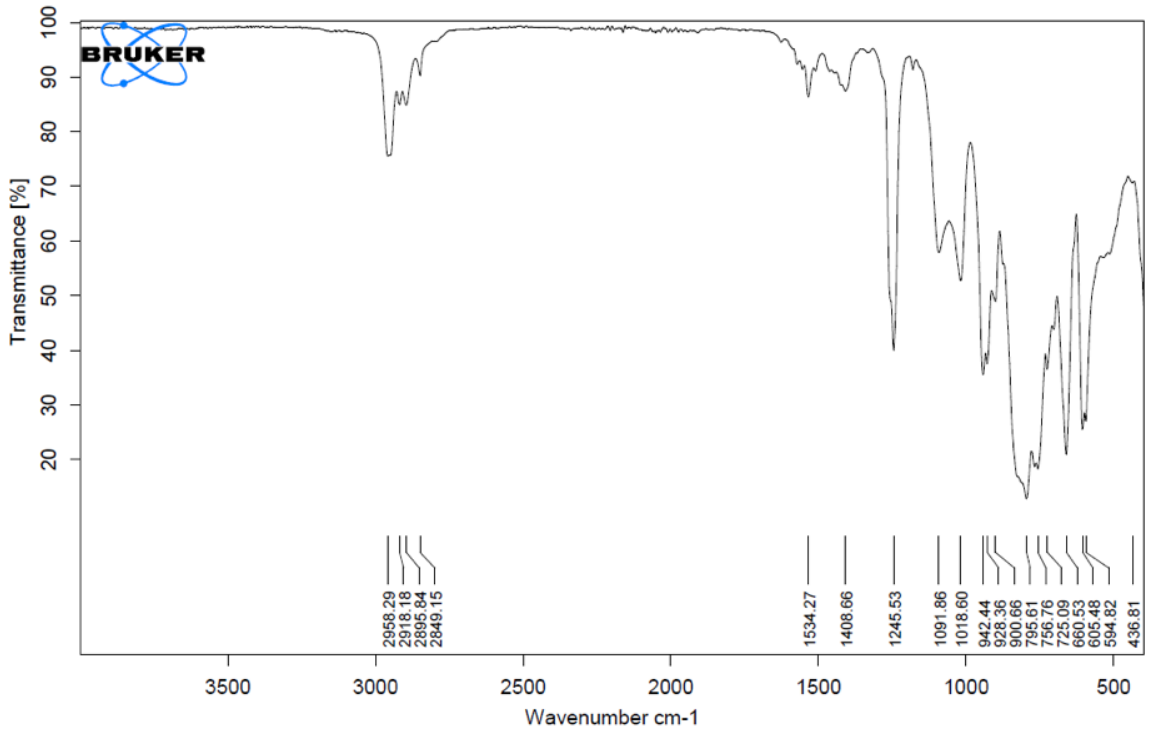

Figure S8: FTIR spectrum of **5**.

S4 SQUID Data

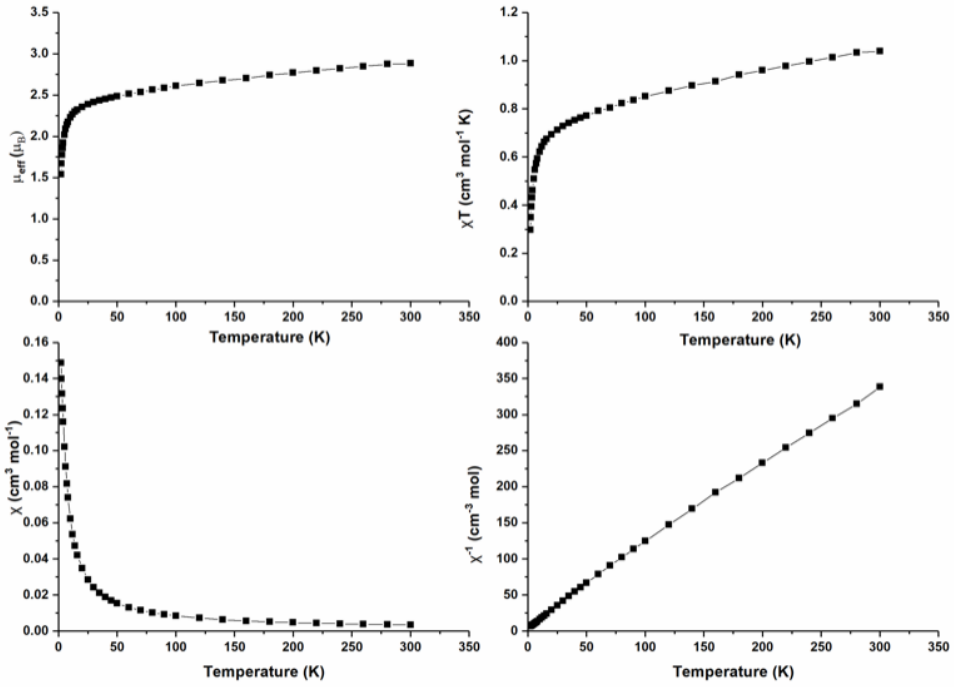

Figure S9: Variable-temperature SQUID data of a powdered sample of **4**.

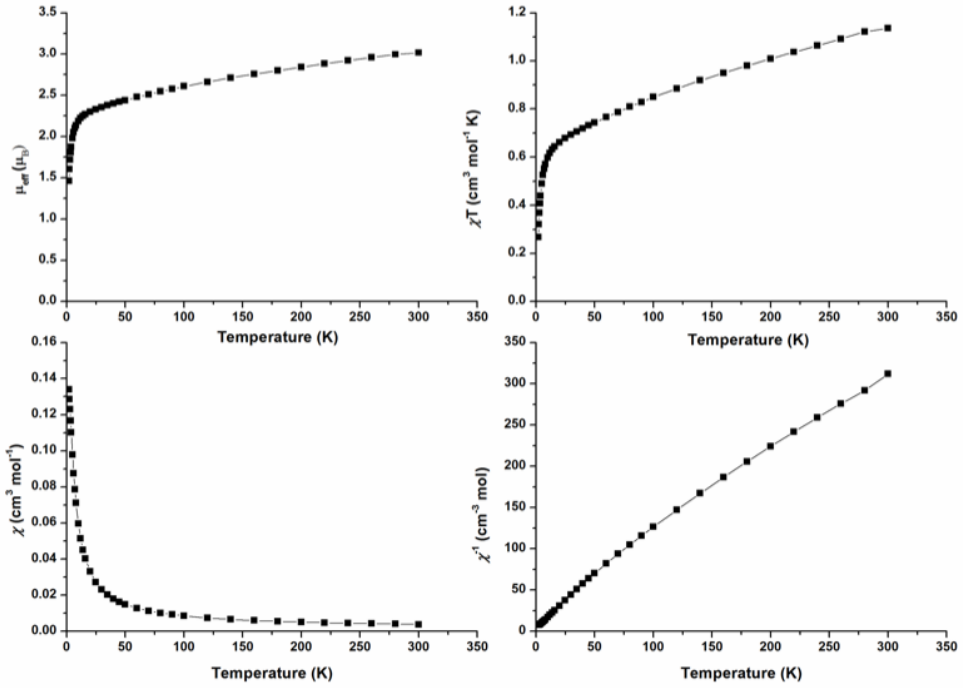

Figure S10: Variable-temperature SQUID data of a powdered sample of **5**.

S5 UV/Vis/NIR Spectra

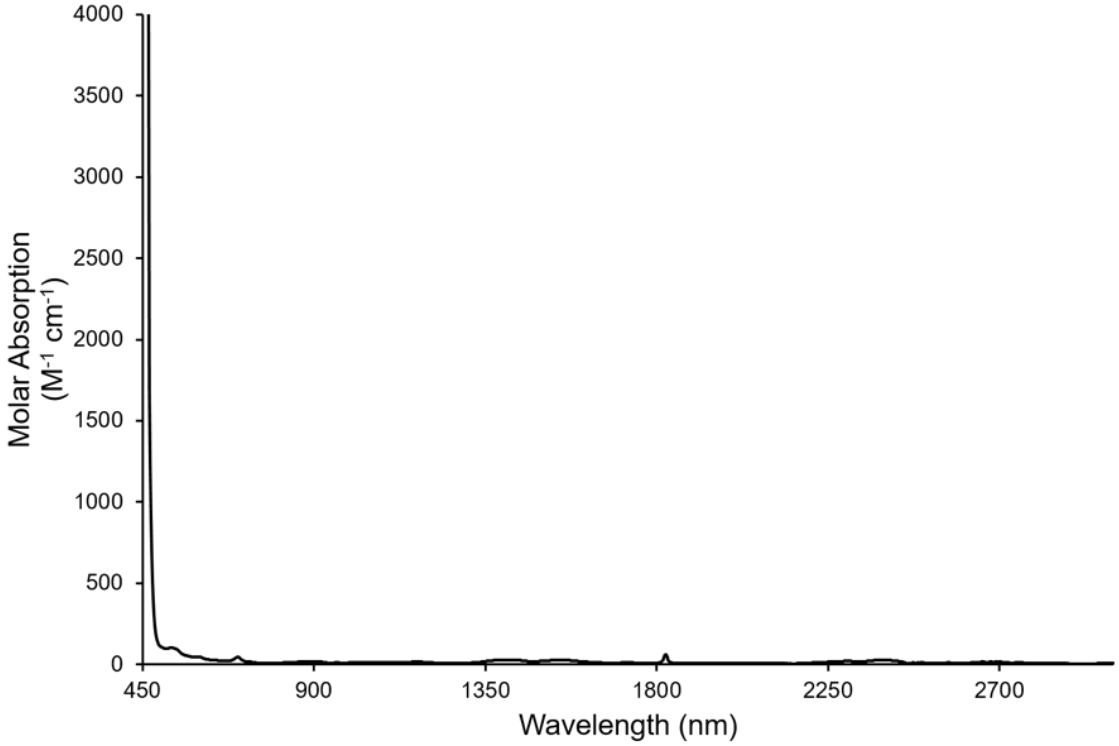

Figure S11: UV/Vis/NIR spectrum of **4**.

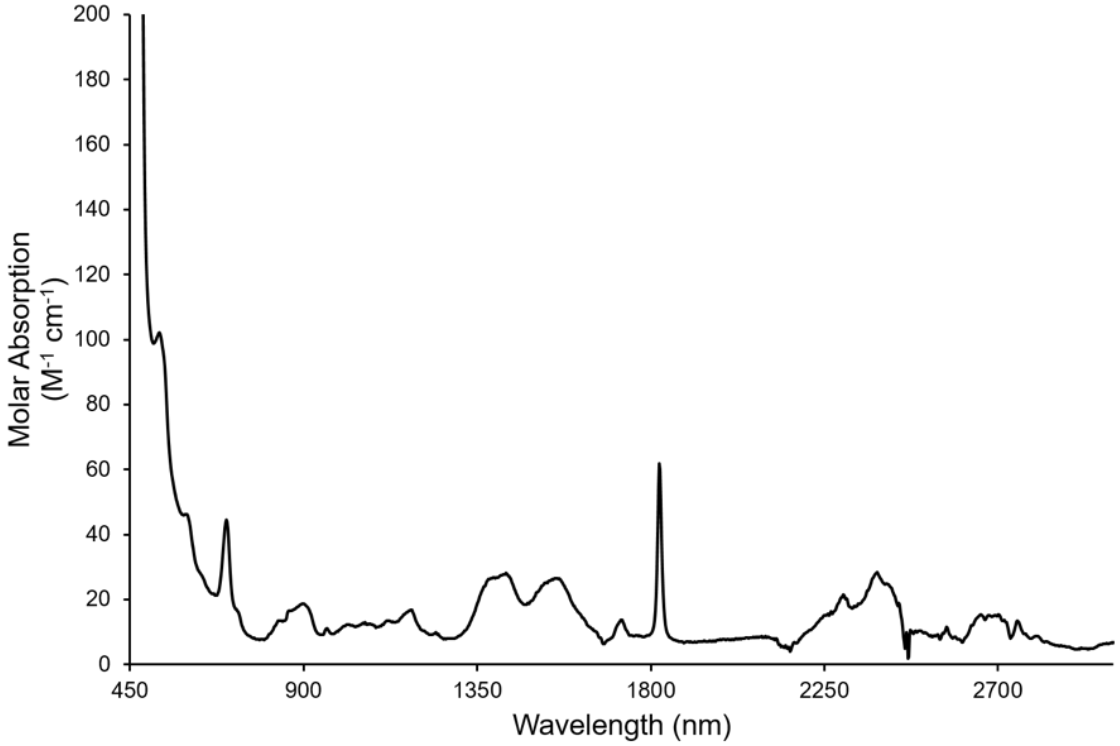

Figure S12: UV/Vis/NIR spectrum of **4** zoomed in between 450-2800 nm.

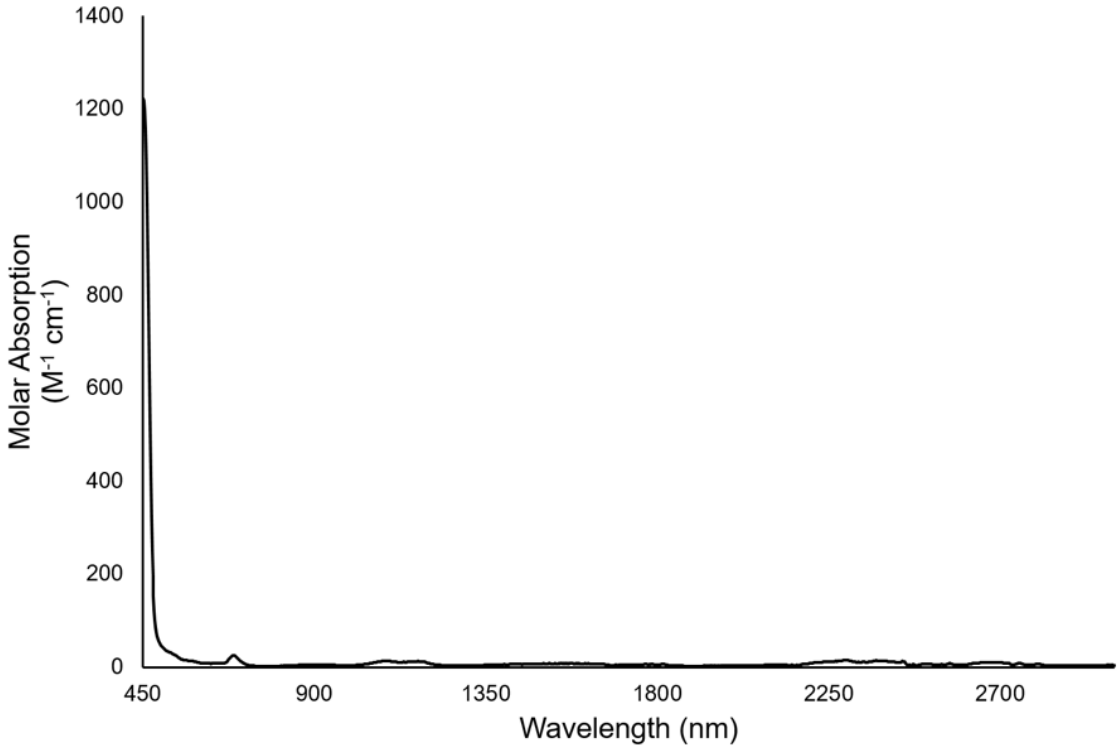

Figure S13: UV/Vis/NIR spectrum of **5**.

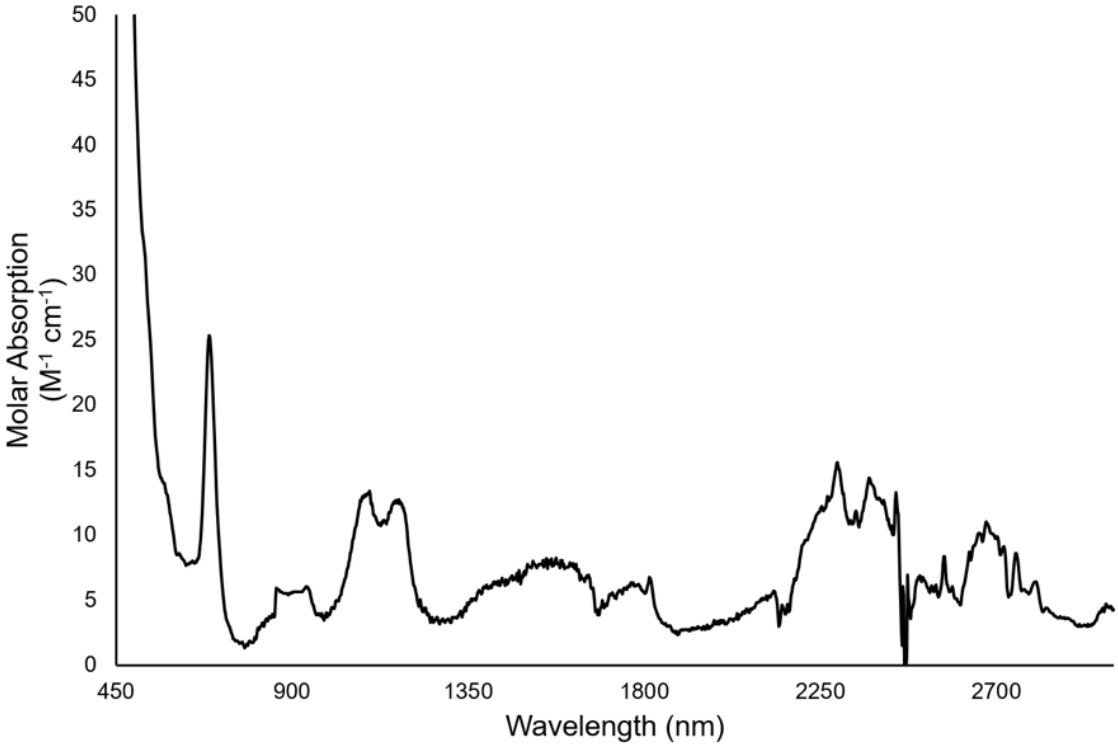

Figure S14: UV/Vis/NIR spectrum of **5** zoomed in between 450-2800 nm.

S6 Computational Modelling

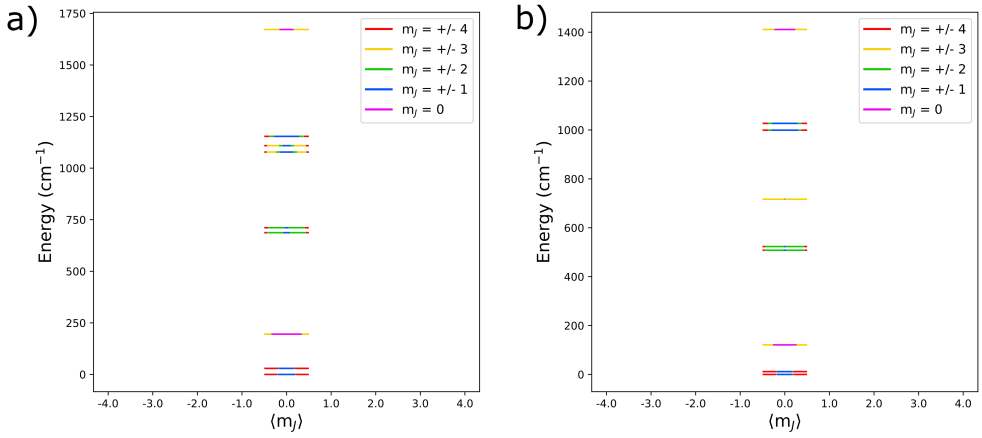

Figure S15: Eigenstates of the *ab initio* CF Hamiltonian for a) **4** and b) **5**, calculated with CASSCF(2,7)-SO using 11 and 9 triplet and singlet roots, respectively, and the QZP+QZP+DZP basis. The segmented lines illustrate the composition of each state in terms of the total angular momentum eigenfunctions $|m_J\rangle$.

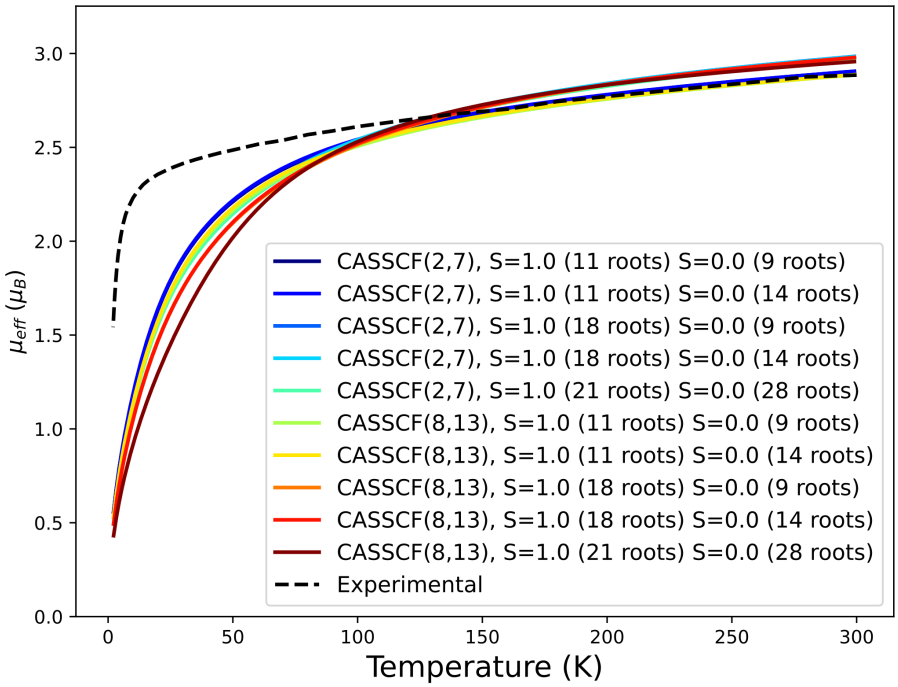

Figure S16: μ_{eff} vs. T curves derived from CASSCF-SO calculations on **4**, using a TZP+DZP+DZ basis set.

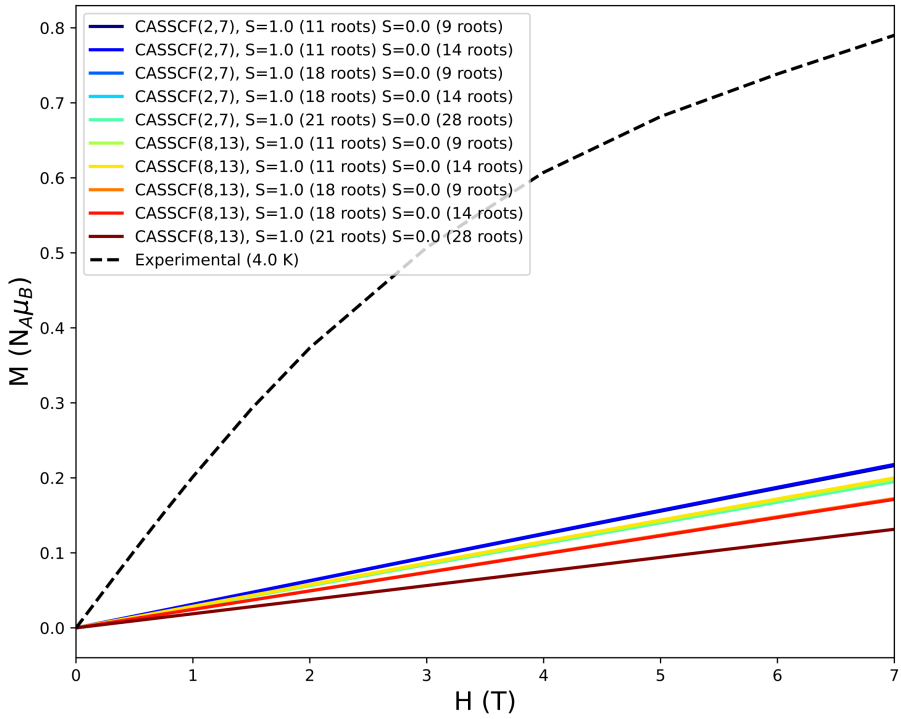

Figure S17: M vs. H curves derived from CASSCF-SO calculations on **4**, using a TZP+DZP+DZ basis set.

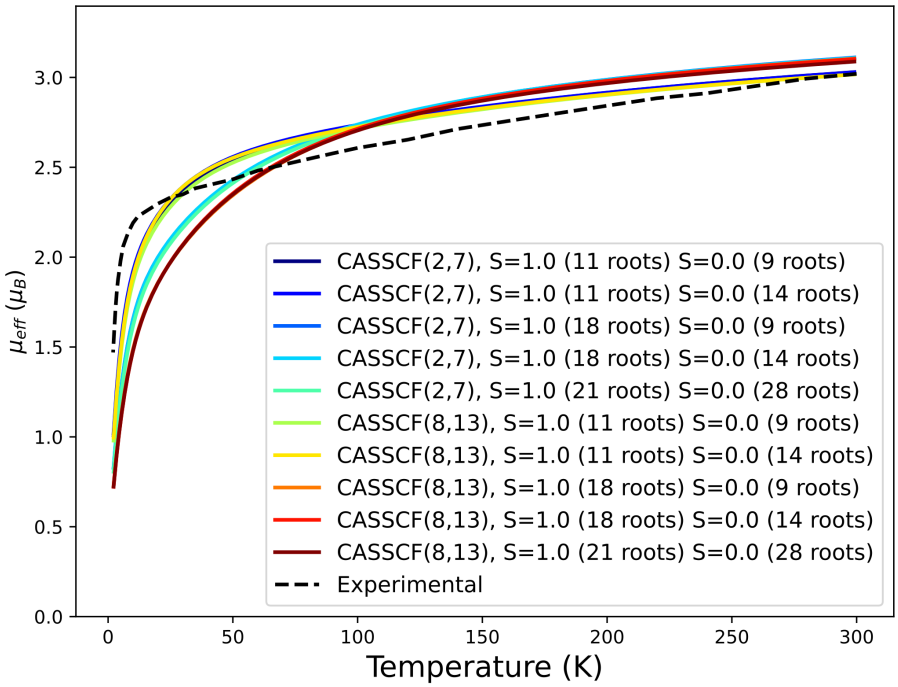

Figure S18: μ_{eff} vs. T curves derived from CASSCF-SO calculations on **5**, using a TZP+DZP+DZ basis set.

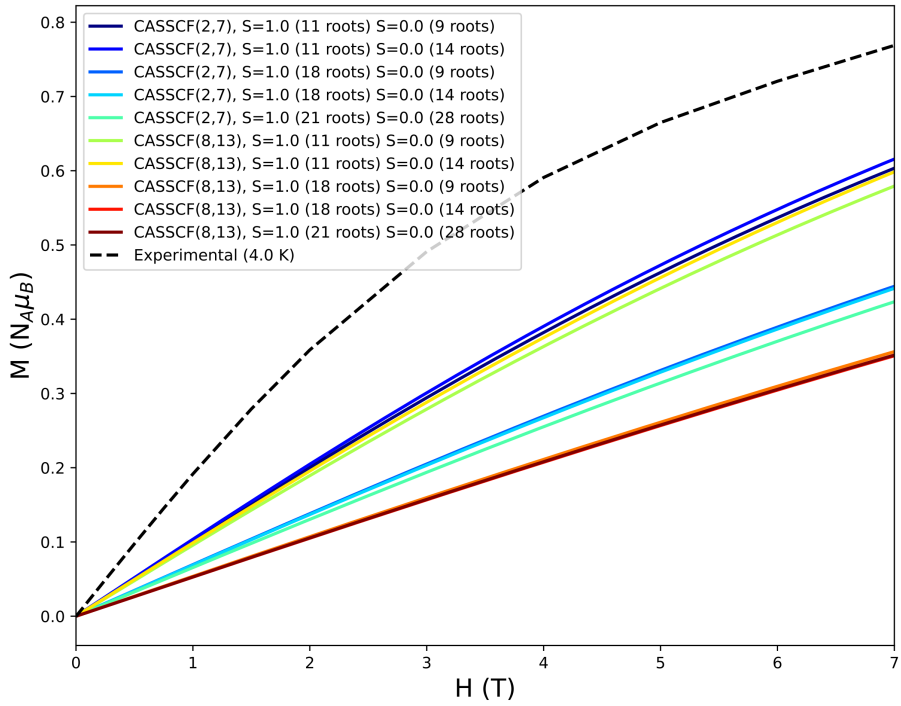

Figure S19: M vs. H curves derived from CASSCF-SO calculations on **5**, using a TZP+DZP+DZ basis set.

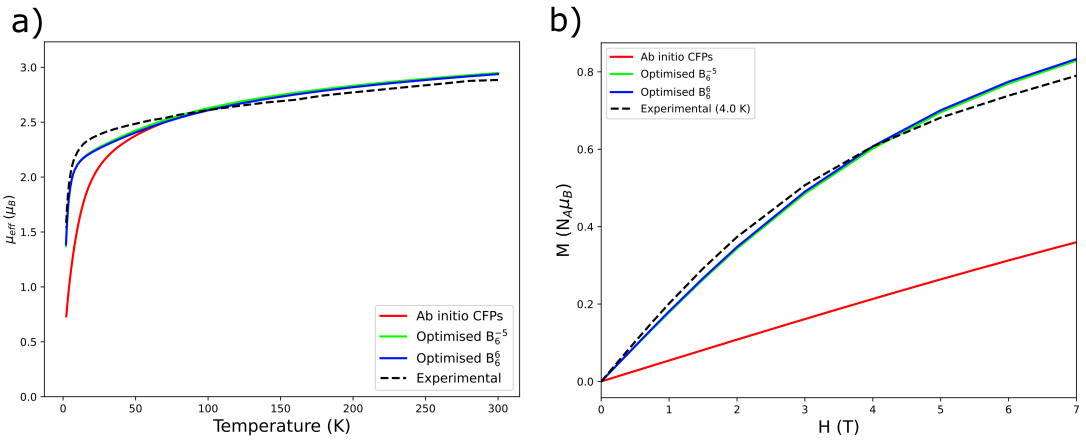

Figure S20: a) μ_{eff} vs. T and b) M vs. H curves of **4** derived from different CF Hamiltonians. For the optimised sets, only the indicated CFP was fitted to the experimental data, while the other parameters were kept fixed to their *ab initio* values.

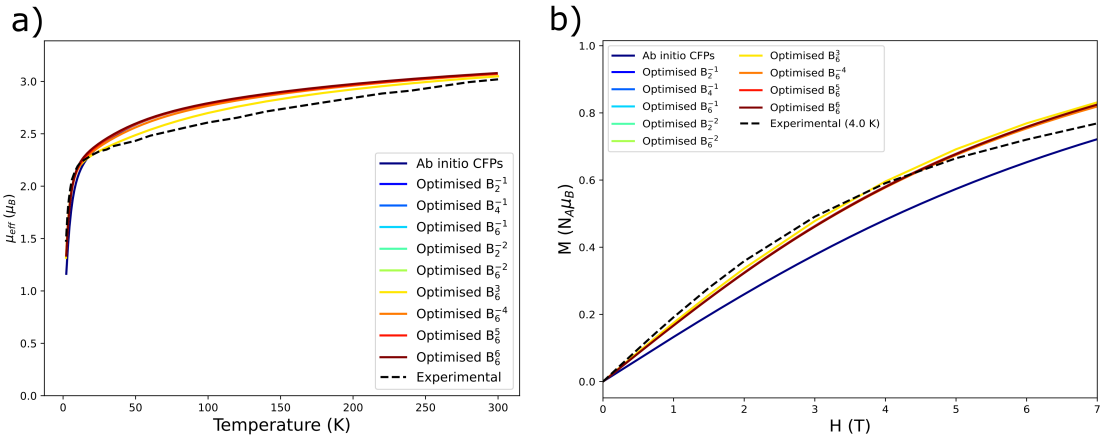

Figure S21: a) μ_{eff} vs. T and b) M vs. H curves of **5** derived from different CF Hamiltonians. For the optimised sets, only the indicated CFP was fitted to the experimental data, while the other parameters were kept fixed to their *ab initio* values.

S7 Computational Tables

Table S1: CFPs of $[U^{IV}OF_3]^-$ derived from CASSCF(2,7)-SO with 11 triplet and 9 singlet roots, using a QZP-QZP-DZP basis set.

k	q	B_k^q value /cm^{-1}
2	-2	0.0
2	-1	0.0
2	0	-136.3
2	1	0.0
2	2	0.0
4	-4	0.0
4	-3	10453.1
4	-2	0.0
4	-1	0.0
4	0	285.6
4	1	0.0
4	2	0.0
4	3	-470.1
4	4	0.0
6	-6	7.3
6	-5	0.0
6	-4	0.0
6	-3	516.7
6	-2	0.0
6	-1	0.0
6	0	-118.0
6	1	0.0
6	2	0.0
6	3	-23.2
6	4	0.0
6	5	0.0
6	6	80.7

Table S2: Energies and $|m_J\rangle$ percentage contributions for the *ab initio* CF eigenstates of **4**, as obtained from CASSCF(2,7)-SO (11 triplet and 9 singlet roots, QZP-QZP-DZP basis set).

	$\|m_J\rangle$ percentage contributions								
Energy /cm^{-1}	$\|-4\rangle$	$\|-3\rangle$	$\|-2\rangle$	$\|-1\rangle$	$\|0\rangle$	$\|1\rangle$	$\|2\rangle$	$\|3\rangle$	$\|4\rangle$
0.0	28.74	0.21	0.97	20.03	0.09	20.03	0.97	0.21	28.74
29.4	31.49	0.29	0.67	17.32	0.45	17.32	0.67	0.29	31.49
195.4	0.18	15.34	0.93	0.40	66.32	0.40	0.93	15.34	0.18
687.2	6.34	0.53	35.94	6.89	0.59	6.89	35.94	0.53	6.34
711.2	9.44	0.34	35.66	4.36	0.41	4.36	35.66	0.34	9.44
1078.0	5.42	21.34	8.63	14.46	0.28	14.46	8.63	21.34	5.42
1109.0	6.46	26.79	7.91	8.73	0.22	8.73	7.91	26.79	6.46
1154.0	11.80	1.39	9.12	27.68	0.04	27.68	9.12	1.39	11.80
1672.0	0.13	33.77	0.17	0.13	31.60	0.13	0.17	33.77	0.13

Table S3: Energies and $|m_J\rangle$ percentage contributions for the *ab initio* CF eigenstates of **5**, as obtained from CASSCF(2,7)-SO (11 triplet and 9 singlet roots, QZP-QZP-DZP basis set).

	$\|\mathbf{m_J}\rangle$ **percentage contributions**								
Energy /cm^{-1}	$\|-4\rangle$	$\|-3\rangle$	$\|-2\rangle$	$\|-1\rangle$	$\|0\rangle$	$\|1\rangle$	$\|2\rangle$	$\|3\rangle$	$\|4\rangle$
0.0	30.71	0.20	1.70	17.18	0.40	17.18	1.70	0.20	30.71
11.6	31.86	0.16	0.64	17.29	0.10	17.29	0.64	0.16	31.86
121.0	0.16	23.11	0.21	0.34	52.35	0.34	0.21	23.11	0.16
508.1	4.59	0.05	42.49	2.83	0.09	2.83	42.49	0.05	4.59
523.2	6.92	0.47	40.17	2.25	0.38	2.25	40.17	0.47	6.92
716.9	0.06	49.06	0.38	0.49	0.00	0.49	0.38	49.06	0.06
999.2	13.40	0.32	5.85	30.33	0.21	30.33	5.85	0.32	13.40
1027.0	12.22	0.05	8.52	29.12	0.18	29.12	8.52	0.05	12.22
1411.0	0.09	26.57	0.03	0.16	46.29	0.16	0.03	26.57	0.09

Table S4: CFPs of **4** derived from CASSCF(2,7)-SO with 11 triplet and 9 singlet roots, using a QZP-QZP-DZP basis set.

k	**q**	$\mathbf{B_k^q}$ **value /cm^{-1}**
2	-2	-157.3
2	-1	-64.3
2	0	183.4
2	1	-283.7
2	2	122.0
4	-4	-125.2
4	-3	7455.3
4	-2	-152.3
4	-1	241.9
4	0	347.2
4	1	-180.7
4	2	-241.4
4	3	-9312.6
4	4	-1.5
6	-6	349.1
6	-5	204.3
6	-4	-33.8
6	-3	57.6
6	-2	-27.4
6	-1	-62.3
6	0	-85.9
6	1	12.7
6	2	-27.0
6	3	-261.6
6	4	18.5
6	5	-19.4
6	6	-76.4

Table S5: CFPs of **5** derived from CASSCF(2,7)-SO with 11 triplet and 9 singlet roots, using a QZP-QZP-DZP basis set.

k	q	B_k^q value /cm^{-1}
2	-2	9.6
2	-1	251.3
2	0	283.0
2	1	146.7
2	2	-35.7
4	-4	-8.5
4	-3	-3910.3
4	-2	-13.4
4	-1	-33.4
4	0	125.4
4	1	84.0
4	2	-128.8
4	3	10386.3
4	4	115.5
6	-6	211.3
6	-5	39.7
6	-4	20.8
6	-3	-135.4
6	-2	15.5
6	-1	14.6
6	0	-73.2
6	1	-40.5
6	2	-11.4
6	3	271.5
6	4	31.2
6	5	29.3
6	6	-211.0

Table S6: RMSDs of energy levels and of pseudo-doublet energy gaps calculated with respect to *ab initio* CF data. Only optimised CFPs yielding a residual change of at least 90% are shown.

4			**5**		
Optimised CFP	Energy RMSD /cm^{-1}	Pseudo-doublet gap RMSD /cm^{-1}	Optimised CFP	Energy RMSD /cm^{-1}	Pseudo-doublet gap RMSD /cm^{-1}
B_2^1	57.6	108.9	B_2^{-1}	3.7	5.9
B_4^1	68.7	161.3	B_4^{-1}	2.9	6.6
B_6^1	25.3	77.7	B_6^{-1}	3.5	4.9
B_4^2	37.8	97.9	B_2^{-2}	2.6	4.3
B_4^3	206.8	25.3	B_4^{-2}	22.7	49.4
B_6^{-3}	93.4	17.7	B_4^2	20.9	45.9
B_6^{-5}	13.2	14.4	B_6^{-2}	2.4	4.8
B_6^6	23.8	19.9	B_6^3	43.1	2.9
			B_4^{-4}	27.6	66.6
			B_6^{-4}	7.8	11.1
			B_6^5	1.7	1.9
			B_6^6	11.1	2.1

Table S7: Relative energies of the second and third CF eigenstates obtained after fitting one CFP from the *ab initio* set to magnetic susceptibility and powder magnetisation data. Note that the different selections of CFPs for the two complexes were chosen so that the overall energy spectrum was minimally affected after optimisation.

4				
Optimised CFP	Initial CFP value	Optimised CFP value	1st excited state /cm^{-1}	2nd excited state /cm^{-1}
B_6^{-5}	204.3	572.4	6.8	185.0
B_6^6	-76.4	-1032.0	6.5	196.0
5				
Optimised CFP	Initial CFP value	Optimised CFP value	1st excited state /cm^{-1}	2nd excited state /cm^{-1}
B_2^{-2}	9.6	30.6	8.5	119.0
B_2^{-1}	251.3	109.3	8.4	118.0
B_4^{-1}	-33.4	59.7	8.5	121.0
B_6^{-4}	20.8	-167.2	8.4	136.0
B_6^{-2}	15.5	-9.3	8.5	120.0
B_6^{-1}	14.6	121.1	8.4	117.0
B_6^3	271.5	-256.6	7.9	198.0
B_6^5	29.3	-32.3	8.5	119.0
B_6^6	-211.0	-391.2	8.8	126.0

Table S8: Energies and $|m_J\rangle$ percentage contributions for the *ab initio* CF eigenstates of $[U^{IV}(N'')_3]^+$ (**4** without the oxo anion), as obtained from CASSCF(2,7)-SO (11 triplet and 9 singlet roots, QZP-QZP-DZP basis set).

	$\|m_J\rangle$ percentage contributions								
Energy /cm^{-1}	$\|-4\rangle$	$\|-3\rangle$	$\|-2\rangle$	$\|-1\rangle$	$\|0\rangle$	$\|1\rangle$	$\|2\rangle$	$\|3\rangle$	$\|4\rangle$
0.0	0.00	0.1	0.27	0.44	98.37	0.44	0.27	0.10	0.00
160.5	0.07	0.02	0.20	49.51	0.43	49.51	0.20	0.02	0.07
266.6	0.09	0.03	0.15	49.50	0.45	49.50	0.15	0.03	0.09
1053.4	0.02	0.05	49.77	0.09	0.14	0.09	49.77	0.05	0.02
1073.5	0.02	0.09	49.44	0.26	0.39	0.26	49.44	0.09	0.02
2828.7	0.07	49.80	0.08	0.02	0.07	0.02	0.08	49.80	0.07
2946.2	0.08	49.77	0.06	0.03	0.15	0.03	0.06	49.77	0.08
3807.4	49.85	0.07	0.01	0.07	0.00	0.07	0.01	0.07	49.85
3825.4	49.81	0.08	0.03	0.09	0.00	0.09	0.03	0.08	49.81

References

(1) S. T. Liddle, *Angewandte Chemie International Edition*, 2015, **54**, 8604–8641.

(2) N. Kaltsoyannis and S. T. Liddle, *Chem*, 2016, **1**, 659–662.

(3) R. Taylor, *Chem*, 2016, **1**, 662–663.

(4) S. Ion, *Chem*, 2016, **1**, 663–665.

(5) J. P. Day and L. M. Venanzi, *Journal of the Chemical Society A*, 1966, 197–200.

(6) I. Castro-Rodríguez and K. Meyer, *Chemical Communications*, 2006, 1353–1368.

(7) B. M. Gardner, D. M. King, F. Tuna, A. J. Wooles, N. F. Chilton and S. T. Liddle, *Chemical Science*, 2017, **8**, 6207–6217.

(8) M. W. Rosenzweig, F. W. Heinemann, L. Maron and K. Meyer, *Inorganic Chemistry*, 2017, **56**, 2792–2800.

(9) F. Gendron, B. Le Guennic and J. Autschbach, *Inorganic Chemistry*, 2014, **53**, 13174–13187.

(10) N. A. Siladke, K. R. Meihaus, J. W. Ziller, M. Fang, F. Furche, J. R. Long and W. J. Evans, *Journal of the American Chemical Society*, 2012, **134**, 1243–1249.

(11) C. A. Hutchison and G. A. Candela, *Journal of Chemical Physics*, 1957, **27**, 707–710.

(12) K. S. Pedersen, K. R. Meihaus, A. Rogalev, F. Wilhelm, D. Aravena, M. Amoza, E. Ruiz, J. R. Long, J. Bendix and R. Clérac, *Angewandte Chemie International Edition*, 2019, **58**, 15650–15654.

(13) C. Görller-Walrand and K. Binnemans, Rationalization of crystal-field parametrization, in *Handbook on the Physics and Chemistry of Rare Earths*, Elsevier, 1996, vol. 23, ch. 155, pp. 121–283.

(14) J. Su, P. D. Dau, H.-T. Liu, D.-L. Huang, F. Wei, W. H. E. Schwarz, J. Li and L.-S. Wang, *Journal of Chemical Physics*, 2015, **142**, 134308.

(15) J. J. Sakurai and S. F. Tuan, *Modern Quantum Mechanics*, Addison-Wesley Pub. Co, Reading, 1994.

(16) A. Streitwieser and U. Mueller-Westerhoff, *Journal of the American Chemical Society*, 1968, **90**, 7364–7364.

(17) N. Edelstein, G. Lamar, F. Mares and A. Streitwieser, *Chemical Physics Letters*, 1971, **8**, 399–402.

(18) D. G. Karraker, J. A. Stone, E. R. Jones and N. Edelstein, *Journal of the American Chemical Society*, 1970, **92**, 4841–4845.

(19) A. H. H. Chang and R. M. Pitzer, *Journal of the American Chemical Society*, 1989, **111**, 2500–2507.

(20) R. G. Hayes and N. Edelstein, *Journal of the American Chemical Society*, 1972, **94**, 8688–8691.

(21) K. D. Warren, *Inorganic Chemistry*, 1975, **14**, 3095–3103.

(22) B. S. Newell, A. K. Rappé and M. P. Shores, *Inorganic Chemistry*, 2010, **49**, 1595–1606.

(23) S. Fortier, B. C. Melot, G. Wu and T. W. Hayton, *Journal of the American Chemical Society*, 2009, **131**, 15512–15521.

(24) F. M. Chadwick, A. Ashley, G. Wildgoose, J. M. Goicoechea, S. Randall and D. O'Hare, *Dalton Transactions*, 2010, **39**, 6789–6793.

(25) L. A. Seaman, S. Fortier, G. Wu and T. W. Hayton, *Inorganic Chemistry*, 2011, **50**, 636–646.

(26) S. Fortier, J. L. Brown, N. Kaltsoyannis, G. Wu and T. W. Hayton, *Inorganic Chemistry*, 2012, **51**, 1625–1633.

(27) J. L. Brown, S. Fortier, R. A. Lewis, G. Wu and T. W. Hayton, *Journal of the American Chemical Society*, 2012, **134**, 15468–15475.

(28) D. Patel, W. Lewis, A. J. Blake, S. T. Liddle, F. Tuna and E. J. McInnes, *Angewandte Chemie (International Edition)*, 2013, **52**.

(29) A. J. Lewis, U. J. Williams, P. J. Carroll and E. J. Schelter, *Inorganic Chemistry*, 2013, **52**, 7326–7328.

(30) B. M. Gardner, G. Balázs, M. Scheer, F. Tuna, E. J. McInnes, J. McMaster, W. Lewis, A. J. Blake and S. T. Liddle, *Angewandte Chemie*, 2014, **126**, 4573–4577.

(31) D. M. King, J. McMaster, F. Tuna, E. J. McInnes, W. Lewis, A. J. Blake and S. T. Liddle, *Journal of the American Chemical Society*, 2014, **136**, 5619–5622.

(32) D. P. Halter, H. S. La Pierre, F. W. Heinemann and K. Meyer, *Inorganic Chemistry*, 2014, **53**, 8418–8424.

(33) B. M. Gardner, G. Balázs, M. Scheer, F. Tuna, E. J. McInnes, J. McMaster, W. Lewis, A. J. Blake and S. T. Liddle, *Nature Chemistry*, 2015, **7**, 582–590.

(34) T. M. Rookes, B. M. Gardner, G. Balázs, M. Gregson, F. Tuna, A. J. Wooles, M. Scheer and S. T. Liddle, *Angewandte Chemie International Edition*, 2017, **56**, 10495–10500.

(35) M. Gregson, E. Lu, D. P. Mills, F. Tuna, E. J. McInnes, C. Hennig, A. C. Scheinost, J. McMaster, W. Lewis, A. J. Blake et al., *Nature Communications*, 2017, **8**, 1–11.

(36) E. Lu, J. T. Boronski, M. Gregson, A. J. Wooles and S. T. Liddle, *Angewandte Chemie*, 2018, **130**, 5604–5609.

(37) E. Lu, A. J. Wooles, M. Gregson, P. J. Cobb and S. T. Liddle, *Angewandte Chemie*, 2018, **130**, 6697–6701.

(38) J. T. Boronski, L. R. Doyle, J. A. Seed, A. J. Wooles and S. T. Liddle, *Angewandte Chemie*, 2020, **132**, 301–305.

(39) J. A. Seed, H. R. Sharpe, H. J. Futcher, A. J. Wooles and S. T. Liddle, *Angewandte Chemie International Edition*, 2020, **59**, 15870–15874.

(40) J. A. Seed, M. Gregson, F. Tuna, N. F. Chilton, A. J. Wooles, E. J. McInnes and S. T. Liddle, *Angewandte Chemie*, 2017, **129**, 11692–11696.

(41) S. Fortier, N. Kaltsoyannis, G. Wu and T. W. Hayton, *Journal of the American Chemical Society*, 2011, **133**, 14224–14227.

(42) C. J. Windorff and W. J. Evans, *Organometallics*, 2014, **33**, 3786–3791.

(43) D. P. Mills, F. Moro, J. McMaster, J. Van Slageren, W. Lewis, A. J. Blake and S. T. Liddle, *Nature Chemistry*, 2011, **3**, 454–460.

(44) A. Zalkin, J. G. Brennan and R. A. Andersen, *Acta Crystallographica Section C: Crystal Structure Communications*, 1988, **44**, 1553–1554.

(45) D. E. Smiles, G. Wu and T. W. Hayton, *Journal of the American Chemical Society*, 2014, **136**, 96–99.

(46) R. E. Jilek, N. C. Tomson, R. L. Shook, B. L. Scott and J. M. Boncella, *Inorganic Chemistry*, 2014, **53**, 9818–9826.

(47) K. C. Mullane, A. J. Lewis, H. Yin, P. J. Carroll and E. J. Schelter, *Inorganic Chemistry*, 2014, **53**, 9129–9139.

(48) D. R. Kindra and W. J. Evans, *Chemical Reviews*, 2014, **114**, 8865–8882.

(49) T. K. Todorova, L. Gagliardi, J. R. Walensky, K. A. Miller and W. J. Evans, *Journal of the American Chemical Society*, 2010, **132**, 12397–12403.

(50) M. Spivak, K. D. Vogiatzis, C. J. Cramer, C. d. Graaf and L. Gagliardi, *Journal of Physical Chemistry A*, 2017, **121**, 1726–1733.

(51) D. M. King, P. A. Cleaves, A. J. Wooles, B. M. Gardner, N. F. Chilton, F. Tuna, W. Lewis, E. J. McInnes and S. T. Liddle, *Nature Communications*, 2016, **7**, 1–14.

(52) K. Stevens, *Proceedings of the Physical Society. Section A*, 1952, **65**, 209.

(53) A. Abragam and B. Bleaney, *Electron paramagnetic resonance of transition ions*, Oxford University Press, 2012.

(54) L. Ungur and L. F. Chibotaru, *Chemistry–A European Journal*, 2017, **23**, 3708–3718.

(55) N. F. Chilton, R. P. Anderson, L. D. Turner, A. Soncini and K. S. Murray, *Journal of Computational Chemistry*, 2013, **34**, 1164–1175.

(56) L. F. Chibotaru and L. Ungur, *Journal of Chemical Physics*, 2012, **137**, 064112.

(57) D. M. King, F. Tuna, J. McMaster, W. Lewis, A. J. Blake, E. J. McInnes and S. T. Liddle, *Angewandte Chemie*, 2013, **125**, 5021–5024.

(58) J. D. Rinehart and J. R. Long, *Chemical Science*, 2011, **2**, 2078–2085.

(59) N. Chilton, D. Collison, E. McInnes, R. Winpenny and A. Soncini, *Nature Communications*, 2013, **4**, 2551.

(60) N. F. Chilton, *Inorganic Chemistry*, 2015, **54**, 2097–2099.

(61) J. Sievers, *Zeitschrift für Physik B Condensed Matter*, 1982, **45**, 289–296.

(62) I. Fdez. Galván, M. Vacher, A. Alavi, C. Angeli, F. Aquilante, J. Autschbach, J. J. Bao, S. I. Bokarev, N. A. Bogdanov, R. K. Carlson, L. F. Chibotaru, J. Creutzberg, N. Dattani, M. G. Delcey, S. S. Dong, A. Dreuw, L. Freitag, L. M. Frutos, L. Gagliardi, F. Gendron, A. Giussani, L. González, G. Grell, M. Guo, C. E. Hoyer, M. Johansson, S. Keller, S. Knecht, G. Kovačević, E. Källman, G. Li Manni, M. Lundberg, Y. Ma, S. Mai, J. P. Malhado, P. Å. Malmqvist, P. Marquetand, S. A. Mewes, J. Norell, M. Olivucci, M. Oppel, Q. M. Phung, K. Pierloot, F. Plasser, M. Reiher, A. M. Sand, I. Schapiro, P. Sharma, C. J. Stein, L. K. Sørensen, D. G. Truhlar, M. Ugandi, L. Ungur, A. Valentini, S. Vancoillie, V. Veryazov, O. Weser, T. A. Wesołowski, P.-O. Widmark, S. Wouters, A. Zech, J. P. Zobel and R. Lindh, *Journal of Chemical Theory and Computation*, 2019, **15**, 5925–5964.

(63) B. O. Roos, R. Lindh, P.-Å. Malmqvist, V. Veryazov and P.-O. Widmark, *Journal of Physical Chemistry A*, 2004, **108**, 2851–2858.

(64) B. O. Roos, R. Lindh, P.-Å. Malmqvist, V. Veryazov and P.-O. Widmark, *Chemical Physics Letters*, 2005, **409**, 295–299.

(65) R. A. Andersen, *Inorganic Chemistry*, 1979, **18**, 1507–1509.

(66) A. Fürstner, M. Alcarazo, R. Goddard and C. W. Lehmann, *Angewandte Chemie International Edition*, 2008, **47**, 3210–3214.

(67) S. Fortier, J. L. Brown, N. Kaltsoyannis, G. Wu and T. W. Hayton, *Inorganic Chemistry*, 2012, **51**, 1625–1633.

(68) P. B. Hitchcock, M. F. Lappert, L. Maron and A. V. Protchenko, *Angewandte Chemie International Edition*, 2008, **47**, 1488–1491.

Chapter 4

Paper two: "Hyperion: a New Computational Tool for Relativistic Ab Initio Hyperfine Coupling"

Hyperion: a New Computational Tool for Relativistic *Ab Initio* Hyperfine Coupling

Letitia Birnoschi[1] and Nicholas F. Chilton[1]

[1]Department of Chemistry, The University of Manchester, Oxford Road, Manchester, M13 9PL, United Kingdom

Abstract

Herein we describe Hyperion, a new program for computing relativistic picture-change-corrected magnetic resonance parameters from scalar relativistic active space wavefunctions, with or without spin-orbit coupling (SOC) included *a posteriori*. Hyperion also includes a new orbital decomposition method for assisting active space selection for calculations of hyperfine coupling. For benchmarking purposes we determine hyperfine coupling constants of selected alkali metal, transition metal and lanthanide atoms, based on complete active space self-consistent field spin-orbit calculations in OpenMolcas. Our results are in excellent agreement with experimental data from atomic spectroscopy, as well as theoretical predictions from 4-component relativistic calculations.

1 Introduction

Magnetic resonance spectroscopy techniques, such as Electron Paramagnetic Resonance (EPR) and Nuclear Magnetic Resonance (NMR), are capable of providing very accurate information on the interactions between electron spins, nuclear spins and external magnetic fields. The information available from EPR and NMR spectra is often encoded, via iterative fitting of the experimental data to a model spin Hamiltonian, in a set of effective parameters, each related to a specific type of coupling between magnetic entities. Quantities probing interactions between electron and nuclear spins, namely EPR hyperfine coupling constants (HFCCs) and paramagnetic NMR shifts, depend strongly on unpaired electron (spin) density[1,2] and can therefore be used to measure effects due to chemical bonding. For example,

a recent study employed HFCCs as proxies for covalency in a series of actinide complexes.[3]

The steady evolution of electronic structure algorithms has made it computationally feasible to study heavy-element complexes fully *ab initio*. As the atomic number increases, relativistic effects become more important, to the extent where they cannot be regarded as mere perturbations of the Schrödinger picture; instead, a 4-component Dirac formalism becomes necessary. The onset of the relativistic regime is especially important for magnetic interactions, which couple the electronic and positronic degrees of freedom of a Dirac spinor, therefore requiring an explicit description of the latter. Hence, theoretical frameworks developed for magnetic properties such as hyperfine coupling (HFC) must account for relativistic effects – both spin-independent (scalar relativistic, SR) and spin-dependent (e.g. spin-orbit coupling, SOC) to ensure a wide range of applicability and to keep up with the latest experimental advances.

HFC between an unpaired electron spin $\mathbf{S}$ and a nuclear spin $\mathbf{I}_\mathrm{N}$ is most frequently modelled non-relativistically as the sum of anisotropic dipolar coupling, known as the spin-dipole (SD) mechanism, and isotropic Fermi Coupling (FC):[4]

$$\widehat{\mathrm{H}}_\mathrm{SD} = \frac{\mu_0}{4\pi}\, g_\mathrm{e}\mu_\mathrm{B} g_\mathrm{N}\mu_\mathrm{N} \left\{ \frac{3(\mathbf{I}_\mathrm{N}\cdot\mathbf{r}_\mathrm{N})(\mathbf{r}_\mathrm{N}\cdot\mathbf{S})}{\mathbf{r}_\mathrm{N}^5} - \frac{\mathbf{I}_\mathrm{N}\cdot\mathbf{S}}{\mathbf{r}_\mathrm{N}^3} \right\}, \qquad \widehat{\mathrm{H}}_\mathrm{FC} = \frac{2\mu_0}{3}\, g_\mathrm{e}\mu_\mathrm{B} g_\mathrm{N}\mu_\mathrm{N}\, \rho_\mathrm{N}^{\alpha-\beta}, \quad (1)$$

where we use μ_0, g_e, μ_B g_N, μ_N and $\mathbf{I}_\mathrm{N}$ to denote the vacuum permeability, electron g-factor, Bohr magneton, nuclear g-factor, nuclear magneton and nuclear spin vector, respectively; $\mathbf{r}_\mathrm{N} = \mathbf{r} - \mathbf{R}_\mathrm{N}$ is the position vector of the unpaired electron with respect to the magnetic nucleus. The strength of FC is proportional to the spin population at the magnetic nucleus, $\rho_\mathrm{N}^{\alpha-\beta}$, thus providing a convenient probe for spin delocalisation in a molecule. Although the single-configurational view of electronic structure suggests that this term arises solely through s-type atomic orbital (AO) contributions to the singly-occupied molecular orbital (SOMO), several factors complicate this interpretation.

Differences between the interaction of core spin-up and spin-down electrons with the unpaired spin give rise to *spin polarisation* (SP),[2] which give additional contributions to the isotropic HFC and cannot be described by a single electronic configuration. Thus, the quantitative interpretation of HFCCs requires quantum chemical techniques to model the electronic structure accurately and capture SP effects. For this purpose, there are two possible

solutions: spin-unrestricted single configurational methods, such as Unrestricted Hartree-Fock (UHF) and Unrestricted Kohn-Sham Density Functional Theory (UKS-DFT), which offer low computational cost at the expense of broken spin symmetry, and more expensive spin-adapted multiconfigurational methods, which preserve spin symmetry and are designed to handle electron correlation.

Unrestricted DFT is currently the most widely used approach for determining HFCCs, due to the lower computational cost relative to wavefunction-based (*ab initio*) algorithms. Hybrid functionals give good predictions for HFCCs of organic radicals and transition metal complexes,[5,6] however, the accuracy of these results is believed to be caused by fortuitous error cancellation.[7] Moreover, a recent study[8] shows that the best choice of functional for HFC is system-dependent. Aside from HFC-related shortcomings, the single-configurational framework underlying Kohn-Sham DFT is inappropriate for describing static correlation, an important feature of f-element complexes. Such systems require a multiconfigurational approach, usually in the form of active space wavefunction optimisation techniques such as Complete Active Space Self-Consistent Field (CASSCF), in order to obtain meaningful predictions of energies and molecular properties.

Although far from black-box, active space algorithms are not only cheaper than fully-correlated alternatives such as Full Configuration Interaction or Coupled Cluster methods, but also more flexible, as the active space is user-defined. This framework can be leveraged to obtain accurate theoretical HFCCs by including, in addition to static correlation, a selection of dynamical correlation effects (e.g. SP) that significantly influence HFC. The challenge, then, is developing a strategy for choosing computationally feasible active spaces that result in accurate theoretical HFCCs. Previous studies employing multireference configuration interaction (MR-CI) algorithms have already analysed the convergence of HFCCs with respect to CI excitation level, orbital selection threshold and basis set completeness.[2,9–16] However, most of the established trends are only applicable to the non-relativistic regime; in particular, the observations about AO contributions to HFCCs result directly from the delta distribution form of the FC term (Equation 1, right), which is specific to the non-relativistic Schrödinger-Pauli framework.[17] Relativistic treatments of HFC hence require new work to establish updated guidelines for theoretical investigations.

Fully-relativistic 4-component approaches are unfeasible for all but the simplest systems,[18,19] unless combined with a low-cost electronic structure algorithm such as Dirac-Hartree-Fock

(DHF)[20] or DFT.[21] As such, multiple strategies that decouple the upper (electronic) and lower (positronic) components of the Dirac Hamiltonian have been developed to lower the cost of relativistic calculations for application to real molecular systems. Use of a decoupling transformation is, in effect, a change in the reference frame of the wavefunction, and therefore it must also be applied to the property operators; ignoring this second step leads to the so-called Picture-Change Error (PCE).[22] Due to the picture-change correction, relativistic property operators are different from their non-relativistic counterparts and, in the case of relativistic HFC, the isotropic contribution is no longer proportional to the spin density at the nucleus.

Approximate (quasi-relativistic) decoupling techniques, such as the regular approximation (RA) and Douglas-Kroll-Hess (DKH), are now fairly widespread and provide excellent predictions for the energies of most relativistic systems.[23,24] These 2-component approaches can be simplified further by disregarding spin-dependent effects, yielding a 1-component scalar relativistic formalism. For magnetic resonance applications, the Zeroth-Order Regular Approximation (ZORA) is widely used in combination with DFT[25–28]. Despite providing a good description of valence properties,[29,30] ZORA affords large errors for core-dependent properties of heavy-element systems (e.g. core-hole X-Ray excitations or absolute nuclear shielding tensors);[29,31] DKH is significantly more accurate in this respect. Indeed, HFCCs obtained using SR-DKH2 operators are in good agreement with experiment,[32,33] although Lan et al[34] show that a higher-order decoupling transformation (DKH3) is needed for a converged relativistic HFC picture. Quasi-relativistic HFCCs can also be derived via the Infinite-Order Regular Approximation (IORA), and when combined with a multiconfigurational wavefunction method, this approach produces highly accurate atomic hyperfine structure constants for alkali and coinage metals.[35]

Exact 2-component decoupling schemes are also available, together with 1-component SR variants. For the purpose of theoretical HFC, these offer two main improvements over quasi-relativistic theories: there is no uncertainty regarding the appropriate order of decoupling, and picture-change corrections are straightforward to implement via matrix multiplication. The eXact-2-Component (X2C)[36–38] and Normalised Elimination of the Small Component (NESC)[39] approaches are two popular, fully numerical, choices for theoretical studies of relativistic HFC. In such cases, it is worth keeping in mind that the form of the relativistic HFC operator changes on a case-by-case basis, since the picture-change transformation is only defined as a numerical matrix.

Our goal was to devise a general methodology for determining relativistic, picture-change-corrected HFCCs for chemical systems of arbitrary size and complexity. With this in mind, we developed Hyperion, a Python-based program that computes SR-X2C-decoupled magnetic resonance parameters from complete active space (CAS) or restricted active space (RAS) wavefunctions, with or without spin-orbit coupling (SOC) added *a posteriori* (CASSCF-SO/RASSCF-SO); a similar method has been developed in parallel by Autschbach and co-workers, and implemented as part of OpenMolcas.[38] Although our code has to-date been tested only with OpenMolcas, Hyperion is a stand-alone package that can be straightforwardly extended to allow inputs from other quantum chemical software. Herein, we demonstrate the use of Hyperion to obtain HFCCs of selected atoms, and benchmark our results against experimental data from atomic spectroscopy and predictions from 4-component calculations. As well as showing the performance of Hyperion, we demonstrate various strategies for tackling specific combinations of electron correlation, SR and SOC effects, highlighting both merits and limitations of CASSCF-SO/RASSCF-SO methods. The comparatively small number of electrons and high symmetry of atoms mean that high levels of theory are achievable with relatively little computational cost, but as our goal is to extend our approach to molecules in the near future, we work with usual electronic structure approximations, such as contracted basis sets and RAS sub-spaces of limited size, which are the only feasible strategies for molecular calculations.

2 Theory

2.1 SR-X2C magnetic properties

The starting point for any relativistic treatment of magnetic properties is the 4-component Dirac equation under a scalar potential V and a vector potential $\mathbf{A}$:

$$c\begin{pmatrix} V/c & \boldsymbol{\sigma}\cdot(\widehat{\mathbf{p}}+e\mathbf{A}) \\ \boldsymbol{\sigma}\cdot(\widehat{\mathbf{p}}+e\mathbf{A}) & V/c-2m_{\mathrm{e}}c \end{pmatrix}\begin{pmatrix}\psi^{\mathrm{U}}\\ \psi^{\mathrm{L}}\end{pmatrix} = E\begin{pmatrix}\psi^{\mathrm{U}}\\ \psi^{\mathrm{L}}\end{pmatrix}, \tag{2}$$

where $\boldsymbol{\sigma}$ is the 3-vector of Pauli spin matrices, $\widehat{\mathbf{p}}$ is the electron linear momentum operator, m_{e} is the electron mass and c is the speed of light in vacuum; SI units are used throughout this work. We represent all 4-component operators in block form, with each matrix element denoting a 2-component operator. Note that, in 2-component equations, $\boldsymbol{\sigma} = 2\,\mathbf{s}$, where $\mathbf{s}$ is the electron spin vector.

The Dirac wavefunction, also known as a 4-component spinor, has an upper component (sometimes referred to as the large component) ψ^{U} that describes electronic degrees of freedom, as well as a lower component (or small component) ψ^{L} describing positronic degrees of freedom. In order for equation 2 to approach the correct non-relativistic limit, the basis sets chosen for ψ^{U} and ψ^{L} must obey the restricted kinetic balance (RKB) condition, namely that, for an upper component basis set $\{\phi_\mu\}$, the lower component basis set is $\left\{\frac{\boldsymbol{\sigma}\cdot\widehat{\mathbf{p}}}{2m_{\mathrm{e}}c}\,\phi_\mu\right\}$. Although using RKB alone is formally justified only in the absence of magnetic fields, this approach is reasonable, as the magnetic-field-dependent terms are treated as a perturbation herein (*vide infra*). By substituting the RKB condition into the 4-component Hamiltonian, we arrive at the modified Dirac equation,[40]

$$\widehat{\mathbf{H}}_{\mathrm{mDE}}\begin{pmatrix}\psi^{\mathrm{U}}\\ \chi^{\mathrm{U}}\end{pmatrix} = E\begin{pmatrix}1 & 0\\ 0 & \frac{1}{2m_{\mathrm{e}}c^2}\widehat{\mathrm{T}}\end{pmatrix}\begin{pmatrix}\psi^{\mathrm{U}}\\ \chi^{\mathrm{U}}\end{pmatrix}, \tag{3}$$

with

$$\widehat{\mathbf{H}}_{\mathrm{mDE}} = \begin{pmatrix}V & \widehat{\mathrm{T}}\\ \widehat{\mathrm{T}} & \frac{1}{4m_{\mathrm{e}}^2c^2}\widehat{\mathrm{W}}-\widehat{\mathrm{T}}\end{pmatrix} + \frac{e}{2m_{\mathrm{e}}}\begin{pmatrix}0 & (\boldsymbol{\sigma}\cdot\mathbf{A})(\boldsymbol{\sigma}\cdot\widehat{\mathbf{p}})\\ (\boldsymbol{\sigma}\cdot\widehat{\mathbf{p}})(\boldsymbol{\sigma}\cdot\mathbf{A}) & 0\end{pmatrix} \tag{4}$$

$$\widehat{\mathrm{T}} = \frac{\widehat{\mathbf{p}}\cdot\widehat{\mathbf{p}}}{2m_{\mathrm{e}}}, \tag{5}$$

$$\widehat{\mathrm{W}} = (\boldsymbol{\sigma}\cdot\widehat{\mathbf{p}})V(\boldsymbol{\sigma}\cdot\widehat{\mathbf{p}}). \tag{6}$$

Notice that the lower component of (2) has been replaced by the pseudo-upper component χ^{U}, which can be represented in the same basis as that used for ψ^{U}. Additionally, the modified Dirac Hamiltonian (equation 4) has been separated into **A**-independent and **A**-dependent contributions; we henceforth treat the **A**-dependent term as a first-order perturbation, $\widehat{\mathbf{H}}^{(1)}$. Using the Dirac relation, we re-write $\widehat{\mathrm{W}}$ as

$$(\boldsymbol{\sigma}\cdot\widehat{\mathbf{p}})V(\boldsymbol{\sigma}\cdot\widehat{\mathbf{p}}) = \widehat{\mathbf{p}}V\cdot\widehat{\mathbf{p}} + i\boldsymbol{\sigma}\cdot\widehat{\mathbf{p}}V\times\widehat{\mathbf{p}} \tag{7}$$

and discard the **σ**-dependent term to obtain a spin-free 4-component operator. By ignoring the spin-dependent contribution, this relativistic formalism becomes compatible with the 1-component framework employed by most electronic structure packages, including

OpenMolcas. The resulting spin-free (SF) modified Dirac operator is

$$\widehat{\mathbf{H}}^{(0)}_{\text{SF-mDE}} = \begin{pmatrix} V & \widehat{\mathrm{T}} \\ \widehat{\mathrm{T}} & \frac{1}{4m_e^2c^2}\widehat{\mathbf{p}}V\cdot\widehat{\mathbf{p}} - \widehat{\mathrm{T}} \end{pmatrix}, \tag{8}$$

which shall serve as the zeroth-order (unperturbed) Hamiltonian within our theoretical framework.

Scalar-relativistic eXact-2-Component (SR-X2C) theory[41,42] can be employed to determine a unitary transformation $\widehat{\mathbf{U}}$ (equation 9) that block-diagonalises $\widehat{\mathbf{H}}^{(0)}_{\text{SF-mDE}}$ and decouples the electronic degrees of freedom from the positronic degrees of freedom. The electronic problem can then be solved by diagonalisation of the upper-upper ($\widehat{\mathbf{H}}^{(0)}_{\text{SF-X2C,UU}}$) component of the transformed Hamiltonian, without any reference to the other 2-component blocks.

$$\widehat{\mathbf{U}}^\dagger\, \widehat{\mathbf{H}}^{(0)}_{\text{SF-mDE}}\, \widehat{\mathbf{U}} = \begin{pmatrix} \widehat{\mathrm{H}}^{(0)}_{\text{SF-X2C,UU}} & 0 \\ 0 & \widehat{\mathrm{H}}^{(0)}_{\text{SF-X2C,LL}} \end{pmatrix}, \qquad \widehat{\mathbf{U}} = \begin{pmatrix} \widehat{\mathrm{U}}_{\text{UU}} & \widehat{\mathrm{U}}_{\text{UL}} \\ \widehat{\mathrm{U}}_{\text{LU}} & \widehat{\mathrm{U}}_{\text{LL}} \end{pmatrix}. \tag{9}$$

The electronic-only perturbation operator is obtained in an analogous manner, by applying the same unitary transformation to $\widehat{\mathbf{H}}^{(1)}$ and then reading off the upper-upper block,

$$\widehat{\mathrm{H}}^{(1)}_{\text{SF-X2C,UU}} = \frac{e}{2m_e}\left\{\widehat{\mathrm{U}}^\dagger_{\text{UU}}(\boldsymbol{\sigma}\cdot\mathbf{A})(\boldsymbol{\sigma}\cdot\widehat{\mathbf{p}})\widehat{\mathrm{U}}_{\text{LU}} + \widehat{\mathrm{U}}^\dagger_{\text{LU}}(\boldsymbol{\sigma}\cdot\widehat{\mathbf{p}})(\boldsymbol{\sigma}\cdot\mathbf{A})\widehat{\mathrm{U}}_{\text{UU}}\right\}. \tag{10}$$

As this work pertains only to electronic properties, we henceforth drop the UU subscript from Hamiltonian operator notation.

The interaction between electrons and magnetic fields (electron-Zeeman interaction), and electrons and nuclear spins (HFC) can be derived from (10) through substitution of the appropriate vector potential (equations 11 and 12, respectively),

$$\mathbf{A}_{\text{Zee}} = \frac{1}{2}\,\mathbf{B}\times(\mathbf{r}-\mathbf{R}_{\text{G}}), \tag{11}$$

$$\mathbf{A}_{\text{N}} = g_{\text{N}}\mu_{\text{N}}\,\frac{\mu_0}{4\pi}\left(\mathbf{I}_{\text{N}}\times\frac{\mathbf{r}_{\text{N}}}{r^3_{\text{N}}}\right), \tag{12}$$

where $\mathbf{B}$ denotes an external magnetic field and $\mathbf{R}_{\text{G}}$ is the chosen gauge origin. Note that, for the vector potential $\mathbf{A}_{\text{N}}$ induced by a magnetic nucleus N, we have assumed a point-like magnetic dipole distribution. Alternatively, a Gaussian distribution model (Equations 13 and 14) can be used – this is also implemented in Hyperion, however results herein

employ the point nucleus expression for simplicity.

$$\mathbf{A}_{\mathrm{N},\eta} = -g_{\mathrm{N}}\mu_{\mathrm{N}}\,\frac{\mu_0}{4\pi}\,\mathbf{I}_{\mathrm{N}} \times \boldsymbol{\nabla} \int \frac{G_\eta(|\mathbf{R}-\mathbf{R}_{\mathrm{N}}|)}{|\mathbf{r}-\mathbf{R}|} d\mathbf{R}, \tag{13}$$

$$G_\eta(|\mathbf{R}-\mathbf{R}_{\mathrm{N}}|) = \left(\frac{\eta}{\pi}\right)^{3/2} e^{-\eta|\mathbf{R}-\mathbf{R}_{\mathrm{N}}|^2} \tag{14}$$

The electronic HFC perturbation operator within the SF-X2C framework is therefore

$$\widehat{\mathrm{H}}^{(1)}_{\text{N,SF-X2C}} = \widehat{\mathrm{H}}^{\text{FC+SD}}_{\text{N,SF-X2C}} + \widehat{\mathrm{H}}^{\text{PSO}}_{\text{N,SF-X2C}}\ , \tag{15}$$

$$\begin{aligned}\widehat{\mathrm{H}}^{\text{FC+SD}}_{\text{N,SF-X2C}} = \mu_{\mathrm{B}} g_{\mathrm{N}} \mu_{\mathrm{N}}\,\frac{\mu_0}{4\pi}\,\boldsymbol{\sigma}\cdot\Bigg\{ &\widehat{\mathrm{U}}^{\dagger}_{\mathrm{UU}}\left(-\frac{\mathbf{r}_{\mathrm{N}}}{r^3_{\mathrm{N}}}\cdot\boldsymbol{\nabla} + \frac{\mathbf{r}_{\mathrm{N}}}{r^3_{\mathrm{N}}}\,\boldsymbol{\nabla}^{\top}\right)\widehat{\mathrm{U}}_{\mathrm{LU}} \\ &+ \widehat{\mathrm{U}}^{\dagger}_{\mathrm{LU}}\left(-\frac{\mathbf{r}_{\mathrm{N}}}{r^3_{\mathrm{N}}}\cdot\boldsymbol{\nabla} + \frac{\mathbf{r}_{\mathrm{N}}}{r^3_{\mathrm{N}}}\,\boldsymbol{\nabla}^{\top}\right)^{\dagger}\widehat{\mathrm{U}}_{\mathrm{UU}}\Bigg\}\cdot\mathbf{I}_{\mathrm{N}}\ ,\end{aligned} \tag{16}$$

$$\widehat{\mathrm{H}}^{\text{PSO}}_{\text{N,SF-X2C}} = i\ \mu_{\mathrm{B}} g_{\mathrm{N}} \mu_{\mathrm{N}}\,\frac{\mu_0}{4\pi}\,\left\{-\widehat{\mathrm{U}}^{\dagger}_{\mathrm{UU}}\left(\frac{\mathbf{r}_{\mathrm{N}}}{r^3_{\mathrm{N}}}\times\boldsymbol{\nabla}\right)\widehat{\mathrm{U}}_{\mathrm{LU}} + \widehat{\mathrm{U}}^{\dagger}_{\mathrm{LU}}\left(\frac{\mathbf{r}_{\mathrm{N}}}{r^3_{\mathrm{N}}}\times\boldsymbol{\nabla}\right)^{\dagger}\widehat{\mathrm{U}}_{\mathrm{UU}}\right\}\cdot\mathbf{I}_{\mathrm{N}}\ , \tag{17}$$

where we distinguish between a spin-dependent contribution, $\widehat{\mathrm{H}}^{\text{FC+SD}}_{\text{N,SF-X2C}}$, and an imaginary, spin-independent contribution, $\widehat{\mathrm{H}}^{\text{PSO}}_{\text{N,SF-X2C}}$. The former reduces to the sum of the FC and SD operators in the non-relativistic limit, while the latter represents the interaction between the electronic orbital angular momentum and the nuclear spin, and is known as the paramagnetic spin-orbit coupling (PSO) term.

It is worth highlighting that (16) does not include a delta-function, that would imply only contributions at the nucleus and characteristic of traditional interpretations of FC; as shown by Kutzelnigg,[17] this hallmark only arises in the non-relativistic limit of a 2-component framework. As a result, relativistic spin-dependent HFC cannot be interpreted as a combination of classical dipolar coupling (SD term) and an FC term sampling the spin density at nucleus N.[4]

2.2 Spin Hamiltonian parametrisations

The cornerstone of EPR theory is the spin Hamiltonian, an effective operator describing all the relevant magnetic interactions as couplings in a $(2S+1)$-dimensional space, where S is the spin quantum number of the system. The HFC spin Hamiltonian is

$$\widehat{\mathrm{H}}_{\text{Spin}} = \mathbf{I}_{\mathrm{N}}\cdot\boldsymbol{a}_{\mathrm{N}}\cdot\mathbf{S}, \tag{18}$$

where the HFC tensor $\boldsymbol{a}_{\mathrm{N}}$ quantifies the strength and anisotropy of the interaction. Quantum mechanical determinations of EPR parameters are based on mapping *ab initio* operators onto the spin Hamiltonian and differentiating to obtain the tensor components of $\boldsymbol{a}_{\mathrm{N}}$:

$$a_{\mathrm{N},kl} = \left.\frac{\partial^2 \widehat{\mathrm{H}}_{\mathrm{N}}^{(1)}}{\partial I_{\mathrm{N},k}\, \partial S_l}\right|_{I_{\mathrm{N},k}, S_l = 0}, \qquad k = x, y, z. \tag{19}$$

In a spin-free/scalar relativistic framework, provided the electronic system is spin-only (negligible SOC), the tensor components are computed as

$$a_{\mathrm{N},kl} = \frac{\left\langle \widehat{\mathrm{h}}_{\mathrm{N},k} \right\rangle}{\left\langle \widehat{\mathrm{S}}_z \right\rangle}, \tag{20}$$

where we have defined the vector operator $\widehat{\mathbf{h}}_{\mathrm{N}}$ as

$$\widehat{\mathrm{h}}_{\mathrm{N},k} = \left.\frac{\partial \widehat{\mathrm{H}}_{\mathrm{N}}^{(1)}}{\partial I_{\mathrm{N},k}}\right|_{I_{\mathrm{N},k}}. \tag{21}$$

Note that in the case of spin-adapted electronic structure approaches, such as spin-adapted CASSCF, the spin projection expectation value $\left\langle \widehat{\mathrm{S}}_z \right\rangle$ is exactly equal to S.

This spin-only parametrisation is not appropriate, however, for systems exhibiting non-negligible SOC, as S is no longer a good quantum number. Instead, the size of the model space is chosen as the number of low-lying electronic states in the SO-coupled energy spectrum, resulting in an effective $2\mathcal{S}+1$ multiplet, where $\mathcal{S}$ is the pseudospin quantum number. Replacing S with $\mathcal{S}$ in equation (18) yields the pseudospin Hamiltonian, from which the elements of symmetrised tensor $\boldsymbol{a}_{\mathrm{N}}\boldsymbol{a}_{\mathrm{N}}^{\top}$ are computed via the method of Chibotaru:[43]

$$\left(\boldsymbol{a}_{\mathrm{N}}\boldsymbol{a}_{\mathrm{N}}^{\top}\right)_{kl} = \frac{3}{\mathcal{S}(\mathcal{S}+1)(2\mathcal{S}+1)} \sum_{I,J}^{2\mathcal{S}+1} \left\langle I \left| \widehat{\mathrm{h}}_{\mathrm{N},k} \right| J \right\rangle \left\langle J \left| \widehat{\mathrm{h}}_{\mathrm{N},l} \right| I \right\rangle, \tag{22}$$

where $|I\rangle$ and $|J\rangle$ denote eigenstates in the pseudospin manifold. A similar approach is widely used to derive g-tensors for strongly SO-coupled systems.[44] The eigenvectors and eigenvalues of the symmetrised tensors correspond to the principal axes and the squared principal values of the original tensors; as a result, the pseudospin parametrisation yields *unsigned* g-values and HFCCs.

2.3 HFC orbital decomposition

One aspect of theoretical determination of HFCCs using multi-configurational methods is choosing the most appropriate active space. This is largely a task of trial and error, for which it is hard to define general rules. Hence, we have developed an orbital decomposition method to assess the involvement of particular MOs in the spin-dependent HFCC of a spin-free state Ψ^{SS}. To do so, we use the second quantisation formalism to represent the expectation value of each vector operator component $\widehat{\mathrm{h}}^{\text{FC+SD}}_{\mathrm{N},k}$ as a sum over pairs of MOs $\{\mu\nu\}$:

$$\left\langle \Psi^{SS} \left| \widehat{\mathrm{h}}^{\text{FC+SD}}_{\mathrm{N},k} \right| \Psi^{SS} \right\rangle = \sum_{\mu\nu} \left\langle \mu \left| \widehat{\mathrm{O}}_{\mathrm{N},zk} \right| \nu \right\rangle \left\langle \Psi^{SS} \left| \widehat{a}^{\dagger}_{\mu\alpha}\widehat{a}_{\nu\alpha} - \widehat{a}^{\dagger}_{\mu\beta}\widehat{a}_{\nu\beta} \right| \Psi^{SS} \right\rangle \tag{23}$$

$$= \sum_{\mu\nu} \left\langle \mu \left| \widehat{\mathrm{O}}_{\mathrm{N},zk} \right| \nu \right\rangle P^{\alpha-\beta}_{\mu\nu}, \tag{24}$$

where $\widehat{a}^{\dagger}$ and $\widehat{a}$ denote spin-orbital creation and annihilation operators, respectively, and $P^{\alpha-\beta}_{\mu\nu}$ is a spin density matrix element. We have used $\widehat{\mathrm{O}}_{\mathrm{N},zk}$ to denote the $l = z$ components of a rank-2 tensor operator defined as

$$\begin{aligned} \widehat{\mathrm{O}}_{\mathrm{N},lk} = \mu_{\mathrm{B}}\, \widehat{\mathrm{U}}^{\dagger}_{\mathrm{UU}} \left(-\delta_{lk} \frac{\mathbf{r}_{\mathrm{N}}}{r^3_{\mathrm{N}}} \cdot \boldsymbol{\nabla} + \frac{r_{\mathrm{N},l}}{r^3_{\mathrm{N}}}\, \partial_k \right) \widehat{\mathrm{U}}_{\mathrm{LU}} \\ + \mu_{\mathrm{B}}\, \widehat{\mathrm{U}}^{\dagger}_{\mathrm{LU}} \left(-\delta_{lk} \frac{\mathbf{r}_{\mathrm{N}}}{r^3_{\mathrm{N}}} \cdot \boldsymbol{\nabla} + \frac{r_{\mathrm{N},l}}{r^3_{\mathrm{N}}}\, \partial_k \right)^{\dagger} \widehat{\mathrm{U}}_{\mathrm{UU}}. \end{aligned} \tag{25}$$

Note that $\widehat{\mathbf{O}}_{\mathrm{N}}$ represents the spatial part of $\mathbf{h}^{\text{FC+SD}}_{\mathrm{N,SF\text{-}X2C}}$, as derived via equations 16 and 21.

We consider each term from the summation in (24) separately, combine the $k = x, y, z$ components of $\widehat{\mathbf{O}}_{\mathrm{N},z}$ via the vector norm, and divide the result by the spin projection to obtain a two-dimensional symmetric matrix $\boldsymbol{\mathcal{M}}$ with elements

$$\mathcal{M}_{\mu\nu} = \frac{\left\| \left\langle \mu \left| \widehat{\mathbf{O}}_{\mathrm{N},z} \right| \nu \right\rangle \right\| \; P^{\alpha-\beta}_{\mu\nu}}{\left\langle \widehat{\mathrm{S}}_z \right\rangle} = \frac{1}{\left\langle \widehat{\mathrm{S}}_z \right\rangle} \sqrt{\sum_k \left\langle \mu \left| \widehat{\mathrm{O}}_{\mathrm{N},zk} \right| \nu \right\rangle^2}\, P^{\alpha-\beta}_{\mu\nu}. \tag{26}$$

The $\boldsymbol{\mathcal{M}}$ matrix contains the same information as the spin-dependent HFCC, albeit in a modified form wherein MO degrees of freedom are not integrated out. We note that the factor of $\left\langle \widehat{\mathrm{S}}_z \right\rangle^{-1}$, which reduces to S^{-1} for spin-free states, mimics the expression for HFC operators in the spin-only formalism. With this representation, the diagonal elements $\mathcal{M}_{\mu\mu}$ can be interpreted as individual orbital contributions, while the coupling between two different orbitals is quantified by $\mathcal{M}_{\mu\nu} + \mathcal{M}_{\nu\mu} = 2\mathcal{M}_{\mu\nu}$.

Inspired by Density Matrix Renormalisation Group (DMRG) entanglement diagrams,[45] we designed a similar pictorial representation of orbital involvement in HFC (Figure 1), using the matrix elements of $\mathcal{M}$. Individual orbital contributions are shown as markers on the circumference of a circle, while pairwise contributions are shown as chords, colour-coded by order of magnitude.

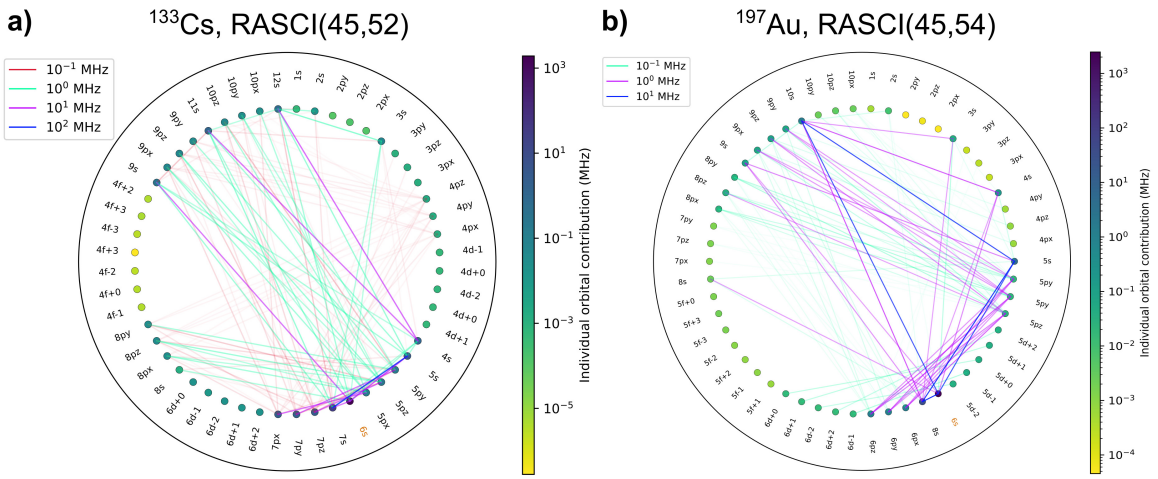

Figure 1: HFC orbital decomposition diagrams obtained from relativistic determinations of HFCCs using Hyperion. **a** - ^{133}Cs atom, RASCI(45,52) using CASSCF(11,15)-optimised orbitals; **b** - ^{197}Au atom, RASCI(45,54) using RASSCF(19,26)-optimised orbitals. Lines across the diagram correspond to off-diagonal matrix elements of $\mathcal{M}$. Individual orbital contributions, as indicated by circular markers, correspond to diagonal matrix elements $\mathcal{M}_{\mu\mu}$.

It is worth emphasising that this model is based on a CI-type wavefunction that is not relaxed after applying the first-order HFC perturbation, and that our orbital decomposition diagrams only show a static picture of HFC. To further understand this, we adopt the *direct/indirect* terminology used by Engels[11] to describe the influence of specific configurations in a CI wavefunction. The HFC orbital decomposition matrix $\mathcal{M}$ for a given electronic state is computed via its spin density matrix, which is completely determined by the CI expansion. The *direct* influence of an (active) orbital or pair of orbitals, as indicated by $\mathcal{M}$, is then proportional to the total CI contribution from all configurations where the orbitals of interest are singly-occupied. However, the spin density associated with one orbital can vary between different active space selections, due to the *indirect* effect of all the other correlated orbitals. Therefore, the active space selection should not be based solely on the orbital decomposition diagram. HFC calculations should be carried out both with and without a specific orbital in the CAS/RAS to determine the magnitude of its indirect effect.

3 Computational details

All electronic structure calculations use a local version of OpenMolcas v19.11 adapted to print the X2C decoupling matrices, while the spatial HFC integrals are evaluated analytically with Libcint.[46] Full ANO-RCC basis sets[47–51] are used throughout to ensure sufficient flexibility and to maintain consistency with previous relativistic HFC studies.[36,38,52] The electronic wavefunction is optimised using either the complete active space self-consistent field (CASSCF) approach[53] or a restricted active space (RAS) approach[54] with (RASSCF) or without orbital optimisation (RASCI). Where necessary, SOC is added *a posteriori* using the RASSI method.[55] To keep RAS calculations tractable, the RAS2 sub-space is restricted to the partially occupied shells. As such, for $^2S_{1/2}$ systems, only the singly-occupied s orbital is included in RAS2, while for transition metals or lanthanides with partially-filled d or f shells, respectively, RAS2 is made up of the valence nd or nf and $(n+1)$s orbitals as required.

4 Results and discussion

4.1 Spin polarisation vs. electron correlation

We take this opportunity to discuss a conceptual aspect that is often encountered in computational HFC literature: the overlap between spin polarisation and electron correlation. Both effects have physical interpretations related to the interaction between electrons in a many-electron system, however a distinction arises in electronic structure theory due to the use of single-configurational (also known as mean-field) references with respect to which perturbations such as SP, static correlation and dynamic correlation are described.

Unrestricted Hartree-Fock (UHF) theory is the simplest wavefunction-based electronic structure framework that accounts for SP, albeit not accurately, due to spin contamination. The UHF wavefunction can be expressed as a perturbation expansion from a restricted open-shell Hartree-Fock (ROHF) reference, with the first-order term comprising only single excitations.[56] It can be deduced that SP arises mainly from singly-excited configurations; a spin-adapted CI ansatz with singles (S-CI) should therefore be able to provide a more accurate, non-spin-contaminated description of SP.[2]

Electron correlation – the instantaneous interaction of electrons, which is not captured by a mean-field ansatz – is also routinely described by a CI wavefunction, which is most ac-

curate when all possible excitations in the given Fock space are included (Full CI, FCI). The correlation energy is defined as the difference between the FCI and the reference Hartree-Fock energies. For open-shell systems represented in a spin-adapted framework (i.e. with a ROHF reference), it follows that electron correlation includes an SP contribution,[56] whose magnitude directly relates to the overall weighting of single excitations in the CI expansion. Note, however, that if a UHF reference is used instead, the boundary between SP and "other" correlation becomes unclear. This is fortunately not a concern herein, as we employ spin-adapted wavefunction methods exclusively.

In a comprehensive review of the spin-polarisation model for HFC, Chipman[2] refers to *second- and higher-order correlation effects*/*true correlation*, thus dividing spin-polarising single excitations from other excited configurations sampled by FCI. While this split view helps balance computational efficiency with accuracy in multi-configurational calculations, it has also lead to a prevalence in the HFC literature of single-excitation-only results, with no discussion of higher-order effects.[38,52] This is likely a safe approximation for systems such as simple organic radicals,[57] however there is no reason to assume *a priori* that the SP contribution to HFC is more important than contributions from higher-order excitations. In fact, early work shows that high-level CI approximations are required even for second period atoms to achieve quantitative agreement with experiment.[13] For the atomic systems studied here, we attempt to include most correlation afforded by a chosen active space using either CASSCF or, where this is unfeasible, RASSCF/RASCI with single and double excitations.

4.2 Alkali metals

We first apply our methodology to study the hyperfine structure of atoms in the alkali series. This is a popular test set for theoretical HFC computations, requiring a good description of electron correlation, as well as an appropriate treatment of relativistic effects for the heavier elements.[19,58,59] Table 1 shows predicted (unsigned) HFCCs for the $^2S_{1/2}$ ground state of each alkali atom, determined via active space electronic structure methods. We note that our CASSCF(1,1) results are very close to the 4-component Hartree-Fock data reported by Talukdar,[19] suggesting that, at least for the direct contribution to HFC, relativistic effects are correctly accounted for with the X2C decoupling in Hyperion. In order to include correlation contributions to the spin density, the active space must be expanded beyond the SOMO; the CAS size is limited to a maximum of 18 orbitals and we turn to RAS methods to explore electron correlation effects in a larger orbital space. Note that, due to the computational

scaling of RAS algorithms, we restrict the RAS2 subspace to the SOMO. HFCCs converge the fastest when the CASSCF algorithm is used, with CASSCF(11,15) results within approximately 10% of experimental HFC data for all alkali metals. This contrasts with RASSCF and RASCI results, which display slower convergence with active space size and only reach CASSCF accuracy when the majority of MOs are correlated.

Table 1: Unsigned isotropic HFCCs in MHz computed for the ground state of alkali atoms. The RAS1, RAS2 and RAS3 columns indicate the number of atomic shells – separated by angular momentum – included in each subspace. Experimental HFCCs and HFCCs calculated using 4-component methods – namely, Hartree-Fock (4c-HF) and the Z-vector coupled cluster approach with singles and doubles (Z-vector 4c-CCSD) – are reproduced from reference [19].

Atom	Wavefunction	RAS1	RAS2	RAS3	|A|
^{7}Li	4c-HF				288.2
	CASSCF(1,1)	-	1×s	-	282.3
	CASSCF(3,10)	-	4×s, 2×p	-	367.9
	CASSCF(3,15)	-	4×s, 2×p, 1×d	-	367.9
	CASSCF(3,14)	-	5×s, 3×p	-	395.7
	RASSCF(3,29)	1×s	1×s	6×s, 7×p	392.8
	Z-vector 4c-CCSD				399.1
	Experimental				**401.7**
^{23}Na	4c-HF				633.4
	CASSCF(1,1)	-	1×s	-	639.2
	CASSCF(9,13)	-	2×s, 2×p, 1×d	-	724.6
	CASSCF(9,14)	-	3×s, 2×p, 1×d	-	794.2
	CASSCF(11,15)	-	4×s, 2×p, 1×d	-	801.9
	RASSCF(11,35)	2×s, 1×p	1×s	6×s, 6×p, 1×d	820.9
	RASSCF(11,40)	2×s, 1×p	1×s	6×s, 6×p, 2×d	839.6
	Z-vector 4c-CCSD				875.6
	Experimental				**885.8**
^{39}K	4c-HF				151.0
	CASSCF(1,1)	-	1×s	-	152.9
	CASSCF(9,13)	-	2×s, 2×p, 1×d	-	184.0
	CASSCF(9,14)	-	3×s, 2×p, 1×d	-	197.1
	CASSCF(11,15)	-	4×s, 2×p, 1×d	-	203.3
	CASSCF(11,16)	-	5×s, 2×p, 1×d	-	210.7
	RASSCF(19,39)	3×s, 2×p	1×s	6×s, 6×p, 1×d	203.6
	Z-vector 4c-CCSD				226.6
	Experimental				**230.8**

Atom	Wavefunction	RAS1	RAS2	RAS3	|A|
^{85}Rb	4c-HF				666.9
	CASSCF(1,1)	-	1×s	-	691.9
	CASSCF(9,13)	-	2×s, 2×p, 1×d	-	831.2
	CASSCF(11,15)	-	4×s, 2×p, 1×d	-	906.5
	RASSCF(19,26)	1×s, 1×p, 1×d	1×s	1×s, 1×p, 1×d, 1×f	859.1
	RASCI(37,54)	4×s, 3×p, 1×d	1×s	5×s, 6×p, 1×d, 1×f	908.8
	Z-vector 4c-CCSD				986.5
	Experimental				**1011.9**
^{133}Cs	4c-HF				1495.5
	CASSCF(1,1)	-	1×s	-	1539.1
	CASSCF(9,13)	-	2×s, 2×p, 1×d	-	1863.9
	CASSCF(9,14)	-	3×s, 2×p, 1×d	-	2024.6
	CASSCF(11,15)	-	4×s, 2×p, 1×d	-	2041.3
	RASCI(35,40)	5×s, 4×p	1×s	5×s, 4×p, 1×d	2083.2
	RASCI(35,47)	5×s, 4×p	1×s	5×s, 4×p, 1×d, 1×f	2095.7
	Z-vector 4c-CCSD				2218.2
	Experimental				**2298.1**
^{223}Fr	4c-HF				5518.0
	CASSCF(1,1)	-	1×s	-	5240.1
	CASSCF(9,13)	-	2×s, 2×p, 1×d	-	6277.0
	CASSCF(11,15)	-	4×s, 2×p, 1×d	-	6685.7
	RASCI(43,57)	6×s, 5×p	1×s	5×s, 6×p, 1×d, 1×f	6940.0
	Z-vector 4c-CCSD				7584.5
	Experimental				**7654.0**

The balance of doubly-occupied and virtual (unoccupied) orbitals in the CAS/RAS has a crucial influence on HFCC accuracy; it is not sufficient to augment a minimal active space with core orbitals, as appropriate virtual orbitals are needed to correlate them. A similar observation was made by Talukdar in a relativistic coupled-cluster study[19] that emphasises the need for high-energy unoccupied orbitals to correlate inner-core electrons. From our results, we deduce that radial correlation, introduced via virtual shells with the same angular momentum as the core shells,[60] has the most significant effect on HFCCs. Compare, for example, the HFCCs obtained from CASSCF(9,13) and CASSCF(9,14); the virtual s shell included in the latter leads to a 6-8% improvement in accuracy. For calculations that include orbital optimisation (i.e. CASSCF or RASSCF), a good basic principle for active space selection is to include one radially correlating virtual shell for each doubly occupied shell in the active space. However, the exponential scaling of CASSCF severely restricts this strategy and as such, the largest CAS selections reported herein include only one virtual shell of

each angular momentum.

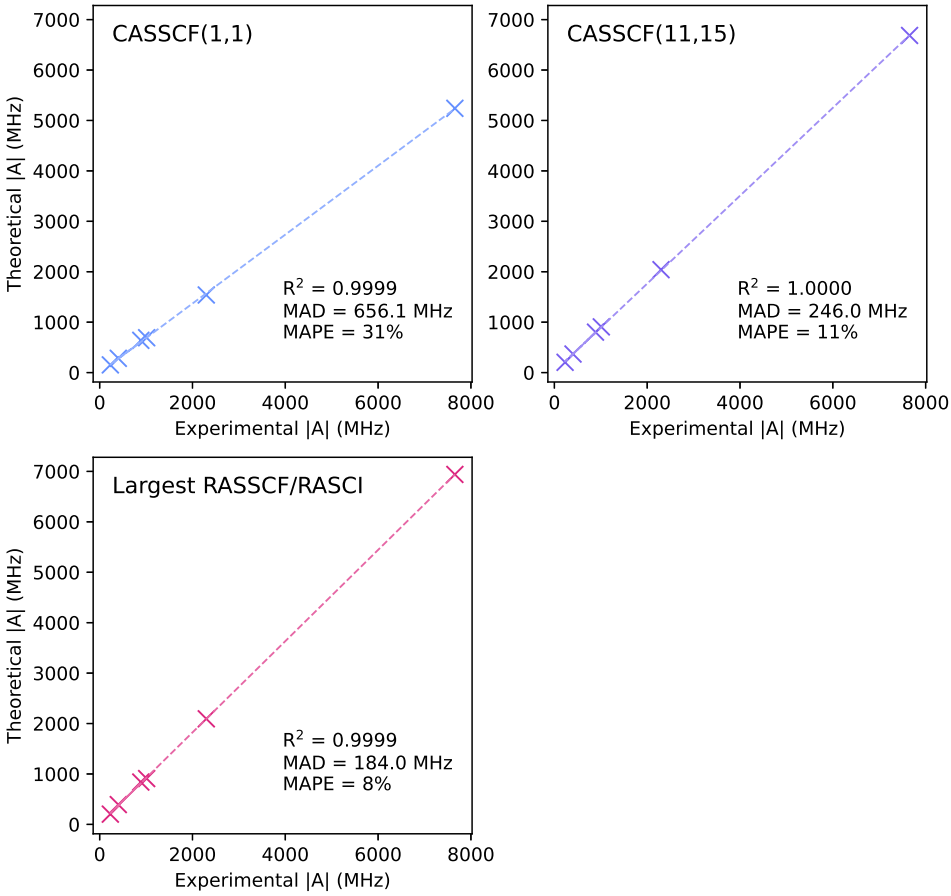

Figure 2: Comparison of experimental vs. theoretical unsigned HFCCs for alkali atoms. Each panel corresponds to an active space approximation and shows the line of best fit, R^2 coefficient, mean absolute deviation (MAD), and mean absolute percentage error (MAPE). The *Largest RASSCF/RASCI* data set comprises RAS-type models closest to the configuration interaction with singles and doubles (CISD) limit, subject to subspace size constraints imposed by OpenMolcas. Experimental HFCCs are reproduced from reference [19].

It is also interesting to analyse the influence of polarisation basis functions. The inclusion of one virtual d shell in CASSCF affects the HFCCs of all alkali by 4-5% (except Li), suggesting an angular correlation[60] effect related to the presence of core p electrons. Extrapolating, we postulate that for core shells with the highest angular momentum l, virtual shells with angular momentum of at least $l + 1$ are needed to capture angular correlation. Note that although previous theoretical work highlights the slow convergence of correlation energy with maximum angular momentum[61] – indicating that an accurate description of correlation likely requires much higher angular momenta – similar effects on HFCCs have only been explored for light atoms.[10,13] Nevertheless, testing this hypothesis here is unfeasible given the computational limitations of CASSCF and RASSCF algorithms; we therefore limit our approach to include one virtual d shell for atoms Na-Fr and additionally one virtual f

shell for Rb-Fr. Our calculations on the alkali group reach 11% mean absolute percentage error (MAPE) with the largest CASSCF model, and 8% MAPE with the largest RASSCF/RASCI; deviations from experiment appear to be systematic regardless of active space size, as evidenced by the R^2 values close to 1 (Figure 2).

Spin-dependent HFCCs are known to be particularly sensitive to correlation effects from inner-core electrons; to investigate this, we performed RASSCF and RASCI calculations with RAS1 subspaces spanning most of the core region. All RASCI calculations are performed with CASSCF(11,15) optimised orbitals for consistency. Orbital decomposition analysis of RASCI results (Figure 1a) reveals a trend of decreasing HFC contribution with increasing angular momentum. Most s and p orbitals are strongly coupled by the HFC operator and make significant (> 10 MHz) direct contributions to the HFCC. The influence of (virtual) polarisation functions (4-5% increase in HFCC accuracy) is not reflected by the relatively insignificant contributions ($< 10^{-3}$ MHz) shown in the orbital decomposition diagram. Therefore, such functions have a predominantly indirect effect, displacing spin density from orbitals with significant HFC contributions. Occupied d and f shells show similarly small orbital decomposition contributions and, additionally, our calculations suggest their inclusion leads to insignificant variations in the computed HFCC. As such, we conclude that core d and f orbitals of alkali atoms can be safely left out of the RAS1 subspace for the purpose of HFCC determinations. We note that the error with respect to experimental HFCCs plateaus around 10% for RASCI (Figure 3), which could be a consequence of the restricted excitation level and/or the basis set size.

In order to assess the trade-off between accuracy and cost in a CAS/RAS-based electronic structure strategy, we compare our results for the alkali atoms with the HFCCs computed by Talukdar[19] using Z-vector 4-component coupled cluster with singles and doubles (4c-CCSD), Table 1. The 4c-CCSD results display undoubtedly better agreement with experiment, with all absolute deviations below 1.5%; note, however, that these HFCCs are obtained using uncontracted, 4-component, quadruple-zeta basis sets with 338-656 spinors for Rb-Fr[62] (the size of the spinor space explored in the 4c-CCSD calculations is slightly smaller, as a virtual energy cutoff is applied). By contrast, we employ 1-component contracted ANO-RCC basis sets, which contain the equivalent of 186-240 spinors (not including g orbitals) for Rb-Fr. While calculations with large uncontracted bases are achievable for small systems, they become prohibitively expensive as the number of atoms and the complexity of the electronic structure increase. The main goal of this work is to devise a scalable approach

that can be extended to larger systems in the future; as such, we make use of common electronic structure approximations, such as contracted basis sets and RAS1/RAS3 subspaces limited to no more than 35 orbitals, even though they are not strictly necessary for atoms. Considering the strong dependence of HFCCs on basis set size, as well as the fact that our calculations explore a relatively limited parameter space, consistent *circa* 10% deviations from experiment are therefore very encouraging.

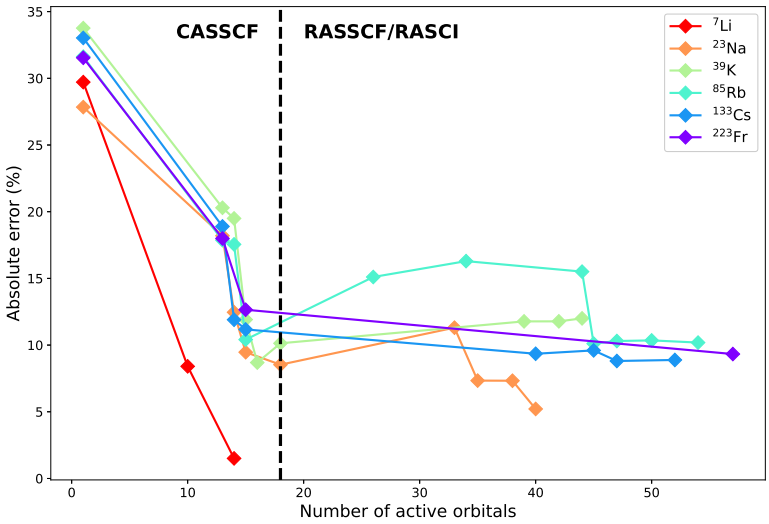

Figure 3: Evolution of HFCC absolute error with active space size for alkali atoms. Absolute errors are computed with respect to experimental data from reference [19].

Lastly, the issue of orbital optimisation in RAS calculations bears discussion. The Super-CI algorithm employed by OpenMolcas "folds" single excitations involving inactive and secondary orbitals into the active MO coefficients,[53] thus capturing more correlation than a CI-only calculation with the same parameters. Theoretically, orbital optimisation should allow for accurate HFCCs to be obtained with relatively little computational expense, since the active space needs only be large enough to capture the significant correlation contributions to HFC; indeed, this proves true for CASSCF, however for RASSCF, the results are unpredictable. In the case of light alkali (Li-K), it was possible to run RASSCF calculations involving the entire core s and p manifold, together with polarisation functions, which produced HFCCs in excellent agreement with experiment. On the other hand, this approach is prohibitive for heavier atoms – even if memory is not a limitation, orbital optimisation is slow and prone to convergence issues. We therefore only employ RASCI for large active space calculations on Rb-Fr. RASSCF calculations involving fewer active orbitals were also attempted, however the resulting HFCCs were on average less accurate than those from RASCI. It appears that the excitation level restriction severely hinders the efficiency of orbital optimisation; stochastic CASSCF[63] and DMRG-CASSCF methods[64] are likely to provide

more accurate HFCCs, however due to additional uncertainty introduced by approximate CI solvers, such algorithms are not explored herein.

4.3 Coinage metals

The treatment of HFC in coinage metals is very similar to that of the alkali metals, given they both have configurationally-pure $^2S_{1/2}$ ground states. A notable point of difference is the valence d shell which, unlike the core-like d shells in alkali atoms, imparts a significant contribution to the HFCC. Correlating the entire valence region is therefore not feasible with CASSCF, and in this case RASSCF is the only option. We find that the benefits of a larger active space outweigh the limitations due to excitation level restrictions, leading to a net improvement in HFCC accuracy from CASSCF to RASSCF (Table 2). This contrasts with the behaviour observed for the alkali metals, indicating that it is perhaps the nature of the correlated orbitals (valence vs. core), rather than the CI approximation, that makes the biggest difference to theoretical HFCCs.

All RASCI calculations reported herein were performed using a RASSCF(19,26)-optimised orbital space for all coinage metals. Surprisingly, correlating most of the s and p manifold changes the initial RASSCF HFCCs very little; the largest variations are observed in calculations that correlate additional polarisation shells. We observe improvements of 2-6% upon including one f shell in the orbital optimisation step (c.f RASCI results in Tables 2 and S2). Despite the significant challenges associated with these elements, Hyperion HFCCs derived from RASSF(19,26) display a 12% MAPE (Figure 4, lower left panel), while HFCCs calculated from the largest RASCI for each atom have a 10% MAPE (Figure 4, lower right panel). The R^2 coefficients close to unity indicate that deviations from experiment are systematic for all the main active space selections.

Some notable differences between the coinage metals and the alkali are highlighted by the orbital decomposition analysis. Figure 1 shows orbital decomposition diagrams obtained from RASCI calculations on ^{133}Cs and ^{197}Au atoms; while both systems have a $6s^1$ ground configuration, their core configurations set them apart, which is reflected by the observed HFC. Compared to ^{133}Cs, ^{197}Au exhibits stronger coupling between d orbitals, as well as a more significant contributions from the f polarisation shell (however, the latter could be a consequence of including this shell in the orbital optimisation step). Nevertheless, in both cases the largest contributions to HFC are concentrated around orbitals 5s-7p, with additional non-negligible couplings involving the most diffuse s and p functions.

Table 2: Unsigned isotropic HFCCs in MHz computed for the ground states of Cu, Ag and Au. The RAS1, RAS2 and RAS3 columns indicate the number of atomic shells – separated by angular momentum – included in each subspace. Experimental HFCCs are reproduced from reference [59].

Atom	Wavefunction	RAS1	RAS2	RAS3	|A|
^{63}Cu	CASSCF(11,6)	-	1×s, 1×d	-	4137.3
	CASSCF(19,14)	-	3×s, 2×p, 1×d	-	4604.9
	RASSCF(19,19)	1×s, 1×p, 1×d	1×s	1×s, 1×p, 1×d	4611.3
	RASSCF(19,26)	1×s, 1×p, 1×d	1×s	1×s, 1×p, 1×d, 1×f	4831.4
	RASSCF(19,35)	1×s, 1×p, 1×d	1×s	1×s, 1×p, 1×d, 1×f, 1×g	4813.7
	RASSCF(29,45)	3×s, 2×p, 1×d	1×s	3×s, 2×p, 1×d, 1×f, 1×g	5004.8
	RASCI(29,50)	3×s, 2×p, 1×d	1×s	5×s, 6×p, 1×d, 1×f	5036.5
	Experimental				**5866.9**
^{107}Ag	CASSCF(11,6)	-	1×s, 1×d	-	1325.1
	CASSCF(19,14)	-	3×s, 2×p, 1×d	-	1455.1
	RASSCF(19,19)	1×s, 1×p, 1×d	1×s	1×s, 1×p, 1×d	1481.1
	RASSCF(19,26)	1×s, 1×p, 1×d	1×s	1×s, 1×p, 1×d, 1×f	1594.6
	RASCI(37,54)	4×s, 3×p, 1×d	1×s	5×s, 6×p, 1×d, 1×f	1620.6
	RASCI(47,59)	4×s, 3×p, 2×d	1×s	5×s, 6×p, 1×d, 1×f	1619.4
	Experimental				**1712.5**
^{197}Au	CASSCF(11,6)	-	1×s, 1×d	-	2362.1
	CASSCF(19,14)	-	3×s, 2×p, 1×d	-	2536.0
	RASSCF(19,19)	1×s, 1×p, 1×d	1×s	1×s, 1×p, 1×d	2608.3
	RASSCF(19,26)	1×s, 1×p, 1×d	1×s	1×s, 1×p, 1×d, 1×f	2733.6
	RASCI(45,54)	5×s, 4×p, 1×d	1×s	4×s, 5×p, 1×d, 1×f	2704.6
	Experimental				**3049.7**

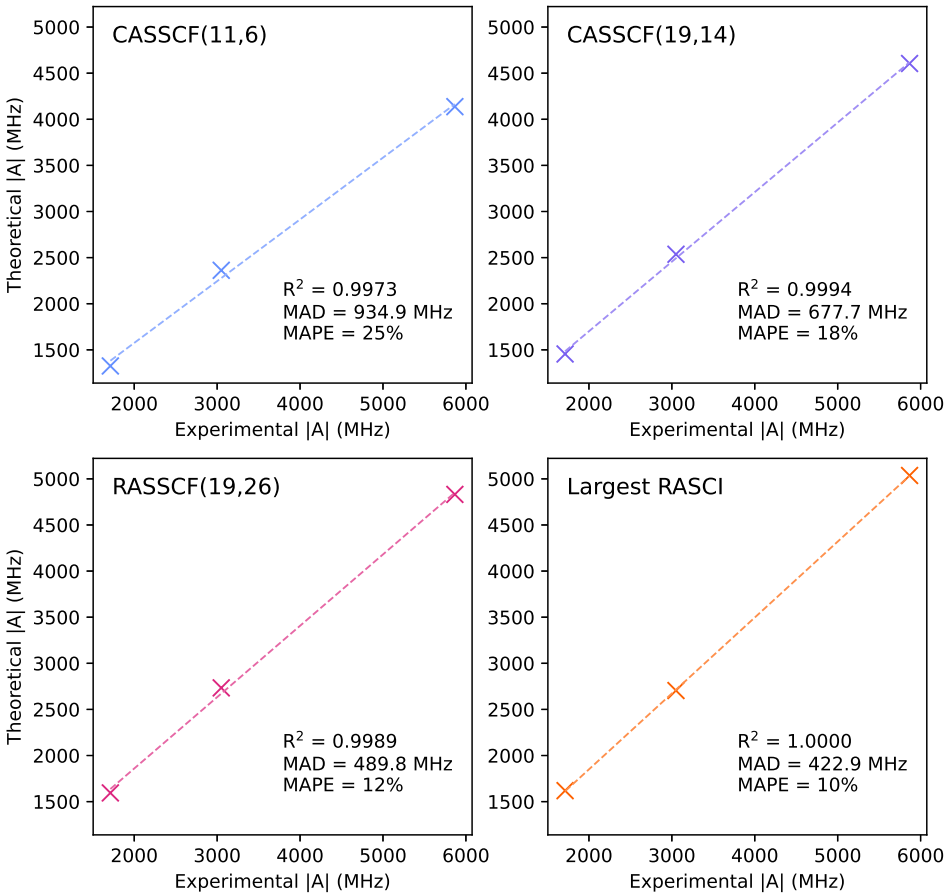

Figure 4: Comparison of experimental vs. theoretical unsigned HFCCs for coinage metals. Each panel corresponds to an active space approximation and shows the line of best fit, R^2 coefficient, mean absolute deviation (MAD), and mean absolute percentage error (MAPE). The *Largest RASCI* data set comprises RAS-type models closest to the configuration interaction with singles and doubles (CISD) limit, subject to subspace size constraints imposed by OpenMolcas. Experimental HFCCs are reproduced from reference [59].

4.4 Groups VI-B (Cr) and VIII-B (Fe)

The hyperfine structure of transition metal (TM) atoms with partially-filled d shells is by far the most challenging to model due to a number of competing factors. The orbital angular momentum couples to the nuclear spin through the PSO mechanism and the resulting HFCC contribution is similar in magnitude to the spin-dependent FC+SD contribution (Figure S3). Both SOC and spin density must therefore be modelled accurately. On the one hand, the RASSI approach requires a sufficient number of spin-adapted states in order to represent the SOC states accurately, where the number of optimised roots corresponds to the lowest-energy Russell-Saunders (LS) terms (Table 3). Additional LS terms were included for ^{101}Ru, ^{183}W and ^{189}Os to obtain a converged ordering of SO energies at the minimal CASSCF-SO level.

On the other hand, the electronic states of TM atoms exhibit significant mixing between

Table 3: Number of spin-adapted roots optimised for each spin S and corresponding LS terms

Atom	Number of roots	LS terms
^{53}Cr	1 ($S = 3$), 6 ($S = 2$)	^{7}S, ^{5}D, ^{5}S
^{95}Mo	1 ($S = 3$), 6 ($S = 2$)	^{7}S, ^{5}D, ^{5}S
^{183}W	1 ($S = 3$), 5 ($S = 2$), 3 ($S = 1$)	^{7}S, ^{5}D, ^{3}P
^{57}Fe	12 ($S = 2$)	^{5}D, ^{5}F
^{101}Ru	7 ($S = 2$), 7 ($S = 1$)	^{5}F, ^{3}F
^{189}Os	12 ($S = 2$), 10 ($S = 1$)	^{5}D, ^{5}F, ^{3}P, ^{3}F

$n\mathrm{d}^N(n+1)\mathrm{s}^2$ and $n\mathrm{d}^{N+1}(n+1)\mathrm{s}^1$ configurations; these have competing influences on the form of the valence s orbital, as optimised singly-occupied s functions are usually more radially expanded than doubly-occupied s functions.[60] The $\mathcal{O}(r_\mathrm{N}^{-3})$ dependence of the HFC operator amplifies such differences, leading to computed HFCCs that are very sensitive to variations in the CI expansion. This proves particularly problematic when CASSCF/RASSCF orbitals are averaged over states dominated by different configurations, such as the low-lying ^{5}D ($3\mathrm{d}^6 4\mathrm{s}^2$) and ^{5}F ($3\mathrm{d}^7 4\mathrm{s}^1$) terms of ^{57}Fe.[67,68] Note that CASSCF(8,6)-SO HFCCs for ^{101}Ru are in much better agreement with experiment than ^{57}Fe HFCCs (Figure 5); this is because the ^{101}Ru ^{5}F term is sufficiently energetically separated and can be modelled without requiring additional quintet roots in the spin-adapted CASSCF step. Similar state-averaging effects are observed in the quintet levels of ^{53}Cr and ^{95}Mo.

Although relatively small in magnitude, the spin-dependent part of TM HFCCs depends on SP and higher-order correlation, similar to the spin-only HFCCs of alkali and coinage metals. Unlike the $^2\mathrm{S}_{1/2}$ systems however, the expanded RAS2 subspace precludes large RAS optimisations. Therefore, calculations that correlate the entire core region were only feasible with RASCI for 3d TMs, however this still gave very good results (Figure 5). While ^{57}Fe HFCCs are overall improved compared to CASSCF(8,6)-SO, ^{53}Cr HFCCs are slightly worse, with the exception of the $^5\mathrm{S}_2$ level. We note that the RASCI-SO energies determined for ^{53}Cr do not match the ordering observed experimentally and that the wrong ground state is predicted, indicating inaccuracies in the electronic wavefunction that are reflected in the calculated HFCCs. RASSCF-SO calculations correlating the valence shells were performed for all six atoms, yielding HFCCs that are overall less accurate compared to CASSCF-SO for

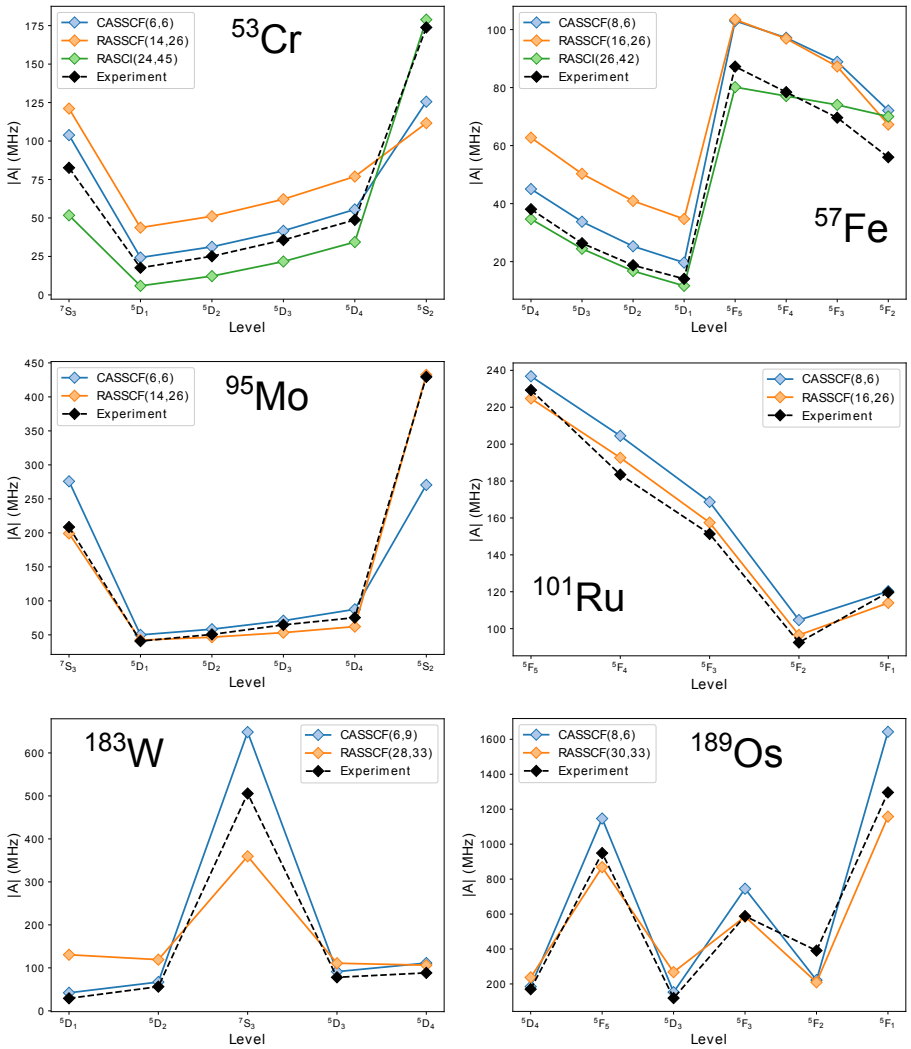

Figure 5: Unsigned HFCCs computed by HYPERION for selected energy levels of Cr group and Fe group atoms. Experimental HFCCs are reproduced from references [65] (^{53}Cr), [66] (^{95}Mo, ^{183}W), [67] and [68] (^{57}Fe), [69] (^{101}Ru) and [70] (^{189}Os).

the 3d and 5d TMs. The improvement with RASSCF observed for ^{95}Mo and ^{101}Ru can be justified by their well separated ground terms, which prevents state contamination during the RASSCF optimisation.

Overall, it appears that minimal CASSCF-SO provides the most balanced model for the hyperfine structure of TMs, with errors around 25%. Approaches that include more correlation effects can theoretically improve the accuracy of the FC+SD term, however in practice such calculations – unless they approach the full correlation limit – have undesired side-effects that worsen the quality of the SO-coupled wavefunctions, which propagates to the computed HFCCs.

4.5 Lanthanides

The hyperfine structure of lanthanide (Ln) atoms is dominated by the PSO term, with previous work suggesting minor contributions from core polarisation.[71] As the 6s orbital and the 4f manifold are energetically well separated, CI effects between the two are negligible and the HFC response is expected to arise predominantly from the 4f shell. Hence, we compute the HFCCs of multiple levels in $4f^N 6s^2$ Ln atoms using a minimal CASSCF(N,7)-SO, with the number of optimised roots (Table 4) selected using a similar approach to Section 4.4.

Table 4: CASSCF(N,7)-SO optimised LS terms for each Ln atom

Atom	LS terms
^{141}Pr	^{4}I
^{143}Nd	^{5}I
^{147}Pm	^{6}H
^{147}Sm	^{7}F, ^{5}D
^{151}Eu	^{8}S
^{159}Tb	^{6}H, ^{4}I
^{161}Dy	^{5}I
^{165}Ho	^{4}I
^{167}Er	^{3}H, ^{3}F, ^{1}G
^{169}Tm	^{2}F

Predicted HFCCs (Table 5) are in remarkable agreement with experiment overall.[72] The poorest agreement is observed for ^{151}Eu and ^{165}Ho; the former has a spin-only septet ground state, which only exhibits spin-dependent HFC (no PSO contribution), and hence requires a more sophisticated treatment of correlation. Inaccuracies in the latter could also be due to missing CI effects, as indicated in previous work,[72] but increasing the active space with CASSCF or RASSCF methods had no appreciable impact on the calculated HFCCs here.

Table 5: Unsigned isotropic HFCCs in MHz determined for Ln atoms. For each computed HFCC, the absolute deviation from experiment is shown in MHz ($|\Delta|$) and in percentage points ($|\Delta_{\%}|$). Experimental HFCCs are reproduced from reference [72].

Atom	Level	$\lvert\mathbf{A}^{\text{FC+SD}}\rvert$	$\lvert\mathbf{A}^{\text{PSO}}\rvert$	$\lvert\mathbf{A}^{\text{tot}}\rvert$	$\lvert\mathbf{A}^{\text{expt}}\rvert$	$\lvert\mathbf{\Delta}\rvert$	$\lvert\mathbf{\Delta}_{\%}\rvert$
^{141}Pr	$^4I_{9/2}$	28.6	933.9	962.5	926.2	36.3	3.9
	$^4I_{11/2}$	13.9	759.4	773.4	730.4	43.0	5.9
	$^4I_{13/2}$	0.4	654.8	655.1	613.2	41.9	6.8
	$^4I_{15/2}$	13.3	587.0	573.8	541.6	32.2	5.9

Atom	Level	$\lvert\mathbf{A}^{\mathrm{FC+SD}}\rvert$	$\lvert\mathbf{A}^{\mathrm{PSO}}\rvert$	$\lvert\mathbf{A}^{\mathrm{tot}}\rvert$	$\lvert\mathbf{A}^{\mathrm{expt}}\rvert$	$\lvert\boldsymbol{\Delta}\rvert$	$\lvert\boldsymbol{\Delta}_{\%}\rvert$
^{143}Nd	$^5I_4$	6.2	207.5	201.3	195.7	5.7	2.9
	$^5I_5$	3.8	163.1	159.3	153.7	5.6	3.6
	$^5I_6$	1.7	137.7	135.9	130.6	5.3	4.1
	$^5I_7$	0.3	121.8	122.1	117.6	4.5	3.8
	$^5I_8$	2.4	111.2	113.6	110.5	3.1	2.8
^{147}Pm	$^6H_{7/2}$	42.0	472.3	430.4	447.1	16.7	3.7
^{147}Sm	$^7F_1$	34.8	70.4	35.6	33.5	2.1	6.2
	$^7F_2$	28.6	70.4	41.8	41.2	0.6	1.5
	$^7F_3$	20.4	70.4	50.0	50.2	0.2	0.4
	$^7F_4$	11.2	70.4	59.2	59.7	0.5	0.8
	$^7F_5$	1.7	70.4	68.7	69.1	0.4	0.6
	$^7F_6$	7.7	70.4	78.1	78.4	0.2	0.3
^{151}Eu	$^8S_{7/2}$	1.8	0.0	1.8	20.1	18.3	91.3
^{159}Tb	$^6H_{15/2}$	25.2	720.0	745.2	673.8	71.4	10.6
	$^6H_{13/2}$	2.8	773.4	770.7	682.9	87.8	12.8
	$^6H_{11/2}$	34.0	856.8	822.9	729.0	93.9	12.9
^{161}Dy	$^5I_8$	2.7	124.9	127.6	116.2	11.4	9.8
	$^5I_7$	0.3	136.8	137.1	126.8	10.3	8.2
	$^5I_6$	1.9	154.6	152.7	139.6	13.1	9.4
	$^5I_5$	4.3	183.2	178.9	162.0	17.0	10.5
	$^5I_4$	6.9	233.2	226.2	205.2	21.0	10.2
^{165}Ho	$^4I_{15/2}$	28.6	1253.7	1225.1	800.6	424.5	53.0
	$^4I_{13/2}$	0.7	1398.4	1399.0	937.2	461.8	49.3
	$^4I_{11/2}$	29.8	1621.9	1651.7	1035.1	616.6	59.6
	$^4I_{9/2}$	61.5	1994.5	2056.0	1137.7	918.3	80.7
^{167}Er	$^3H_6$	9.2	136.2	127.0	120.5	6.5	5.4
	$^3F_4$	16.8	147.1	130.4	121.8	8.5	7.0
	$^3H_5$	4.7	158.0	162.7	159.5	3.2	2.0
	$^3H_4$	5.2	168.4	173.6	173.4	0.2	0.1
	$^3F_3$	4.6	149.8	145.2	143.5	1.7	1.2
	$^3F_2$	14.4	217.9	203.5	167.1	36.3	21.7
^{169}Tm	$^2F_{7/2}$	48.4	433.0	384.7	374.1	10.5	2.8
	$^2F_{5/2}$	115.8	577.4	693.2	704.6	11.5	1.6

5 Conclusions

We have presented a new computational package, Hyperion, that enables the evaluation of relativistic picture-change-corrected magnetic resonance parameters from CASSCF-SO and RASSCF-SO wavefunctions, along with a new orbital decomposition method to assist in choosing appropriate active spaces for HFCC calculations. We used this code to study the hyperfine structure of alkali metal, transition metal and lanthanide atoms in order to understand the range of applicability afforded by this approach. Our best predicted HFCCs

are within 10% accuracy for alkali, 15% for coinage metals and 20% for lanthanides (although the vast majority of Ln HFCCs deviate less than 10% from the experimental value). The hyperfine structure of group VI-B (Cr) and group VIII-B (Fe) transition metals proved to be the most challenging to model, however, despite the larger percentage errors, we obtain theoretical HFCCs that closely follow experimentally-observed trends. Based on these results, we devised a number of guidelines for modelling HFC in systems exhibiting important correlation effects, strong SOC or a combination of both. In future work, these guidelines will be refined by using Hyperion to study HFC in molecular systems.

6 Acknowledgements

The authors thank The University of Manchester Computational Shared Facility for computational resources, The Ministry of Defence (PhD studentship to L.B.), and The Royal Society (University Research Fellowship to N.F.C.).

Supplementary Information

S1 Investigation of active space selection using orbital decomposition analysis

To investigate the influence of various orbital optimisation strategies on the computed HFCCs, we choose two small test systems, the ^{7}Li atom and the ^{14}N atom, and represent both using an ANO-RCC...8s7p basis set (containing 8 s functions and 7 sets of p functions). We have already shown that active spaces comprising only s and p shells are sufficient to obtain ^{7}Li HFCCs in excellent agreement with experiment; meanwhile, previous work[9,13,14] suggests that our chosen basis set is insufficient to achieve quantitative agreement with the experimental ^{14}N HFCC, $A = 10.4509$ MHz.[9] Nevertheless, in this case we are interested not in the accuracy of the computed HFCC, but in the HFC orbital decomposition analysis.

We aim to model HFC in the full orbital space, which is achievable via RASCI(3,29) for the chosen test systems. Figures S1 and S2 show orbital decomposition diagrams for the $^{2}S_{1/2}$ ground state of ^{7}Li and for the $^{4}S_{3/2}$ ground state of ^{14}N, respectively; all diagrams are obtained from RASCI(3,29) calculations using CASSCF- and RASSCF-optimised orbitals. It is immediately apparent that, as the number of optimised orbitals increases, the diagrams become more sparse and the HFC response is focused into a smaller subset of the orbital space. Surprisingly, CASSCF and RASSCF orbitals obtained using the same active space selection give rise to extremely similar diagrams - the same pairwise couplings are observed in both cases, with only a few small changes in magnitude. The most noticeable difference is the coupling between optimised orbitals, which appears to be slightly stronger when RASSCF is used. The larger HFCCs observed for calculations using RASSCF orbitals are likely a result of this stronger coupling, especially as the variations in HFCC are small.

These observations suggest that, within the multiconfigurational electronic structure framework, large active space optimisations of the orbital space result in the most effective representation of HFC. Compared to active space size, the constraints introduced by a RAS ansatz appear to have a minimal effect on the HFC orbital decomposition and the resulting HFCC. Of course, these conclusions are based on a limited number of small systems and might have limited applicability; further investigation is necessary to establish the validity of such trends in larger, more complex systems.

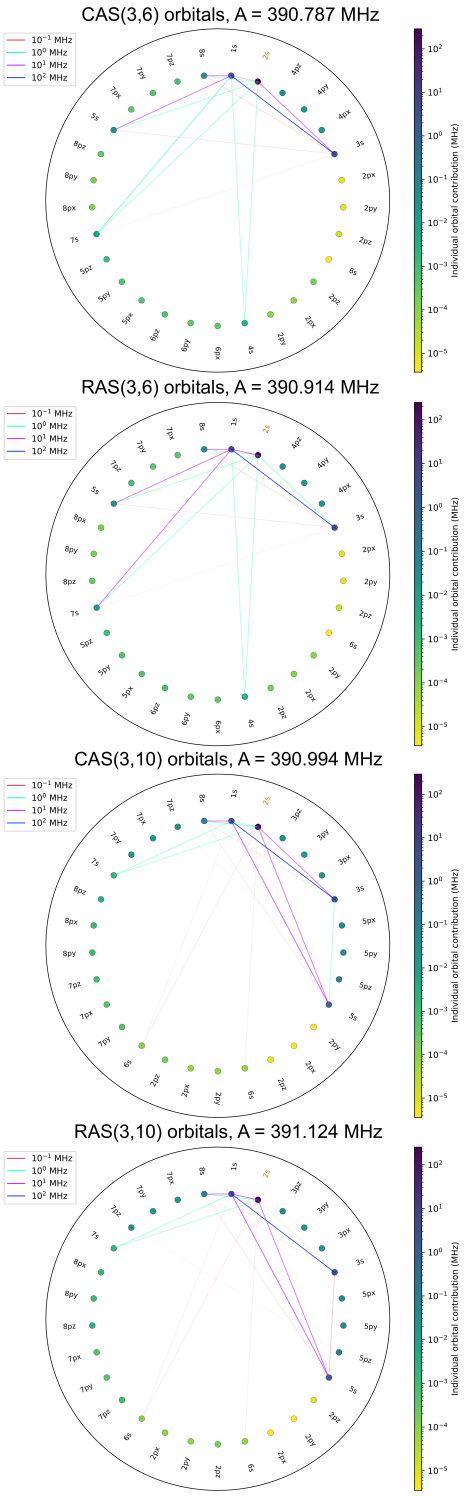

Figure S1: ^{7}Li HFCCs and HFC orbital decomposition diagrams determined from RASCI(3,29) wavefunctions using different CASSCF/RASSCF-optimised orbitals. Orbitals are labelled according to the dominant AO basis function contribution. Orange labels correspond to RAS2 orbitals.

Finally, it is worth highlighting that orbital energy is not a good indicator of the contribution to HFC. In both ^{7}Li and ^{14}N, high-energy diffuse functions couple most strongly with the SOMO and the other valence orbitals, while "mid-range" orbitals (e.g. 2p-dominated functions in ^{7}Li, 5p-dominated functions in ^{14}N) have much smaller contributions. In the context of theoretical HFCC determinations, this is not a new observation; Feller and Davidson remarked, in a 1988 study of second-period atomic HFCCs,[12] that "[…] *the choice of energy as the selection criterion is probably far from optimal for properties other than energy. However, when an entire group of properties is desired (including the energy) it may be as good a choice as any other.*" In *ab initio* studies that target HFCC accuracy, it is therefore essential to explore orbital selection criteria that are not energy-based; this is particularly relevant given the recent developments around automated active space selection methodologies.[73–75]

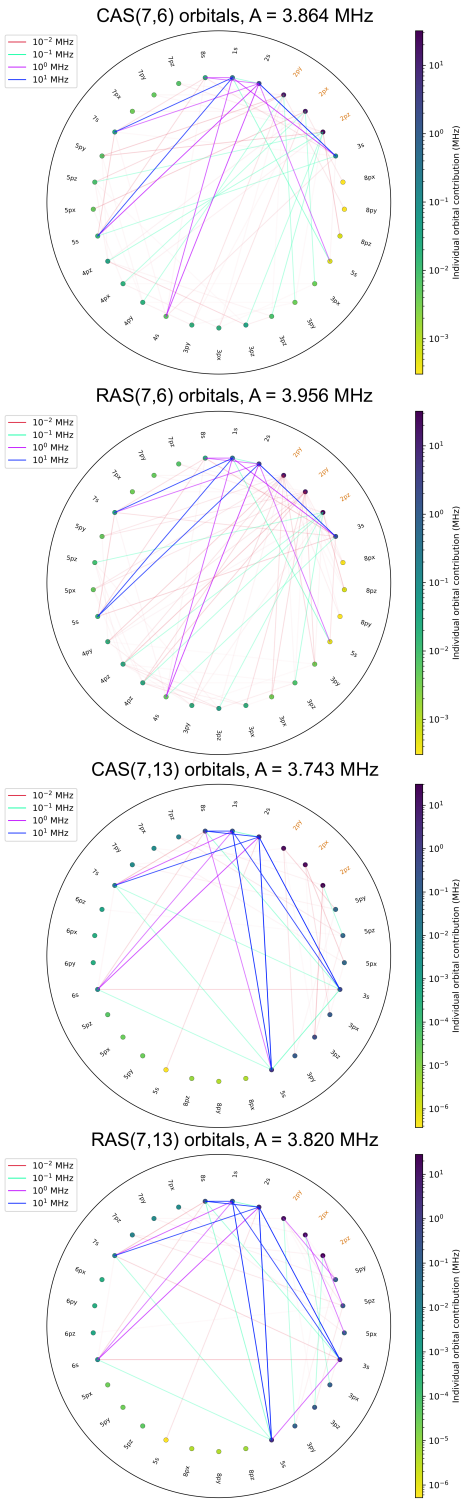

Figure S2: ^{14}N HFCCs and HFC orbital decomposition diagrams determined from RASCI(3,29) wavefunctions using different CASSCF/RASSCF-optimised orbitals. Orbitals are labelled according to the dominant AO basis function contribution. Orange labels correspond to RAS2 orbitals.

S2 Additional results

S2.1 Alkali

Table S1: Isotropic HFCCs (unsigned) in MHz computed for the ground state of alkali atoms. The RAS1, RAS2 and RAS3 columns indicate the number of atomic shells - separated by angular momentum - included in each subspace. Experimental HFCCs are reproduced from reference [19].

Atom	Wavefunction	RAS1	RAS2	RAS3	|A|
^{7}Li	CASSCF(3,14)	-	8×s, 2×p	-	378.1
	Experimental				**401.7**
^{23}Na	CASSCF(11,14)	-	5×s, 3×p	-	775.4
	CASSCF(11,18)	-	4×s, 3×p, 1×d	-	810.2
	RASSCF(11,33)	2×s, 1×p	1×s	6×s, 7×p	785.7
	RASSCF(11,38)	2×s, 1×p	1×s	6×s, 7×p, 1×d	820.8
	Experimental				**885.8**
^{39}K	CASSCF(11,14)	-	5×s, 3×p	-	185.8
	CASSCF(11,18)	-	4×s, 3×p, 1×d	-	207.4
	RASSCF(19,42)	3×s, 2×p	1×s	6×s, 7×p, 1×d	203.6
	RASSCF(19,44)	3×s, 2×p	1×s	6×s, 6×p, 2×d	203.1
	Experimental				**230.8**
^{85}Rb	CASSCF(11,14)	-	5×s, 3×p	-	834.3
	RASSCF(27,30)	2×s, 2×p, 1×d	1×s	1×s, 1×p, 1×d, 1×f	789.2
	RASSCF(27,34)	2×s, 2×p, 1×d	1×s	2×s, 2×p, 1×d, 1×f	847.0
	RASSCF(37,44)	4×s, 3×p, 1×d	1×s	4×s, 3×p, 1×d, 1×f	855.0
	RASCI(27,45)	4×s, 3×p	1×s	5×s, 7×p, 1×d	909.6
	RASCI(37,50)	4×s, 3×p, 1×d	1×s	5×s, 7×p, 1×d	907.2
	RASCI(37,47)	4×s, 3×p, 1×d	1×s	5×s, 6×p, 1×d	907.6
	Experimental				**1011.9**
^{133}Cs	RASCI(35,47)	5×s, 4×p	1×s	6×s, 6×p, 1×d	2070.9
	RASCI(43,51)	4×s, 4×p, 1×d	1×s	6×s, 6×p, 1×d	2066.2
	RASCI(45,52)	5×s, 4×p, 1×d	1×s	6×s, 6×p, 1×d	2066.8
	RASCI(45,45)	5×s, 4×p, 1×d	1×s	5×s, 4×p, 1×d	2077.4
	RASCI(45,52)	5×s, 4×p, 1×d	1×s	5×s, 4×p, 1×d, 1×f	2093.9
	Experimental				**2298.1**

S2.2 Coinage metals

Table S2: Isotropic HFCCs (unsigned) in MHz computed via RASCI using RASSCF(19,19)-optimised orbitals. The RAS1, RAS2 and RAS3 columns indicate the number of atomic shells - separated by angular momentum - included in each subspace. Experimental HFCCs are reproduced from reference [59].

Atom	Wavefunction	RAS1	RAS2	RAS3	|A|
^{63}Cu	RASCI(29,47)	3×s, 2×p, 1×d	1×s	6×s, 7×p, 1×d	4793.4
	RASCI(29,48)	3×s, 2×p, 1×d	1×s	6×s, 5×p, 1×d, 1×f	4908.1
	RASCI(29,49)	3×s, 2×p, 1×d	1×s	6×s, 6×p, 2×d	4826.8
	Experimental				**5866.9**
^{107}Ag	RASCI(47,52)	4×s, 3×p, 2×d	1×s	5×s, 6×p, 1×d	1495.4
	RASCI(47,57)	4×s, 3×p, 2×d	1×s	5×s, 6×p, 2×d	1505.1
	RASCI(47,59)	4×s, 3×p, 2×d	1×s	5×s, 6×p, 1×d, 1×f	1512.7
	Experimental				**1712.5**
^{197}Au	RASCI(45,47)	5×s, 4×p, 1×d	1×s	4×s, 5×p, 1×d	2598.0
	RASCI(45,54)	5×s, 4×p, 1×d	1×s	4×s, 5×p, 1×d, 1×f	2645.9
	Experimental				**3049.7**

S2.3 Groups VI-B (Cr) and VIII-B (Fe)

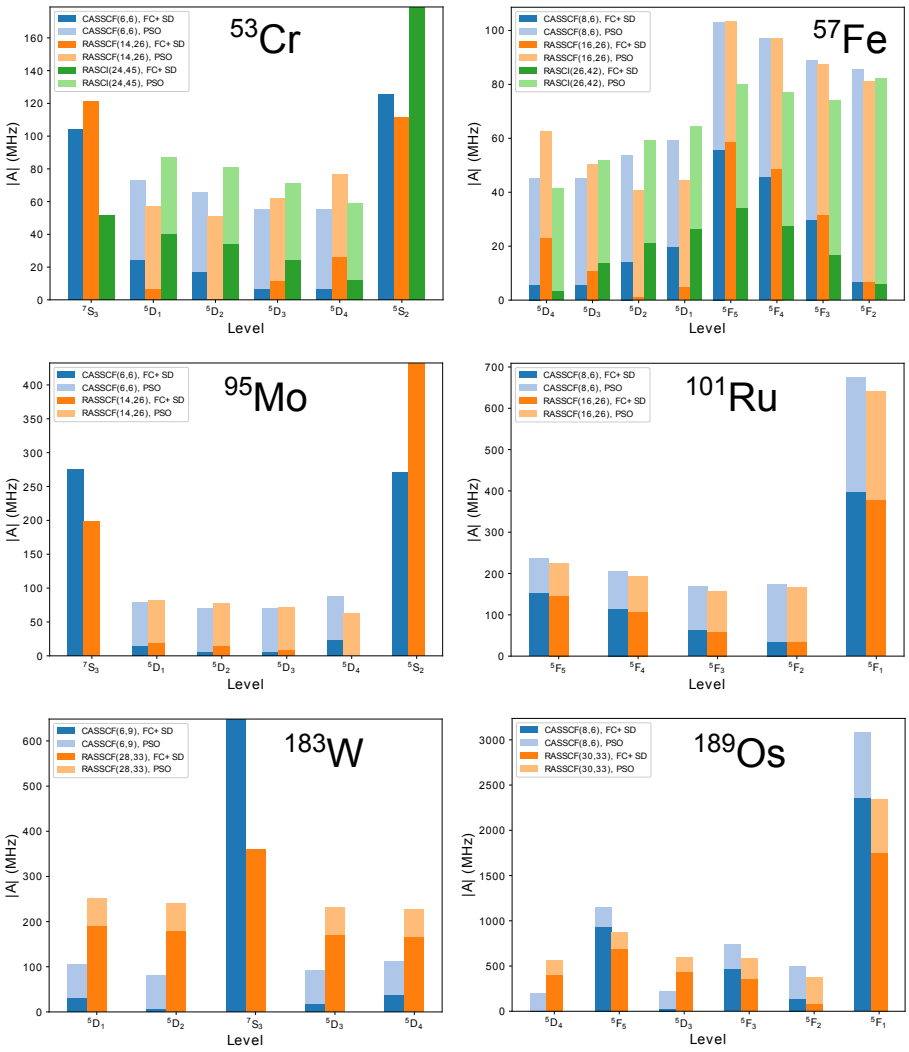

Figure S3: Spin-dependent (FC+SD) and spin-independent (PSO) unsigned HFCCs computed by HYPERION for selected energy levels of Cr group and Fe group atoms.

References

(1) G. N. L. Mar, Spin Delocalization and Electronic Structure, in *NMR of Paramagnetic Molecules*, Academic Press, 1973, pp. 85–126.

(2) D. M. Chipman, *Theoretica Chimica Acta*, 1992, **82**, 93–115.

(3) A. Formanuik, A.-M. M. Ariciu, F. Ortu, R. Beekmeyer, A. Kerridge, F. Tuna, E. J. L. McInnes and D. P. Mills, *Nature Chemistry*, 2017, **9**, 578–583.

(4) M. Bennati, *eMagRes*, 2017, **6**, 271–282.

(5) L. Hermosilla, P. Calle, J. M. García De La Vega and C. Sieiro, *Journal of Chemical Physics*, 2005, **109**, 1114–1124.

(6) S. Kossmann, B. Kirchner and F. Neese, *Molecular Physics*, 2007, **105**, 2049–2071.

(7) B. Engels, Ab Initio Post-Hartree-Fock Calculations of Hyperfine Coupling Tensors and Their Comparison with DFT Approaches, in *Calculation of NMR and EPR Parameters: Theory and Applications*, WILEY-VCH, 2004, ch. 30, pp. 483–492.

(8) M. Witwicki, P. K. Walencik and J. Jezierska, *Journal of Molecular Modeling*, 2020, **26**, DOI: 10.1007/s00894-019-4268-0.

(9) B. Engels, S. D. Peyerimhoff and E. R. Davidson, *Molecular Physics*, 1987, **62**, 109–127.

(10) B. Engels and S. D. Peyerimhoff, *Molecular Physics*, 1989, **67**, 583–600.

(11) B. Engels, *Chemical Physics Letters*, 1991, **179**, 398–404.

(12) D. Feller and E. R. Davidson, *Journal of Chemical Physics*, 1988, **88**, 7580–7587.

(13) C. W. Bauschlicher, S. R. Langhoff, H. Partridge and D. P. Chong, *Journal of Chemical Physics*, 1988, **89**, 2985–2992.

(14) C. W. Bauschlicher, *Journal of Chemical Physics*, 1990, **92**, 518–521.

(15) I. Carmichael, *Journal of Chemical Physics*, 1989, **91**, 1072–1078.

(16) M. L. Munzarova, P. Kubacek and M. Kaupp, *Journal of the American Chemical Society*, 2000, **122**, 11900–11913.

(17) W. Kutzelnigg, *Theoretica Chimica Acta*, 1988, **73**, 173–200.

(18) R. Arratia-Perez and D. A. Case, *Journal of Chemical Physics*, 1983, **79**, 4939–4949.

(19) K. Talukdar, S. Sasmal, M. K. Nayak, N. Vaval and S. Pal, *Physical Review A*, 2018, **98**, 1–8.

(20) H. M. Quiney and P. Belanzoni, *Chemical Physics Letters*, 2002, **353**, 253–258.

(21) S. Gohr, P. Hrobárik, M. Repiský, S. Komorovský, K. Ruud and M. Kaupp, *Journal of Physical Chemistry A*, 2015, **119**, 12892–12905.

(22) M. Barysz and A. J. Sadlej, *Theoretical Chemistry Accounts*, 1997, **97**, 260–270.

(23) T. Saue, *ChemPhysChem*, 2011, **12**, 3077–3094.

(24) W. Liu, *Handbook of Relativistic Quantum Chemistry*, Springer Nature, 2016.

(25) E. Van Lenthe, A. Van Der Avoird and P. E. Wormer, *Journal of Chemical Physics*, 1998, **108**, 4783–4796.

(26) P. Belanzoni, E. Van Lenthe and E. J. Baerends, *Journal of Chemical Physics*, 2001, **114**, 4421–4433.

(27) F. Aquino, B. Pritchard and J. Autschbach, *Journal of Chemical Theory and Computation*, 2012, **8**, 598–609.

(28) P. Verma and J. Autschbach, *Journal of Chemical Theory and Computation*, 2013, **9**, 1932–1948.

(29) J. Autschbach, *Theoretical Chemistry Accounts*, 2004, **112**, 52–57.

(30) J. Autschbach, *Molecular Physics*, 2013, **111**, 2544–2554.

(31) J. Autschbach, Relativistic Effects on Magnetic Resonance Parameters and Other Properties of Inorganic Molecules and Metal Complexes, in *Relativistic Methods for Chemists*, Springer Netherlands, 2010, pp. 521–598.

(32) I. Malkin, O. L. Malkina, V. G. Malkin and M. Kaupp, *Chemical Physics Letters*, 2004, **396**, 268–276.

(33) E. Malkin, I. Malkin, O. L. Malkina, V. G. Malkin and M. Kaupp, *Physical Chemistry Chemical Physics*, 2006, **8**, 4079–4085.

(34) T. N. Lan, Y. Kurashige and T. Yanai, *Journal of Chemical Theory and Computation*, 2014, **11**, 73–81.

(35) M. Filatov and D. Cremer, *Journal of Chemical Physics*, 2004, **121**, 5618–5622.

(36) J. Autschbach, *Journal of Chemical Theory and Computation*, 2017, **13**, 710–718.

(37) A. Wodyński and M. Kaupp, *Journal of Physical Chemistry A*, 2019, **123**, 5660–5672.

(38) R. Feng, T. J. Duignan and J. Autschbach, *Journal of Chemical Theory and Computation*, 2020, 1–8.

(39) M. Filatov, W. Zou and D. Cremer, *Journal of Physical Chemistry A*, 2012, **116**, 3481–3486.

(40) K. G. Dyall and K. Fægri, Jr., *Introduction to relativistic quantum chemistry*, Oxford University Press, New York, 2007.

(41) W. Kutzelnigg and W. Liu, *Molecular Physics*, 2006, **104**, 2225–2240.

(42) W. Liu and W. Kutzelnigg, *Journal of Chemical Physics*, 2007, **126**, DOI: 10.1063/1.2710258.

(43) L. F. Chibotaru, Ab Initio Methodology for Pseudospin Hamiltonians of Anisotropic Magnetic Complexes, in *Advances in Chemical Physics*, John Wiley & Sons, Ltd, 2013, pp. 397–519.

(44) H. Bolvin, *ChemPhysChem*, 2006, **7**, 1575–1589.

(45) K. Boguslawski, P. Tecmer, Ö. Legeza and M. Reiher, *Journal of Physical Chemistry Letters*, 2012, **3**, 3129–3135.

(46) Q. Sun, *Journal of Computational Chemistry*, 2015, **36**, 1664–1671.

(47) B. O. Roos, R. Lindh, P. Å. Malmqvist, V. Veryazov and P. O. Widmark, *Journal of Physical Chemistry A*, 2004, **108**, 2851–2858.

(48) B. O. Roos, V. Veryazov and P. O. Widmark, *Theoretical Chemistry Accounts*, 2004, **111**, 345–351.

(49) B. O. Roos, R. Lindh, P. Å. Malmqvist, V. Veryazov and P. O. Widmark, *Chemical Physics Letters*, 2005, **409**, 295–299.

(50) B. O. Roos, R. Lindh, P. Å. Malmqvist, V. Veryazov and P. O. Widmark, *Journal of Physical Chemistry A*, 2005, **109**, 6575–6579.

(51) B. O. Roos, R. Lindh, P. Å. Malmqvist, V. Veryazov, P. O. Widmark and A. C. Borin, *Journal of Physical Chemistry A*, 2008, **112**, 11431–11435.

(52) K. Sharkas, B. Pritchard and J. Autschbach, *Journal of Chemical Theory and Computation*, 2015, **11**, 538–549.

(53) B. O. Roos, *International Journal of Quantum Chemistry*, 1980, **18**, 175–189.

(54) P. Å. Malmqvist, A. Rendell and B. O. Roos, *Journal of Physical Chemistry*, 1990, **94**, 5477–5482.

(55) P. Å. Malmqvist, B. O. Roos and B. Schimmelpfennig, *Chemical Physics Letters*, 2002, **357**, 230–240.

(56) H. Kollmar and V. Staemmler, *Theoretica Chimica Acta*, 1978, **48**, 223–239.

(57) E. Giner, L. Tenti, C. Angeli and N. Ferré, *Journal of Chemical Theory and Computation*, 2017, **13**, 475–487.

(58) L. Tterlikkis, S. Mahanti and T. Das, *Physical Review*, 1968, **176**, 10–19.

(59) I. Lindgren and A. Rosén, Relativistic Self-Consistent-Field Calculations With Application To Atomic Hyperfine Interaction Part III: Comparison Between Theoretical and Experimental Hyperfine-Structure Results, in *Case Studies in Atomic Physics*, Elsevier, 1975, pp. 197–298.

(60) T. Helgaker and P. R. Taylor, Gaussian Basis Sets and Molecular Integrals, in *Modern Electronic Structure Theory*, World Scientific, 1995, pp. 725–856.

(61) W. Kutzelnigg, *Theoretica Chimica Acta*, 1985, **68**, 445–469.

(62) K. G. Dyall, *Journal of Physical Chemistry A*, 2009, **113**, 12638–12644.

(63) G. L. Manni, S. D. Smart and A. Alavi, *Journal of Chemical Theory and Computation*, 2016, **12**, 1245–1258.

(64) S. Battaglia, S. Keller and S. Knecht, *Journal of Chemical Theory and Computation*, 2018, **14**, 2353–2369.

(65) A. Jarosz, D. Stefańska, M. Elantkowska, J. Ruczkowski, A. Buczek, B. Furmann, P. Głowacki, A. Krzykowski, Pitkowski, E. Stachowska and J. Dembczyński, *Journal of Physics B: Atomic, Molecular and Optical Physics*, 2007, **40**, 2785–2797.

(66) S. Büttgenbach, *Hyperfine Structure in 4d- and 5d-Shell Atoms*, Springer-Verlag Berlin Heidelberg, 1982.

(67) W. J. Childs and L. S. Goodman, *Physical Review*, 1966, **148**, 74–78.

(68) J. Dembczyński, W. Ertmer, U. Johann and P. Stinner, *Zeitschrift für Physik A Atoms and Nuclei*, 1980, **294**, 313–317.

(69) D. H. Forest, R. A. Powis, E. C. Cochrane, J. A. Griffith and G. Tungate, *Journal of Physics G: Nuclear and Particle Physics*, 2014, **41**, DOI: 10.1088/0954-3899/41/2/025106.

(70) S. Kröger, G. Başar, A. Baier and G. H. Guthöhrlein, *Physica Scripta*, 2002, **65**, 56–68.

(71) W. J. Childs, H. Crowsswhite, L. S. Goodman and V. Pfeufer, *Journal of the Optical Society of America B*, 1984, **1**, 22–29.

(72) K. T. Cheng and W. J. Childs, *Physical Review A*, 1985, **31**, 2775–2784.

(73) C. J. Stein and M. Reiher, *CHIMIA*, 2017, **71**, 170–176.

(74) D. King and L. Gagliardi, *Journal of Chemical Theory and Computation*, 2021, **17**, 2817–2831.

(75) Y. Lei, B. Suo and W. Liu, *Journal of Chemical Theory and Computation*, 2021, **17**, 4846–4859.

Chapter 5

Paper three: ”A Relativistic Quantum Chemical Investigation of Actinide Covalency Measured by EPR Spectroscopy”

A Relativistic Quantum Chemical Investigation of Actinide Covalency Measured by EPR Spectroscopy

Letitia Birnoschi[1] and Nicholas F. Chilton[1]

[1]Department of Chemistry, The University of Manchester, Oxford Road, Manchester, M13 9PL, United Kingdom

Abstract

We investigate actinide covalency effects in two $AnCp_3^{tt}$ (An = Th, U) complexes using the recently developed Hyperion package to obtain relativistic g-tensors and hyperfine coupling constants from CASSCF-SO, RASSCF-SO and RASCI-SO wavefunctions. HYSCORE simulations using the computed parameters are then compared to experimental data reported by Formanuik and coworkers, in order to assess the performance of fully *ab initio* models of ligand hyperfine coupling. The extent of covalency in $AnCp_3^{tt}$ is quantified via Mulliken spin population analysis, which uncovers different patterns in the spin density transfer between An and the ligand atoms.

1 Introduction

The actinide (An) series is a key area of interest within chemical science, attracting research efforts from experimentalists and theorists alike.[1–4] Despite this interest, the inherent radiological hazards of working with An elements, as well as the need for specialist equipment, have made progress in this area slow. To this day, our understanding of An bonding and properties is limited, lagging behind other regions in the periodic table. Of particular interest is the concept of An covalency, believed to arise due to the more expanded nature of 5f orbitals relative to 4f orbitals[5] in the predominantly ionic lanthanides (Ln).

Actinide chemistry is influenced by strong relativistic effects, as well as non-trivial electronic structures, where 5f, 6d and 7s valence orbitals are all involved in bonding. This combination is rarely observed in the rest of the periodic table, hence any insight into An properties based on periodic trends is severely limited. As such, the most viable solution is a hybrid approach involving both experimental and theoretical methods. Indeed, X-ray absorption[6] and magnetic resonance techniques[7,8] are now popular choices for studies of An covalency, often complemented by computational electronic structure calculations such as DFT or RASSCF-SO.

In 2017, Formanuik *et al* published the first pulsed EPR study of An complexes,[9] with a focus on correlating hyperfine coupling (HFC) measurements with covalency. The strength of HFC, quantified by hyperfine coupling constants (HFCCs), depends on the unpaired electron (spin) density distribution and varies as r_{N}^{-3}, where r_{N} is the distance between magnetic nucleus N and the spin density. In traditional non-relativistic interpretations, isotropic HFCCs arise solely due to spin density at the position of the magnetic nucleus,[10] and therefore report directly on spin delocalisation. The picture is not so clear in relativistic theory,[11] but still, small variations in the spin density distribution lead to noticeable changes in HFCCs, hence measurement of HFC is a particularly precise probe for covalency. Formanuik derived spin populations – used to quantify An covalency – for the ligand atoms in both An complexes using a classical point-dipole model of HFC, with added spin polarisation contributions determined by fitting the simulated HYSCORE spectra to experimental data. Empirical parameters from studies of HFC in cyclopentadienyl radicals were used to define the relationship between spin populations and HFCCs.

Unfortunately, such approximations are inappropriate for actinide complexes, as the strong relativistic effects preclude the use of non-relativistic HFCC expressions. Instead, a relativistic model – based on the Dirac equation or a variant thereof[12] – must be employed, thus introducing the need for a quantum chemical approach. Although such a strategy comes with a significant increase in complexity and computational cost, the overall number of model parameters is reduced, leading to increased interpretability and reproducibility. Aside from the ability to account for relativistic effects at the appropriate level of theory, quantum chemical methods can provide estimates for spin populations which are completely decoupled from HFCC determinations. As such, the need for empirical parameters is eliminated, and the only free parameters are those introduced at the onset of the electronic structure optimisation step. Thereafter, spin populations and HFC parameters are

straightforwardly determined from the electronic structure results.

Recently, we presented the newly developed Hyperion code for computing relativistic HFCCs from first-principles electronic structure calculations. We used complete active space and restricted active space self-consistent field methods (CASSCF/RASSCF)[13,14] to account for spin polarisation/electron correlation in a flexible manner and, where necessary, additionally included spin-orbit coupling (SOC) via a state-interaction approach (CASSCF-SO/RASSCF-SO);[15] this yielded very good results for a wide selection of atomic systems. Herein, we employ the same methodology with Hyperion to calculate HFCCs for the two $AnCp_3^{tt}$ complexes studied by Formanuik *et al* (Figure 1), with the aim of assessing the performance of a fully *ab initio* model when applied to non-trivial systems, and to determine the implications of using a relativistic treatment for assessing covalency in actinide compounds.

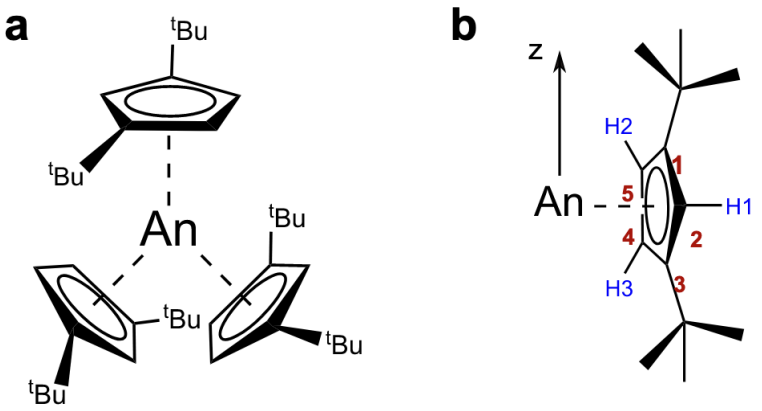

Figure 1: a: Schematic of the $AnCp_3^{tt}$ structure; **b**: Pseudo-C_3 z axis and numbering convention used for identifying C(Cp) atoms (red) and H(Cp) atoms (blue).

2 Theory

Starting from the 4-component Dirac equation, relativistic expressions for the Zeeman and the HFC operator can be determined by adding in – via minimal coupling – vector potentials arising from external and nuclear magnetic fields, respectively. The additional terms are treated as first-order perturbations to the field-free Dirac equation. This 4-component model is then simplified via scalar-relativistic eXact-2-Component (SR-X2C) decoupling, wherein a unitary transformation, known as the picture-change transformation, is applied to the zeroth order Hamiltonian and to the perturbation operators. As a result, the relativistic wavefunction and properties can be determined within the 1-component framework underlying most electronic structure packages.

The SF-X2C-transformed perturbation operator for HFC can be expressed as

$$\hat{\mathrm{H}}^{(1)}_{\mathrm{N,SF\text{-}X2C}} = \hat{\mathrm{H}}^{\mathrm{FC+SD}}_{\mathrm{N,SF\text{-}X2C}} + \hat{\mathrm{H}}^{\mathrm{PSO}}_{\mathrm{N,SF\text{-}X2C}} \,, \tag{1}$$

$$\begin{aligned}\hat{\mathrm{H}}^{\mathrm{FC+SD}}_{\mathrm{N,SF\text{-}X2C}} = 2\,\mu_{\mathrm{B}} g_{\mathrm{N}} \mu_{\mathrm{N}}\, \frac{\mu_0}{4\pi}\, \mathbf{I}_{\mathrm{N}} \cdot \Bigg\{ & \hat{\mathrm{U}}^{\dagger}_{\mathrm{UU}} \left(-\frac{\mathbf{r}_{\mathrm{N}}}{r^3_{\mathrm{N}}} \cdot \boldsymbol{\nabla} + \frac{\mathbf{r}_{\mathrm{N}}}{r^3_{\mathrm{N}}}\, \boldsymbol{\nabla}^{\top} \right) \hat{\mathrm{U}}_{\mathrm{LU}} \\ & + \hat{\mathrm{U}}^{\dagger}_{\mathrm{LU}} \left(-\frac{\mathbf{r}_{\mathrm{N}}}{r^3_{\mathrm{N}}} \cdot \boldsymbol{\nabla} + \frac{\mathbf{r}_{\mathrm{N}}}{r^3_{\mathrm{N}}}\, \boldsymbol{\nabla}^{\top} \right)^{\dagger} \hat{\mathrm{U}}_{\mathrm{UU}} \Bigg\} \cdot \hat{\mathbf{S}} \,,\end{aligned} \tag{2}$$

$$\hat{\mathrm{H}}^{\mathrm{PSO}}_{\mathrm{N,SF\text{-}X2C}} = i\,\mu_{\mathrm{B}} g_{\mathrm{N}} \mu_{\mathrm{N}}\, \frac{\mu_0}{4\pi}\, \mathbf{I}_{\mathrm{N}} \cdot \left\{ -\hat{\mathrm{U}}^{\dagger}_{\mathrm{UU}} \left(\frac{\mathbf{r}_{\mathrm{N}}}{r^3_{\mathrm{N}}} \times \boldsymbol{\nabla} \right) \hat{\mathrm{U}}_{\mathrm{LU}} + \hat{\mathrm{U}}^{\dagger}_{\mathrm{LU}} \left(\frac{\mathbf{r}_{\mathrm{N}}}{r^3_{\mathrm{N}}} \times \boldsymbol{\nabla} \right)^{\dagger} \hat{\mathrm{U}}_{\mathrm{UU}} \right\} \,, \tag{3}$$

where $\hat{\mathrm{U}}_{\mathrm{UU}}$ and $\hat{\mathrm{U}}_{\mathrm{LU}}$ represent blocks of the SR-X2C decoupling matrix, $\hat{\mathbf{S}}$ is the one-electron spin operator, $\mathbf{I}_{\mathrm{N}}$ is the nuclear spin vector and $\mathbf{r}_{\mathrm{N}}$ denotes the electron position vector with respect to nucleus N. μ_{B}, g_{N}, μ_{N} and μ_0 have their usual meanings of Bohr magneton, nuclear g-factor, nuclear magneton and vacuum permeability, respectively, and i denotes the imaginary unit.

In equation 1, we distinguish between a spin-dependent contribution, $\hat{\mathrm{H}}^{\mathrm{FC+SD}}_{\mathrm{N,SF\text{-}X2C}}$, and an imaginary, spin-independent contribution, $\hat{\mathrm{H}}^{\mathrm{PSO}}_{\mathrm{N,SF\text{-}X2C}}$. The former reduces to the sum of the Fermi-coupling (FC) and the spin-dipolar (SD) operators in the non-relativistic limit, while the latter represents the interaction between the electronic orbital angular momentum and the nuclear spin, and is known as the paramagnetic spin-orbit coupling (PSO) term. The Zeeman perturbation operator can be similarly divided into a spin-Zeeman term and an orbital-Zeeman term. It is worth highlighting that (2) does not include a delta-function characteristic of the FC interaction; as shown by Kutzelnigg,[11] this hallmark only arises in the non-relativistic limit of a 2-component framework. Hence, relativistic spin-dependent HFC cannot be interpreted as a combination of classical dipolar coupling (SD term) and an FC term sampling the spin density at nucleus N.[10]

In the spin-only limit (no unquenched orbital angular momentum), the PSO term is zero, and elements of the HFC tensor $\boldsymbol{a}_{\mathrm{N}}$ can be evaluated with respect to a spin-free (SF) state

Ψ^{SS} as

$$a_{\mathrm{N},kl} = \frac{1}{S}\left\langle \Psi^{SS} \left| \left(\frac{\partial^2 \hat{\mathrm{H}}^{\mathrm{FC+SD}}_{\mathrm{N,SF\text{-}X2C}}}{\partial \mathbf{I}_{\mathrm{N}}\, \partial \hat{\mathbf{S}}} \right)_{kl} \right| \Psi^{SS} \right\rangle, \qquad (4)$$
$$k, l = x, y, z\,.$$

This is equivalent to mapping the *ab initio* HFC operator onto an effective spin Hamiltonian,

$$\hat{\mathrm{H}}_{\mathrm{spin}} = \mathbf{I}_{\mathrm{N}} \cdot \boldsymbol{a}_{\mathrm{N}} \cdot \mathbf{S}\,, \qquad (5)$$

whose model space is the $2S + 1$ spin multiplet represented by Ψ^{SS}. We note that there are reports in the literature of spin-only parametrisations of HFC in SO-coupled systems, requiring the PSO contribution to be treated as a second-order perturbation. This approach is not employed herein – Hyperion computes spin-only HFCCs via equation 4.

For systems where S is not a good quantum number, we use the pseudospin ($\mathcal{S}$) parametrisation, where the model space – known as the pseudospin multiplet – encompasses the lowest-energy $2\mathcal{S} + 1$ states in the SO-coupled spectrum. Replacing S with $\mathcal{S}$ in (5) yields the pseudospin Hamiltonian, from which the elements of symmetrised HFC tensor $\boldsymbol{a}_{\mathrm{N}}\boldsymbol{a}_{\mathrm{N}}^{\top}$ are computed via the method of Chibotaru:[16]

$$\left(\boldsymbol{a}_{\mathrm{N}}\boldsymbol{a}_{\mathrm{N}}^{\top}\right)_{kl} = \frac{3}{\mathcal{S}(\mathcal{S}+1)(2\mathcal{S}+1)} \sum_{\mu,\nu}^{2\mathcal{S}+1} \left\langle \Psi_\mu \left| \frac{\partial\, \hat{\mathrm{H}}^{(1)}_{\mathrm{N,SF\text{-}X2C}}}{\partial I_{\mathrm{N},k}} \right| \Psi_\nu \right\rangle \left\langle \Psi_\nu \left| \frac{\partial\, \hat{\mathrm{H}}^{(1)}_{\mathrm{N,SF\text{-}X2C}}}{\partial I_{\mathrm{N},l}} \right| \Psi_\mu \right\rangle, \qquad (6)$$

where Ψ_μ and Ψ_ν denote eigenstates in the pseudospin manifold. A similar expression for the symmetrised g-tensor can be obtained by replacing the HFC operator derivative in (6) with the derivative of the Zeeman perturbation operator with respect to a component of the external magnetic field. The eigenvectors and eigenvalues of the symmetrised tensors correspond to the principal axes and the squared principal values of the original tensors; as a result, the pseudospin parametrisation yields *unsigned* g-values and HFCCs. We use an approximate methodology, described in Section S1, to determine the missing signs and employ the resulting HFCCs to simulate HYSCORE spectra of the $\mathrm{AnCp}_3^{\mathrm{tt}}$ complexes.

3 Computational details

All electronic structure calculations use the CASSCF-SO/RASSCF-SO implementation in OpenMolcas v20.10.[17] Molecular geometries from the crystal structures reported in [9] are

used without any further adjustment. [In reality, the geometry of the complexes relaxes in solution, and this influences the effective EPR parameters, however geometry optimisations of An complexes are beyond the scope of this work. We note in passing that, although the computational work in [9] uses optimised geometries, these do not include the cyclopentadienyl ring substituents; the ^{t}Bu groups have a critical influence on $AnCp_3^{tt}$ HFC due to steric repulsion, which likely persists in solution.] Atoms are represented using ANO-RCC basis sets[18–22] of TZP quality on An, DZP on C(Cp), H(Cp) and tertiary C(^{t}Bu), and MB on all other atoms. HFCCs, g-values and corresponding principal axes are determined from electronic structure data using the Hyperion package. The *hyperion2easyspin* utility within Hyperion is then employed to generate EasySpin[23] input files containing the EPR parameters, followed by HYSCORE simulations via *saffron*.[24]

HYSCORE simulations of the $ThCp_3^{tt}$ complex are carried out at $B_0 = 351.6$ mT ($g_{\parallel}$) and at $B_0 = 366.3$ mT ($g_{\perp}$), with $\tau = 130$ ns and t_1 and t_2 incremented from 0.2 μs to 5.3 μs in steps of 0.02 μs (256 points). 181 orientations (knots) are computed explicitly, using a spectrometer frequency of 9.614 GHz and a microwave excitation bandwidth of 62.5 MHz. Experimental spectra are rendered using 30 contour levels in the following ranges: 0.018−1.5 (^{13}C HYSCORE, $g_{\perp}$), 0.05−1.5 (^{1}H HYSCORE, $g_{\perp}$) and 0.15−1.5 (^{13}C HYSCORE and ^{1}H HYSCORE, $g_{\parallel}$). Simulated spectra are rendered using 20 contour levels between 0.15 and 2 (^{13}C HYSCORE) and between 0.5 and 5 (^{1}H HYSCORE).

^{1}H HYSCORE simulations of UCp_3^{tt} are carried out at $B_0 = 244.3$ mT (g_x) and at $B_0 = 450.4$ mT (g_y), with $\tau = 200$ ns and t_1 and t_2 incremented from 0.2 μs to 5.3 μs in steps of 0.02 μs (256 points). 31 orientations (knots) are computed explicitly, using a spectrometer frequency of 9.723 GHz and a microwave excitation bandwidth of 62.5 MHz. Experimental spectra are rendered using 30 contour levels between 0.3 and 2, while simulated spectra are shown using 20 contour levels between 0.15 and 2. We note that, for both complexes, we employ the same HYSCORE simulation parameters as Formanuik *et al.*

All HYSCORE simulations reported herein use the experimental frozen solution g-values, and we assume that frozen solution-phase HFCCs, as well as the orientation of the principal HFC axes with respect to the main magnetic axes, are identical to those of the crystal structure. Note that we use the principal g-axes and HFC axes determined from *ab initio* data via Hyperion and as such, each electronic structure model (choice of CAS/RAS and number of optimised states) yields a different set of directions (Figures S1 and S2).

Due to the steep scaling of pulsed EPR simulations,[24] it is necessary to limit the number of magnetic nuclei included in the *saffron* step. To determine ^{13}C HYSCORE spectra of $ThCp^{tt}_3$, we use a representative set of five ^{13}C nuclei, comprising three C(Cp) (labelled as C1, C2 and C4 in the XRD structure), one tertiary C(^{t}Bu) (C6) and one primary C(^{t}Bu) (C26). ^{1}H HYSCORE simulations of the same complex employ four ^{1}H nuclei, of which three are H(Cp) atoms from the same cyclopentadienyl ring, while the fourth is a representative H(^{t}Bu) atom (H8 in the XRD structure). Using the Hyperion-calculated g-axes and HFC parameters, the HFC matrices of the selected nuclei are rotated into the g-tensor eigenframe for the purpose of HYSCORE simulations. We note that the representative sets of nuclei are selected on the basis of symmetry arguments (axiality of $ThCp^{tt}_3$ g-values, pseudo-mirror plane bisecting the cyclopentadienyl plane), variations in spin population and distance from the An center; more details are provided in Section S5.1.

Unlike $ThCp^{tt}_3$, the rhombicity of the UCp^{tt}_3 g-values requires nuclei from all Cp^{tt} groups to be included in HYSCORE simulations, which quickly becomes unfeasible. We therefore define two sets of H(Cp) nuclei based on distances measured in the crystal structure: set **1** includes all in-plane (H1-type) nuclei and the three out-of-plane (H2/H3-type) nuclei closest to U, while set **2** includes all in-plane nuclei and the three out-of-plane nuclei located farthest from U. Given the geometry fluctuations in solution and assuming no drastic change in the U-Cp centroid distance, we expect the HYSCORE signal of H(Cp) in solution to be roughly an average between the two sets.

4 Results and discussion

4.1 Electronic structure

We first benchmark our electronic structure calculations against the experimental g-values measured for the crystal structures of $AnCp^{tt}_3$. For $ThCp^{tt}_3$, the measured $g_{\parallel} = 1.974$ and $g_{\perp} = 1.880$ indicate the presence of spin-orbit coupling (as they significantly deviate from the free electron g-value), despite the fact that the ground state is well described by the $6d^1_{z^2}$ configuration and hence the orbital angular momentum of the 6d shell is mainly quenched. A state-averaged (SA) CASSCF(1,12) calculation considering the 6d and 5f orbitals and including all 12 doublet states, followed by mixing by SO coupling reveals that the SO ground Kramers doublet is dominated by the lowest-energy spin-free doublet state

($6d^1_{z^2}$), with small contributions from the first two excited SF doublet states, which appear to be a pseudo-degenerate pair with hybrid 6d/5f singly-occupied molecular orbitals (SOMOs). All subsequent SA-CASSCF-SO and SA-RASSCF-SO calculations therefore only include the lowest three SF states. We note that the energies of the lowest SO-coupled excited states, 15199 cm^{-1} and 15373 cm^{-1}, are in close agreement with the first strong absorption, $\epsilon = 15600$ cm^{-1}, observed in the solution-phase UV-Vis spectrum.[9]

Table 1: $ThCp^{tt}_3$ active orbitals included in state-averaged CASSCF-SO/RASSCF-SO with 3 spin doublet roots.

Active space	**RAS1**	**RAS2**	**RAS3**
CASSCF(1,12)	-	5×6d, 7×5f	-
RASSCF(19,27)	9×π_{Cp}	3×6d	6×π^*_{Cp}, 2×6d, 4×5f, 7s, $7p_{x,y}$
RASSCF(27,36)	6s, 3×6p, 9×π_{Cp}	3×6d	6×π^*_{Cp}, 2×6d, 4×5f, 7s, 3×7p, 8s

Electron correlation effects involving the cyclopentadienyl groups are then added via a RASSCF-SO approach, where occupied and unoccupied π-type valence orbitals are included in the RAS1 and RAS3 subspaces, respectively (Table 1). To keep the computational cost feasible, only the SOMOs of the 3 optimised states are kept in the RAS2 subspace, while all other Th virtual orbitals are assigned to RAS3. The complex chemistry of actinides is a consequence of non-trivial bonding modes involving some or all of the 5f, 6d, 7s and 7p orbitals. Our electronic structure calculations therefore include all such orbitals that are stable in – i.e. do not rotate out of – the active space. As we are interested in modelling HFC, we also investigate the effects of correlating outer core electrons using a RAS(27,36) model (Table 1) that includes Th 6s and 6p functions in RAS1, as well the 8s orbital in RAS3. We note that this active space yields the most accurate $g_\perp$, Table 2, while RASSCF(19,27)-SO yields the best prediction for $g_\parallel$; nevertheless, all g-values are in good agreement with experiment, especially considering that the experiment is conducted on a frozen solution and the calculations are performed using the crystalline geometry.

Table 2: $ThCp^{tt}_3$ g-values calculated from active space electronic structure data. Note: owing to the C_1 symmetry of the XRD structure, the two $g_\perp$ values are not coincident.

Active space	$\mathbf{g}_\parallel$	$\mathbf{g}_\perp$	$\mathbf{g}_\perp$
CASSCF(1,12)	1.975	1.827	1.821
RASSCF(19,27)	1.973	1.831	1.826
RASSCF(27,36)	1.983	1.870	1.866
Experiment	1.974	1.880	1.880

The U centre in UCp^{tt}_3 has an idealised $5f^3$ configuration associated with a $^4I_{9/2}$ Russel-Saunders ground term; this is split by the ligand field, resulting in a Kramers doublet ground state which can be modelled as an effective $\mathcal{S} = 1/2$. Herein, we limit CASSCF and RASSCF optimisations of UCp^{tt}_3 to include only 13 spin quartets and 11 spin doublets (corresponding to the ^4I and ^2H LS terms, respectively, which are the lowest-lying terms for each spin multiplicity), so as to minimise the impact of state averaging on the predicted magnetic properties. It is immediately apparent (Table 4) that the minimal CAS(3,7) does not capture the magnitude and rhombicity of the experimental g-values ($g_x = 3.645$, $g_y = 2.563$, $g_z < 0.5$);[9] increasing the number of optimised states has no effect on the accuracy of these results. Significant improvement is observed upon correlating π_{Cp}-type orbitals using a RASSCF(21,30)-SO ansatz, Tables 3 and 4.

The computational cost of RASSCF calculations scales more steeply for UCp^{tt}_3 compared to $ThCp^{tt}_3$, owing to the larger RAS2 subspace required. As a result, larger active spaces become unfeasible and, in order to correlate more electrons, we resort to a RASCI-SO approach (where the orbitals are not optimised) using RASSCF(21,30) orbitals. Upon augmenting the RAS(21,30) space with U 6s and 6p (RASCI(29,34)) and U 8s (RASCI(29,35)), the g_y value is significantly improved (Table 4), indicating that the U outer core region influences in-plane magnetisation, just as it was observed for $ThCp^{tt}_3$.

Table 3: UCp^{tt}_3 active orbitals included in state-averaged CASSCF-SO/RASSCF-SO with 13 spin quartet roots and 11 spin doublet roots.

Active space	RAS1	RAS2	RAS3
CAS(3,7)	-	7×5f	-
RAS(21,30)	9×π_{Cp}	7×5f	6×π^*_{Cp}, 4×6d, 7s, 3×7p
RAS(29,34)	6s, 3×6p, 9×π_{Cp}	7×5f	6×π^*_{Cp}, 4×6d, 7s, 3×7p
RAS(29,35)	6s, 3×6p, 9×π_{Cp}	7×5f	6×π^*_{Cp}, 4×6d, 7s, 3×7p, 8s

Table 4: UCp^{tt}_3 g-values calculated from active space electronic structure data

Active space	g_x	g_y	g_z
CASSCF(3,7)	2.524	0.301	0.031
RASSCF(21,30)	4.117	1.860	0.357
RASCI(29,34)	4.020	2.241	0.403
RASCI(29,35)	4.014	2.192	0.388
Experiment[a]	3.645	2.563	< 0.5
Experiment[b]	3.050	1.650	< 0.5

[a] Crystal structure

[b] Frozen solution

4.2 Hyperfine coupling

The accuracy of theoretical HFCCs is significantly impacted by the quality of optimised molecular orbitals (MOs), as shown in previous work. State-averaged calculations of $ThCp^{tt}_3$ (Section 4.1) combine a ground state having an axial spin density distribution with 2 highly excited states (ca. $\epsilon = 15300$ cm^{-1}) having in-plane spin density distributions. Hence, it is possible that the state-averaged MOs underlying the ground state wavefunction do not provide an adequate description of ligand HFC. In order to control for this possibility, we carry out state-specific (SS) RASSCF optimisations of the ground doublet for $ThCp^{tt}_3$, Table 5, and determine ground state HFCCs using a spin-only parametrisation. Taking advantage of the larger RAS1 and RAS3 selections available due to the one-orbital RAS2 subspace, we

additionally correlate σ_{Cp}-type orbitals in SS-RASSCF(39,38), therefore allowing for spin density delocalisation over C(Cp)-C(Cp), C(Cp)-C(^{t}Bu) and C(Cp)-H(Cp) σ bonds.

Table 5: $ThCp^{tt}_3$ active orbitals included to describe the ground state in state-specific CASSCF/RASSCF.

Active space	**RAS1**	**RAS2**	**RAS3**
RASSCF(19,26)	9×π_{Cp}	6d_{z^2}	6×π^*_{Cp}, 4×6d, 2×5f, 7s, 3×7p
RASSCF(27,36)	6s, 3×6p, 9×π_{Cp}	6d_{z^2}	6×π^*_{Cp}, 4×6d, 4×5f, 7s, 3×7p, 8s
RASSCF(39,38)	6×σ_{Cp}, 6s, 3×6p, 9×π_{Cp}	6d_{z^2}	6×π^*_{Cp}, 4×6d, 7s, 7p_z, 6×σ^*_{Cp}

^{13}C HYSCORE spectra of $ThCp^{tt}_3$ simulated using HYPERION-calculated parameters are shown in Figures 2 and 3. Preliminary simulations with different subsets of nuclei reveal that the ridges observed in the $B_0 = 351.6$ mT ($g_{\|}$) spectrum at $\nu_N \pm 0.5$ MHz, $\nu_N \pm 1$ MHz and $\nu_N \pm 1.5$ MHz (where ν_N is the nuclear Larmor frequency) are due to C(Cp), 3° C(^{t}Bu) and 1° C(^{t}Bu) nuclei, respectively. None of the state-specific calculations reproduce the ridge corresponding to 3° C(^{t}Bu) and, as such, state-averaged calculations yield overall the best simulations of the $g_{\|}$ spectrum. Meanwhile, the $g_{\perp}$ spectrum is most accurately approximated by the largest state-specific calculation, SS-RASSCF(39,38), which appears to correctly reproduce the anisotropy – encoded in the ridge curvature – of ^{13}C HFC matrices. The larger state-averaged calculations, SA-RASSCF(19,27)-SO and SA-RASSCF(27,36)-SO, yield HFCCs of the correct magnitude – encoded in the ridge length – however the simulated ridges lie mostly along the anti-diagonal corresponding to the nuclear Larmor frequency.

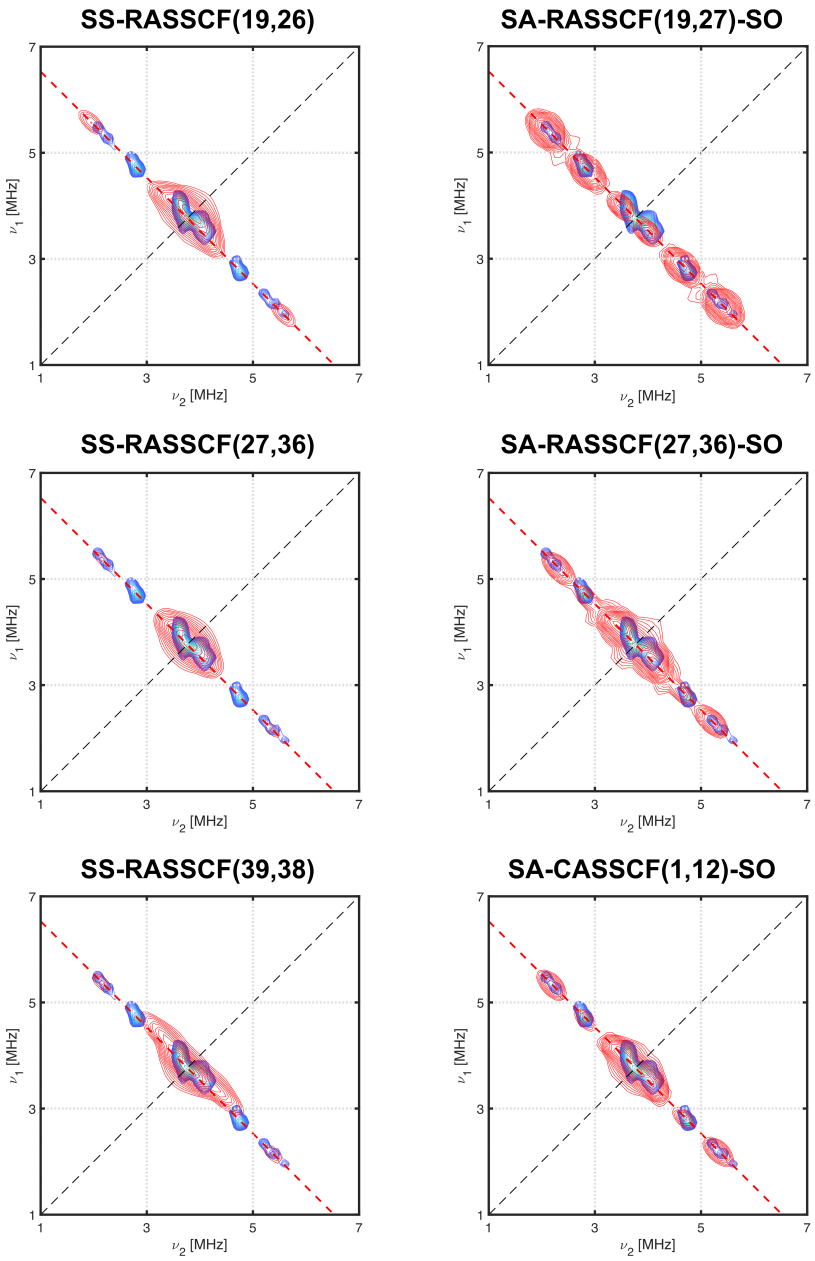

Figure 2: Experimental HYSCORE spectra in the ^{13}C region at $B_0 = 351.6$ mT ($g_\parallel$) for $ThCp_3^{tt}$ (blue contours). HYSCORE simulations (red contours) include HFC matrices of 5 representative nuclei: three C(Cp), one 3° C(^{t}Bu) and one 1° C(^{t}Bu).

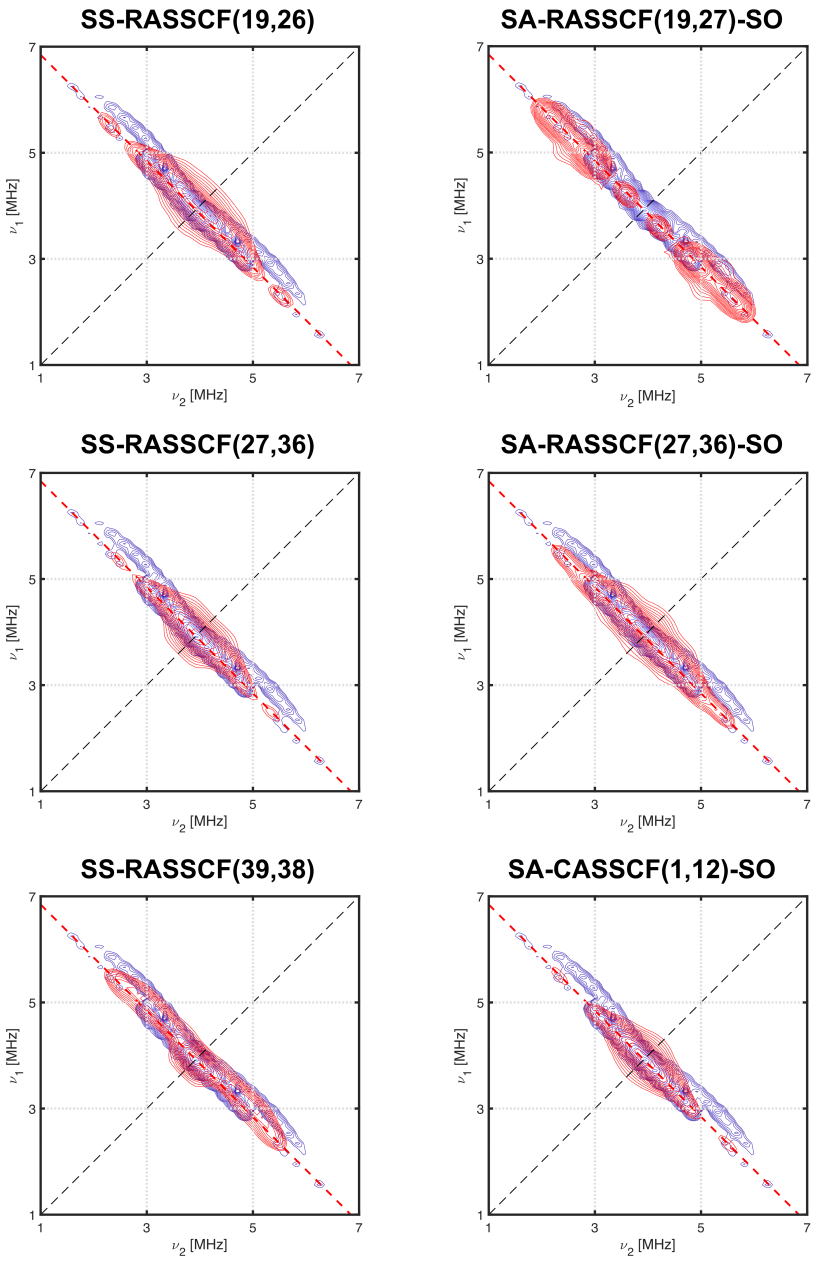

Figure 3: Experimental HYSCORE spectra in the ^{13}C region at $B_0 = 366.3$ mT ($g_\perp$) for $ThCp_3^{tt}$ (blue contours). HYSCORE simulations (red contours) include HFC matrices of 5 representative nuclei: three C(Cp), one 3° C(^{t}Bu) and one 1° C(^{t}Bu).

^{1}H HYSCORE simulations show little variation with respect to the size of the active space, hence we only show data from the largest calculations, SS-RASSCF(39,38) (Figure 4) and SA-RASSCF(27,36)-SO (Figure S6). We obtain different simulated signals depending on which subset of H(Cp) nuclei is selected; herein, labels H(Cp1), H(Cp2) and H(Cp3) indicate nuclei from different cyclopentadienyl groups. Since all simulated ridges overlap with parts of the experimental spectrum, we deduce that the frozen solution HYSCORE spectrum samples a combination of different H(Cp) and H(^{t}Bu) local environments. The central feature at $g_\perp$, corresponding to near-zero HFC, is likely caused by weakly coupled nuclei, such as those of the solvent molecule. Compared to state-specific results, state-averaged calculations result in HYSCORE signals of decreased intensity, Figure S6, displaying essentially no variation

between different cyclopentadienyl rings.

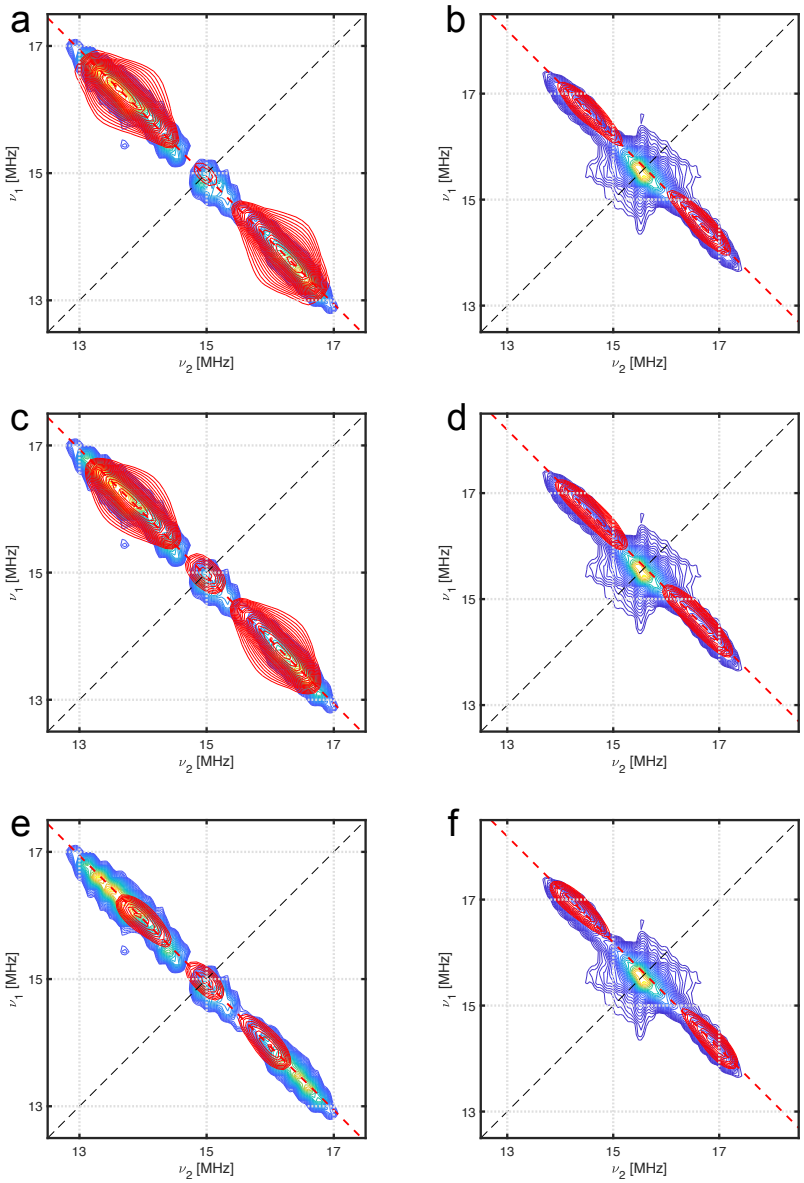

Figure 4: Experimental HYSCORE spectra in the ^{1}H region for $ThCp^{tt}_3$ (blue contours); left: $B_0 = 366.3$ mT ($g_{||}$), right: $B_0 = 351.6$ mT ($g_{\perp}$). Simulations (red contours) use EPR parameters calculated from SS-RASSCF(39,38) and include all three H(Cp) atoms from one cyclopentadienyl ring and one H(^{t}Bu) atom (H8 in the XRD structure). **a**, **b**: H(Cp1)+H(^{t}Bu); **c**, **d**: H(Cp2)+H(^{t}Bu); **e**, **f**: H(Cp3)+H(^{t}Bu)

It is instructive to compare our CASSCF(1,12)-SO simulations with the point-dipole simulations in [9], as both localise all spin density on An and hence do not include spin polarisation. The crucial point of difference is the treatment of electron spin: while Formanuik *et al* model HFC as a classical interaction between two point-like magnetic dipoles, the quantum mechanical framework employed herein implicitly involves a delocalised spin density distribution, derived from our relativistic calculations. Such theoretical aspects clearly influence $AnCp^{tt}_3$ hyperfine structure, as their inclusion allows us to capture more features of the HYSCORE spectra.

We use Mulliken spin population analysis[25] (Section S3) to quantify spin delocalisation across ligand atoms. For $ThCp_3^{tt}$, SS-RASSCF(39,38) gives Mulliken spin populations of 0.0044, 0.0089, 0.0040, -0.0003 and -0.0005 for nuclei C1-C5, respectively, and 0.0011, -0.0014 and -0.0020 for H1-H3, respectively. Note that all electronic structure calculations, other than the minimal CASSCF(1,12)-SO, yield C(Cp) spin populations with a clear C2>C1,3>C4,5 trend. Despite differences between models, the Mulliken spin populations are close to the values derived by Formanuik *et al* from ^{13}C HYSCORE: 0.010 for C2 and 0.002 for C1/C3; meanwhile, the C2 spin population of 0.014, determined from ^{1}H data, is an overestimate.

Figures 5 and 6 show ^{1}H HYSCORE simulations of UCp_3^{tt} at g_x and g_y, obtained using active space electronic structure models of increasing size. We note that set **2** simulations at g_x (Figure 5, right-hand side) start out much more diffuse than the measured signal and diminish as more An orbitals are correlated. Meanwhile, in set **1** simulations, only the features closest to ν_N show noticeable changes with active space size. Less variability is observed for the g_y orientation (Figure 6); but, despite the differences between peak positions, owing to a slight overestimation of the largest ^{1}H HFCCs, all major features of the experimental spectrum are captured.

Spin population analysis of UCp_3^{tt} is complicated by the extensive mixing between spin-free states due to strong SOC (Table S1). Herein, we focus on Mulliken spin populations derived for the fourth quartet SF state, which has the highest weighting in the ground Kramers doublet wavefunction. H(Cp) spin populations range between -0.0001 and -0.0004, regardless of active space or state, a result which is two orders of magnitude lower than the 0.019 value reported in [9]. But, given the good reproduction of the experimental HYSCORE spectra based on the relativistic multi-configurational calculations here, this discrepancy highlights the shortcomings of non-relativistic HFC models in the case of strongly SO-coupled systems: large HFCCs must be ascribed to large spin populations when the PSO term is completely neglected.

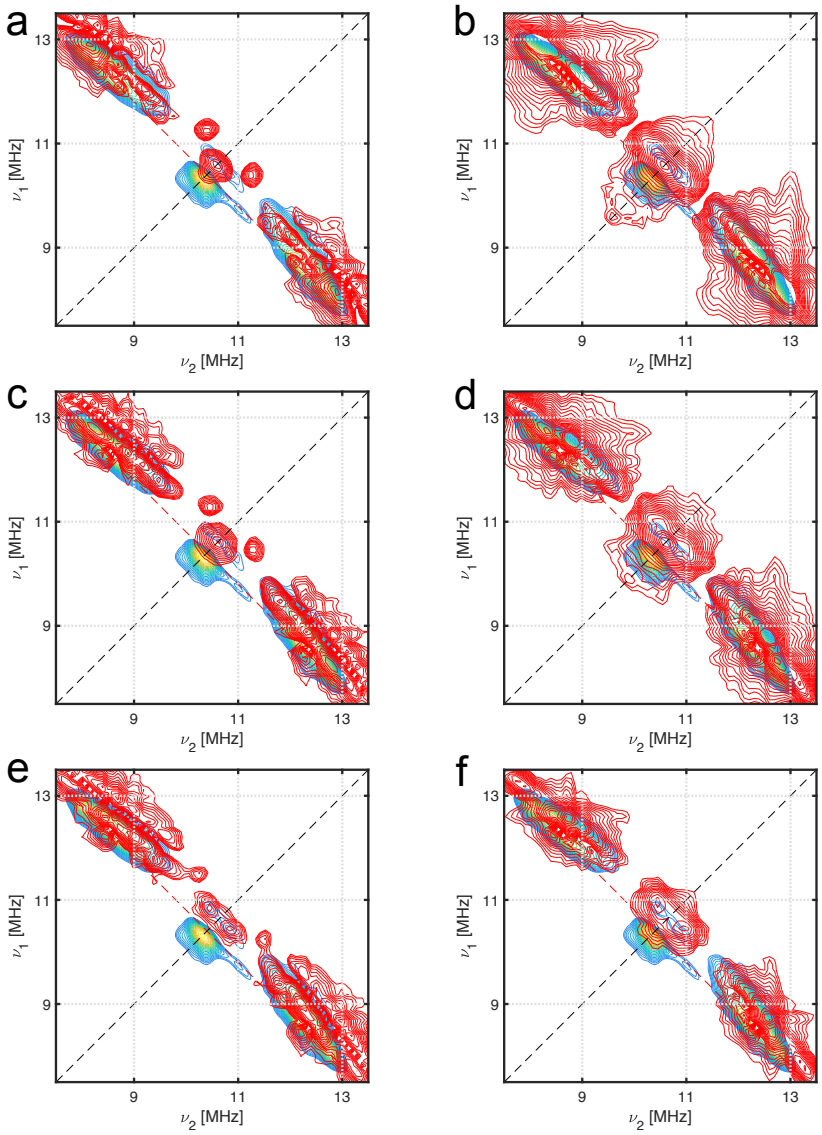

Figure 5: UCp^{tt}_3 HYSCORE spectra, ^{1}H region, $B_0 = 244.3$ mT (near g_x). Simulations (red) include H(Cp) nuclei from set **1** (left) and set **2** (right). **a**, **b**: RASSCF(21,30)-SO; **c**, **d**: RASCI(29,34)-SO; **e**, **f**: RASCI(29,35)-SO.

Although no HYSCORE signal could be measured in the ^{13}C region for UCp^{tt}_3,[9] C(Cp) spin populations from electronic structure calculations provide a useful point of comparison with $ThCp^{tt}_3$. We note that C(Cp) spin populations obtained from CASSCF(3,7)-SO differ in both magnitude and sign from the populations derived from larger calculations; however, as the minimal CASSCF-SO model fails to reproduce the magnitude and anisotropy of the UCp^{tt}_3 g-tensor, these populations are likely inaccurate. C(Cp) spin populations derived from RASCI(29,35)-SO fall between -0.0023 and -0.0038 for C1-C3; these values are in stark contrast with the positive populations of the equivalent atoms in $ThCp^{tt}_3$. Smaller spin populations, ranging from -0.0004 to -0.0014, are observed for C4- and C5-type nuclei, in line with the Th complex. It appears that, relative to a purely ionic picture, spin density transfer between Cp^{tt} and An occurs primarily via atoms at the C1, C2 and C3 positions for both complexes. Considering also the Mulliken spin populations at An, 0.96 for Th and 3.03

for U, we deduce that the $Cp^{tt} \rightarrow$ An dative bond leads to spin density transfer away from Th(III) in $ThCp_3^{tt}$ and to spin density transfer towards U(III) in UCp_3^{tt}.

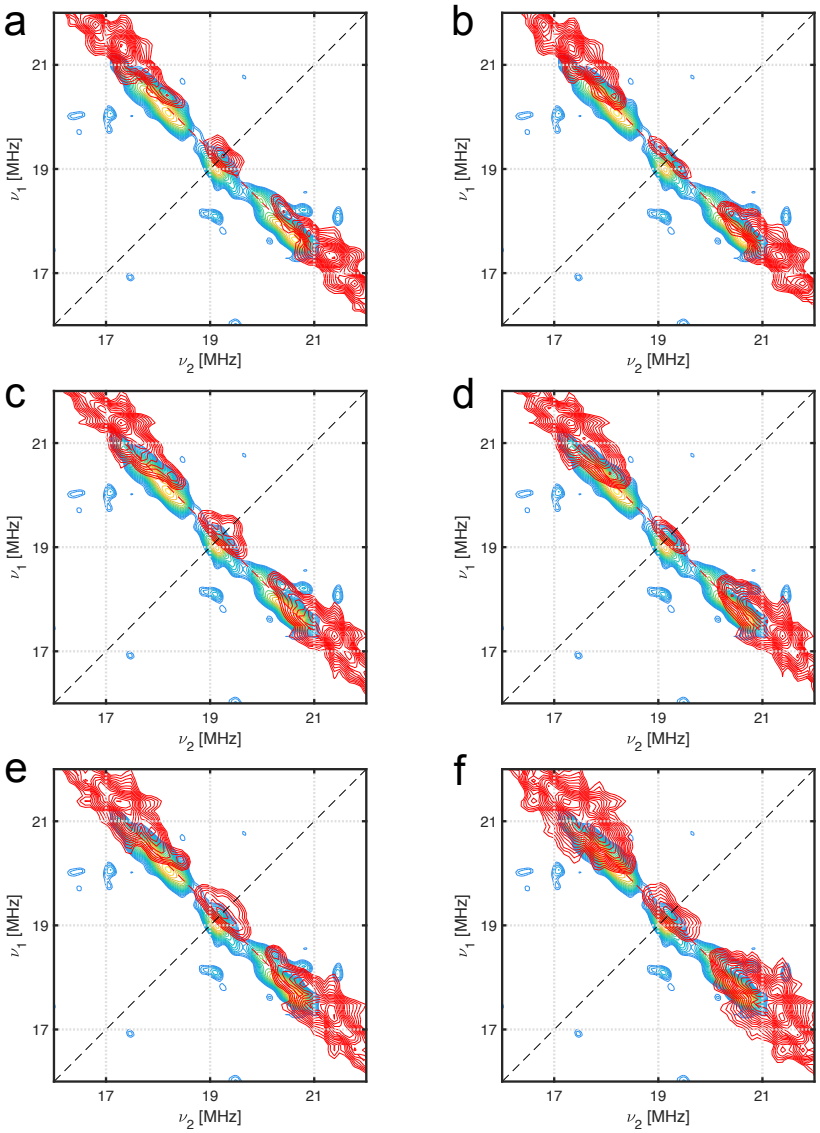

Figure 6: UCp_3^{tt} HYSCORE spectra, ^{1}H region, $B_0 = 450.4$ mT (near g_y). Simulations (red) include H(Cp) nuclei from set **1** (left) and set **2** (right). **a**, **b**: RASSCF(21,30)-SO; **c**, **d**: RASCI(29,34)-SO; **e**, **f**: RASCI(29,35)-SO.

Orbital decomposition analysis of the HFC matrices (Section S6) reveals similar patterns of pairwise orbital contributions – which are proportional to the probability of spin density transfer between orbitals – for unsubstituted C(Cp) and the H(Cp) bonded to them; compare, for example, Figures S8 and S10 (atoms C2 and H1) and Figures S9 and S11 (atoms C4 and H2). The orbital decomposition diagram for out-of-plane unsubstituted C(Cp) (C4) features weaker pairwise terms relative to out-of-plane substituted C(Cp) (C1, Figure S7) and in-plane C(Cp) (C2, Figure S8); this is consistent with our observations from Mulliken spin population analysis.

For $ThCp_3^{tt}$, C(Cp) and H(Cp) HFC matrices appear to be dominated by Cp $\pi_2 \rightarrow$ Cp π_3^* and

Cp $\pi_2 \rightarrow$ Th 6d excitations. Herein, we have used π_1, π_2 and π_3^* to label the valence π-type MOs of the cyclopentadienyl groups based on the number of nodal planes, which, according to MO theory, determines the MO energy; although our electronic structure approach is more complex than basic MO theory, this is a useful strategy to classify the 9 bonding π_{Cp} MOs ($3 \times \pi_1$ and $6 \times \pi_2$) and the 6 anti-bonding π^*_{Cp} MOs (all π_3^*). Some Cp $\pi_1 \rightarrow$ Cp π_3^* and Th $6p_{x,y} \rightarrow$ Cp π_3^* contributions are observed for the in-plane atoms (C2, Figure S8, and H1, Figure S10), however as our calculations yield strongly hybridised Th $6p_{x,y}$–Cp π_1 MOs, both types of contributions are likely due to interactions between ligand atoms. The inclusion of σ_{Cp} and σ^*_{Cp} MOs in SS-RASSCF(39,38) has a significant impact, with $\sigma_{Cp} \rightarrow \sigma^*_{Cp}$ excitations manifesting as strong contributions to the HFC matrices of C1, C2 and H1 (Figures S7, S8 and S10, respectively). In future work, it would be beneficial to also investigate σ_{Cp} correlation effects in UCp^{tt}_3, perhaps using multiconfigurational techniques that can accommodate larger active spaces.[26–30]

The orbital decomposition diagrams for C(Cp) and H(Cp) in UCp^{tt}_3 are overall more sparse than their $ThCp^{tt}_3$ equivalents, particularly in the case of C(Cp). Metal-ligand spin density transfer appears to occur mainly via Cp $\pi_2 \rightarrow$ U 6d excitations. Unlike the Th complex, we observe strong U $6p_{x,y} \rightarrow 7p_{x,y}$ pairwise contributions in the orbital decompositions for C1, C2 and H1, i.e. the positions in the cyclopentadienyl ring associated with the largest spin populations. We note that Hyperion's orbital decomposition scheme only takes into account the spin-dependent (FC+SD) part of the HFC operator, therefore the (likely significant) PSO interactions are not included in this breakdown.

5 Conclusions

We employed active space electronic structure techniques, together with the recently-developed Hyperion program, to derive relativistic g-tensors and relativistic hyperfine coupling parameters for two $AnCp^{tt}_3$ complexes, which were previously characterised by Formanuik *et al* using experimental pulsed EPR techniques. Simulated HYSCORE spectra based on the calculated parameters were then used to benchmark our electronic structure calculations against experiment.

We modelled electron correlation and spin-orbit coupling effects on the electronic structure and on magnetic properties of $AnCp^{tt}_3$, and discussed the influence of various parameters, such as active space composition, number of optimised electronic states and state-

averaging molecular orbitals. We showed that good predictions of ligand HFCCs can be obtained from a fairly minimal electronic structure model, provided that relativity is accounted for, and that the non-relativistic interpretation of HFC is unreliable, particularly when SOC is strong. Based on theoretical g-tensor determinations, we uncovered a link between spin polarisation of C(Cp) atoms, modelled using an expanded active space, and in-plane magnetisation. Additionally, we showed that the most accurate HYSCORE simulations for $ThCp^{tt}_3$ require a state-specific electronic structure model for the $g_\perp$ spectrum and a state-averaged model for the $g_\parallel$ spectrum.

Finally, to gain insight into An-ligand bonding and the extent of covalency, we employed Mulliken spin population analysis, which showed that the two $AnCp^{tt}_3$ complexes differ in the direction of spin density transfer between An and the Cp^{tt} ligands. The extent of spin delocalisation appears to be diminished for the U complex, with only C(Cp) atoms having spin populations significantly different from zero. By contrast, spin polarisation in $ThCp^{tt}_3$ extends as far as H(Cp), for which spin populations are the same order of magnitude as C(Cp) spin populations. Although they are not a direct measure of An covalency, the effects on H(Cp) show that spin populations beyond the first coordination sphere can be affected by the ligating metal and, as such, empirical parameters derived from bare radicals have limited applicability.

Mulliken spin populations on the An atoms suggest that actinide covalency is slightly stronger in the Th complex, which is the opposite conclusion to the study by Formanuik *et al.* However, we ascribe covalency to a deviation of ± 0.04 from the spin population in the idealised ionic bonding model; this minuscule difference, coupled with the well-known basis set dependence of the Mulliken population scheme,[31] indicates that further evidence is required to support our conclusion.

One possible avenue for improvement is to complement the Mulliken analysis presented herein with other spin density partitioning schemes: formalisms such as Löwdin,[32] Hirshfeld,[33] natural population analysis (NPA),[34] quantum theory of atoms in molecules (QTAIM)[35] and LoProp,[36] although primarily used for charge density analysis, are also applicable to spin density. Note, however, that spin populations determined via different partitioning schemes display noticeable differences, as shown by Neese;[37] hence, it is possible that employing multiple formalisms will introduce confusion, rather than clarity.

Overall, the phenomenon of actinide covalency is by far too complex to be accurately quantified by a single number. It is therefore important to verify observations regarding actinide covalency by using multiple experimental and theoretical techniques, as well as extending the study to cover a larger set of complexes, which shall constitute the subject of future work.

Supplementary Information

S1 Signs of pseudospin HFCCs

Although sign information is lost when modelling HFC using a pseudospin Hamiltonian, the signs of HFCCs influence HYSCORE simulations. We therefore developed a methodology for approximating HFCC signs in order to obtain simulated HYSCORE spectra that can be compared to experimental measurements. This method is implemented as an extension to the Hyperion package.

As shown in equation (1) from the main text, the HFC operator can be split into a spin-dependent FC+SD contribution and a spin-independent PSO contribution; partial HFCCs are obtained by replacing the full HFC operator in equation (6) with either the FC+SD part or the PSO part. Note that, since this method ignores any cross terms, the partial HFCCs do not add up to the total HFCCs; nevertheless, in practice, the cross terms are relatively small.

It is therefore possible to deduce the relative signs of the partial and the total HFCCs by comparing magnitudes. This is the first approximation in our methodology, as the three sets of HFCCs are defined with respect to different sets of main axes. To minimise the error introduced in this step, HFCCs to be compared are grouped in a way that maximises the overlap between their corresponding eigenvectors.

In the following step, we take advantage of the *a posteriori* inclusion of SOC in our chosen electronic structure approach, drawing parallels between spin-only (signed) HFCCs derived from CASSCF/RASSCF and pseudospin HFCCs derived from CASSCF-SO/RASSCF-SO. This is done by rotating the FC+SD spin-only tensor, $\boldsymbol{a}^{\text{FC+SD}}_{\text{spin-only};(\mathbf{x},\mathbf{y},\mathbf{z})}$, from the molecular frame $(\mathbf{x},\mathbf{y},\mathbf{z})$ into the eigenframe $(\mathbf{e}_{\mathcal{S},1},\mathbf{e}_{\mathcal{S},2},\mathbf{e}_{\mathcal{S},3})$ of the FC+SD pseudospin tensor:

$$\boldsymbol{a}^{\text{FC+SD}}_{\text{spin-only};\mathcal{S}} = \begin{pmatrix} \mathbf{e}_{\mathcal{S},1} & \mathbf{e}_{\mathcal{S},2} & \mathbf{e}_{\mathcal{S},3} \end{pmatrix} \boldsymbol{a}^{\text{FC+SD}}_{\text{spin-only};(\mathbf{x},\mathbf{y},\mathbf{z})} \begin{pmatrix} \mathbf{e}_{\mathcal{S},1} \\ \mathbf{e}_{\mathcal{S},2} \\ \mathbf{e}_{\mathcal{S},3}. \end{pmatrix} \tag{S1}$$

The signs of the diagonal elements of $\boldsymbol{a}^{\text{FC+SD}}_{\text{spin-only};\mathcal{S}}$ are then assigned to the FC+SD pseudospin HFCCs - in the limit of equivalence between the spin-only and pseudospin parametrisations, this becomes exact. Signs for the total pseudospin HFCCs are obtained by combining the relative sign information inferred in the first step with the absolute signs of the FC+SD

eigenvalues deduced in the second step.

The second approximation underlying our methodology is therefore introduced by the forced equivalence between a spin-only multiplet and the set of SO-coupled states forming the pseudospin multiplet. This is, of course, inexact since a SO state is a superposition of multiple spin-free states. Moreover, results depend on which spin-free state is chosen for the comparison. Fortunately, we find this strategy to be straightforward when applied to the $AnCp_3^{tt}$ complexes investigated in this work. $ThCp_3^{tt}$ is, to a good approximation, a $6d^1$ doublet and as such, there is a natural correspondence between the lowest energy spin-free state and the lowest-energy SO state. In the case of UCp_3^{tt}, the ground Kramers doublet has a predominant spin quartet character (see Section S1) and we find that applying our strategy using any of the 13 spin-free quartet states considered herein yields consistent results for all ligand HFCCs studied.

S2 SO states of UCp_3^{tt}

Table S1: Composition of the lowest-energy Kramers doublet (SO states 1 and 2) of UCp_3^{tt} in terms of quartet SF states. SF state indices are assigned in order of increasing energy, such that SF state 1 is the lowest-energy quartet SF state. Note that only the lowest 6 quartet SF states make significant contributions to the ground Kramers doublet in all calculations, and that SF state 4 has the most significant contribution in all calculations that include ligand correlation effects.

	SO state 1		SO state 2	
Calculation	**SF state**	**Weight (%)**	**SF state**	**Weight (%)**
CASSCF(3,7)-SO	1	16.65	1	16.65
	2	15.61	2	15.61
	3	14.91	3	14.91
	4	14.47	4	14.47
	5	12.98	5	12.98
RASSCF(21,30)-SO	4	23.42	4	23.42
	5	20.60	5	20.60
	6	12.39	6	12.39
	3	11.61	3	11.61
	2	9.52	2	9.52
RASCI(29,34)-SO	4	23.66	4	23.66
	5	20.91	5	20.91
	6	14.08	6	14.08
	3	10.48	3	10.48
	2	8.49	2	8.49

Calculation	SO state 1 SF state	SO state 1 Weight (%)	SO state 2 SF state	SO state 2 Weight (%)
RASCI(29,35)-SO	4	23.49	4	23.49
	5	20.57	5	20.57
	6	13.61	6	13.61
	3	10.63	3	10.63
	2	8.95	2	8.95

S3 Mulliken spin population analysis

Table S2: Mulliken spin populations of $ThCp^{tt}_3$ atoms. Columns **a**-**f** correspond to electronic structure calculations; **a**: SA-CASSCF(1,12)-SO; **b**: SS-RASSCF(19,26); **c**: SA-RASSCF(19,27)-SO; **d**: SS-RASSCF(27,36); **e**: SA-RASSCF(27,36)-SO; **f**: SS-RASSCF(39,38). Atom labels are consistent with the crystal structure reported in reference [9]. For the 1°C(^{t}Bu) and H(^{t}Bu) atom groups, the minimum and maximum spin populations are reported. Atoms C26 and H8 are included in the HYSCORE simulations reported in the main text, while H41 is the H(^{t}Bu) atom closest to the Th center.

Atom	a	b	c	d	e	f
Th	0.9367	0.9784	0.9674	0.9625	0.9574	0.9617
C(Cp1)						
C1	0.0073	0.0037	0.0038	0.0051	0.0052	0.0044
C2	0.0074	0.0092	0.0107	0.0083	0.0090	0.0089
C3	0.0071	0.0034	0.0035	0.0047	0.0046	0.0040
C4	0.0013	-0.0022	-0.0016	-0.0009	-0.0006	-0.0003
C5	0.0012	-0.0025	-0.0019	-0.0012	-0.0008	-0.0005
C(Cp2)						
C14	0.0072	0.0035	0.0035	0.0049	0.0049	0.0042
C15	0.0079	0.0099	0.0115	0.0090	0.0097	0.0095
C16	0.0077	0.0041	0.0042	0.0053	0.0054	0.0046
C17	0.0014	-0.0016	-0.0010	-0.0006	-0.0002	0.0000
C18	0.0012	-0.0027	-0.0022	-0.0013	-0.0010	-0.0006
C(Cp3)						
C27	0.0075	0.0042	0.0044	0.0055	0.0054	0.0047
C28	0.0072	0.0091	0.0106	0.0082	0.0089	0.0087
C29	0.0062	0.0023	0.0024	0.0038	0.0038	0.0032
C30	0.0012	-0.0025	-0.0020	-0.0011	-0.0008	-0.0005
C31	0.0013	-0.0022	-0.0015	-0.0010	-0.0006	-0.0003
3°C(^{t}Bu)						
C6	-0.0002	-0.0004	-0.0002	-0.0003	-0.0002	-0.0003
C10	-0.0002	-0.0004	-0.0002	-0.0003	-0.0002	-0.0003
C19	-0.0004	-0.0006	-0.0004	-0.0005	-0.0004	-0.0005
C23	-0.0004	-0.0006	-0.0005	-0.0005	-0.0004	-0.0005
C32	-0.0003	-0.0004	-0.0003	-0.0004	-0.0003	-0.0004
C36	-0.0002	-0.0004	-0.0003	-0.0003	-0.0003	-0.0003

Atom	a	b	c	d	e	f
H(Cp1)						
H1	0.0010	0.0011	0.0011	0.0011	0.0010	0.0011
H2	-0.0014	-0.0017	-0.0016	-0.0014	-0.0014	-0.0014
H3	-0.0020	-0.0024	-0.0022	-0.0020	-0.0019	-0.0020
H(Cp2)						
H22	0.0011	0.0011	0.0011	0.0011	0.0010	0.0011
H23	-0.0011	-0.0014	-0.0013	-0.0011	-0.0012	-0.0011
H24	-0.0019	-0.0023	-0.0021	-0.0019	-0.0018	-0.0019
H(Cp3)						
H43	0.0009	0.0010	0.0010	0.0009	0.0009	0.0009
H44	-0.0015	-0.0017	-0.0017	-0.0014	-0.0015	-0.0014
H45	-0.0016	-0.0020	-0.0019	-0.0016	-0.0016	-0.0016
1°C(^{t}Bu)						
C26	0.0003	0.0001	0.0002	0.0001	0.0002	0.0001
min	0.0000	-0.0001	-0.0001	-0.0001	-0.0001	-0.0001
max	0.0005	0.0004	0.0005	0.0003	0.0004	0.0004
H(^{t}Bu)						
H8	-0.0003	-0.0004	-0.0004	-0.0003	-0.0003	-0.0003
H41	-0.0012	-0.0013	-0.0012	-0.0012	-0.0011	-0.0012
min	-0.0012	-0.0013	-0.0012	-0.0012	-0.0011	-0.0012
max	0.0003	0.0003	0.0002	0.0003	0.0003	0.0001

Table S3: Mulliken spin populations of UCp^{tt}_3 atoms, as determined from CASSCF(3,7)-SO.

Atom	SF state 1	SF state 2	SF state 3	SF state 4	SF state 5	SF state 6
U	2.9780	2.9746	2.9744	2.9677	2.9675	2.9671
C(Cp1)						
C1	0.0015	0.0016	0.0019	0.0020	0.0024	0.0021
C2	0.0014	0.0011	0.0015	0.0012	0.0011	0.0012
C3	0.0014	0.0015	0.0018	0.0020	0.0024	0.0023
C4	0.0015	0.0020	0.0016	0.0029	0.0023	0.0027
C5	0.0016	0.0020	0.0018	0.0027	0.0025	0.0024
C(Cp2)						
C14	0.0016	0.0014	0.0021	0.0018	0.0023	0.0021
C15	0.0014	0.0013	0.0013	0.0013	0.0010	0.0011
C16	0.0014	0.0014	0.0021	0.0020	0.0023	0.0023
C17	0.0015	0.0017	0.0019	0.0020	0.0030	0.0026
C18	0.0015	0.0017	0.0019	0.0018	0.0029	0.0027
C(Cp3)						
C27	0.0014	0.0022	0.0012	0.0026	0.0018	0.0022
C28	0.0013	0.0014	0.0009	0.0009	0.0011	0.0011
C29	0.0016	0.0022	0.0013	0.0025	0.0019	0.0019
C30	0.0016	0.0019	0.0020	0.0028	0.0024	0.0026
C31	0.0015	0.0018	0.0020	0.0029	0.0024	0.0027
H(Cp1)						
H1	0.0000	-0.0001	0.0000	0.0000	0.0000	0.0000
H2	-0.0001	-0.0001	-0.0001	-0.0001	0.0000	0.0000
H3	-0.0001	-0.0001	-0.0001	0.0000	0.0000	0.0000
H(Cp2)						
H22	-0.0001	0.0000	-0.0001	0.0000	0.0000	0.0000
H23	-0.0001	-0.0001	-0.0001	-0.0001	0.0000	-0.0001
H24	-0.0002	-0.0001	-0.0001	0.0000	-0.0001	0.0000
H(Cp3)						
H43	-0.0001	0.0000	-0.0001	0.0000	0.0000	0.0000
H44	-0.0001	-0.0001	-0.0001	0.0000	-0.0001	0.0000
H45	-0.0001	-0.0001	-0.0001	0.0000	-0.0001	-0.0001

Table S4: Mulliken spin populations of UCp_3^{tt} atoms, as determined from RASCI(29,35)-SO.

Atom	SF state 1	SF state 2	SF state 3	SF state 4	SF state 5	SF state 6
U	3.0474	3.0430	3.0429	3.0332	3.0332	3.0336
C(Cp1)						
C1	-0.0034	-0.0038	-0.0031	-0.0032	-0.0043	-0.0031
C2	-0.0023	-0.0031	-0.0017	-0.0031	-0.0028	-0.0032
C3	-0.0039	-0.0039	-0.0034	-0.0034	-0.0034	-0.0018
C4	-0.0033	-0.0016	-0.0036	-0.0010	-0.0004	-0.0013
C5	-0.0027	-0.0016	-0.0029	-0.0009	-0.0004	-0.0016
C(Cp2)						
C14	-0.0030	-0.0041	-0.0019	-0.0028	-0.0033	-0.0026
C15	-0.0026	-0.0026	-0.0032	-0.0038	-0.0025	-0.0040
C16	-0.0033	-0.0042	-0.0020	-0.0023	-0.0034	-0.0021
C17	-0.0031	-0.0026	-0.0023	-0.0007	-0.0020	-0.0010
C18	-0.0034	-0.0028	-0.0025	-0.0014	-0.0021	-0.0002
C(Cp3)						
C27	-0.0037	-0.0017	-0.0048	-0.0031	-0.0013	-0.0033
C28	-0.0022	-0.0021	-0.0030	-0.0030	-0.0038	-0.0021
C29	-0.0033	-0.0023	-0.0046	-0.0035	-0.0026	-0.0049
C30	-0.0025	-0.0024	-0.0013	-0.0006	0.0000	-0.0009
C31	-0.0033	-0.0034	-0.0016	-0.0004	-0.0011	-0.0014
H(Cp1)						
H1	-0.0002	-0.0002	-0.0001	-0.0001	-0.0002	-0.0001
H2	-0.0004	-0.0003	-0.0003	-0.0002	-0.0003	-0.0002
H3	-0.0003	-0.0002	-0.0002	-0.0001	-0.0001	-0.0001
H(Cp2)						
H22	-0.0002	-0.0001	-0.0003	-0.0002	-0.0001	-0.0002
H23	-0.0004	-0.0004	-0.0003	-0.0002	-0.0003	-0.0003
H24	-0.0004	-0.0003	-0.0004	-0.0002	-0.0001	-0.0001
H(Cp3)						
H43	-0.0002	-0.0002	-0.0002	-0.0002	-0.0002	-0.0001
H44	-0.0004	-0.0003	-0.0004	-0.0002	-0.0001	-0.0002
H45	-0.0003	-0.0003	-0.0002	-0.0001	-0.0001	-0.0002

S4 Principal directions of the theoretical g-tensors

Herein we show the orientation of the calculated g-tensor principal axes with respect to the molecular structure of $ThCp^{tt}_3$, Figure S1, and UCp^{tt}_3, Figure S2. Note that the state-specific (SS) calculations on $ThCp^{tt}_3$ yield three isotropic g-values ($g = 2$) and hence the resulting principal axes follow the molecular reference frame directions. In this case, a straightforward correspondence between theoretical and experimental g-values does not exist. Nevertheless, for the HYSCORE simulations presented in this work, we assign the experimental $g_{\|}$ value to the direction that lies closest to the pseudo-C_3 axis, which is consistent with the results of state-averaged calculations.

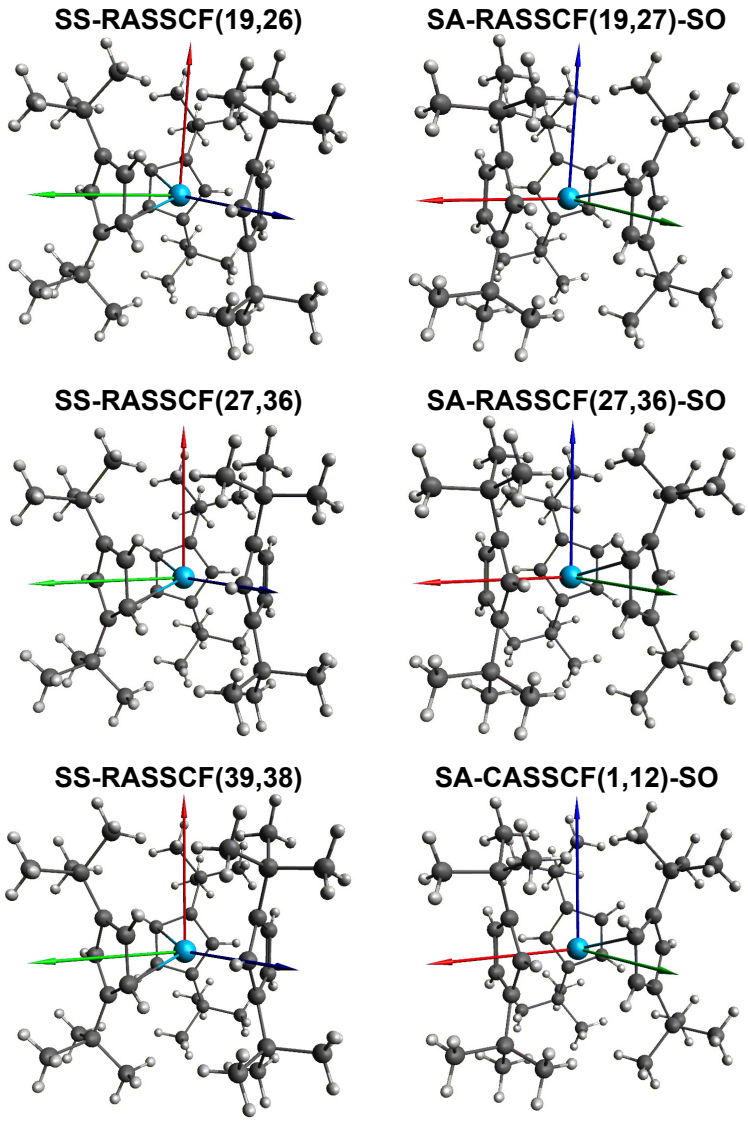

Figure S1: Principal axes for the g-tensor of $ThCp^{tt}_3$, as calculated via HYPERION from electronic structure data. Axes corresponding to g_x and g_y (i.e. $g_{\perp}$) are shown in red and green, respectively. The blue axis corresponds to g_z ($g_{\|}$).

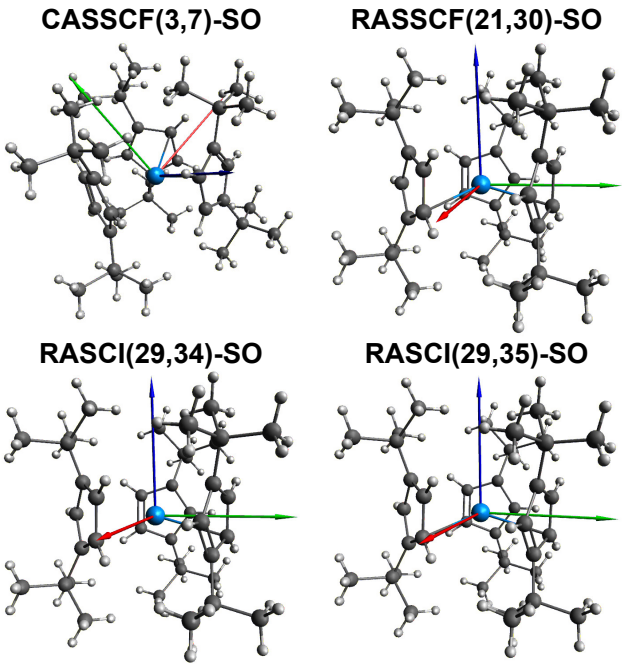

Figure S2: Principal axes for the g-tensor of UCp^{tt}_3, as calculated via Hyperion from electronic structure data. Axes corresponding to g_x, g_y and g_z are shown in red, green and blue, respectively.

S5 Additional HYSCORE simulations

S5.1 Choice of representative nuclei

At the the most general level, HFC strength, as measured by HFCCs, is determined by the spin density at the magnetic nucleus of interest – usually quantified by the spin population – and by the distance from the paramagnetic center (here, the An atom). We use these criteria to choose a small number of representative nuclei from the $AnCp^{tt}_3$ XRD structures; HFC parameters for these nuclei are then included in HYSCORE simulations. In both complexes, the largest Mulliken spin populations are associated with C(Cp) and H(Cp) atoms, which are therefore expected to make the most significant contribution to the ^{13}C and ^{1}H HYSCORE spectra, respectively. For UCp^{tt}_3, only ^{1}H HYSCORE experimental data is available, and we use the U-H(Cp) distances calculated from the XRD coordinates to define two sets of 6 representative H(Cp) nuclei, as described in the Computational details section of the main text.

The increased computational cost of HYSCORE simulations for $ThCp^{tt}_3$, particularly ^{13}C HYSCORE, precludes selections of more than 5 nuclei; hence, more complex selection criteria are needed. Due to the axially-symmetric g-values of $ThCp^{tt}_3$, we assert that equivalent nuclei associated with different cyclopentadienyl rings give rise to similar HYSCORE features. In practice, this assertion only proves true for state-averaged results; EPR parameters

from state-specific calculations yield subtly different HYSCORE signals for the three Cp^{tt} groups in the solid-state unit cell. The differences are most pronounced for ^{13}C spectra obtained from SS-RASSCF(39,38) results, Figures S3 and S4. Overall, the best agreement with experiment is observed for simulations with Cp1 nuclei, which we henceforth consider representative of C(Cp) HFC in frozen solution.

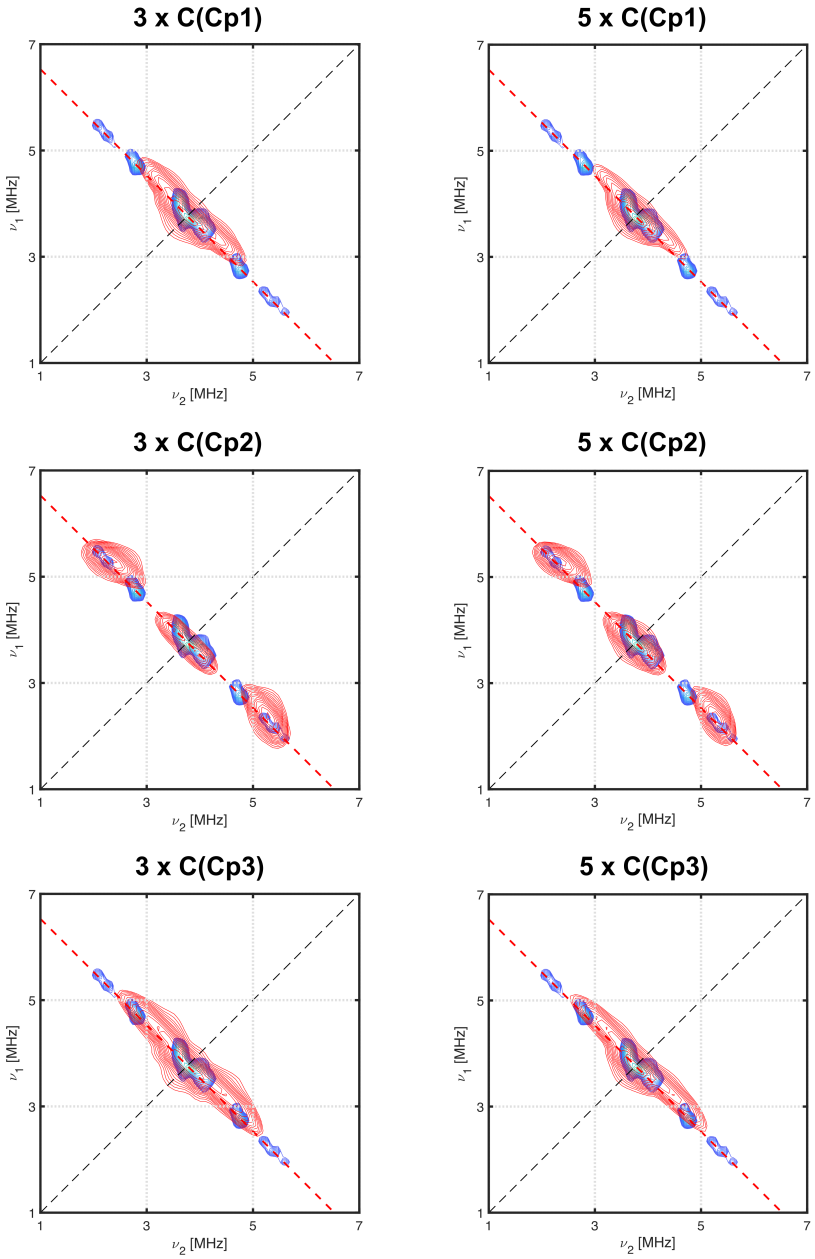

Figure S3: Experimental HYSCORE spectra (blue contours) in the ^{13}C region for $ThCp^{tt}_3$, measured at $B_0 = 351.6$ mT ($g_{\parallel}$). Simulations (red contours) use EPR parameters calculated from SS-RASSCF(39,38); only parameters for selected C(Cp) nuclei are included in the HYSCORE simulation.

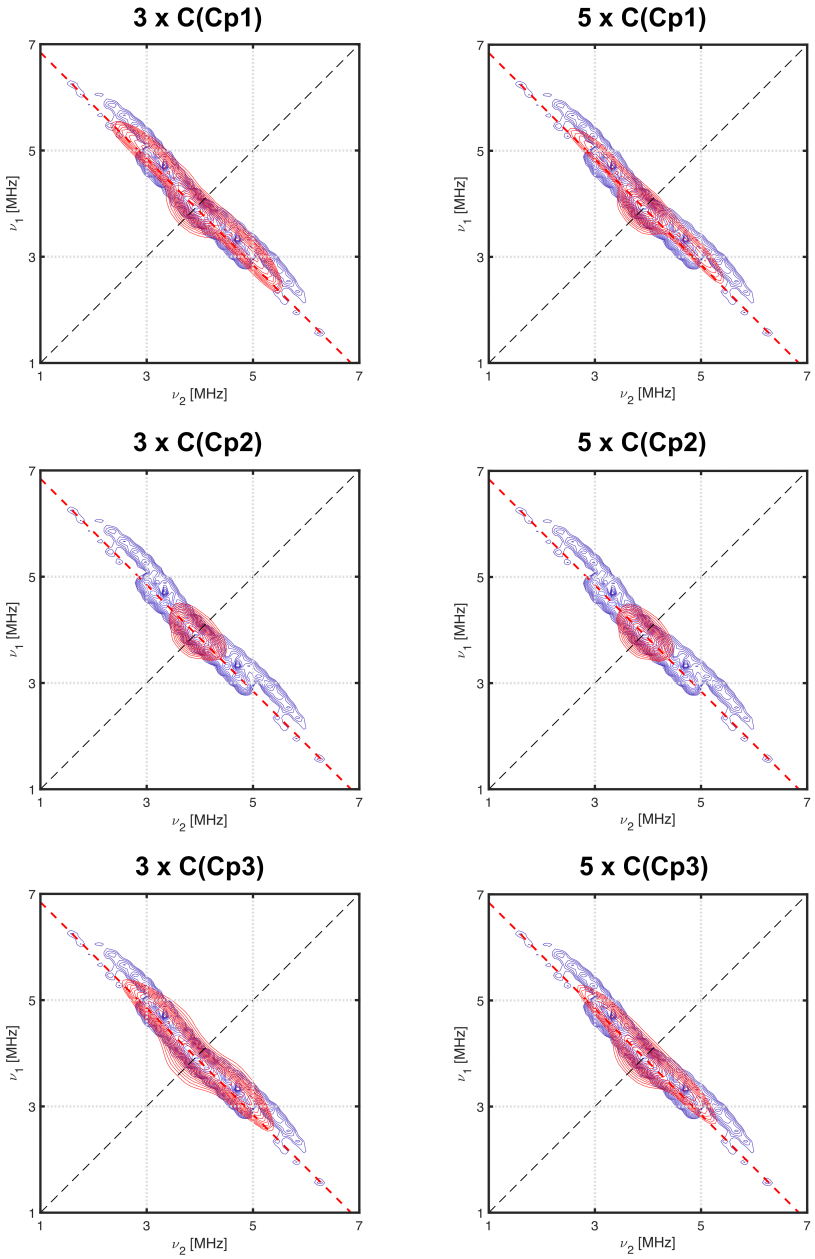

Figure S4: Experimental HYSCORE spectra (blue contours) in the ^{13}C region for ThCp$^{tt}_3$, measured at $B_0 = 366.3$ mT ($g_\perp$). Simulations (red contours) use EPR parameters calculated from SS-RASSCF(39,38); only parameters for selected C(Cp) nuclei are included in the HYSCORE simulation.

In addition to splitting ligand nuclei by Cp^{tt} group, we also investigate selections of three C(Cp), with one in-plane nucleus (C2-type), one out-of-plane substituted nucleus (C1/C3-type) and one out-of-plane unsubstituted nucleus (C4/C5-type). The omission of two C(Cp) nuclei appears to have a minor impact – a slight decrease in intensity – on the simulated HYSCORE spectra, and we conclude that the $3\times$C(Cp1) simulation provides the best balance between computational cost and accuracy. To complete the set of representative ^{13}C nuclei, we additionally include one tertiary C(^{t}Bu) from the Cp1 group (C6) and one primary C(^{t}Bu) (C26); both are selected based on their distance from Th in the crystal structure.

We use a similar strategy to select a set of ^{1}H nuclei, comprising three H(Cp) from one Cp^{tt} group and one H(^{t}Bu). However, HYSCORE simulations that include atom H41, having the smallest Th-H(^{t}Bu) distance, result in unusually intense HYSCORE features, as well as poor agreement with the spectrum measured at $g_\perp$ (Figure S5). This is most likely a consequence of the uncharacteristically large spin population associated with H41 (Table S2); it is unclear whether this is a limitation of the minimal basis used for H(^{t}Bu) in our electronic structure calculations, or whether such high spin densities are a feature of the crystal structure, but are not prevalent in frozen solution. Nevertheless, we observe significant improvement in the accuracy of HYSCORE simulations (Figures 4 and S6) upon replacing HFC parameters of H41 with those calculated for H8, which has a Mulliken spin population closer to typical H(^{t}Bu) values.

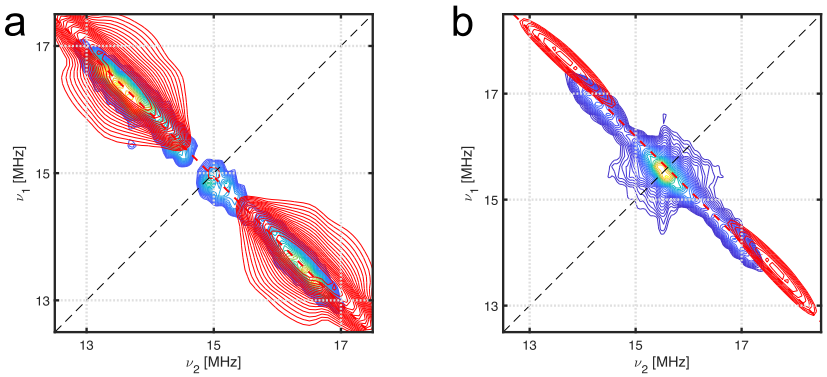

Figure S5: Experimental HYSCORE spectra in the ^{1}H region for ThCp$^{tt}_3$ (blue contours); **a**: $B_0 = 351.6$ mT ($g_\parallel$), **b**: $B_0 = 366.3$ mT ($g_\perp$). Simulations (red contours) use EPR parameters calculated from SS-RASSCF(39,38) and include all three H(Cp1) atoms and the H(^{t}Bu) atom lying closest to the Th center in the XRD structure (H41).

S5.2 ^{1}H HYSCORE spectra from state-averaged ThCp$_3^{tt}$ calculations

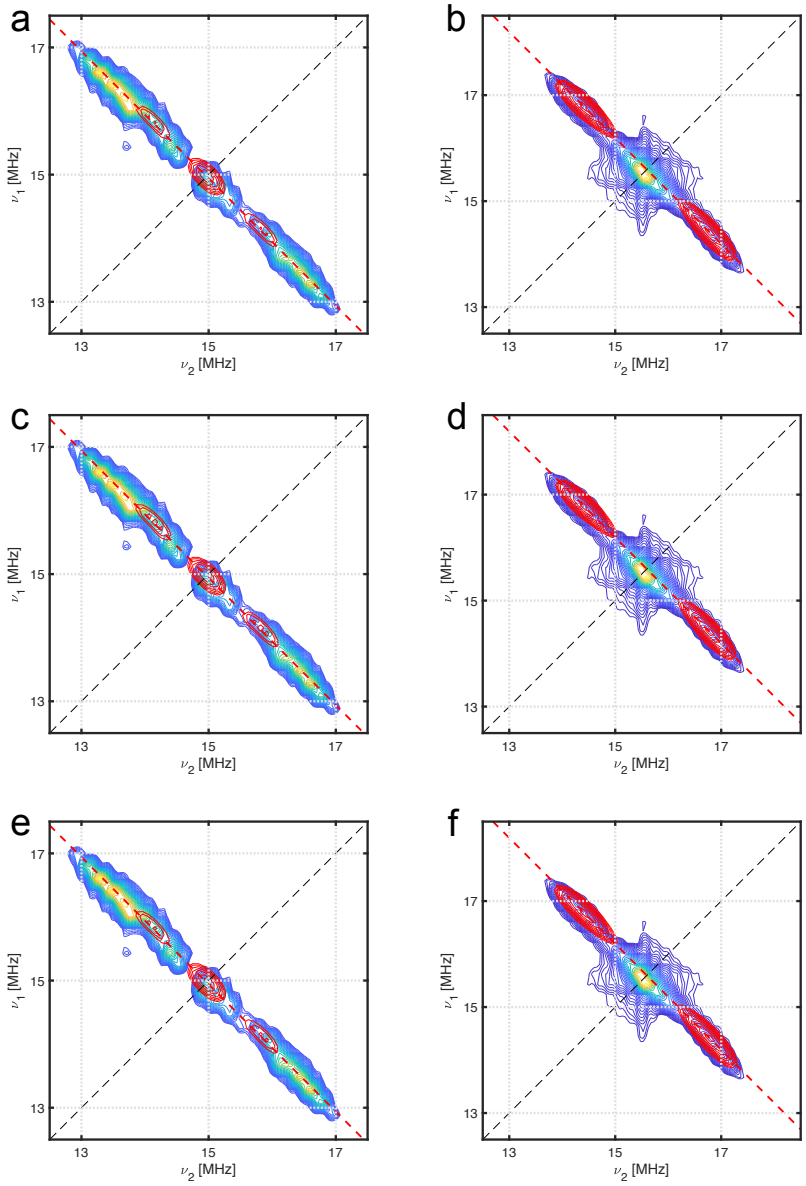

Figure S6: Experimental HYSCORE spectra in the ^{1}H region for ThCp$_3^{tt}$ (blue contours); left: $B_0 = 351.6$ mT ($g_{\parallel}$), right: $B_0 = 366.3$ mT ($g_{\perp}$). Simulations (red contours) use EPR parameters calculated from SA-RASSCF(27,36)-SO and include all three H(Cp) atoms from one cyclopentadienyl ring and one H(^{t}Bu) atom (H8 in the XRD structure). **a**, **b**: H(Cp1)+H(^{t}Bu); **c**, **d**: H(Cp2)+H(^{t}Bu); **e**, **f**: H(Cp3)+H(^{t}Bu)

S6 Orbital decomposition analysis

Below, we show HFC orbital decomposition diagrams generated by Hyperion for ligand atoms representative of different C(Cp) and H(Cp) local environments within $AnCp_3^{tt}$. The vertices represent RASSCF-optimised MOs, which are linear combinations of AOs from all atoms in $AnCp_3^{tt}$. As such, their labels are only approximate, as they represent an idealised picture where there is no mixing between An and ligand MOs. Although most labels could be unambiguously assigned, we observe strong mixing between Th $6p_{x,y}$ and Cp π_1 orbitals, which may complicate the interpretation of the orbital decomposition.

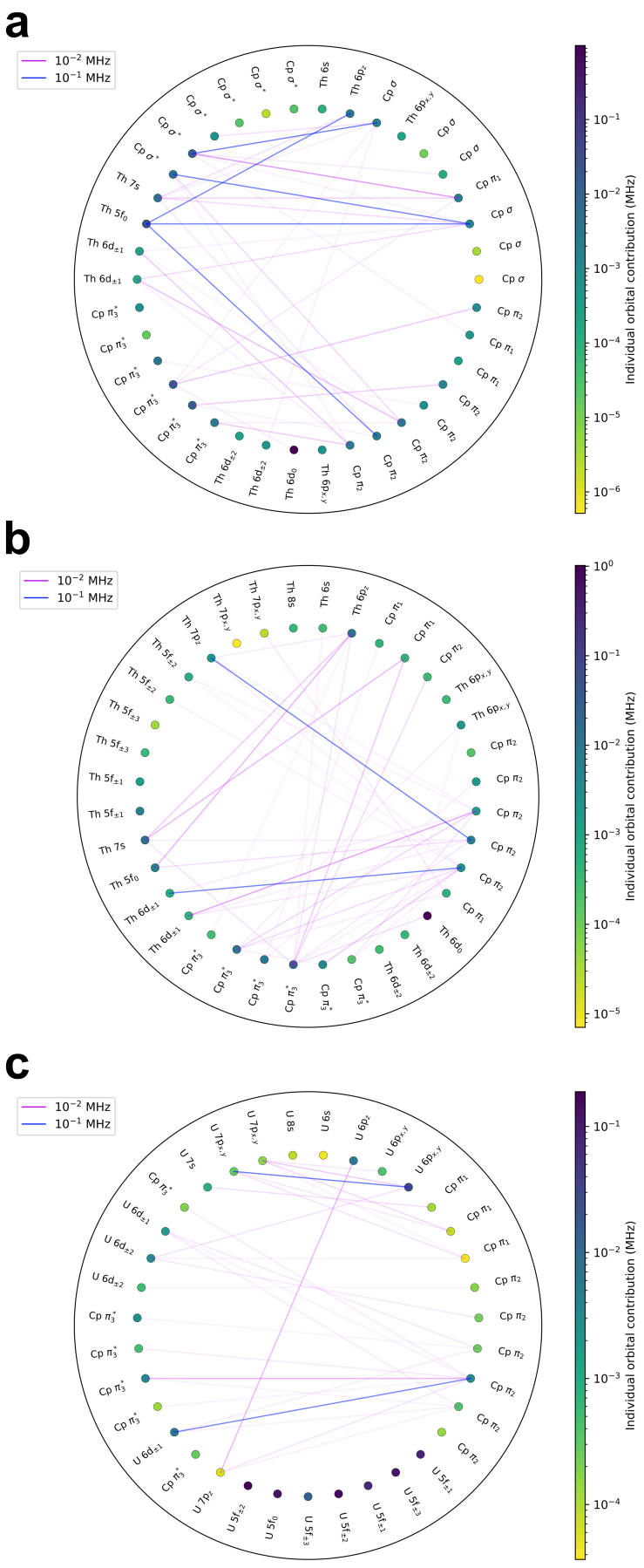

Figure S7: HFC orbital decomposition diagrams for nucleus C1 (as labelled in the XRD structure). Only pairwise contributions $> 10^{-2}$ MHz are shown. **a**: $ThCp_3^{tt}$, SF state 1 ($S = 1/2$), SS-RASSCF(39,38); **b**: $ThCp_3^{tt}$, SF state 1 ($S = 1/2$), SS-RASSCF(27,36); **c**: UCp_3^{tt}, SF state 4 ($S = 3/2$), SS-RASCI(29,35)

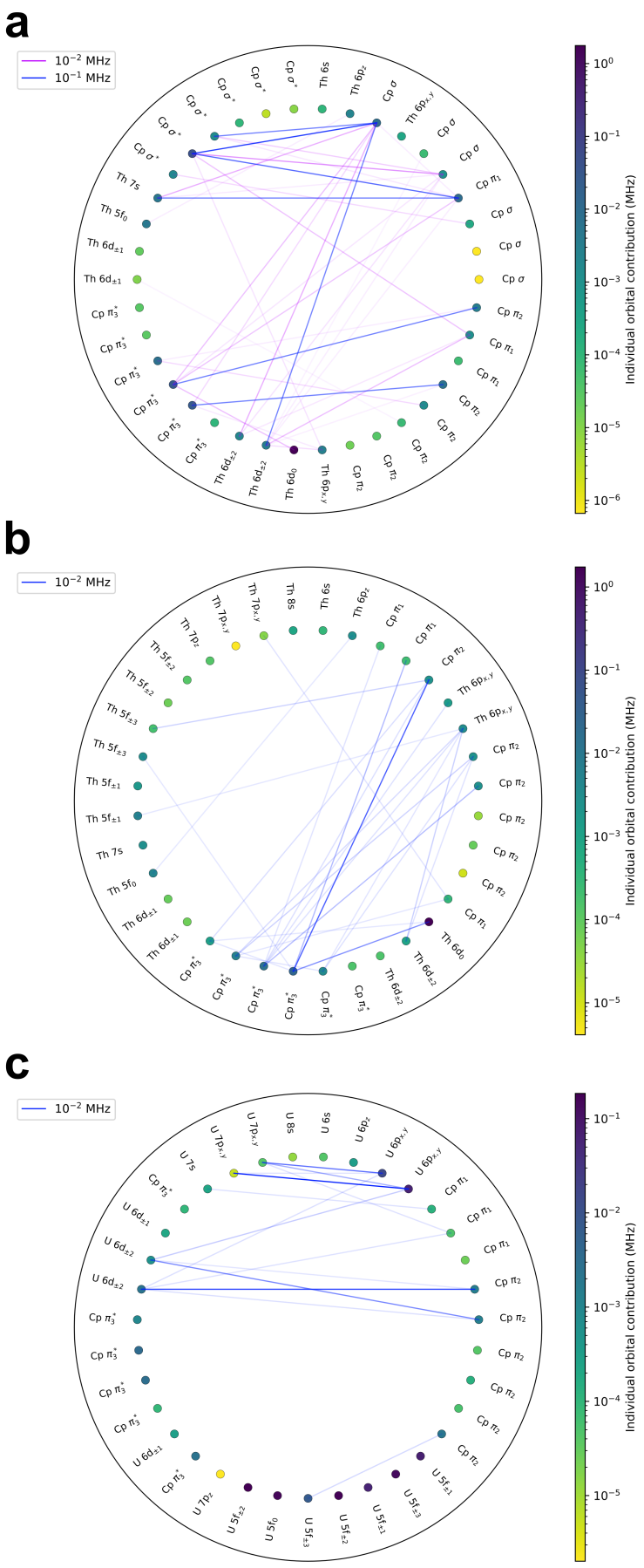

Figure S8: HFC orbital decomposition diagrams for nucleus C2 (as labelled in the XRD structure). Only pairwise contributions $> 10^{-2}$ MHz are shown. **a**: $ThCp_3^{tt}$, SF state 1 ($S = 1/2$), SS-RASSCF(39,38); **b**: $ThCp_3^{tt}$, SF state 1 ($S = 1/2$), SS-RASSCF(27,36); **c**: UCp_3^{tt}, SF state 4 ($S = 3/2$), SS-RASCI(29,35)

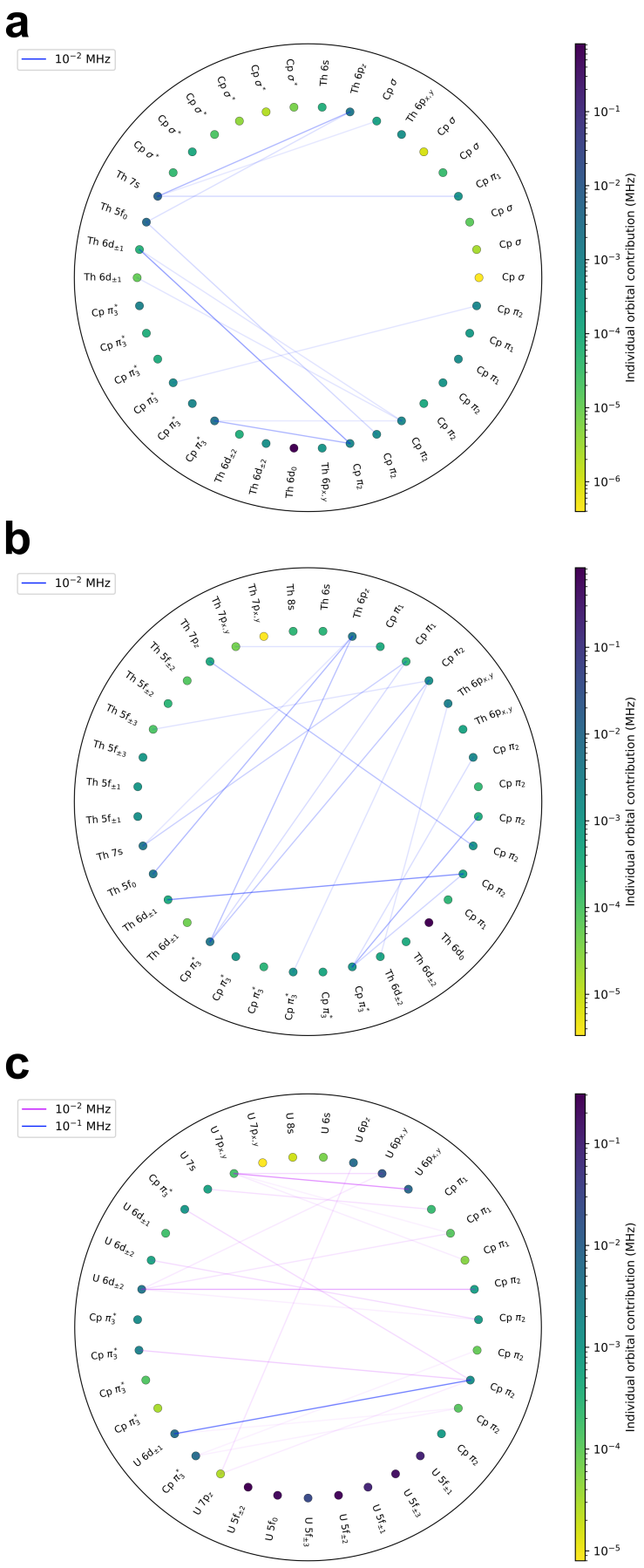

Figure S9: HFC orbital decomposition diagrams for nucleus C4 (as labelled in the XRD structure). Only pairwise contributions $> 10^{-2}$ MHz are shown. **a**: $ThCp_3^{tt}$, SF state 1 ($S = 1/2$), SS-RASSCF(39,38); **b**: $ThCp_3^{tt}$, SF state 1 ($S = 1/2$), SS-RASSCF(27,36); **c**: UCp_3^{tt}, SF state 4 ($S = 3/2$), SS-RASCI(29,35)

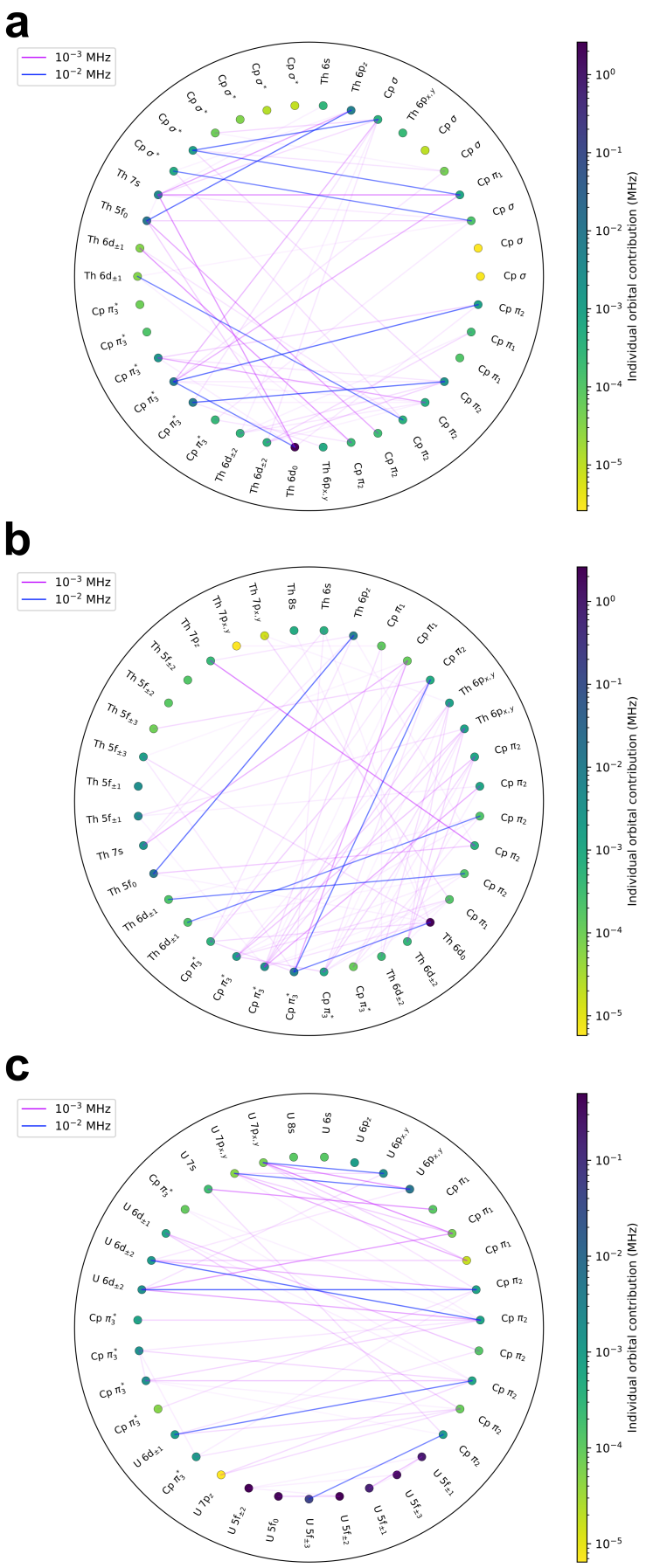

Figure S10: HFC orbital decomposition diagrams for nucleus H1 (as labelled in the XRD structure). Only pairwise contributions $> 10^{-3}$ MHz are shown. **a**: $ThCp_3^{tt}$, SF state 1 ($S = 1/2$), SS-RASSCF(39,38); **b**: $ThCp_3^{tt}$, SF state 1 ($S = 1/2$), SS-RASSCF(27,36); **c**: UCp_3^{tt}, SF state 4 ($S = 3/2$), SS-RASCI(29,35)

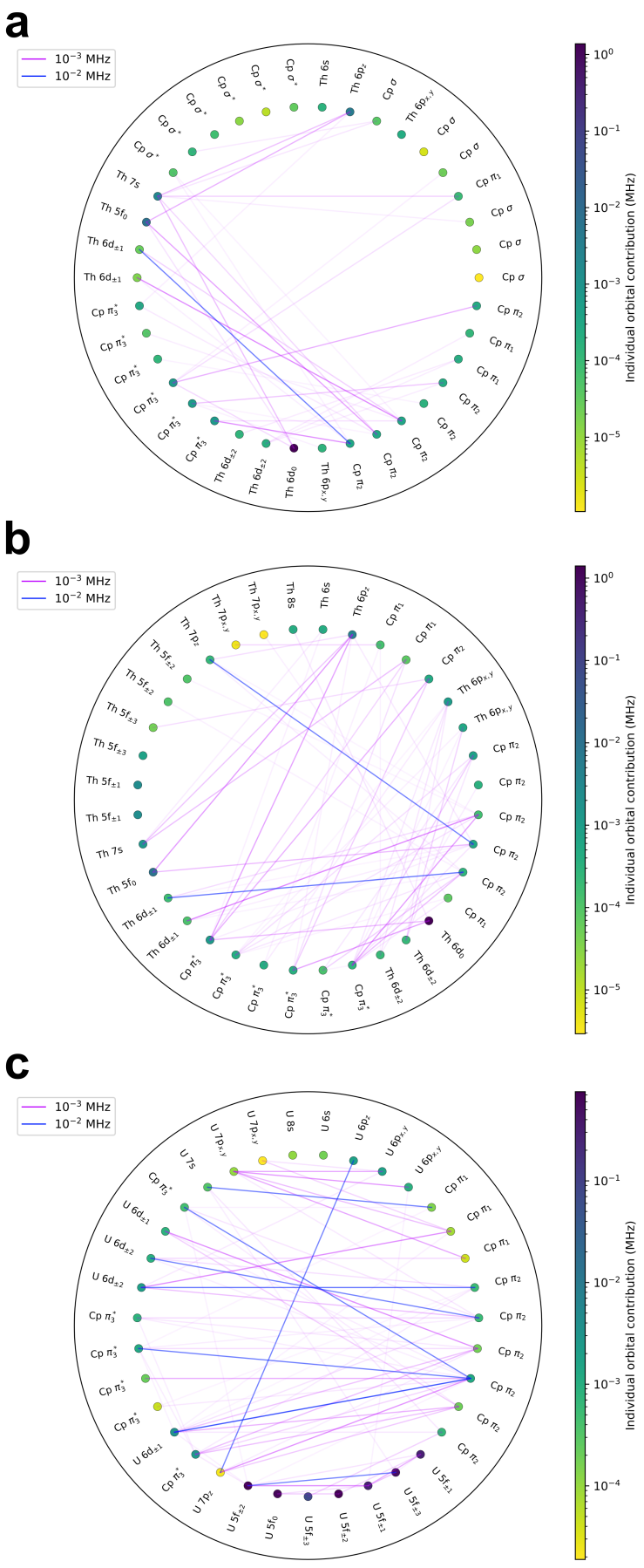

Figure S11: HFC orbital decomposition diagrams for nucleus H2 (as labelled in the XRD structure). Only pairwise contributions $> 10^{-3}$ MHz are shown. **a**: $ThCp_3^{tt}$, SF state 1 ($S = 1/2$), SS-RASSCF(39,38); **b**: $ThCp_3^{tt}$, SF state 1 ($S = 1/2$), SS-RASSCF(27,36); **c**: UCp_3^{tt}, SF state 4 ($S = 3/2$), SS-RASCI(29,35)

References

(1) M. Roger, L. Belkhiri, P. Thuéry, T. Arliguie, M. Fourmigué, A. Boucekkine and M. Ephritikhine, *Organometallics*, 2005, **24**, 4940–4952.

(2) E. J. Schelter, P. J. Hay, T. Cantat, K. C. Jantunen, D. E. Morris, B. L. Scott, C. J. Burns, J. L. Kiplinger and C. R. Graves, *Journal of the American Chemical Society*, 2008, **130**, 17537–17551.

(3) D. D. Schnaars, A. J. Gaunt, T. W. Hayton, M. B. Jones, I. Kirker, N. Kaltsoyannis, I. May, S. D. Reilly, B. L. Scott and G. Wu, *Inorganic Chemistry*, 2012, **51**, 8557–8566.

(4) M. P. Kelley, J. Su, M. Urban, M. Luckey, E. R. Batista, P. Yang and J. C. Shafer, *Journal of the American Chemical Society*, 2017, **139**, 9901–9908.

(5) W. W. Lukens, M. Speldrich, P. Yang, T. J. Duignan, J. Autschbach and P. Kögerler, *Dalton Transactions*, 2016, **45**, 11508–11521.

(6) D. C. Sergentu, T. J. Duignan and J. Autschbach, *Journal of Physical Chemistry Letters*, 2018, **9**, 5583–5591.

(7) M. Autillo, L. Guerin, T. Dumas, M. S. Grigoriev, A. M. Fedoseev, S. Cammelli, P. L. Solari, D. Guillaumont, P. Guilbaud, P. Moisy, H. Bolvin and C. Berthon, *Chemistry - A European Journal*, 2019, 4435–4451.

(8) S. L. Staun, D. C. Sergentu, G. Wu, J. Autschbach and T. W. Hayton, *Chemical Science*, 2019, **10**, 6431–6436.

(9) A. Formanuik, A.-M. M. Ariciu, F. Ortu, R. Beekmeyer, A. Kerridge, F. Tuna, E. J. L. McInnes and D. P. Mills, *Nature Chemistry*, 2017, **9**, 578–583.

(10) M. Bennati, *eMagRes*, 2017, **6**, 271–282.

(11) W. Kutzelnigg, *Theoretica Chimica Acta*, 1988, **73**, 173–200.

(12) K. G. Dyall and K. Fægri, Jr., *Introduction to relativistic quantum chemistry*, Oxford University Press, New York, 2007.

(13) B. O. Roos, *International Journal of Quantum Chemistry*, 1980, **14**, 175–189.

(14) P. Å. Malmqvist, A. Rendell and B. O. Roos, *Journal of Physical Chemistry*, 1990, **94**, 5477–5482.

(15) P. Å. Malmqvist, B. O. Roos and B. Schimmelpfennig, *Chemical Physics Letters*, 2002, **357**, 230–240.

(16) L. F. Chibotaru, Ab Initio Methodology for Pseudospin Hamiltonians of Anisotropic Magnetic Complexes, in *Advances in Chemical Physics*, John Wiley & Sons, Ltd, 2013, pp. 397–519.

(17) F. Aquilante, J. Autschbach, A. Baiardi, S. Battaglia, V. A. Borin, L. F. Chibotaru, I. Conti, L. De Vico, M. Delcey, I. F. Galván, N. Ferré, L. Freitag, M. Garavelli, X. Gong, S. Knecht, E. D. Larsson, R. Lindh, M. Lundberg, P. Å. Malmqvist, A. Nenov, J. Norell, M. Odelius, M. Olivucci, T. B. Pedersen, L. Pedraza-González, Q. M. Phung, K. Pierloot, M. Reiher, I. Schapiro, J. Segarra-Martí, F. Segatta, L. Seijo, S. Sen, D. C. Sergentu, C. J. Stein, L. Ungur, M. Vacher, A. Valentini and V. Veryazov, *Journal of Chemical Physics*, 2020, **152**, 214117.

(18) B. O. Roos, R. Lindh, P. Å. Malmqvist, V. Veryazov and P. O. Widmark, *Journal of Physical Chemistry A*, 2004, **108**, 2851–2858.

(19) B. O. Roos, V. Veryazov and P. O. Widmark, *Theoretical Chemistry Accounts.*, 2004, **111**, 345–351.

(20) B. O. Roos, R. Lindh, P. Å. Malmqvist, V. Veryazov and P. O. Widmark, *Chemical Physics Letters*, 2005, **409**, 295–299.

(21) B. O. Roos, R. Lindh, P. Å. Malmqvist, V. Veryazov and P. O. Widmark, *Journal of Physical Chemistry A*, 2005, **109**, 6575–6579.

(22) B. O. Roos, R. Lindh, P. Å. Malmqvist, V. Veryazov, P. O. Widmark and A. C. Borin, *Journal of Physical Chemistry A*, 2008, **112**, 11431–11435.

(23) S. Stoll and A. Schweiger, *Journal of Magnetic Resonance*, 2006, **178**, 42–55.

(24) S. Stoll and R. D. Britt, *Physical Chemistry Chemical Physics*, 2009, **11**, 6614–6625.

(25) R. S. Mulliken, *Journal of Chemical Physics*, 1955, **23**, 1833.

(26) G. L. Manni, S. D. Smart and A. Alavi, *Journal of Chemical Theory and Computation*, 2016, **12**, 1245–1258.

(27) S. Knecht, E. D. Hedegård, S. Keller, A. Kovyrshin, Y. Ma, A. Muolo, C. J. Stein and M. Reiher, *CHIMIA*, 2016, **70**, 244–251.

(28) S. Battaglia, S. Keller and S. Knecht, *Journal of Chemical Theory and Computation*, 2018, **14**, 2353–2369.

(29) J. E. Smith, B. Mussard, A. A. Holmes and S. Sharma, *Journal of Chemical Theory and Computation*, 2017, **13**, 5468–5478.

(30) Q. Sun, J. Yang and G. K. L. Chan, *Chemical Physics Letters*, 2017, **683**, 291–299.

(31) P. Belanzoni, E. Van Lenthe and E. J. Baerends, *Journal of Chemical Physics*, 2001, **114**, 4421–4433.

(32) P. O. Löwdin, *Advances in Quantum Chemistry*, 1970, **5**, 185–199.

(33) F. L. Hirshfeld, *Theoretica Chimica Acta*, 1977, **44**, 129–138.

(34) A. E. Reed and F. Weinhold, *Journal of Chemical Physics*, 1985, **83**, 1736–1740.

(35) R. F. Bader, *Chemical Reviews*, 1991, **91**, 893–928.

(36) L. Gagliardi, R. Lindh and G. Karlström, *Journal of Chemical Physics*, 2004, **121**, 4494–4500.

(37) F. Neese, *eMagRes*, 2017, **6**, 1–22.

Chapter 6

Conclusion

This work represents an exploration of actinide bonding through the lens of magnetic properties, using *ab initio* CASSCF-SO and RASSCF-SO techniques to describe the electronic structure. We describe Hyperion, a new software package implemented to compute relativistic picture-change-corrected g-values and HFCCs from active space wavefunctions, with relativistic effects included via the SF-X2C formalism. Additionally, we present a novel orbital decomposition approach, implemented as part of Hyperion, designed to inform the active space selection process by providing insight into the orbital interactions underlying predicted HFCCs.

We observe that, within a CASSCF-SO/RASSCF-SO framework, the number of optimised roots in a strongly SO-coupled system has the most significant impact on the accuracy of predicted magnetic properties. This number should be large enough to ensure an adequate basis of spin-free states is used to represent the SO Hamiltonian; however, MO state-averaging, which is a feature of all multi-state MCSCF algorithms, worsens the quality of the lowest energy wavefunction(s), leading to erroneous predictions of magnetisation and other related properties. As ligand effects are weaker than inter-electron repulsion and SOC for all SO-coupled systems studied herein, Russel-Saunders coupling principles can be applied to choose an optimal set of roots.

Our findings suggest that the best active space choice is dictated by which molecular property is targeted; in particular, although a good description of the electronic structure – as quantified by electronic energies – is achievable with a relatively small number of active orbitals, more expansive active space selections are necessary if accurate HFCCs are desired. Naturally, the principles of quantum chemistry dictate that calculated properties are only reliable if they are based on a qualitatively correct wavefunction, hence, in the *ab initio* study of molecular properties, good wavefunctions are a pre-requisite.

Based on the An complexes studied herein, and using predicted magnetic properties to judge accuracy, we deduce that molecules containing hard ligands, such as the oxo and imido groups in *Paper one*, are best described using a minimal CAS(N,7), where N is the number of 5f electrons. Meanwhile, the influence of soft ligands, such as Cp^{tt} in *Paper three*, can only be captured by correlating frontier bonding and antibonding ligand orbitals, in addition to An valence orbitals. We note, however, that these conclusions are based on a small number of An molecules and should therefore be verified by investigating a larger

number of complexes.

Finally, we show that the combined theoretical and experimental study of hyperfine coupling in An molecules is a promising approach for investigating the intricacies of An bonding. However, care must be taken to account for SR and SOC relativistic effects at the appropriate level of theory. The *ab initio* electronic structure description can be fine-tuned by benchmarking against experimental HFCCs or, where these cannot be easily determined, against HYSCORE spectra. Subsequently, spin delocalisation can be quantified via Mulliken spin population and used to draw conclusions about An covalency.

Chapter 7

Outlook

We have introduced a new strategy for studying actinide covalency, based on *ab initio* determinations of HFCCs using the Hyperion package; there is significant potential for further refinement, and this chapter outlines some possible future directions. Although only traditional CASSCF-SO and RASSCF-SO algorithms are employed herein, newer implementations, such as DMRGSCF[1,2] or stochastic CASSCF,[3] can potentially unlock further insight into An bonding by making larger active spaces accessible. The choice of electronic structure method should be made on a case-by-case basis, taking into account the system size and symmetry (or lack thereof) and using chemical intuition to assess the bonding interactions (e.g. hard/soft ligands, An-An bonds). It is possible that one quantum chemistry program does not provide any suitable algorithms to treat a particular system; for such situations, we emphasise that Hyperion is a stand-alone package, which can easily be extended to allow inputs from other software, such as PySCF,[4] which provides a number of novel multiconfigurational electronic structure algorithms,[5–7] and DIRAC,[8] which can determine molecular properties within a fully relativistic 4-component framework.

There is scope for improvement in the theoretical framework underlying Hyperion; in particular, an X2C-based formalism for including SOC in the wavefunction[9] would make the present approach more consistent. Additionally, Hyperion's orbital decomposition scheme could be made more powerful by using a perturbed spin density matrix – determined via a perturbative electronic structure algorithm – to compute approximate HFC matrices (and, hence, the orbital decomposition matrix $\mathcal{M}$) in the full orbital basis, instead of just the active space. This strategy is inspired by the so-called "B_K and A_K method" used in an early HFC study to quantify the orbital contributions neglected by multireference CI approximations.[10] Currently, it is unclear which perturbative method is best suited for this application and whether this idea is computationally feasible for experimentally-relevant molecules. Although the B_K and A_K method appears to have been relegated to the past, similar strategies could potentially fare better in the current context of electronic structure theory, given the variety of perturbative techniques available and their rapid advancement.[11–14]

Perhaps the most important future development is the implementation of NMR shifts within Hyperion. Relativistic paramagnetic (pNMR) shifts can be straightforwardly incorporated within the currently-used RKB-based formalism. To ensure that the pNMR shifts can be computed for electronic states of arbitrary degeneracy, the RKB-based formalism is best

combined with Soncini and Van Den Heuvel's approach,[15–17] which was previously employed in non-relativistic *ab initio* studies.[18–22] Note, however, that a secondary (diamagnetic) reference must be used to extract pNMR shifts from experimental NMR spectra; the diamagnetic reference should be similar to the original molecule, such that differences between the diamagnetic contributions to the NMR shifts are minimised. In practice, diamagnetic NMR shift variations are on the order of 1 ppm, which is negligible for all magnetic nuclei except for ^{1}H.[21] Therefore, approaches that only compute pNMR shifts are unsuitable for ^{1}H NMR, as theoretical predictions cannot be benchmarked against reliable experimental quantities.

Diamagnetic NMR shifts are more challenging to determine *ab initio*, particularly in relativistic theory, as a diamagnetic term does not appear in the field-dependent Dirac Hamiltonian when the RKB approximation is used.[23] Most previous work on *ab initio* full NMR shifts – including both the diamagnetic and the paramagnetic contributions – uses Kohn-Sham DFT methods; this is true for both non-relativistic[24,25] and relativistic studies.[26–32] There is currently a lack of knowledge around relativistic, multiconfigurational models of full NMR shifts and, consequently, a lack of computational tools developed for this purpose. The most straightforward solution to this problem is to use non-relativistic property operators and only include relativistic effects in the wavefunction optimisation; however, this introduces a picture-change error which, if significant, can invalidate the result.

Alternatively, the Restricted Magnetic Balance (RMB)[28] approximation or the Orbital Decomposition Approach[†] (ODA)[26,27] can be used to obtain relativistic perturbation operators that include a diamagnetic contribution. To date, existing applications of RMB and ODA are exclusively DFT-based; to the best of our knowledge, neither have been implemented within a multiconfigurational framework. It is worth noting, however, that replacing the RKB condition with RMB in our formalism also requires changing the operators used for first-order properties (g-values and HFCCs), as well as the X2C transformation and the X2C-decoupled zeroth order Hamiltonian. The last two pose some practical difficulties, as any changes to the X2C procedure have to be implemented in the electronic structure software, unless support for Hamiltonians computed externally is available.

Finally, there is a renewed interest in local approximations (diagonal local approximation to the unitary decoupling matrix, DLU) to relativistic decoupling methods, as suggested by recent literature;[29–32] Franzke *et al* recently derived and implemented a DLU-X2C model of NMR shielding tensors within unrestricted DFT.[30–32] Although an extension to multiconfigurational theories is, once again, not obvious, DLU methods have a lower computational cost relative to their non-local counterparts, and are hence worth considering for applications to large molecules.

[†]The ODA approach, used in relativistic calculations of second-order magnetic properties, should not be confused with the HFC orbital decomposition scheme proposed in *Paper two* of this thesis. The two are only similar in name.

References

(1) S. Knecht, E. D. Hedegård, S. Keller, A. Kovyrshin, Y. Ma, A. Muolo, C. J. Stein and M. Reiher, *CHIMIA*, 2016, **70**, 244–251.

(2) S. Battaglia, S. Keller and S. Knecht, *Journal of Chemical Theory and Computation*, 2018, **14**, 2353–2369.

(3) G. L. Manni, S. D. Smart and A. Alavi, *Journal of Chemical Theory and Computation*, 2016, **12**, 1245–1258.

(4) Q. Sun, X. Zhang, S. Banerjee, P. Bao, M. Barbry, N. S. Blunt, N. A. Bogdanov, G. H. Booth, J. Chen, Z. H. Cui, J. J. Eriksen, Y. Gao, S. Guo, J. Hermann, M. R. Hermes, K. Koh, P. Koval, S. Lehtola, Z. Li, J. Liu, N. Mardirossian, J. D. McClain, M. Motta, B. Mussard, H. Q. Pham, A. Pulkin, W. Purwanto, P. J. Robinson, E. Ronca, E. R. Sayfutyarova, M. Scheurer, H. F. Schurkus, J. E. Smith, C. Sun, S. N. Sun, S. Upadhyay, L. K. Wagner, X. Wang, A. White, J. D. Whitfield, M. J. Williamson, S. Wouters, J. Yang, J. M. Yu, T. Zhu, T. C. Berkelbach, S. Sharma, A. Y. Sokolov and G. K. L. Chan, *Journal of Chemical Physics*, 2020, **153**.

(5) J. E. Smith, B. Mussard, A. A. Holmes and S. Sharma, *Journal of Chemical Theory and Computation*, 2017, **13**, 5468–5478.

(6) Q. Sun, J. Yang and G. K. L. Chan, *Chemical Physics Letters*, 2017, **683**, 291–299.

(7) M. R. Hermes, R. Pandharkar and L. Gagliardi, *Journal of Chemical Theory and Computation*, 2020, **16**, 4923–4937.

(8) T. Saue, R. Bast, A. S. P. Gomes, H. J. A. Jensen, L. Visscher, I. A. Aucar, R. Di Remigio, K. G. Dyall, E. Eliav, E. Fasshauer, T. Fleig, L. Halbert, E. D. Hedegård, B. Helmich-Paris, M. Iliaš, C. R. Jacob, S. Knecht, J. K. Laerdahl, M. L. Vidal, M. K. Nayak, M. Olejniczak, J. M. H. Olsen, M. Pernpointner, B. Senjean, A. Shee, A. Sunaga and J. N. van Stralen, *Journal of Chemical Physics*, 2020, **152**, 204104.

(9) J. Liu and L. Cheng, *Journal of Chemical Physics*, 2018, **148**.

(10) B. Engels, *Chemical Physics Letters*, 1991, **179**, 398–404.

(11) P. Pulay, *International Journal of Quantum Chemistry*, 2011, **111**, 3273–3279.

(12) S. Battaglia and R. Lindh, *Journal of Chemical Theory and Computation*, 2020, **16**, 1555–1567.

(13) C. Angeli, R. Cimiraglia and J.-P. Malrieu, *Journal of Chemical Physics*, 2002, **117**, 9138–9153.

(14) L. Freitag, S. Knecht, C. Angeli and M. Reiher, *Journal of Chemical Theory and Computation*, 2017, **13**, 451–459.

(15) W. Van Den Heuvel and A. Soncini, *Physical Review Letters*, 2012, **109**, 13–17.

(16) W. Van Den Heuvel and A. Soncini, *Journal of Chemical Physics*, 2013, **138**.

(17) A. Soncini and W. Van Den Heuvel, *Journal of Chemical Physics*, 2013, **138**.

(18) F. Gendron, B. Pritchard and J. Autschbach, *Inorganic Chemistry*, 2014, **53**, 8577–8592.

(19) F. Gendron, K. Sharkas and J. Autschbach, *Journal of Physical Chemistry Letters*, 2015, **6**, 2183–2188.

(20) B. Martin and J. Autschbach, *Journal of Chemical Physics*, 2015, **142**.

(21) J. Autschbach, *NMR calculations for paramagnetic molecules and metal complexes*, Elsevier Ltd, 2015, vol. 11, pp. 3–36.

(22) F. Gendron and J. Autschbach, *Journal of Chemical Theory and Computation*, 2016, **2**.

(23) W. Kutzelnigg, *Physical Review A - Atomic, Molecular, and Optical Physics*, 2003, **67**, 12.

(24) G. L. Stoychev, A. A. Auer and F. Neese, *Journal of Chemical Theory and Computation*, 2018, **14**, 4756–4771.

(25) L. Lang, E. Ravera, G. Parigi, C. Luchinat and F. Neese, *Journal of Physical Chemistry Letters*, 2020, **11**, 8735–8744.

(26) Y. Xiao, W. Liu, L. Cheng and D. Peng, *Journal of Chemical Physics*, 2007, **126**, 44102.

(27) Y. Xiao, D. Peng and W. Liu, *Journal of Chemical Physics*, 2007, **126**, 081101.

(28) S. Komorovský, M. Repiský, O. L. Malkina, V. G. Malkin, I. Malkin Ondík and M. Kaupp, *Journal of Chemical Physics*, 2008, **128**.

(29) Y. J. Franzke and J. M. Yu, *Journal of Chemical Theory and Computation*, 2022, **18**, 323–343.

(30) Y. J. Franzke and F. Weigend, *Journal of Chemical Theory and Computation*, 2019, **15**, 1028–1043.

(31) Y. J. Franzke, F. Mack and F. Weigend, *Journal of Chemical Theory and Computation*, 2021.

(32) S. Gillhuber, Y. J. Franzke and F. Weigend, *Journal of Physical Chemistry A*, 2021, **125**, 9707–9723.

Appendices

Appendix A

Number of CSFs in spin-adapted CASSCF

Herein we derive the number of high-spin configuration state functions (CSFs) which appear in the CI expansion of a spin-adapted CASSCF wavefunction. The number of active electrons, N_e, the number of active orbitals, N_o, and the spin quantum number, S, are regarded as fixed parameters.

The total number of Slater determinants that can be formed by distributing N_e electrons among $2N_\mathrm{o}$ spin-orbitals is

$$N_\mathrm{det}(N_\mathrm{e}, N_\mathrm{o}) = \binom{2N_\mathrm{o}}{N_\mathrm{e}}. \tag{A.1}$$

Slater determinants are eigenfunctions of the spin projection operator, $\widehat{S}_z$, and hence have a well-defined spin projection M. The number of Slater determinants with a specific M can be expressed as all possible arrangements of N_α *spin-up* electrons among N_o α-spin-orbitals, multiplied by all possible arrangements of N_β *spin-down* electrons among N_o β-spin-orbitals: [1]

$$N_M^\mathrm{det} = \binom{N_\mathrm{o}}{N_\alpha}\binom{N_\mathrm{o}}{N_\beta} = \binom{N_\mathrm{o}}{N_\mathrm{e}/2 + M}\binom{N_\mathrm{o}}{N_\mathrm{e}/2 - M}. \tag{A.2}$$

Reference [1] provides a general equation relating the number of high-spin ($S = M$) CSFs to the number of Slater determinants:

$$N_{S=M,M}^\mathrm{CSF} = N_M^\mathrm{det} - N_{M+1}^\mathrm{det}. \tag{A.3}$$

As only high-spin configurations are required for spin-adapted CASSCF, we henceforth replace the spin projection quantum number M with the spin quantum number S.

Substituting Equation A.2 into A.3 yields

$$N_{S,M=S}^\mathrm{CSF} = \binom{N_\mathrm{o}}{N_\mathrm{e}/2 + S}\binom{N_\mathrm{o}}{N_\mathrm{e}/2 - S} - \binom{N_\mathrm{o}}{N_\mathrm{e}/2 + S + 1}\binom{N_\mathrm{o}}{N_\mathrm{e}/2 - S - 1}. \tag{A.4}$$

Expanding the binomial coefficients and creating a common denominator,

$$
\begin{aligned}
N_{S,M=S}^{\text{CSF}} = & \left[\left(\frac{N_\text{e}}{2}+S+1\right)\left(N_\text{o}-\frac{N_\text{e}}{2}+S+1\right)-\left(N_\text{o}-\frac{N_\text{e}}{2}-S\right)\left(\frac{N_\text{e}}{2}-S\right)\right] \\
& \times \frac{N_\text{o}!\; N_\text{o}!}{(N_\text{o}+1-{}^{N_\text{e}}\!/_2+S)!\;\;({}^{N_\text{e}}\!/_2-S)!\;\;(N_\text{o}-{}^{N_\text{e}}\!/_2-S)!\;\;({}^{N_\text{e}}\!/_2+S+1)!} \\
= & \; (2S+1)(N_\text{o}+1)\times\frac{1}{(N_\text{o}+1)^2}\times\frac{(N_\text{o}+1)!}{(N_\text{o}+1-{}^{N_\text{e}}\!/_2+S)!\;\;({}^{N_\text{e}}\!/_2-S)!} \\
& \times \frac{(N_\text{o}+1)!}{(N_\text{o}-{}^{N_\text{e}}\!/_2-S)!\;\;({}^{N_\text{e}}\!/_2+S+1)!}\,.
\end{aligned}
$$

Finally, we obtain

$$
N_{S,M=S}^{\text{CSF}} = \frac{2S+1}{N_\text{o}+1}\binom{N_\text{o}+1}{{}^{N_\text{e}}\!/_2-S}\binom{N_\text{o}+1}{{}^{N_\text{e}}\!/_2+S+1}, \tag{A.5}
$$

wherein the right-hand side is identical to that of Equation 2.5.

References

(1) T. Helgaker, P. Jørgensen and J. Olsen, *Molecular Electronic-Structure Theory*, John Wiley & Sons Ltd., 2000.